

PEOPLE'S DEMOCRATIC REPUBLIC OF ALGERIA
MINISTRY OF HIGHER EDUCATION AND SCIENTIFIC RESEARCH
M'HAMED BOUGARA-BOUMERDES UNIVERSITY



Faculty of Technology

Doctoral thesis

Presented by:

M. OULAD BRAHIM Abdelmoumin

With a view to obtaining a DOCTORATE degree in:
Major: Mechanical Engineering
Option: Mechanics and Engineering

Quantification and localization of cracks in steel specimens using improved artificial neural networks with experimental validation

In front of the jury composed of:

KADRI Mohamed	Professor	UMBB	President
BOUMEDIENE Faiza	Professor	USTHB	Examiner
DJEBILI Omar	Professor	UMBB	Examiner
AKNOUCHE Hamid	Professor	UMBB	Examiner
BELAIDI Idir	Professor	UMBB	Director
CAPOZUCCA Roberto	Professor	Polytechnic University of Marche	Co-Director
KHATIR Samir	Pr. Assistant	University of Ghent Belgium	Invited

Academic year 2022/2023

Abstract

Cracks in any structure are undesirable since they frequently lead to the structure's fracture or failure. API X 70 steel is a critical component in pipeline manufacturing; additionally, it is prone to cracking due to the harsh working conditions it is subjected during its service operation (s). The current fracture detection methods either require disassembly of the tube's substructure for visual inspection or external excitation of the relevant area of the tube for subsequent dynamic analyses...etc; as a result, these approaches are highly complex and time consuming. For crack identification in pipeline steel, a simplified crack identification approach is provided in this work. The crack identification method is straightforward and based on simple stress, strain, and displacement measurements of load and absorbed energy at recognized places. Finite Element Analysis was used in the study, which was done using ABAQUS, a well-known commercial finite element tool.

Intelligent systems have recently been praised for solving complicated difficult, multidimensional issues. Artificial neural networks (ANN) have had a lot of success in solving these challenges, although they do have some limitations. The current work examines the application of the WOA-ANN hybrid model for crack length prediction using various inputs such as strains, stresses, and displacements to assess the technique's accuracy. The proposed method is, nevertheless, compared to GA-ANN, AOA-ANN, and WOABAT-ANN. The use of ANN in combination with metaheuristic optimization techniques aims to increase its significance. The weight of neuronal connection is significant. Some biases are also linked to neurons. Based on the input and goal output values supplied, connection weights and biases are changed to give the least possible error function. This method is commonly referred to as back propagation (BP). The explored approach is relevant to real-world engineering applications and regulates the status of structures. The evolution of fracture mechanics parameters is studied using standard ASTM test specimens. After modeling the tests with the Finite Element Method (FEM), the numerical model is then evaluated with experimental test analysis. With the mesoscopic GTN damage model, FEM is utilized to analyze the tensile failure process of one-sided notch samples and extract the data required for WOA-ANN. Our model is now ready to forecast various scenarios after collecting the data. When compared to other crack detection approaches, the findings produced utilizing WOA-ANN is effective.

Keywords: API X 70 Steel, FEM-GTN damage model, GA-ANN, AOA-ANN, WOA-BAT-ANN, and Crack identification.

Résumé

Les fissures dans n'importe quelle structure sont indésirables car elles conduisent fréquemment à la fracture ou à la défaillance de la structure. L'acier API X 70 est un composant essentiel dans la fabrication de pipelines ; de plus, il est sujet à la fissuration en raison des conditions de travail difficiles auxquelles il est soumis lors de sa ou ses opérations de service. Les méthodes actuelles de détection de rupture nécessitent soit le démontage de la sous-structure du tube pour une inspection visuelle, soit une excitation externe de la zone concernée du tube pour des analyses dynamiques ultérieures...etc ; par conséquent, ces approches sont très complexes et prennent du temps. Pour l'identification des fissures dans l'acier des pipelines, une approche simplifiée d'identification des fissures est fournie dans ce travail. La méthode de détection des fissures est simple et basée sur de simples mesures de contrainte, de déformation et de déplacement de la charge et de l'énergie absorbée à des endroits reconnus. L'analyse par éléments finis a été utilisée dans l'étude, qui a été réalisée à l'aide d'ABAQUS, un outil d'éléments finis commercial bien connu. Les systèmes intelligents ont récemment été salués pour la résolution de problèmes complexes, difficiles et multidimensionnels. Les réseaux de neurones artificiels (RNA) ont eu beaucoup de succès dans la résolution de ces défis, bien qu'ils aient certaines limites. Les travaux en cours examinent l'application du modèle hybride WOA-ANN pour la prédiction de la longueur des fissures en utilisant diverses entrées telles que les déformations, les contraintes et les déplacements pour évaluer la précision de la technique. La méthode proposée est néanmoins comparée à GA-ANN, AOA-ANN et WOABAT-ANN. L'utilisation d'ANN en combinaison avec des techniques d'optimisation métaheuristique vise à accroître son importance. Le poids de la connexion neuronale est important. Certains biais sont également liés aux neurones. Sur la base des valeurs d'entrée et de sortie d'objectif fournies, les poids et biais de connexion sont modifiés pour donner la fonction d'erreur la plus faible possible. Cette méthode est communément appelée rétropropagation (BP). L'approche explorée est pertinente pour les applications d'ingénierie du monde réel et régule le statut des structures. L'évolution des paramètres de la mécanique de la rupture est étudiée à l'aide d'éprouvettes normalisées ASTM. Après avoir modélisé les tests avec la méthode des éléments finis (FEM), le modèle numérique est ensuite évalué avec une analyse expérimentale des tests. Avec le modèle de dommage mésoscopique GTN, FEM est utilisé pour analyser le processus de rupture en traction d'échantillons d'entaille unilatérale et extraire les données requises pour WOA-ANN. Notre modèle est maintenant prêt à prévoir divers scénarios après la collecte des données. Par rapport à d'autres approches de détection de fissures, les résultats obtenus à l'aide de WOA-ANN sont efficaces.

Mots-clés : Acier API X 70, modèle d'endommagement FEM-GTN, GA-ANN, AOA-ANN, WOA-BAT-ANN et identification des fissures.

الملخص

تعتبر ظاهرة الشقوق والتصدع في الأنابيب أو أي نوع من الهياكل ظاهرة غير مرغوب فيها، وتكون هذه الظاهرة ناجمة عن ظروف العمل القاسية التي قد تتعرض لها مختلف خطوط الأنابيب، والتي يعتبر الفولاذ APIX70 أحد أهم المكونات الرئيسية في تصنيعها.

قصد مواجهة هذه الظاهرة والحد منها، تتطلب الأمر إيجاد طرق وأساليب للكشف عن الكسور أو الشقوق، وذلك إما من خلال تفكيك البنية التحتية للأنبوب للفحص البصري، أو الإثارة الخارجية للمنطقة ذات الصلة من الأنبوب للتحليلات الديناميكية اللاحقة... الخ، ونظرا لأن ميزة هذه الأساليب التعقيد وأنها تستغرق وقتا طويلا للكشف عن الشقوق في خطوط الأنابيب الفولاذية، فإنه يتم اللجوء إلى آلية مبسطة للكشف عنها، تعتمد أساسا على قياسات الضغط والاجهاد والازاحة البسيطة للحمل والطاقة الممتصة في الأماكن المتعرف عليها، ثم استخدام العناصر المحددة في الدراسة، والتي تم إجراؤها باستخدام ABAQUS وهي أداة تجارية معروفة للعناصر المحددة.

تجدر الإشارة أنه في الآونة الأخيرة قد تم الإشادة بالأنظمة الذكية، من حيث قدرتها على حل المشكلات الصعبة للغاية والمتعددة الأبعاد، أين حققت الشبكات العصبية الاصطناعية ANN نجاحا كبيرا في حل هذه التحديات، على الرغم من وجود بعض القيود عليها.

يدرس العمل المقدم تطبيق النموذج الهجين WOA-ANN للتنبؤ بطول الشق باستخدام مدخلات مختلفة مثل السلالات والضغط والتجهيز من أجل تقييم دقة التقنية. الطريقة المقترحة، مع ذلك، بالمقارنة مع GA-ANN و AOA-ANN و WOABAT-ANN يهدف استخدام ANN مع تقنيات التحسين metaheuristic إلى زيادة أهميتها. وزن الاتصال العصبي مهم. ترتبط بعض التحيزات أيضاً بالخلايا العصبية. استناداً إلى قيم المدخلات والمخرجات الهدف المقدمة، يتم تغيير أوزان الاتصال والتحيزات لإعطاء أقل خطأ ممكن. يشار إلى أن هذه الطريقة عموماً تعرف باسم الانتشار الخلفي (BP) الطريقة المستكشفة ذات صلة بالتطبيقات الهندسية في العالم الحقيقي وتنظم حالة الهياكل، أين يتم دراسة تطور معلمات ميكانيكا الكسر باستخدام عينات اختبار ASTM القياسية. ثم يتم تقييم النموذج التحليلي من خلال تحليل الاختبار التجريبي بعد نمذجة الاختبارات باستخدام طريقة العناصر المحدودة (FEM) مع نموذج تلف GTN الوسيط، يتم استخدام FEM لتحليل عملية فشل الشد لعينات الشق من جانب واحد واستخراج البيانات المطلوبة لـ WOA-ANN. نمودجنا جاهز الآن للتنبؤ بالسيناريوهات المختلفة بعد جمع البيانات. عند مقارنتها بأساليب اكتشاف الشقوق الأخرى، تكون النتائج التي تم التوصل إليها باستخدام WOA-ANN فعالة .

الكلمات المفتاحية: فولاذ API X 70، نموذج ضرر FEM-GTN، GA-ANN، AOA-ANN، WOA-BAT-ANN، وتحديد الكراك.

Research Publications

Journal Articles

A Oulad Brahim, I Belaidi, Samir Khatir, E Magagnini, R Capozucca, M Abdel Wahab. Experimental crack identification of API X70 steel pipeline using improved Artificial Neural Networks based on Whale Optimization Algorithm. *Mechanics of Materials*, 2022. *Impact Factor: 4.137*

Doi: <https://doi.org/10.1016/j.mechmat.2021.104200>

A Oulad Brahim, Idir Belaidi, Samir Khatir, Erica Magagnini, Roberto Capozucca, Magd Abdel Wahab. Prediction of Gurson Damage Model Parameters Coupled with Hardening Law Identification of Steel X70 Pipeline Using Neural Network. *Metals and Materials International*, 2021. *Impact Factor: 3.451*

Doi: <https://doi.org/10.1007/s12540-021-01024-4>

A Oulad Brahim, Idir Belaidi, Samir Khatir, Erica Magagnini, Roberto Capozucca, Magd Abdel Wahab. Sensitivity analysis of the GTN damage parameters at different temperature for dynamic fracture propagation in X70 pipeline steel using neural network FRATTURA ED INTEGRITA STRUTTURALE 2021.

Doi: [10.3221/igf-esis.58.32](https://doi.org/10.3221/igf-esis.58.32)

A Oulad Brahim, I Belaidi , S. Khatir , C Le Thanh , S Mirjalili and M Abdel Wahab. Strength prediction of a steel pipe having a hemi-ellipsoidal corrosion defect repaired by GFRP composite patch using artificial neural network. *Composite Structures*. *Impact Factor: 6.603*

Doi: <https://doi.org/10.1016/j.compstruct.2022.116299>

A Oulad Brahim, I Belaidi , N. Fahem, S. Khatir . Prediction of the peak load and crack initiation energy of dynamic brittle fracture in X70 steel pipes using an improved artificial neural network and extended Finite Element Method. *Theoretical and Applied Fracture Mechanics* *Impact Factor: 4.374*

Doi: <https://doi.org/10.1016/j.tafmec.2022.103627>

N Fahem, I.Belaidi , **A.Oulad Brahim**, M.Noori , S.Khatir and M Abdel Wahab. Prediction of resisting force and tensile load reduction in GFRP composite materials using Artificial Neural Network-Enhanced Jaya Algorithm. *Composite Structures*. *Impact Factor: 6.603*

Doi: <https://doi.org/10.1016/j.compstruct.2022.116326>

A Zara, I Belaidi, **A Oulad Brahim**, , S Khatir, D Boutchicha, M Abdel Wahab. Damage detection in GFRP composite structures by Improved Artificial Neural Network using new optimization techniques. *Composite Structures*. *Impact Factor: 6.603*

Doi: <https://doi.org/10.1016/j.compstruct.2022.116475>

A Zara, I Belaidi, **A Oulad Brahim**, S Khatir, R Capozucca, M Abdel Wahab. Notch Depth Identification in CFRP Composite Beams Based on Modal Analysis Using Artificial Neural Network. Recent Advances in Structural Health Monitoring and Engineering Structures. [Doi: https://doi.org/10.1007/978-981-19-4835-0_7](https://doi.org/10.1007/978-981-19-4835-0_7)

Conference Proceedings

A Oulad Brahim, I Belaidi, S. Khatir, E. Magagnini and R. Capozucca. Best prediction for a patch design using BCMO in a cracked pipeline repaired by CFRP. The 10th International Conference on Fracture Fatigue and Wear (FFW 2022), *Ghent university, Belgium*.

A Oulad Brahim, I Belaidi, S. Khatir, E. Magagnini, R. Capozucca, and M. Abdel Wahab, A neural network based sensitivity analysis of the GTN damage parameters at different temperature for dynamic fracture propagation in X70 pipeline steel. *Ancona, Italy 2021*.

A Oulad Brahim, I Belaidi, S. Khatir, E. Magagnini and R. Capozucca. Experimental and numerical investigation of the notch-hole interaction in tensile test specimen of API X70 steel. *Vietnam, December 2020*.

N Fahem, I Belaidi, **A Oulad Brahim**, S Khatir, R Capozucca, C Le Thanh, and M Abdel Wahab, Whale optimization algorithm used to predict the load absorbed in a multicracks Composite plate. *Vietnam, 13 - 14 December 2021*.

K Leksir, S Lechab, I Belaidi, **A Oulad Brahim**, S Khatir, M Abdelwahab, Characterization of material & Prediction of the load in a cracked composite using Balancing Composite Motion Optimization (BCMO). *Vietnam, 13 - 14 December 2021*.

A Zara, I Belaidi, **A Oulad Brahim**, S Khatir, R Capozucca, C Le Thanh and M Abdel Wahab, Damage identification in CFRP composite beams based on modal analysis using an artificial neural network. *Vietnam, 13 - 14 December 2021*.

Supervisors:

Prof. Belaidi Idir

Prof. Roberto Capozucca.

Examination Committee:

President:	KADRI	Mohammed	Pr	Boumerdes University.
Supervisor:	BELAIDI	Idir	Pr	Boumerdes University.
Co- Supervisor:	CAPOZUCCA	Roberto	Pr	PUM.Italy.
Examiner:	BOUMEDIENE	Faiza	Pr	Bab Ezzouar University.
Examiner:	DJEBILI	Omar	Pr	Boumerdes University.
Examiner:	AKNOUCHE	Hamid	Pr	Boumerdes University.
Invited:	KHATIR	Samir	Pr/Assistant	Ghent University .Belgium.

Research Institute

UMBB University Faculty of Science and technologic, Department of Mechanical Engineering,
LEMI Laboratory

Boumerdes [Tel:+213699406361](tel:+213699406361) [Email: a.ouladbrahim@univ-boumerdes.dz](mailto:a.ouladbrahim@univ-boumerdes.dz) /moumindoc@gmail.com.

Dedicate to my parents

Acknowledgements

I would like to express my deep gratitude to my supervisors, Prof. Belaidi Idir and Prof. Roberto Capozucca, for their patient guidance and valuable advice throughout my research. Without their wholehearted help, consistent support, and encouragement, this work would not have been completed.

I am also thankful to Prof. Khatir Samir from the Laboratory Soete, Department of Electrical Energy, Systems, and Automation, Faculty of Engineering and Architecture, Ghent University, for his kind support and outstanding discussions during my research, which focused on optimization techniques for different kinds of structures.

My heartfelt thanks go to my friends, Mr. Fahem Noureddine, Mr. Zara Abdel Djebbar, and Ms. Zenzen Roumaissa, for their valuable discussions, advice, and encouragement throughout my academic journey.

Additionally, I would like to extend my gratitude to my colleagues at Laboratory LEMI for their kind help and friendly support during my research.

Lastly, my most enormous gratitude goes to my family, especially my parents (Azzeddine, Abdelkadder, Djihad, and Imane), for their unconditional support, love, and encouragement throughout my studies. Their belief in me has been a constant source of motivation and inspiration.

Oulad Brahim Abdelmoumin

UMBB University

July 2023

Table of contents

ABSTRACT	II
الملخص	IV
RESEARCH PUBLICATIONS	V
DEDICATE TO MY PARENTS.....	VIII
ACKNOWLEDGEMENTS.....	IX
TABLE OF CONTENTS.....	X
LIST OF FIGURES	XIV
LIST OF TABLES	XVII
LIST OF SYMBOLS AND ABBREVIATIONS	XVIII
GENERAL INTRODUCTION	XXV
CHAPTER 1: A LITERATURE REVIEW	29
1.1 INTRODUCTION.....	30
1.2 CRACK IDENTIFICATION RESEARCH BACKGROUND.....	31
1.3 A BRIEF INTRODUCTION TO CRACK MODELING	36
1.4 A REVIEW OF CRACK IDENTIFICATION BASED ON STATIC ANALYSIS	37
1.5 DAMAGE ASSESSMENT USING MODAL ANALYSIS	38
1.6 A REVIEW OF NUMERICAL SIMULATION METHODS AND IANNS.....	40
1.7 CONCLUSION.....	46
CHAPTER 2: OVERVIEW OF THE MECHANICS OF PIPELINE MATERIALS AND THE NUMERICAL TECHNIQUES USED.....	47
2.1 INTRODUCTION.....	48
2.2 MAIN CAUSES OF PIPELINE FAILURES	48
2.2.1 Introduction.....	48

2.2.2	<i>Pipeline failures</i>	49
2.3	STEEL.....	50
2.3.1	<i>Classification of steels</i>	51
2.3.2	<i>Welding of carbon steels</i>	52
2.3.3	<i>Weldability of carbon and low alloy steels</i>	54
2.3.4	<i>High elastic limit steels</i>	55
2.3.5	<i>Submerged welding in powder form</i>	56
2.3.6	<i>Process description</i>	56
2.3.7	<i>Application domain</i>	57
2.3.8	<i>Welding defects</i>	58
2.4	FRACTURE MECHANICS	59
2.4.1	<i>General</i>	59
2.4.2	<i>Introduction to linear fracture mechanics</i>	60
2.4.3	<i>Notions of fracture mechanics</i>	60
2.4.3.1	Flat elasticity reminders	60
2.4.3.2	Available energy rate G.....	62
2.4.3.3	Stress intensity factor K.....	63
2.4.4	<i>Application of the finite element method to fracture mechanics</i>	67
2.4.5	<i>Finite element method</i>	68
2.4.5.1	Basic principle.....	68
2.4.5.2	Crack definition.....	68
2.4.6	<i>Cracks in cylindrical pipes under pressure</i>	69
2.5	NEURAL NETWORKS	69
2.5.1	<i>Definition</i>	69
2.5.2	<i>The principal idea</i>	69
2.5.3	<i>Benefits of ANNs</i>	71
2.5.4	<i>Design and types of ANN</i>	72
2.5.5	<i>ANN mechanism</i>	72
2.5.6	<i>Modeling by artificial neural networks (ANN)</i>	73
2.5.6.1	Introduction	73
2.5.6.2	Backpropagation Multilayer Neural Networks	73
2.5.6.3	Learning phase	75
2.5.6.4	Entering data	75
2.5.6.5	Error calculation.....	76
2.5.7	<i>Modification of synaptic weights linking the output layer</i>	76
2.5.8	<i>Recognition (test) and validation phase</i>	79
2.5.8.1	Backpropagation multilayer neural network performance.....	79
2.5.8.2	Methodology and implementation.....	80

2.5.8.3	Programming language used	80
2.5.8.4	Development of ANN models	82
2.6	CONCLUSION	83

CHAPTER 3: PREDICTION OF GTN PARAMETERS USING CHEMICAL

PROPERTIES85

3.1	INTRODUCTION	86
3.2	GTN MODEL CONSTITUTIVE DESCRIPTION	86
3.3	GTN MODEL AND HARDENING PARAMETERS IDENTIFICATION	88
3.4	IDENTIFICATION STRATEGY	89
3.5	PROCEDURE FOR IDENTIFYING MODEL PARAMETERS.....	91
3.6	RESULTS AND DISCUSSIONS	91
3.7	EXPERIMENTAL METHODOLOGY FOR THE ANNGTN MODEL	93
3.8	EXPERIMENTAL AND NUMERICAL ANALYSES	98
3.8.1	<i>Chemical composition of X70 steels used in this work.....</i>	98
3.8.1.1	Preparation of the specimen	98
3.8.1.2	Presentation of results.....	99
3.8.1.3	Analysis and interpretation of results	100
3.8.2	<i>HV10 microhardness test</i>	100
3.8.2.1	Preparation of specimens.....	101
3.8.2.2	Performing microhardness tests.....	102
3.8.2.3	Presentation of results.....	102
3.8.2.4	Results and discussions	104
3.8.3	<i>Experimental Tensile test on a steel pipeline specimen</i>	104
3.8.4	<i>Charpy Test</i>	107
3.9	FINITE ELEMENT MODELLING	108
3.10	RESULTS AND DISCUSSION	110
3.11	PREDICTING AND ANALYZING OF INITIATION AND MAXIMUM IMPACT LOADING.....	119
3.11.1	<i>Artificial neural network (ANN)</i>	119
3.11.2	<i>Results and discussion</i>	121
3.12	CONCLUSION	122

CHAPTER 4: IDENTIFICATION OF A SINGLE CRACK LENGTH IN API X 70 STEEL USING STRESS, STRAIN AND DISPLACEMENT125

4.1	INTRODUCTION	126
4.2	EXPERIMENTAL CRACK IDENTIFICATION OF API X70 STEEL PIPELINE USING IMPROVED ARTIFICIAL NEURAL NETWORKS BASED ON WHALE OPTIMIZATION ALGORITHM.....	126
4.2.1	<i>Numerical models.....</i>	126

4.2.2	<i>Load-displacement simulation curve</i>	128
4.3	EXPERIMENTAL TENSILE TEST OF PIPELINE STEEL	130
4.3.1	<i>The tensile test of a specimen without crack</i>	130
4.3.2	<i>The tensile test of a specimen with cracks</i>	132
4.4	IMPROVED ARTIFICIAL NEURAL NETWORK FOR CRACK PREDICTION USING WOA	134
4.5	RESULTS AND DISCUSSION	136
4.6	CONCLUSION	144

CHAPTER 5: PREDICTION OF THE PEAK LOAD AND CRACK INITIAL ENERGY OF DYNAMIC BRITTLE FRACTURE USING IMPROVED ANN145

5.1	INTRODUCTION.....	146
5.2	COHESIVE SEGMENT APPROACH BASED ON EXTENDED FINITE ELEMENTS.....	146
5.3	EXPERIMENTAL	149
5.3.1	<i>Material characteristics of API X70 steel</i>	149
5.3.2	<i>DWTT specimens and experimental set up</i>	150
5.3.3	<i>CVN specimens and experimental set up</i>	151
5.3.4	<i>Experimental results</i>	152
5.3.4.1	DWTT impact.....	152
5.3.4.2	CVN impact.....	153
5.4	SIMULATION OF CVN IMPACT AND DETERMINATION OF PEAK LOAD AND ABSORBED ENERGY IN DIFFERENT CRACK LENGTHS.....	155
5.4.1	<i>Model dimensions and meshes</i>	155
5.4.2	<i>Material parameters</i>	156
5.4.3	<i>Results and discussion</i>	157
5.5	OPTIMIZATION TECHNIQUE.....	159
5.5.1	<i>Initialization part (Balancing composite motion optimization (BCMO))</i>	159
5.5.2	<i>Identifying the optimal individual and the current global point</i>	160
5.5.3	<i>Training part</i>	161
5.5.4	<i>Results and discussion</i>	162
5.6	CONCLUSION	168

GENERAL CONCLUSION170

REFERENCES175

List of figures

FIGURE 1. 1 DAMAGE DETECTION WITH SHM ARCHITECTURE.	31
FIGURE 2. 2 CAUSES OF PIPELINE FAILURE DURING OPERATION [146].	50
FIGURE 2. 3 STEEL PROCESSING IN THE HEATED ZONE [148].	53
FIGURE 2. 4 INFLUENCE OF TEMPERATURE ON GRAINS [149].	54
FIGURE 2. 5 PRINCIPLE OF SUBMERGED POWDER WELDING.	57
FIGURE 2. 6 WELDING DEFECTS [150].	58
FIGURE 2. 7 THE THREE FAILURE MODES.	65
FIGURE 2. 8 MECHANICAL FIELD ZONES.	65
FIGURE 2. 9 ELLIPTICAL DEFECT IN AN INFINITE PLATE.	66
FIGURE 2. 10 DUCTILE FAILURE OF A PIPE OF AVERAGE DIAMETER UNDER THE EFFECT OF INTERNAL PRESSURE.	69
FIGURE 2. 11 BIOLOGICAL NEURON MODELING.	70
FIGURE 2. 12 TYPES OF ACTIVATION (TRANSFER) FUNCTIONS.	71
FIGURE 2. 13 ARCHITECTURE OF ANNS.	72
FIGURE 2. 14 STRUCTURE OF AN ARTIFICIAL NEURON.	74
FIGURE 2. 15 TOPOLOGY OF A BACKPROPAGATION MULTILAYER NEURAL NETWORK.	74
FIGURE 2. 16 FLOWCHART OF BACKPROPAGATION (HECHT-NIELSEN 1989) [158].	78
FIGURE 2. 17 MAIN PANEL OF THE NETWORK DATA MANAGER APPLICATION.	81
FIGURE 3. 1 SPECIMEN GEOMETRY AND FINITE ELEMENT MODEL OF A NOTCHED TENSILE TEST.	88
FIGURE 3. 2 THE OPTIMAL GTN PARAMETERS.	90
FIGURE 3. 3 PRINCIPLE OF THE INVERSE ANALYSIS METHOD USED FOR THE IDENTIFICATION OF PARAMETERS.	90
FIGURE 3. 4 THE LOAD VS. DISPLACEMENT NUMERICAL AND EXPERIMENTAL CURVE IN THE CASE OF THE COUPLED IDENTIFICATION OF GTN MODEL AND OSGOOD HARDENING LAW.	92
FIGURE 3. 5 ANN DEVELOPMENT STEPS TO PREDICT GTN PARAMETERS AND OSGOOD CONSTANTS.	94
FIGURE 3. 6 ARCHITECTURE OF NEURAL NETWORK.	95
FIGURE 3. 7 THE RESULTS OBTAINED FOR THE PREDICTION OF GTN PARAMETERS AND OSGOOD CONSTANTS AND MECHANICAL PROPERTIES.	97
FIGURE 3. 8 SIMULATION BY FEM VERSUS PREDICTED DATA (RESULTS: VALUES OF EACH PARAMETER).	98
FIGURE 3. 9 TEST SPECIMEN USED FOR CHEMICAL COMPOSITION.	99
FIGURE 3. 10 MECHANICAL POLISHING WITH ABRASIVE PAPERS.	101
FIGURE 3. 11 SPECIMEN FOR THE MICROHARDNESS TEST.	101
FIGURE 3. 12 MICROHARDNESS TESTER USED FOR MICROHARDNESS MEASUREMENTS (VICKERS TYPE).	102
FIGURE 3. 13 THE DISTRIBUTION OF MEASURING POINTS FOR MICROHARDNESS.	102
FIGURE 3. 14 THE VALUES OF MICROHARDNESS (HV 10) DEPENDING ON THE MEASURING POSITION.	103
FIGURE 3. 15 MICROSCOPIC ILLUSTRATION OF EXISTING AREAS ON A SPECIMEN CONTAINING THE WELD BEAD.	104

FIGURE 3. 16 SET UP OF UNIAXIAL TENSILE TESTS WITH TENSILE EXTENSOMETER (A); GEOMETRICAL DIMENSIONS ACCORDING TO EN 10002-1 STANDARD (B).....	105
FIGURE 3. 17 SAMPLE FOR TENSILE TEST (A, B), BUTT JOINT OF API X 70 STEEL USING ARC WELDING (C), STEEL PLATE (D), SAMPLE FOR IMPACT TEST (E).	106
FIGURE 3. 18 RESILIENCE MACHINE AND COOLER	107
FIGURE 3. 19 STANDARDIZED TEST PIECE OF THE IMPACT TEST.....	107
FIGURE 3. 20 TENSILE TEST MODELLING WITH BOUNDARY CONDITIONS: (A) BASE METAL AND (B) WELDED METAL.	109
FIGURE 3. 21 IMPACT TEST MODELLING WITH BOUNDARY CONDITIONS: (A) BASE METAL AND (B) WELDED METAL.	109
FIGURE 3. 22 FE MODEL OF TENSILE TEST SPECIMENS: (A) BASE METAL AND (B) WELDED METAL.	110
FIGURE 3. 23 FE MODEL OF IMPACT TEST SPECIMENS: (A) BASE METAL AND (B) WELDED METAL.	110
FIGURE 3. 24 THE TENSILE TEST FROM EXPERIMENT AND FE ANALYSIS (A AND B – NECKING, AND C AND D – FRACTURE).....	110
FIGURE 3. 25 IMPACT TEST IN EXPERIMENT AND FE ANALYSIS.....	111
FIGURE 3. 26 COMPARISON OF WELD METAL IMPACT TEST BETWEEN EXPERIMENTAL AND FE ANALYSIS.	111
FIGURE 3. 27 ENGINEERING STRESS VERSUS ENGINEERING STRAIN PLOT FOR BASE METAL AND WELD METAL.....	112
FIGURE 3. 28 ENERGY–DISPLACEMENT GRAPH (SIMULATION-IMPACT ENERGY).....	112
FIGURE 3. 29 EXPERIMENTAL AND NUMERICAL FORCE-DISPLACEMENT CURVES FOR THE CVN EXPERIMENT.....	113
FIGURE 3. 30 TRUE STRESS VERSUS TRUE STRAIN AT DIFFERENT TEMPERATURES.	115
FIGURE 3. 31 THE SIMULATED LOAD-DISPLACEMENT CURVE FOR IMPACT TESTING-X70.	117
FIGURE 3. 32 EXAMPLES OF THE EFFECT OF GTN PARAMETERS ON THE RESULTING FRACTURE SURFACE.	119
FIGURE 3. 33 THE FRACTURED IMPACT SPECIMEN: TESTED SPECIMEN (A); SIMULATED SPECIMEN (B).	119
FIGURE 3. 34 ARCHITECTURE OF NEURAL NETWORK.	120
FIGURE 3. 35 THE RESULTS OBTAINED FOR THE PREDICTION OF INITIAL AND MAXIMUM LOADS.	121
FIGURE 3. 36 THE INITIAL AND MAXIMUM LOADS WITH NUMBER OF PARAMETERS GTN MODEL (MIN AND MAX VALUES).....	122
FIGURE 3. 37 THE MAXIMUM LOADS AT DIFFERENT TEMPERATURES AND MAX GTN PARAMETERS VALUES OF IMPACT TESTING.	122
FIGURE 4. 1 BOUNDARY CONDITIONS FOR THE MODELED TENSILE TEST SPECIMENS OF BASE METAL.	127
FIGURE 4. 2 A- MESH REFINEMENT IN THE CRITICAL ZONE B-THE GEOMETRY.	128
FIGURE 4. 3 LOAD-DISPLACEMENT SIMULATION CURVE OF SINGLE EDGE CRACK OF API X70.....	129
FIGURE 4. 4 FRACTURE PROCESS OF API X70 STEEL DURING THE TEST: EXPERIMENT (A) AND FEM SIMULATION (B).	129
FIGURE 4. 5 TEST SPECIMEN WITH A TENSILE EXTENSOMETER IN THE TENSILE TESTING MACHINE.	130
FIGURE 4. 6 STRESS-STRAIN DIAGRAMS OF API X70 PIPELINE STEEL.....	131

FIGURE 4. 7 A PART OF PIPE (A), REMOVAL OF THE TRANSVERSE BASE METAL (B), AND PLATE "1" COMPLETELY FROM BASE METAL (C).	132
FIGURE 4. 8 SPECIMENS USED FOR TENSILE TESTING.....	132
FIGURE 4. 9 TEST SPECIMENS CARRIED OUT FOR TENSILE TESTS ACCORDING TO DIFFERENT CRACK LENGTHS.	133
FIGURE 4. 10 A TYPICAL ANN ARCHITECTURE.....	134
FIGURE 4. 11 DIFFERENT HIDDEN NEURONS WITH DIFFERENT SCENARIOS.	137
FIGURE 4. 12 REGRESSION ANALYSIS: A) DISPLACEMENT, B) STRAIN, C) STRESS.	139
FIGURE 4. 13 PREDICTED CRACK LENGTH USING 61 COLLECTED DATABASES; A-DISPLACEMENT, B-STRAIN, C-STRESS.	140
FIGURE 4. 14 ERROR PERCENTAGE USING 61 COLLECTED DATABASES; A-DISPLACEMENT, B-STRAIN, C-STRESS.	141
FIGURE 5. 1 THE YIELD STRESS AND PLASTIC STRAIN OF API X70 STEEL.	149
FIGURE 5. 2 SPECIMEN AND DIMENSIONS USED FOR DWTT.	150
FIGURE 5. 3 SPECIMEN USED FOR DWTT AND THE IMPACT MACHINE FOR STEEL X70.....	150
FIGURE 5. 4 SPECIMEN AND DIMENSIONS USED FOR CVN AND VARIOUS LOCATIONS.	151
FIGURE 5. 5 SPECIMEN USED FOR CVN AND THE IMPACT MACHINE FOR STEEL X70.....	152
FIGURE 5. 6 THE OBTAINED RESULTS ON THE BASE METAL WITH DWTT.....	152
FIGURE 5. 7 CONTRIBUTION OF DIFFERENT ENERGY COMPONENTS, SUCH AS (EI) INITIATION ENERGY AND (EP) PROPAGATION ENERGY.....	153
FIGURE 5. 8 CVN SPECIMEN WITH AN INITIAL CRACK AND 3D MESHING WITH APPLIED VELOCITY.	155
FIGURE 5. 9 THE TRUE STRESS–STRAIN CURVE AT -196 C FOR API X70 [30]	156
FIGURE 5. 10 VON MISES DISTRIBUTION IN MODEL DURING CRACK INITIATION AND PROPAGATION.....	158
FIGURE 5. 11 A- SHOWS THE CVN TEST SIMULATION RESULT COMPARED TO EXPERIMENTAL OBSERVATION; B- SHOWS THE MAXIMAL CONTACT POINT (PEAK LOAD) AS THE CRACK STARTING ONSET.	159
FIGURE 5. 12 ANN ARCHITECTURE	161
FIGURE 5. 13 DIFFERENT NEURONS WITH DIFFERENT SCENARIOS LOAD.	163
FIGURE 5. 14 DIFFERENT HIDDEN NEURONS WITH DIFFERENT SCENARIOS ENERGY.	163
FIGURE 5. 15 REGRESSION ANALYSIS FOR PEAK LOAD DATA (HIDDEN NEURON=10).	164
FIGURE 5. 16 REGRESSION ANALYSIS FOR ABSORBED ENERGY DATA (HIDDEN NEURON=10).....	164
FIGURE 5. 17 PREDICTED PEAK LOAD USING 31 COLLECTED DATABASES (SCENARIO 1'L= 2.968MM'; SCENARIO 2'L= 4.531MM'; SCENARIO 3'L= 6.093 MM'; SCENARIO 4'L= 7.656 MM'). .	165
FIGURE 5. 18 PREDICTED ABSORBED ENERGY USING 31 COLLECTED DATABASES (SCENARIO 1'L= 2.968MM'; SCENARIO 2'L= 4.531MM'; SCENARIO 3'L= 6.093 MM'; SCENARIO 4'L= 7.656 MM'). .	165
FIGURE 5. 19 ERROR PERCENTAGE OF PEAK LOAD USING 31 COLLECTED DATABASES (SCENARIO 1'L= 2.968MM'; SCENARIO 2'L= 4.531MM'; SCENARIO 3'L= 6.093 MM'; SCENARIO 4'L= 7.656 MM').	166
FIGURE 5. 20 ERROR PERCENTAGE OF ABSORBED ENERGY USING 31 COLLECTED DATABASES (SCENARIO 1'L= 2.968MM'; SCENARIO 2'L= 4.531MM'; SCENARIO 3'L= 6.093 MM'; SCENARIO 4'L= 7.656 MM').	166

List of tables

TABLE 2. 1 ORDINARY STEELS OR UNALLOYED CARBON STEELS.	52
TABLE 2. 2 INFLUENCE OF EQUIVALENT CARBON ON THE WELDABILITY OF STEEL.	55
TABLE 3. 1 IDENTIFIED GTN AND OSGOOD PARAMETERS.	92
TABLE 3. 2 IDENTIFIED GTN AND OSGOOD PARAMETERS FOR SEVERAL TESTS.	93
TABLE 3. 3 PARAMETERS OF INPUT DATA AND TARGETS DATA (1 AND 2).	95
TABLE 3. 4 THE CHEMICAL COMPOSITION OF API 5L X70 STEEL.	99
TABLE 3. 5 REQUIREMENT OF CHEMICAL COMPOSITION FOR GRADE X70 ANALYSIS [27].	99
TABLE 3. 6 MAIN HARDNESS TESTS.	100
TABLE 3. 7 THE VALUES OF MICROHARDNESS (HV 10) FOR DIFFERENT MEASURING POINTS.	103
TABLE 3. 8 RESULTS OF TENSILE TESTS FOR THE BASE METAL.	106
TABLE 3. 9 RESULTS OF TENSILE TESTS FOR THE WELD METAL.	106
TABLE 3. 10 MACRO-CHARACTERISTICS OF CHARPY SPECIMENS CUT FROM X70 PIPE STEEL TESTED FOR DIFFERENT IMPACT POSITION.	108
TABLE 3. 11 ANN-GTN MODEL PARAMETERS.	108
TABLE 3. 12 COMPARISON OF MECHANICAL PROPERTIES FOR THE THREE DIFFERENT SOURCES.	113
TABLE 3. 13 MACRO-CHARACTERISTICS OF CHARPY SPECIMENS CUT FROM X70 PIPE STEEL TESTED FOR IMPACT TESTING.	114
TABLE 3. 14 THERMOPHYSICAL PROPERTIES OF API GRADE X70 STEEL [176].	115
TABLE 3. 15 GTN PARAMETERS USED IN THE SIMULATIONS.	116
TABLE 3. 16 SUMMARY OF EXPERIMENT AND FEM SIMULATION RESULTS FOR THE IMPACT SPECIMEN.	118
TABLE 4. 1 MECHANICAL PROPERTIES OF API X70 STEEL.	131
TABLE 4. 2 COMPARISON BETWEEN THE EXPERIMENTAL AND NUMERICAL RESULTS OF THE TENSILE TEST.	131
TABLE 4. 3 COMPARISON BETWEEN EXPERIMENTAL AND FEA STRESS RESULTS FOR DIFFERENT CRACK LENGTH.	133
TABLE 4. 4 ERROR PERCENTAGE OF PREDICTED WOA, WOA-BAT, AOA, GA-1, AND GA-2 FOR EACH CRACK LENGTH SCENARIO.	142
TABLE 4. 5 CPU TIME OF WOA, WOA-BAT, AOA, AND GA FOR EACH CRACK LENGTH SCENARIO.	143
TABLE 5. 1 MECHANICAL PROPERTIES OF API X70 STEEL [27].	149
TABLE 5. 2 EXPERIMENTAL CONDITIONS FOR DWTT.	151
TABLE 5. 3 ABSORBED ENERGY VALUES FOR THE DIFFERENT ZONES.	154
TABLE 5. 4 RESILIENCE VALUES FOR DIFFERENT ZONES.	154
TABLE 5. 5 ABSORBED ENERGY VALUES FOR THE DIFFERENT TEMPERATURES.	154
TABLE 5. 6 INPUTS AND OUTPUTS PARAMETERS USED IN THIS STUDY.	162
TABLE 5. 7 ERROR PERCENTAGES OF PREDICTED PSO, BCMO AND JAYA ALGORITHM FOR EACH PEAK LOAD SCENARIO.	167
TABLE 5. 8 ERROR PERCENTAGES OF PREDICTED PSO, BCMO AND JAYA ALGORITHM FOR EACH ABSORBED ENERGY SCENARIO.	167

List of symbols and abbreviations

Symbols and abbreviations

Abbreviations

<i>API</i>	<i>American Petroleum Institute</i>
<i>ANN</i>	<i>Artificial neural networks</i>
<i>WOA</i>	<i>Whale Optimisation Algorithm</i>
<i>GA</i>	<i>Genetic Algorithm</i>
<i>AOA</i>	<i>Arithmetic Optimisation Algorithm</i>
<i>WOABAT</i>	<i>Hybrid Whale Optimisation Algorithm</i>
<i>BP</i>	<i>Back Propagation</i>
<i>ASTM</i>	<i>American Society for Testing and Materials</i>
<i>FEM</i>	<i>Finite Element Method</i>
<i>GTN</i>	<i>Gurson-Tvergaard-Needleman (damage model)</i>
<i>PSO</i>	<i>Particle Swarm Optimization</i>
<i>DWTT</i>	<i>Drop Weight Tear Test</i>
<i>CVN</i>	<i>Charpy V-Notch</i>
<i>XFEM</i>	<i>Extended Finite Element Method</i>
<i>BCMO</i>	<i>Balancing Composite Motion Optimization</i>
<i>SHM</i>	<i>Structural Health Monitoring</i>
<i>XIGA</i>	<i>Extended Isogeometric analysis</i>
<i>XFEM-Jaya</i>	<i>Extended Finite Element Method - Jaya</i>

<i>XIGA-Jaya</i>	<i>Extended Isogeometric analysis - Jaya</i>
<i>XFEM-PSO</i>	<i>Extended Finite Element Method - Particle Swarm Optimization</i>
<i>XIGA-PSO</i>	<i>Extended Isogeometric analysis - Particle Swarm Optimization</i>
<i>MLP</i>	<i>Multilayer perceptron</i>
<i>I-Jaya</i>	<i>Improved Jaya</i>
<i>YA</i>	<i>YUKI Algorithm</i>
<i>POD</i>	<i>Proper Orthogonal Decomposition</i>
<i>RBF</i>	<i>Radial Basic Function</i>
<i>TLBO</i>	<i>Teaching Learning Based Optimization</i>
<i>GWO</i>	<i>Gray Wolf Optimizer</i>
<i>CS</i>	<i>Cuckoo Search</i>
<i>GD</i>	<i>gradient descent</i>
<i>CI</i>	<i>Cornwell indicator</i>
<i>IGA</i>	<i>IsoGeometric Analysis</i>
<i>ABC</i>	<i>Artificial bee colony</i>
<i>EA</i>	<i>Evolutionary Algorithm</i>
<i>EABC</i>	<i>Enhanced Artificial Bee Colony</i>
<i>MCI</i>	<i>Modified Cornwell Indicator</i>
<i>MSE</i>	<i>Modal Strain Energy</i>
<i>FRF</i>	<i>Frequency Response Function</i>
<i>SDI</i>	<i>Single Damage Indicator</i>
<i>RSM</i>	<i>Response Surface Model</i>

<i>VCCT</i>	<i>Virtual Crack Closure Technique</i>
<i>FRI</i>	<i>Frequency Reduction Index</i>
<i>MRI</i>	<i>Modal Reduction Index</i>
<i>MAC</i>	<i>Assurance Criteria</i>
<i>CCI</i>	<i>Curvature Change Index</i>
<i>COMAC</i>	<i>Coordinate Modal Assurance Criteria</i>
<i>MLP</i>	<i>Multi-Layer Perceptron</i>
<i>PDP</i>	<i>Parallel Distributed Processing</i>
<i>MSE</i>	<i>Mean Square Error</i>
<i>SSE</i>	<i>Sum of Squared Error</i>
η	<i>(mu) Learning rate</i>
<i>HAZ</i>	<i>Heat - Affected Zone</i>
<i>TF</i>	<i>Melting Temperature</i>
<i>CE</i>	<i>Carbon Equivalent</i>
<i>HSLA</i>	<i>High Strength Low Alloy</i>
<i>SAW</i>	<i>Submerged arc welding</i>
<i>SAWP</i>	<i>Submerged Arc Welding Process</i>
<i>E</i>	<i>Young's modulus [GPa]</i>
σ	<i>Stress [MPa]</i>
ν	<i>Poisson's ratio</i>
μ	<i>Shear Modulus [MPa]</i>
λ	<i>Lame coefficient [N/mm²]</i>

G	<i>Available Energy [J]</i>
G_C	<i>Critical Value of Available Energy</i>
C	<i>Complacency of the cracked structure</i>
K	<i>Stress Intensity Factor [MPa*m^{1/2}]</i>
K_C	<i>Critical Value of Stress Intensity Factor [MPa*m^{1/2}]</i>
K_I	<i>Stress Intensity Factor Direction xx [MPa*m^{1/2}]</i>
K_{II}	<i>Stress Intensity Factor Direction yy [MPa*m^{1/2}]</i>
K_{III}	<i>Stress Intensity Factor Direction zz [MPa*m^{1/2}]</i>
k_T	<i>Stress Concentration Factor</i>
$\prod(u)$	<i>Total deformation energy [(J) or N.m]</i>
Ω	<i>Total volume</i>
Ω_e	<i>Volume Division</i>
K	<i>Global Stiffness Matrix</i>
g	<i>Global Force Vector</i>
q	<i>Vector of Nodal Displacements of The System</i>
DTT	<i>Dynamic Tear Test</i>
σ_{eq}	<i>Macroscopic von Mises equivalent stress [MPa]</i>
σ_e	<i>Yield stress of the base metal in the element [MPa]</i>
σ_m	<i>Macroscopic mean stress [MPa]</i>
f	<i>Pore volume fraction</i>
q_1, q_2, q_3	<i>Correction parameters</i>

f^*	<i>Equivalent void volume fraction</i>
f_c	<i>Void volume fraction at the time when the holes start to coalescence</i>
f_F	<i>Broken void volume fraction when the material is destroyed</i>
f_u	<i>Limit void volume fraction when the stress-bearing capacity is zero</i>
H	<i>Material Constant</i>
n	<i>Strain Hardening Exponent Of The Material</i>
Q	<i>Cost Function</i>
F	<i>Objective function</i>
N	<i>Total number of measured points in the numerical simulations and experimental</i>
f_c	<i>Critical void volume</i>
f_n	<i>Nucleation void size</i>
YS	<i>Yield Strength [MPa]</i>
UTS	<i>Ultimate Tensile Strength [MPa]</i>
UTS_{weld}	<i>Ultimate Tensile Strength Weld [MPa]</i>
EL	<i>Elongation</i>
$YTRatio$	<i>Yield to Tensile Ratio</i>
$KV (BM)$	<i>Charpy strength BM [J]</i>
$KV (FZ)$	<i>Charpy strength FZ [J]</i>
$KV (HAZ)$	<i>Charpy strength HAZ [J]</i>
CE	<i>Carbon Equivalent</i>
$HV10$	<i>Microhardness test [N/mm²]</i>

BM	<i>Base Metal</i>
EW	<i>External Welding</i>
IW	<i>Interior Welding</i>
WM	<i>Welded Metal</i>
HAZ	<i>Heat Affected Zone</i>
ε_n	<i>Mean equivalent plastic strain</i>
s_n	<i>Standard deviation</i>
$SENT$	<i>Single Edge Notch Test</i>
Φ	<i>Gurson yield surface function</i>
f_0	<i>Equivalent pore volume fraction</i>
f_u^*	<i>Limit pore volume fraction when the stress-bearing capacity is zero</i>
f_{growth}^*	<i>Existing void growth</i>
$f_{nucleation}^*$	<i>Nucleation of new voids</i>
$\bar{\varepsilon}^{pl}$	<i>Equivalent plastic strain</i>
$\dot{\bar{\varepsilon}}^{pl}$	<i>Equivalent plastic strain rate</i>
DOF	<i>Degree Of Freedom</i>
w_{ij}	<i>Weights</i>
b_j	<i>Bias</i>
t	<i>Latest iteration</i>
\bar{A}, \bar{C}	<i>Coefficient vectors</i>
\bar{X}	<i>Position vector</i>

\vec{X}^*	<i>Position vector of the best solution</i>
X, Y	<i>Whale located</i>
X^*, Y^*	<i>Prey located</i>
\vec{X}_{rand}	<i>Random position vector</i>
$RMSE$	<i>Root-Mean-Square Error</i>

General introduction

Pipeline transportation is currently of tremendous interest and is essential for the transportation of hydrocarbons. Among the steels employed in construction, API 5L X70 steel occupies a significant position in the mechanical, marine, and particularly the oil industries. Our research focused on analyzing this steel at the level of the ALFAPIPE GHARDAIA Company.

When ensuring the integrity of big industrial structures and components, faults must be taken into account. Additionally, the circumstances for the beginning, propagation, and arrest of fractures caused by these defects must be identified. Pipelines are the most cost-effective and secure way to carry oil and gas in industrial settings. However, as more people use them, the incidence of mishaps has grown substantially. Pipes are components of industrial structures whose degradation involves risks to human life and the environment, as well as operating losses and frequently a large financial loss. The pipes may have defects or micro-cracks due to the manufacturing process, handling accidents, thermal shocks, etc. These defects can develop under the effect of network operating conditions and lead to the formation, over time, of long cracks which will eventually cause the rupture of the pipe and a gas leak.

As this type of network is used in an urban environment, a gas leak could not only lead to severe consequences but also make the replacement of the tube very complicated in terms of time and safety. A good understanding of the process by which defects develop into microcracks that would give rise to a long crack and the phenomenon of propagation of the latter is of paramount importance to prevent losses due to gas leaks and for the control network maintenance.

With advancements in materials science, the process of applying a crack identification technique for engineering infrastructures has emerged as a multidisciplinary study focus for scientific communities. This has made it possible to use new, cutting-edge materials to construct intricate, heavy structures in a lighter manner. Additionally, numerous scholars have extensively developed a number of methodologies in the fields of mechanical, civil, and aerospace engineering due to the scale, complexity, and potential catastrophic effects of these structures. These methods, which are based on behavioral laws and cutting-edge mathematical techniques, have actually made it possible to analyze and evaluate structural states with increasing levels of accuracy and dependability, preventing potential harm that could otherwise result in monetary and human losses.

Generally, damage can be defined as changes that occur in a system and adversely affect its current or future performance. The notion of damage in the context of SHM (Structural Health Monitoring) will be constrained to alterations in the geometric and/or material characteristics of these systems. Changes to the system's boundary conditions are also included.

The objective set in this thesis is to contribute to the development of numerical approaches for the identification of cracks in pipeline steels through the implementation of innovative coupled

methods based on the use of change analysis in mechanical properties and relevant optimization algorithms derived from Soft Computing methods to improve the performance of structural health monitoring systems. To this end, we propose to structure and present our work in this manuscript as follows:

Chapter I: We will discuss the elaboration of a state of the art, based on in-depth bibliographic research, and present the essential methods of identification of cracks found in mechanical data. We will highlight, in particular, the advantage of the analysis by different optimization techniques for identifying cracks based on various indicators of damage as an objective function, which makes it possible to compare the measured and calculated damage. This chapter will be dedicated to presenting optimization techniques that rely on artificial intelligence methods. We will explain the algorithmic and computer approaches relating to the research methods of WOA (Whale Optimization Algorithm), AOA (Arithmetic Optimizer Algorithm), the standard genetic algorithm GA (Genetic Algorithm), the bat BA (Bat Algorithm), and the PSO (Particle Swarm Optimization). We will more explicitly propose the artificial learning technique, known as ANN (Artificial Neural Networks), which will be applied in the rest of our work.

Chapter II: Devoted to general information on steels and processes with studies of the behavior of our steel used in the manufacture of pipelines. We present a reminder of some elements of fracture mechanics and the numerical techniques used.

Chapter III: Devoted to the experimental study of API 5L X70 steel to highlight the chemical composition and the mechanical characteristics of the steel studied. In the second part, we will present a study by numerical simulation, consisting of the validation of our model and is devoted to the study of the effect of different parameters of our chosen GTN model on the mechanical behavior of steel by finite elements ABAQUS and using neural networks.

Chapter IV: Presents the results of crack identification for static analysis based on mechanical properties (stress, strain, and displacement). ANNs are enhanced with WOA, AOA, PSO, WOBAT (Whale Optimization Based Bat Algorithm), and GA algorithms to predict crack length. WOA is used for fast and optimal prediction based on data collected from FEM (Finite Element Method) with numerical validation. Additionally, a modal analysis of an API X 70 steel specimen is performed to collect data based on crack length to test the robustness of the proposed technique. In the last section, the improved ANN using the WOA algorithm is provided by improving ANN parameters to predict crack length correctly. An experimental modal analysis is also provided to validate the proposed approach.

Chapter V: Considered another principal importance in protection opposite of impact problem caused by external accident in the API X70 pipeline steel, represented in the ductile and brittle mode of fracture propagation, based on two experimental tests in specimens of steel pipeline

Drop Weight Tear Test (DWTT) and the impact Charpy (CVN). The results obtained are used to simulate the impact of API X70 pipeline steel at -196 degrees through a numerical approach

based on cohesive segment in extended Finite Element Method (XFEM). The obtained data was used in modeling Machine learning using the Balancing Composite Motion Optimization (BCMO) and Particle Swarm Optimization (PSO), and Jaya algorithm for predicting the peak load and crack initiation energy in a steel X70 with different crack lengths of dynamic brittle fracture values.

A general conclusion will finally synthesize all the obtained results in our various works, and proposals for potential future study perspectives, and will close this manuscript.

Chapter 1: A literature review

1.1 Introduction

Monitoring the integrity of structures (or Structural Health Monitoring, SHM) involves the design, development and implementation of a system detecting, localization and quantifying damage. Generally, damage can be defined as system changes that adversely affect its current or future performance. Therefore, the concept of damage is significant only by the comparison between two different states of the system: the initial state of the system often intact considered healthy, and the momentary state in general, two types of structural condition control techniques generally and particularly in pipeline control are used: non-destructive testing and destructive testing. The first type of techniques is the most used to monitor the integrity of structures or materials without degrading them, unlike the 2nd type. Among the best-known processes relating to this first type, mention may be made of: X and gamma rays; technical processes based on ultrasound, acoustic emissions, etc. Structural Health Monitoring (SHM) techniques are themselves subdivided into two categories: local and global method techniques [1].

We will present in this chapter a synthesis of the research works resulting from the bibliographical references relating to various essential techniques for identifying and localizing damage in the structures, each subdividing itself into several classes of methods.

The artificial neural network (ANN) has become a popular computational approach in the field of damage identification and detection based on the analysis of mechanical properties, due to its ability to establish a nonlinear relationship between the characteristics of structural mechanics and damage information.

Structural Health Monitoring (SHM) is a valuable tool for assessing the condition of a structure. As a result, it ensures that structures are safe and efficient throughout the duration of their lives.

This procedure entails measuring a structure over time, extracting damage-sensitive features from the measurements, and analyzing them to identify the system's current state. Damages should be diagnosed early, non-destructively, and at a minimal cost using assessment methods based on static or dynamic analysis.

In both static and dynamic assessments, different methods of SHM are described in **Figure 1.1** to define damage identification approach.

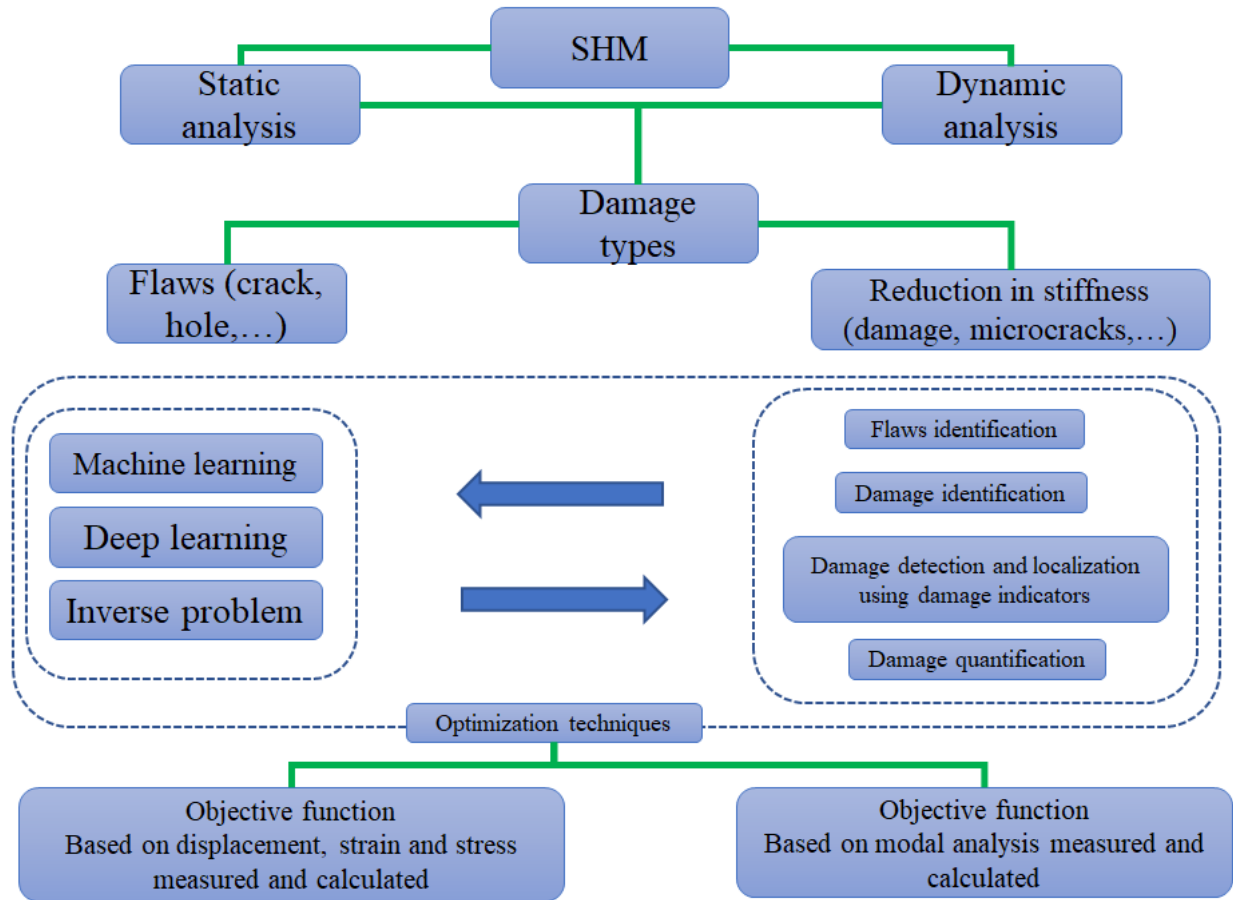


Figure 1. 1 Damage detection with SHM architecture.

1.2 Crack identification research background

In this chapter, new crack identification applications are studied using the ANN technique to improve machine learning. After collecting data, the different algorithm improves the ANN technique by estimating that the exact parameter used identification of the proposed crack with the ANN technique and analysis in the different static and dynamic optimization techniques will be presented in the studies and will be used in our study.

Khatir et al [2] provides a method based on an inverse problem to precisely forecast the sites of cracks in plate constructions. By employing different NURBS orders to reduce the amount of components, XFEM and XIGA are paired with two optimization approaches to predict crack locations with confidence. The advantage of XIGA is shown by using Particle Swarm Optimization (PSO) and the Jaya algorithm to predict crack locations. This work takes into consideration four numerical-optimization methods: XFEM-Jaya, XIGA-Jaya, XFEM-PSO, and XIGA-PSO. Optimizing techniques aim to minimize the difference between calculated displacements and measured strains by minimizing the objective function. The convergence studies of cracks and holes in plates at a variety of positions showed that the Jaya algorithm

significantly outperformed the PSO algorithm for accuracy and speed. A numerical-optimization technique, namely XFEM coupled with Genetic Algorithm (GA), is also used to validate the proposed techniques. XIGA-Jaya is the best performing technique among all examined techniques. Rezaiee-Pajand et al [3] presents a study in order to protect reinforcements from corrosion, it is crucial to reduce the spaces between flexural cracks. Crack spacing is influenced by many factors, such as concrete thickness, concrete compressive strength, specimen dimensions, and the spacing between longitudinal and transverse reinforcements. When the lap-spliced length is insufficient, the strength is reduced and the crack spacing increases. An experiment is conducted to investigate the effects of cross-section height, width, and length of lap-sliced panels on flexural crack spacing. To predict the crack spacing, multilayer perceptron (MLP) neural networks, adaptive neuro-fuzzy inference systems, support vector regressions and least mean squares regressions are used. Compared to other models in this study, the MLP model provides better prediction of crack spacing compared to others. For crack spacing prediction, the most effective features are prioritized based on their mutual information. Furthermore, such beams with lap-spliced bars cannot be determined by the available codes. Ding et al [4] put forward that structural damage diagnosis can be seen as an optimization problem by choosing an appropriate objective function connected to structural parameters to be calculated utilizing optimization techniques. This paper proposes the improved Jaya (I-Jaya) technique as a new heuristic algorithm for structural damage diagnostics. It is based on sparse regularization and Bayesian inference. A new updated equation is employed for the best-yet solution, and a clustering technique is used to replace solutions with poor objective values. This improves the original Jaya algorithm's ability to perform global optimization and makes it more robust. With the suggested I-Jaya technique, an optimization analysis sensitive and robust objective function for efficient and reliable damage diagnostics is developed by sparse regularization and Bayesian inference. Benchmark tests are run to make sure the produced algorithm is getting better.

Numerical studies on a truss structure and experimental validations on a model of an experimental reinforced concrete bridge are conducted to validate the proposed approach. The amount of modal data required for structural damage identification is negligibly less than the total number of unidentified system characteristics. We accommodate for significant measurement

noise and modeling errors. The proposed method, which is based on the I-Jaya algorithm and a modified objective function based on sparse regularization and Bayesian inference, can identify damage accurately and reliably. This suggests that the proposed method is a promising strategy for identifying structural damage using data with significant uncertainties and little measurement information.

In the study provided by Gomes et al [5], delamination is a typical failure condition in laminated composites that causes the layers to separate along their interfaces. This degradation can have a considerable impact on structural performance. Damages like these aren't usually obvious on the surface, but they can lead to catastrophic structural collapses. Because delamination modifies the vibration properties of laminated structures, it can be utilized as an indication for assessing health and the risk of catastrophic failure if it is discovered and recorded in advance. Structural Health Monitoring (SHM) is critical for ensuring structural performance and integrity. The utilization of reduced mode forms and computational techniques, such as the ANN and Genetic Algorithm (GA), were used to develop an optimum methodology for delamination identification on laminated composite plates in this study.

Delamination occurs when the layers of a laminated composite separate along their interfaces, which is a common failure mode. This deterioration has the potential to have a significant influence on structural performance. These kinds of damages aren't always visible on the surface, but they can lead to catastrophic structural failures. Because delamination alters the vibration properties of laminated structures, it can be used as an indicator for measuring health and the danger of catastrophic failure if detected and recorded early. The importance of structural health monitoring (SHM) in assuring structural performance and integrity cannot be overstated. In this study, reduced mode forms and computational approaches such as the Genetic Algorithm (GA) were employed to produce the best methodology for detecting delamination on laminated composite plates.

Benaissa et al. [6] propose a new metaheuristic algorithm that can reduce search space using simple formalism. The search population concentrates on the inside of the local search area, while the rest looks for better search areas globally. The new technique is known as the YUKI Algorithm (YA), and it is used to solve a crack detection problem. We hope to determine crack metrics such as length and direction using a set of measurements gathered on the defective structure. To do this, we employ the so-called model reduction technique, which is based on Proper Orthogonal Decomposition (POD) and validated by Radial Basic Function (RBF). This, by interpolation, aids in forecasting (numerically) the measurement at new sites (out of the collection of sensors). This approach is commonly utilized in this context and has been shown to be quite efficient in terms of computation.

In our investigation of YA's performance, we look at two scenarios: first, the Elastostatic research. Then there's the case of dynamic analysis. We compare the proposed algorithm's performance to that of well-known optimization approaches as Teaching Learning Based

Optimization (TLBO). The Gray Wolf Optimizer (GWO) and Cuckoo Search (CS) (GWO). In comparison to the algorithms stated, the results suggest in this study that YA give more accurate and faster results. Tran et al [7] present an efficient Artificial Neural Network (ANN) for detecting faults in laminated composite structures based on the global search capacity of evolutionary algorithms (EAs). ANN has exploded in popularity in recent decades, thanks to astonishing advancements. However, because it uses backpropagation methods based on gradient descent (GD) approaches, ANN has significant limitations in terms of local minima concerns. As a result presented, the effectiveness and accuracy of ANN are significantly reduced. Based on the global search capability of stochastic algorithms, several researchers have come up with some strategies to combat the local minimal difficulties of ANN by seeking for starting favorable locations to eliminate initial local minima. However, it is well known that in some circumstances, if the network has too many local minima scattered deeply in the search space, those solutions are no longer beneficial, if not even detrimental. As a result, we offer a unique method for training the network that combines the high convergence speed of GD ANN approaches with the global search capacity of EAs. The essential concept is that EAs are used in tandem with ANN during the network training process. This ensures that the network finds the best answer as quickly as possible and avoids becoming stuck in local minima. To improve the worldwide search capacity's efficiency, GA is utilized to build high-quality starting populations based on crossover and mutation operators' abilities, whereas CS with global search capability is employed to find the optimal solution. Furthermore, to deal with the vast amount of data used to train the network, the data of the objective function is vectorized, which reduces the computational cost significantly. The results show that the proposed method outperforms regular ANNs, other hybrid-ANNs, and HGACS in terms of accuracy, and that it takes much less time to compute than HGACS.

A new technique for damage measurement in laminated composite plates utilizing Cornwell indicator (CI) based on Artificial Neural Network (ANN) mixed with Particle Swarm Optimization (PSO) is proposed by Khatir et al [7]. There are two stages to the analysis. For square laminated composite plates with three layers, IsoGeometric Analysis (IGA) is formulated in the first stage. The IGA model is combined with PSO for damage quantification utilizing an inverse problem method using CI as an objective function to minimize the difference between calculated and observed values in the second $[0^\circ/90^\circ/0^\circ]$ stage $[0^\circ/90^\circ/0^\circ]$.

The goal of this work is to evaluate the use of ANN-PSO for damage quantification in composite structures in order to save computational time. The modeling technique is IGA, the input data is CI, and the output data is damage sites and severity. The results show that ANN-PSO-IGA-CI achieves a high level of damage quantification accuracy.

Furthermore, while comparing PSO-IGA-CI to ANNPSO-IGA-CI, it is proved that ANNPSO-IGA-CI saves a significant amount of computing time.

An “ABC-ANN” pavement surface distress detection and classification system is developed by Banharnsakun [8]. It combines an artificial neural network with the artificial bee colony (ABC) technique. The suggested solution uses a thresholding method to separate the pavement image into distressed and non-distressed portions once it has been gathered. The ideal threshold value for segmentation in this stage was chosen using the ABC approach. The vertical distress measure, the horizontal distress measure, and the total number of distress pixels are among the variables that are extracted from a disturbed area and used as input to the ANN. Finally, depending on these input qualities, the ANN is utilized to categorize a distressed area as a particular type of distress, such as a transversal crack, longitudinal crack, or pothole. The experimental results show that the suggested approach is effective at detecting pavement distress and can accurately classify distress types in pavement photos. When compared to existing algorithms, the proposed ABC-ANN technique achieves a 20% boost in accuracy.

The Structural Health Monitoring (SHM) system is now the standard method for managing the detection and identification of deterioration in a wide range of design areas. Every day, the necessity to monitor structural behavior grows, owing to the development of new materials and increasingly complicated structures. As a result, more robust and sensitive SHM procedures and techniques are being developed. The importance of damage detection using intelligent signal processing and optimization techniques based on vibration measures is highlighted in Gomes et al [9] research. Because of the considerable potential (and relative ease of implementation) of the methods mentioned here, they are primarily based on the evaluation of vibrational and modal data. In the form of a brief review, this article examines the application of optimization methods and Artificial Neural Networks (ANN) for structural monitoring. This study serves as a foundation for the development of SHM systems and data analysis. This paper's goal is to assist engineers and researchers in finding a better solution to their specific structural monitoring issues.

In the subject of damage diagnosis of engineering structures based on modal analysis, Artificial Neural Networks (ANN) has recently received greater attention. Zenzen et al [10] provide a novel modified damage indicator that employs a transmissibility technique to increase the LFCR when combined with ANN. The main objective of the proposed damage indicator is to reduce the number of collecting data used in ANN technique for fast prediction and higher accuracy rather than collecting modal analysis data, such as natural frequencies, damping ratios, and mode shapes, or inverse analysis for damage quantification using optimization techniques. Three layers cross-ply $[0^\circ / 90^\circ / 0^\circ]$ composite beams and cross-ply $[0^\circ / 90^\circ / 0^\circ]$ laminated composite plates with multiple and single damage are used to test the proposed approach (s). After analyzing four damage scenarios, the suggested application's dependability and accuracy are proved by forecasting the severity of damages in composite structures.

ANN has evolved into one of the most powerful computational intelligence methods for tackling complicated problems in a variety of domains. However, when back propagation techniques based on gradient descent are used, a key disadvantage of ANN is the prevalent problem of local minima, which obstructs the search for the optimal solution. To overcome this handicap, they propose combining ANN with global search techniques-based evolutionary algorithms. By creating the network using settings that minimize the discrepancy between the actual and planned outputs, Tran-Ngoc et al [11] use a programmable combination of an ANN and the cuckoo search (CS) method, and they make use of CS to improve ANN training parameters (weight and bias). Two numerical models steel beams calibrated using experimental measurements and a large-scale truss bridge are used to evaluate the robustness of the proposed method. The results demonstrate that ANN-CS (ANN-CS) is more accurate and computes faster than ANN and evolutionary algorithm (EA) alone for localizing and quantifying structural deterioration.

1.3 A brief introduction to crack modeling

Most engineering issues are now tackled using FEM, which has the drawback of conformal meshing for tackling crack detection difficulties utilizing the inverse problem. XFEM [12-14] models and analyzes flaws, eliminating the need to re-mesh the computational domain with each new iteration of the optimization technique. When used in conjunction with GAs [15], which have been shown to be a reliable and efficient global search method, the exact placement and orientation of defects can change 'on the fly' as the global optimization iterations progress. Ref. [16] discusses using an optimization strategy within the XFEM framework to find model parameters like the order of various singularities or the thickness of boundary layers. Nonetheless, the authors have generally employed optimization techniques for unconstrained minimization, although there is no obvious dependency of the objective function on the design variables in issues like the one presented here, and GAs prove to be more efficient and reliable methods.

In Ref [17], a numerical simulation of a cracked plate using XIGA was reported under various loads and boundary conditions. The Heaviside function was used to simulate the crack faces, while crack tip enrichment functions were used to model the singularity in the stress field at the fracture tip. The XIGA findings for various crack configurations in the plate were compared to extended finite element method and/or literature data for various types of loads and boundary conditions, demonstrating that XIGA was more accurate. Nguyen et al [18] presented another XIGA to investigate the analysis of through-thickness cracks in thin shell constructions. For the examination of cracked shell structures in real applications, the provided approach is a very promising alternative to the 'standard' XFEM.

Habib et al [19] employed XIGA to model a crack in an orthotropic plate and used crack tip enrichments to replicate singular fields around the crack tip. The geometry was defined using

NURBS and T-splines geometric technologies. T-spline models were subjected to a new local refinement technique. The results were more accurate than those found elsewhere in the literature. The approaches given here can be utilized to apply crack detection based on the inverse problem.

1.4 A review of crack identification based on static analysis

Caddemi and Morassi [20] proposed a technique for identifying a single crack in a beam based on knowledge of damage-induced changes in the static deflection. A comparable linear spring connecting the two neighboring segments of the beam simulates the crack. Sufficient criteria on static measurements were presented and discussed, allowing for the unique identification of the crack. For various boundary conditions, the inverse analysis produced closed-form formulas for the position and severity of the fracture as functions of deflection data. Furthermore, the effect of mistakes caused by noise in the acquisition of experimental data was investigated, and the technique used only tolerates extremely minor errors. Chatzi et al [21] provided an approach for finding and locating faults in plate structures based on inverse analysis utilizing XFEM and Genetic Algorithm (GA). Furthermore, based on updated XFEM, an experimental test was conducted to locate the position of a crack in a plate. After six hours, the estimated crack parameters could be found, according to the results. For elastostatic difficulties, Waisman et al [22] coupled XFEM and GA, where faults were defined as straight cracks, circular holes, and non-regular-shaped holes in square and rectangular plates. After 80 generations, the majority of the results could be predicted. Sun et al [23] introduced a static analysis-based approach that uses XFEM and the Enhanced Artificial Bee Colony (EABC) algorithm to discover and quantify various defects in structures. In order to evaluate the suggested technique, several numerical cases were analyzed after increasing the level of difficulty. After a considerable computational cost, the majority of the results could be found. To obtain data based on displacements, FEM was employed. When data was collected using FEM, the computational cost was higher. Based on the inverse analysis, XIGA was integrated with PSO to identify cracks in two-dimensional linear elastic issues. The advantages of combining XFEM and IGA are present in XIGA. The gap between the calculated and measured displacements was minimized using the objective function. Convergence studies were calculated at various crack places on the plate, and the findings reveal that the proposed technique can identify damage with a minimum accuracy of 95% for the position and maximum accuracy of 98 percent.

A mathematical technique was devised based on the reduction in stiffness to detect changes in stiffness utilizing FEM of the structure and inverse analysis of the displacement data. It was primarily centered on using the Neumann series to simplify the inverse of the algebraic stiffness matrix. The findings revealed that a high number of data minimized the noise effect and ensured damage detection.

1.5 Damage assessment using modal analysis

Because of the growing requirement to diagnose structural degradation, particularly in civil and mechanical engineering structures, structural health monitoring (SHM) has been a major study area in the recent two decades [24-26]. Because they examine structures without removing or harming any structural components, many damage identification indicators are classified as "non-destructive evaluation." The four degrees of damage identification, according to Rytter [28], are:

Level 1: The presence of damage is determined.

Level 2: Locating the damage.

Level 3: Evaluation of the damage's degree.

Level 4: Prediction of the structure's remaining service life.

Without a structural model, vibration-based damage identification methods can identify level 1 and level 2 damage. Level 3 damage identification is possible when paired with a structural model. The goal of this study is to offer identification at levels 2 and 3. The best way to monitor structural health is to compare current dynamic response measurements to those taken previously to determine whether the structure is healthy or damaged. Tiachacht et al [27] proposed a new method for detecting and quantifying damage in two- and three-dimensional constructions. FEM was used to investigate the implementation of the suggested methodology quantitatively. The modified Cornwell Indicator (MCI) was more effective than the regular Cornwell Indicator at detecting damage (CI). The use of a Genetic Algorithm (GA) in SHM was examined for increased accuracy. MCI was measured and calculated to create the objective function. The findings revealed that the proposed indicator was capable of appropriately predicting damaged parts.

Shi et al [26] proposed a method for detecting structural damage based on changes in Modal Strain Energy (MSE) before and after damage. The sensitivity of the MSE with regard to damage was calculated after a brief presentation of damage localization based on MSE for each structural element. The findings showed that the suggested method was noise sensitive, but that it could locate single and multiple defects. Under a 5% measurement noise, damage quantification of two damages was successful with a maximum error of 14 percent. Yan et al [28, 29] produced two studies that combined MSE and generalized flexibility approaches with natural frequencies and mode shapes. The proposed technique has demonstrated good accuracy in locating and assessing damage. Pandey et al [30] investigated damage detection in a structure using dynamic analysis. A structure's flexibility matrix was proposed as a viable method for not only identifying the presence of damage but also for locating the damage. It was demonstrated that the flexibility matrix could be simply and reliably computed by measuring a few lower frequencies of the

structure. Using Frequency Response Function (FRF) data, Hwang and Kim [31] provided an approach for locating and quantifying damage in structures. By minimizing the difference between test and analytic FRFs, the offered technique may detect and quantify structural degradation. Sinou [32] gave a review of damage detection and SHM of mechanical systems based on changes in observed data of linear and non-linear vibrations. Based on modal analysis, the author proposed many damage indicators. The majority of the indicators offered could only detect and locate without being quantified.

Kim and Stubbs [33] presented a Single Damage Indicator (SDI) approach that uses natural frequency fluctuations to find and quantify a single crack in a structure. A fracture location model and a crack size model were established by connecting fractional changes in the modal energies to changes in the natural frequencies brought on by damage like cracks or faults. The efficacy of the crack detection method was then evaluated for various damage situations by locating and sizing cracks in tested beams for which some of the lower natural frequencies were accessible. When the method was applied to test beams, it was discovered that crack location could be properly approximated. The crack size might also be precisely calculated.

Xiang et al [34] employed the wavelet finite element method for numerical simulation to determine the association between multi-damage locations/depths and the natural frequencies of a beam. The results demonstrated that the proposed damage detection method for beam-like structures was a promising solution for multi-damage detection and depth estimation. The mode forms of a damaged beam with fixed-fixed boundary conditions were obtained using a FEM and then extended using a spatial Fourier series. The impact of damage on the harmonics was also explored. Using Fourier coefficients as input, an Artificial Neural Network (ANN) was trained to determine the damage location and magnitude. After gathering more data, the provided technique could be used for damage identification, localisation, and quantification. Stutz et al [35] introduced a structural damage detection method based on a Response Surface Model (RSM). The results demonstrated that the proposed method could detect damage quickly and efficiently. Virtual Crack Closure Technique (VCCT) was used to detect delamination in composite beam structures, and modal flexibility based on dynamic analysis was provided in Ref [36]. The results demonstrated that this technique could accurately detect and localize damage without the need for measurement. Dincal and Stubbs [37] proposed a damage assessment approach based on physical property changes.

Jassim et al [38] published detailed studies for damage identification methods based on modal analysis. The suggested damage detection approaches, such as the Frequency Reduction Index (FRI) and Modal Reduction Index (MRI), were based on changes in natural frequencies and mode shapes.

Model Assurance Criteria (MAC) was discovered to be viable tools for determining the damage index in beam constructions. Furthermore, the Curvature Change Index (CCI) and Coordinate Modal Assurance Criteria (COMAC) were used to predict the location of the crack in beams and

were found to be feasible. Using experimental data, Dahak et al [39] established an approach based on normalized frequencies in cantilever beams. The findings revealed that the proposed technique could only pinpoint the exact site of the damage. Another study examined the Modal Strain Energy (MSE) method and an improved differential evolution algorithm for damage identification in a cross-ply ($0^\circ/90^\circ/0^\circ$) laminated composite beam and a cross-ply ($0^\circ/90^\circ/0^\circ$) square laminated composite plate with numerous damaged parts. Only inverse analysis and an objective function for damage quantification can be used by MSE to locate the damaged piece. After 100 generations and a higher processing cost, the results were discovered. Zenzen et al [40] proposed a strategy based on the inverse problem using the frequency response function as an objective function and multiple optimization techniques to solve the problem. For beams, the results were more accurate than for complicated structures.

1.6 A review of numerical simulation methods and IANNs

The field of pipelines for the transportation of oil and gas has experienced remarkable development with increasing demand for energy. Many companies are working in the manufacture of high-pressure pipes below the specified minimum yield strength, i.e. 60 ksi to 80 ksi (60 MPa to 80 MPa), due to the urgency of these characteristics where fracture accidents are inevitable. We have to rely on the high quality of these pipes to avoid fragile breakage. Pipe failure can occur due to ductile fracture, sometimes resulting from certain conditions that cause cracks to develop and lead to potential environmental and structural damage, economic losses and increased maintenance costs and repair. Control of elongated cracks and mechanical tests are used to determine deformation, but high cost and time are required. Therefore, the finite element method (FEM) has been developed in the analysis and simulation of many Charpy tests in recent years [41-45]. Impact testing techniques were put in place to verify the fracture characteristics of the materials. The Gurson-Tvergaard-Needleman (GTN) damage model [46] is well known, widely applied and used to simulate the dynamic propagation of ductility fractures. Due to the limited set of parameters in this model, it is often adopted in the industrial field. Throughout the development of laboratory-scale fracture toughness experiments, sample sizes continued to increase. In this work, the application of the GTN damage model is presented in the simulation of tensile tests and for the dynamic propagation of fractures in the Charpy test case. The tensile and fracture toughness simulations are applied to a high strength pipe material, namely X70 steel. The results of the numerical model are used to construct a force-displacement curve in order to compare the experimental data with the numerical predictions to identify the parameters of GTN model and the law of coupling with the law of Ramberg-Osgood hardening. The identification has broadened to include a considerable number of experimental tests drawn from our previous works and other works done at ALFAPIPE Ghardaia laboratory. The approach based on micromechanical modelling of materials is an efficient method used in damage analysis. Many models consider a coupling between plasticity and damage, for example for the behaviour of a porous ductile material in the Gurson model [47]. The model was built using many parameters [48, 49]. The description of the model goes through a general study on metallography [50].

Generally, the model is characterized by three mechanisms of evolution of voids, which represents the processes of ductile fracture in metallic materials. The hardening behaviour of the microstructure of the material results in different mechanical properties as a function of different process parameters [51, 52]. For example, GTN model used in study the effect of hydrogen of high-strength steel on the microdamage evolution. [1] Therefore, due to the interaction of many variables in this case, the modelling of mechanical properties according to different process parameters remains complex and requires a lot of data although it is considered as a reasonable solution. Moreover, we can add to this the dependence on chemical composition and manufacturing process [53, 54]. For example, solid solution hardening and microstructure are dependent on the forming conditions and the chemical composition, which provides details of tensile and impact properties in a steel. Therefore, on the basis of a large amount of data, many researchers have studied the underlying relationships between mechanical properties and chemical composition.

Moreover, in the second part ANN model is developed to predict the parameters of the Gurson-Tvergaard-Needleman model (GTN) coupled with hardening law through the prediction properties of traction and impact of API X70 steel pipe as a function of its chemical composition. The importance of each component in the structure is summarized based on recent relevant works. The method of Precipitating carbon (C) allows for the reinforcement of the structural matrices [55]. The higher content of Nickel (Ni), Silicon (Si) and Molybdenum (Mo) and Chromium (Cr) gives great resistance to the steel [56]. Minimization of the ductile-brittle transition temperature is due to the Manganese (Mn) component effect [57], Niobium (Nb), Titanium (Ti) and Vanadium (V) components play a role in retarding recrystallization and limit the growth of austenite grains [58], in the passes of rolling and manufacturing Niobium (Nb) allows to reduce the temperature at the time of recrystallization [59], more details on the effect of accelerated cooling rate and finish rolling temperature on mechanical properties in this paper [2], improvement of tensile strength and toughness by the components vanadium (V) and titanium (Ti) [60], and we can add the study of the influence of carbon (C) on stress corrosion cracking of API X80 steel by used a carburization treatment [61].

The importance in the design of the current pipelines is the sufficient resistance of steels against fractures and ductile rupture of the pipelines should be avoided and their catastrophic consequences with the initiation of the rupture and the propagation of the fracture of the pipeline, while this requires a value of the minimum toughness of the steel necessary to arrest a long-lasting ductile fracture. The mechanical characterizations deduced from tensile testing in the pipeline manufacturing laboratory may be insufficient because breaks can be obtained below the yield strength under normal and special conditions rendering the material in a brittle state. The impact test is a main complement to the tensile test. The impact bending test or the impact test on a notched Charpy specimen is intended to measure the resistance of a material to sudden rupture. The impact test represented by The Charpy V-Notch (CVN) (ASTM International) in Ref [62] is used to determine the fracture value of the toughness of a considerable material in the frame that is easy and more economical method to perform experiments.

The high cost of large-scale experimental campaigns has driven the development of more economical laboratory-scale tests such as the well-known Charpy V-Notch (CVN) impact test, Drop Weight Tear Test (DWTT) in Refs [63, 64] and more recently the Dynamic Tear Test (DT3). For modern pipelines with a wall thickness reaching over 20 mm, the CVN has a relatively small standard specimen size with a cross section of 10 mm × 10 mm [65]. In addition, limited by the test conditions, the results of the Charpy impact test will be affected by certain factors, which have been investigated by many researchers. It is also of great research value to transform non-standard test results into standard results. The influence of the radius of the striker on the energy absorbed by the impact of X80 steel for pipelines was analyzed in Ref [66]. Madhusudhan [67] presented the variation of energy absorbed by changing the pendulum speeds of 5 m/s, 6 m/s, 7 m/s and 9 m/s of maraging steel 300 using Abaqus software. For X70 pipeline Charpy impact testing. Therefore, the corresponding damage models can be validated, calibrated and/or to be implemented in more complex simulations. The Gurson-Tvergaard-Needleman (GTN) [68, 69] damage model is well-known, widely applied and used to simulate dynamic ductility fracture propagation. Due to the limited parameter set in this model, it is often adopted in the industry field. In this work, the application of the GTN damage model for the dynamic propagation of cracks in the Charpy test is studied and the influence of the damage parameters on the initial and maximum fracture load is quantified. At failure, it is applied to a high strength pipe material, namely X70 through a numerical study of a CVN impact experiment. A sensitivity analysis of the GTN damage constants is carried out to evaluate their influence on the initial and maximum load expected at failure. To analyze the simulation data obtained, machine learning approaches are applied and represented by an artificial neural network in order to identify the relative influence of the values of the GTN parameters and temperature changes on the initial and maximum loads of the rupture. The potential predictive capacity of our model is tested by analyzing the outputs of our neural network for the proposed GTN parameter sets.

Structural Health Monitoring (SHM) of pipeline structures is of great interest and constitutes a fundamental element for the transport of hydrocarbons. Among the steels used for construction is API 5L X70 [70], which occupies a very important place in the mechanical, naval and especially oil industry. High-strength steel pipelines allow the transportation of oil and gas at high pressure to increase the capacity, because the thickness of the pipes can be reduced when the strength of the steel of the pipeline is increased, and then the weight can be reduced. In the pipeline industry, pipes need high strength and durability as well as formability, which are important components, as mentioned in Refs. [71, 72]. The high strength and durability of steel allow natural gas and crude oil to be transported over long distances and under high pressure [73]. The resistance of cracking due to hydrogen is an important property, which is added to other properties in an acid medium as described in Ref. [74, 75]. In the H₂S environment problem, resistance to stress corrosion cracking was studied in Refs. [76, 77] and the phenomenon of fatigue in Refs.[78, 79]. The chemical composition of metal alloys and thermomechanical processing has been shown to affect the properties and microstructure of the steel of the transport pipeline[80]. Ensuring the

integrity of large structures and industrial components involves considering the presence of faults and determining the conditions for initiating, propagating, and stopping cracks due to the presence of these faults [81, 82]. In order to identify this propagation phenomenon, we analysed the evolution of the crack within the framework of the elastoplastic fracture mechanics [83]. It consists essentially of experimental tests and numerical validations to allow the measurement of critical fracture properties from samples at the laboratory scale and to reduce the critical value of the fracture energy. More information can be found in the text books [84-86]. Other works are oriented towards the practical use of fracture mechanics [87, 88]. A good suitable design of tubes in terms of weight and strength requires advanced and high strength materials, and more details can be found in Ref. [89]. At the beginning of the development of the failure model, the emphasis was placed on the triaxiality of the constraints and since the in-depth experimental studies. There is a trend within the natural gas transportation industry towards lower operating pressures, temperatures, and the use of higher quality pipeline materials [90]. Moreover, the emergence of these changes in characteristics has come to a great need to accurately predict the stopping behaviour of ductile fracture in metal under these conditions. However, many experts believe that forecasting methods found in the industry require significant improvement, as they are suitable for lower grades of steel and lower operating pressures by the standards of the operating environment as described in Ref. [91]. In the pipeline, there are two types of crack, namely ductile crack, and brittle crack. Since ductile crack occurs at a higher temperature where virtually all pipelines are in service. In pipeline industry applications, it is important to control the propagation and stop the ductile cracks.

An elastic crack propagates unstable for a long time as the crack velocity is less than the decompression rate during initial compression. This is because the decompression rate and crack rate decrease as pressure decreases at the bottom crack [92]. The damage model of GTN is widely applied to simulate the dynamic propagation of ductility fractures. Due to the limited set of parameters in this model, it is often adopted in engineering applications [93]. The GTN mesoscopic damage model is used as a tool to support the FE model of the experimental test process. The provided results have shown that the fracture speed and the pronounced opening angle were in good agreement with the experimental results. Lian [94] simulated the failure process of an X70 high steel pipeline under loading conditions and established the damage mechanics model with hole expansion being a damage variable. Gholipour et al. [95] presented an application based on the GTN damage model, the model simulates with acceptable precision of material fracture and damage evolution for SAE 1010 plain carbon steel. Recently, the ANN technique has been widely used for different applications, such as in the study of surface texture, mechanical properties, the effects of processing parameters on the alteration of mechanical properties, the phenomenon of corrosion and fatigue, damage identification [96-100]. However, ANN was improved based on some challenges using optimization techniques for damage identification in several structures as mentioned in Refs. [101-103].

In the pipeline used in working environment, there is a critical problem to prevent pipeline cracking [104-106], so it is exposed to the onset of the rupture and crack propagation [107]. The

onset of failure occurs due to assembly deformation, base metal defect, and mechanical damage, for example, notching, cracking, corrosion, and erosion [108-111], etc. It arrives at unstable critical fault length or a certain level of stress and starts to propagate. When crack initiates, it arrives at an unstable critical fault length or certain stress level and begins to propagate, and in principle could propagate persistently unless captured by crack barriers and could stop under certain conditions and by technical methods applied to several cases of cracks[112].

Pipelines can be exposed to extreme disfigurement and deformation close to the critical fault zone, resulting from certain handling of transportation and installation with underground operations such as torsion or mechanical biaxial tensile loading from longitudinal deformation, and internal pressure due to the existence

In general, the experimental fracture toughness data obtained from a SENT test may be more appropriate for initial predictions of pipeline fracture under internal pressure than data obtained from standard notched fracture specimens under the bending load and Charpy impact test [113].

In this work, the influences of different notch depths on the mechanical characteristics of the fracture are investigated using Finite Element Method (FEM) during Single Edge Notch Testing (SENT) API X70 pipe steel. The constitutive model of Gurson-Tvergaard-Needleman (GTN) is applied to simulate the growth of voids during the deformation of pipeline for a considerable number of depth cases. SENT test simulations provide numerical results under experimental conditions allowing the creation of big data containing changes in stress and strain for different notch depths.

The application of GTN is used in a number of studies for different cases, and especially in fracture mechanics [114-116]. For machine learning and improvement of an artificial neural network, a number of new optimization techniques has been taken to solve many problems and in different fields [117-122]. YUKI algorithm and POD-RBF were used to identify cracks for elastostatic and dynamic cases [6], Jaya and E-Jaya optimization technique, for crack identification were used in Refs. [123, 124], and more researches on training different optimization codes for crack prediction and identification are presented in Refs [114, 125, 126].

Machine learning has recently received recognition for its capacity and flexibility to solve extremely challenging, multidimensional problems and in many fields too. Artificial neural networks (ANN) had quite a lot of success in overcoming such issues, in this work an ANN-based on different optimization codes has been employed to solve one of these issues. The collected data was used as input in training different optimization techniques to predict notch depth, so the study ended by choosing the best optimization codes NN-YUKI, NN-Jaya, NN-E-Jaya. , cited in this article comparing a number of sufficient scenarios based on the collected experimental and numerical data with actual values, and taking the best prediction of notch depth

on specimens under uniaxial loading according to the maximum stresses supported by each notch depth.

In the current researches, API X70 steel is utilized for long-distance transport under great pressure and is required to meet the best low temperature toughness and structural integrity [127]. The drop weight tear test (DWTT) was established in the mid-1960s as a method to evaluate pipeline steels [128, 129]. Unlike the Charpy test with a certain thickness, e.g. 10 mm, DWTT simulate the actual pipeline steels with the same thickness and represents fracture resistance and transition temperature. To adequately investigate the fracture propagation behaviour, DWTT has a longer fracture path compared with Charpy V-notch test models (CVN) [129, 130]. Furthermore, it is more efficient in evaluating the steel resistance to fracture propagation.

Optimization methods are successful in resolving real-world obstacles. Obtaining a resolution to these systems, nonlinear, and multimodal real-world difficulties normally need careful optimization methods, so essentially metaheuristic algorithms [121, 131, 132] proved to be a good optimization techniques. The universality of metaheuristic algorithms, adds to their efficiency of use and implementation. Metaheuristic algorithms become favorably used to resolve the difficulties in medicine, engineering, pipelines, aerospace, and several extra fields [117, 133, 134].

The application of XFEM is utilized in a number of studies for different domains, and particular in fracture mechanics [135-139], Samir and al used (BCMO) algorithm for comparison with Arithmetic Optimization Algorithm [140], the optimization code Jaya and PSO for crack identification in this study [125, 126], the investigation in fracture toughness and the fracture energy of epoxy-based nanocomposites in Ref [141]

The application of XFEM is used in this study to obtain the values of peak load and absorbed energy at peak load in brittle fractures in the case of impact testing with various crack lengths. A high-strength steel pipeline material is modeled using impact fracture models. Numerical data of peak load and absorbed energy values are used to create data inputs and outputs based on different crack lengths, which are then collected and trained on an improved artificial neural network based on the optimization of the composite balancing motion (BCMO) [142] and Particle Swarm Optimization (PSO) [143], as well as the Jaya algorithm [144] for predicting peak

load and absorbed energy of dynamic brittle fracture values in a steel X70 with different crack lengths. The goal of this project, as well as several optimization strategies, is to use good data and settings to achieve better results.

1.7 Conclusion

Structural Health Monitoring (SHM) plays a crucial role in ensuring the integrity and safety of structures throughout their lifespan. It involves the design, development, and implementation of systems that detect, localize, and quantify damage in structures. Damage is generally defined as changes that adversely affect the current or future performance of the system, and its significance lies in comparing two states of the system: the initial intact state (considered healthy) and the momentary state.

In the context of SHM, two main types of structural condition control techniques are utilized: non-destructive testing and destructive testing. Non-destructive testing techniques, such as X-rays, gamma rays, ultrasound, and acoustic emissions, are widely used to monitor the integrity of structures without causing degradation. On the other hand, destructive testing involves methods that may degrade the structure during the assessment.

The application of artificial neural networks (ANN) has gained popularity in the field of damage identification and detection, particularly when analyzing mechanical properties. ANNs excel at establishing nonlinear relationships between structural mechanic's characteristics and damage information, making them a valuable tool in the SHM process. The ultimate goal of SHM is to diagnose damages early, non-destructively, and cost-effectively. This involves continuous measurement of the structure over time, extracting damage-sensitive features from the measurements, and analyzing them to identify the current state of the system. By utilizing assessment methods based on static or dynamic analysis, SHM ensures that structures remain safe and efficient throughout their operational lives.

In the upcoming chapter, we focus on providing comprehensive information about steels and various processes, along with a detailed examination of the behavior of the specific steel utilized in pipeline manufacturing. Additionally, we offer a recap of essential elements of fracture mechanics and the numerical techniques applied in our studies.

Chapter 2: Overview of the mechanics of pipeline materials and the numerical techniques used

2.1 Introduction

A pipeline is a buried or above-ground conduit used to transport petroleum products and natural gas, whether in liquid or gaseous form. Pipelines are most often constructed from welded steel tubes that are externally or even internally coated and are generally buried in the ground [145].

The transport of hydrocarbons, including petroleum products and natural gas, is carried out through steel pipes from their deposits to the refining areas, distribution centers, and consumption points. In Algeria, the pipeline network was estimated to be more than 19,599 km in 2013, compared to 19,063 km in 2012. Transporting hydrocarbons by pipeline remains the safest method for transporting large quantities of oil and gas over long distances.

In the following section, we will present an overview of the mechanics of pipeline materials and the numerical techniques used in our studies.

2.2 Main causes of pipeline failures

2.2.1 Introduction

Pipeline and tank damage in the oil industry is a well-known issue, often attributed to environmental settings and service conditions. Various types of damage, such as erosion, corrosion, and embrittlement, can significantly impact structures designed for handling petroleum products. These damages may include the presence of cracks, notch holes, and complex geometry defects.

All pipeline steels are susceptible to failure due to internal and external forces, including mechanical and thermal stress, as well as conditions such as creep, fatigue, and erosion. Internal and external corrosion, as well as cracking and manufacturing defects, are also common factors that can lead to harm in pipelines. The primary sources of leaks and ruptures in pipelines, which can occasionally result in catastrophic damage, are internal and external corrosion. Such damage can lead to human harm, environmental pollution, additional repair costs, prolonged pumping stoppage, and more.

An oil or gas pipeline spill can have severe consequences, posing an environmental catastrophe with potential long-term effects on ecosystems. This highlights the critical importance of ensuring the integrity and maintenance of pipeline structures in the oil industry to prevent accidents and minimize environmental impact.

2.2.2 Pipeline failures

Among the parameters influencing the fatigue behavior of pipelines and structures, there are three main categories represented in the following flowchart (**Figure 2. 1**).

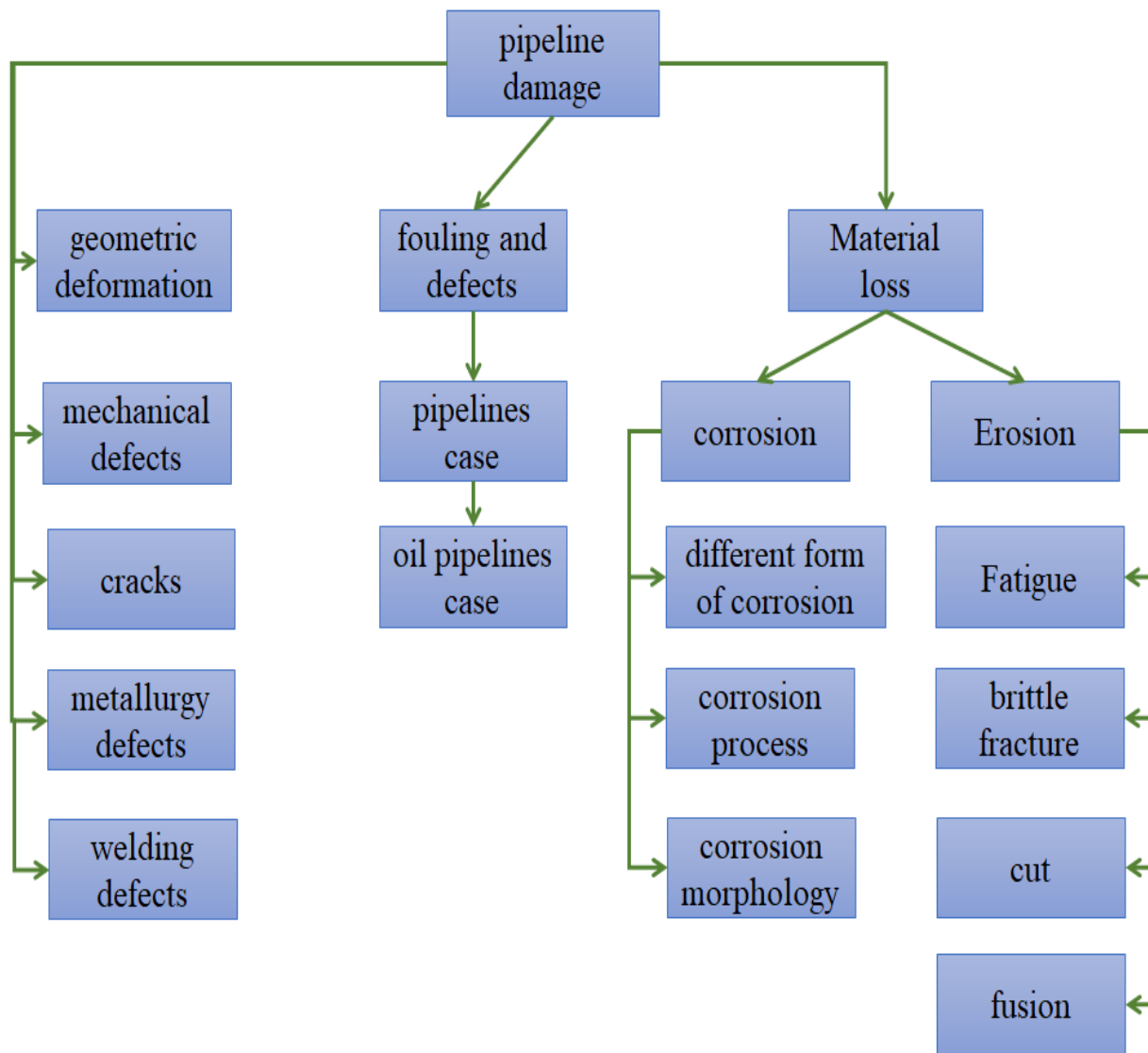


Figure 2. 1 The major categories of damage.

Failures of tubes or pipes under pressure can occur due to various causes, leading to either rupture or a "crack" leak. Some of the common factors behind these failures include pitting or stress corrosion cracking, as well as welding defects. Additionally, ground movements, such as ground slides or earthquakes, can also cause damage to buried pipes (**Figure 2.2**).

Tube operators have extensively studied these issues and possess a wealth of knowledge regarding methods to effectively manage and mitigate them. By understanding the causes of failures and implementing appropriate preventive measures and maintenance strategies, operators

can ensure the safe and reliable operation of pipelines and minimize potential risks associated with pipe failures.

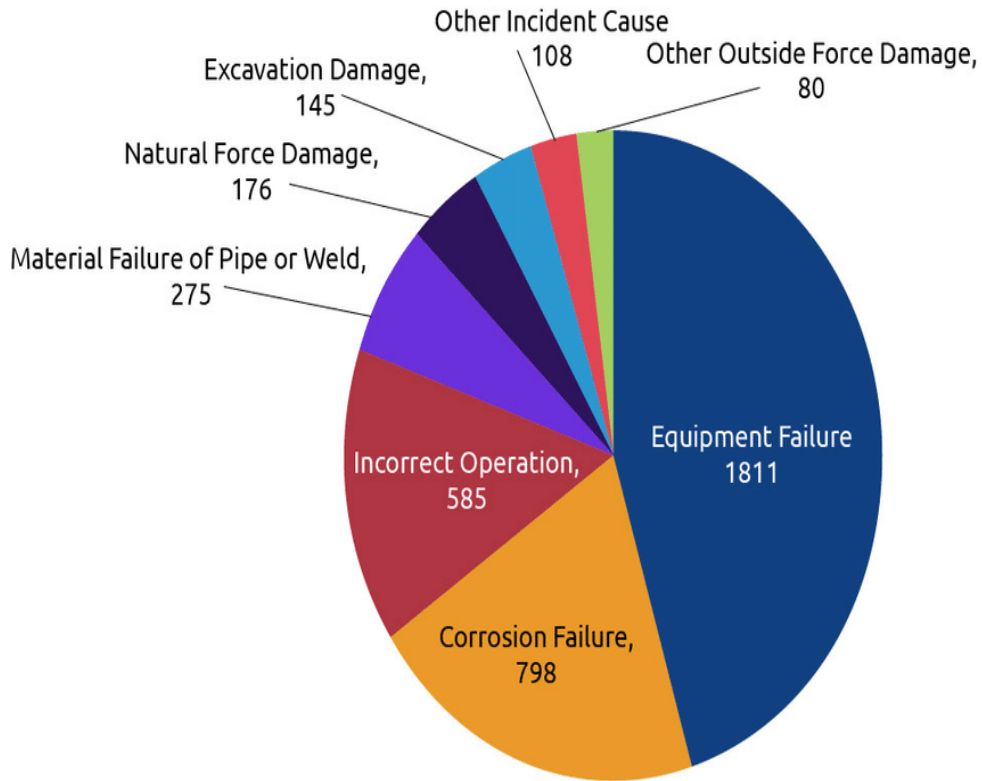


Figure 2. 2 Causes of pipeline failure during operation [146].

More than 90% of in-service fractures are caused by fatigue crack initiation issues and fractures originating from stress concentrations. The breaking strength of the tube will decrease in the presence of a geometric discontinuity like a notch. A local amplification effect of the stress will make this deficiency more harmful because it will diminish the section of the latter by making it more sensitive to the service pressure and to the forces induced by the movements of the earth.

2.3 Steel

Due to its physical, chemical and mechanical properties, steel occupies an important place in the ferrous metals industry, hence its use in various fields such as in the transport by pipeline of hydrocarbons (oil and natural gas).

It is used for the manufacture of pipelines (gas pipelines and oil pipelines) to transport large quantities of hydrocarbons over long distances from their deposits to consumption and processing areas. Today there are more than one million km of pipeline network in operation in the world.

In Algeria, the pipeline network is estimated to be more than 19,599 km, with diameters ranging from 8 to 48 inches (203.2 to 1219.2 mm). For their efficiency, these pipes must meet profitability and safety requirements. More than 95% of the steels used for gas pipelines are high-strength micro-alloyed steels [147]. Steel is an iron-based alloy with a low percentage of carbon added (from 0.008 to about 2.14% by mass). The carbon content has a considerable and complex influence on the properties of the steel, the alloy is rather malleable and it is called "iron" with very low carbon content. Beyond 2.14%, carbon inclusions in graphite form weaken the microstructure and we speak of cast iron. Between these two values, the increase in the carbon content tends to modify the mechanical resistance.

Steel can be classified as "soft, semi-soft, semi-hard, hard, or extra hard" based on traditional classification. We also modify the properties of steels by adding other elements, mainly metallic, and we speak of alloy steels. In addition, we can still greatly modify their characteristics by heat treatments, we then speak of treated steels. In addition to these various potentialities, and compared to other metal alloys, the major interest of steels lies on the one hand in the accumulation of high values in the fundamental mechanical properties: resistance to forces, modulus of elasticity, elastic limit, mechanical resistance, hardness, impact resistance (resilience). Finally, steels are practically entirely recyclable thanks to the scrap metal sector.

As a result, steels remain preferred in almost all areas of technical application, such as: public facilities, building, means of transport, mechanical components.

2.3.1 Classification of steels

Due to the high number of elements added to iron and the wide range of their content, steels have a very large number of different shades. The various types of iron-based alloys can be classified according to their chemical composition or according to their field of use.

The adoption of the latter allows us to identify four families of steels: General purpose carbon steels; Heat treatment steels, alloyed or not; Tool steels; Stainless steels.

✓ Ordinary steels and carbon steels

Standard general purpose steels known as carbon steels are occasionally misnomered. They are used as such, untreated, and account for around 80% of the manufacturing of steel (**Table 2.1**). The following additions and impurities are present in these steels in addition to carbon: manganese (1.2%), silicon (0.6%), sulfur (0.06%), and phosphorus (0.06%). The limiting contents of these elements in these steels are shown by these percentages.

Table 2. 1 Ordinary steels or unalloyed carbon steels.

Grade	Carbon Pourcentage (C)	Strength Smax (MPa) Annealed condition	Uses
Extra soft	$C < 0.15$	330-420	Sheet metal for bodywork, strips, hardware Forgings
Soft	$0.15 < C < 0.20$	370-460	Structural steel, profiles, mechanical construction, current, bolts, ordinary wires
Semi-sweet	$0.20 < C < 0.30$	480-550	Machine parts for mechanical applications Cast parts or frames, forged parts.
Semi-hard	$0.30 < C < 0.40$	550-650	Small tools, elements of agricultural machinery, transmission component
Hard	$0.40 < C < 0.60$	650-750	Arming tool parts, slides, rails and bandages, springs, cutlery, molded and treated parts
Extra hard	$C > 0.60$	$S_{max} > 750$	Machining and cutting tools, cables, spring

Even though they can be found with a variety of mechanical characteristics, common steels do not satisfy all usage requirements. The primary carbon steel characteristics that can be enhanced are:

- hardenability;
- Solderability;
- Heat resistance;
- Resistance to wear and corrosion.

2.3.2 Welding of carbon steels

Steels for welded constructions are hypoeutectoids and their carbon content does not exceed 0.40%. Alongside carbon, we always find in steel some unavoidable elements, whose presence is due to the manufacturing process and which are Manganese, Silicon, Sulfur and Phosphorus.

The welding operation differs from conventional metallurgical operations in that the heating rates are very high, that the maximum temperatures of the various points of the parts vary with their distances from the joint and that the durations of maintenance of these temperatures are very weak. In addition, the metallurgical transformations that appear on cooling, in the heat-affected zone (HAZ) of the welded joint, are accompanied by heat treatments. Experience shows

in fact that the final metallurgical structure at any point of the HAZ depends practically only on the maximum temperature reached at this point, and on the cooling criterion. See **Figure 2. 3**.

There are four types of zones: 1. the melted zone, where the maximum temperature is greater than or equal to the melting temperature; 2. the entirely austenitic zone, where the maximum temperature is between the melting temperature (MT) and the AC3 temperature; 3. The partially austenitic zone, where the maximum temperature is between AC3 and AC1; and 4. The influenced zone (not austenitized) where the maximum temperature is lower than AC1.

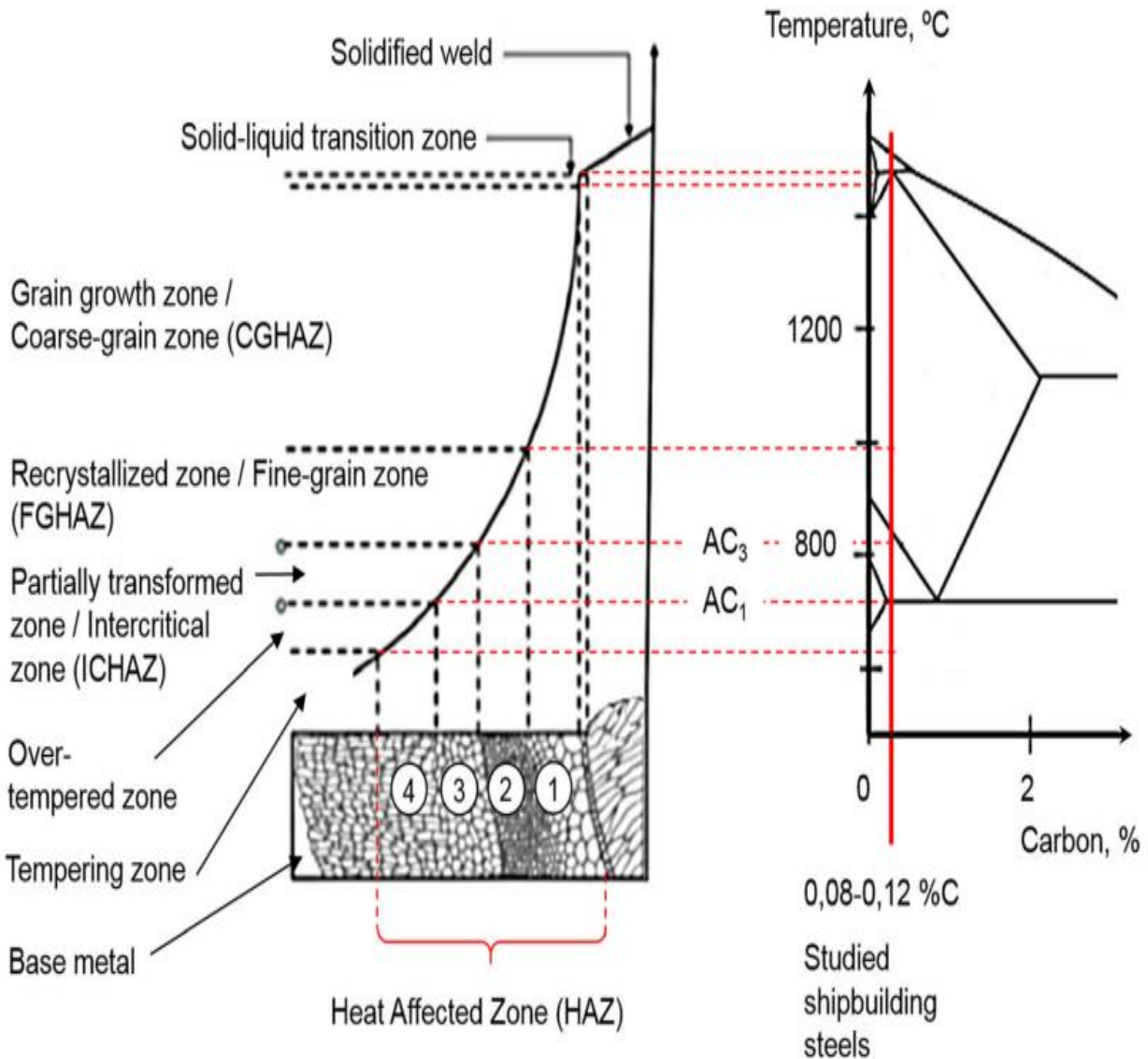


Figure 2. 3 Steel processing in the heated zone [148].

2.3.3 Weldability of carbon and low alloy steels

The weldability of steels depends on the internal structure of the metal in the HAZ after welding. In order to preserve the qualities of the metal to be welded, in particular with regard to ductility, the welded metal must regain an internal structure similar to its initial state.

Figure 2. 4 illustrates the effect of the temperature on the grains of steel, one can notice the zone where one finds austenite, it is in this zone that, in the case where the cooling is too fast, the metal solidifies into martensite rather than ferrite and pearlite, which creates internal stresses [13].

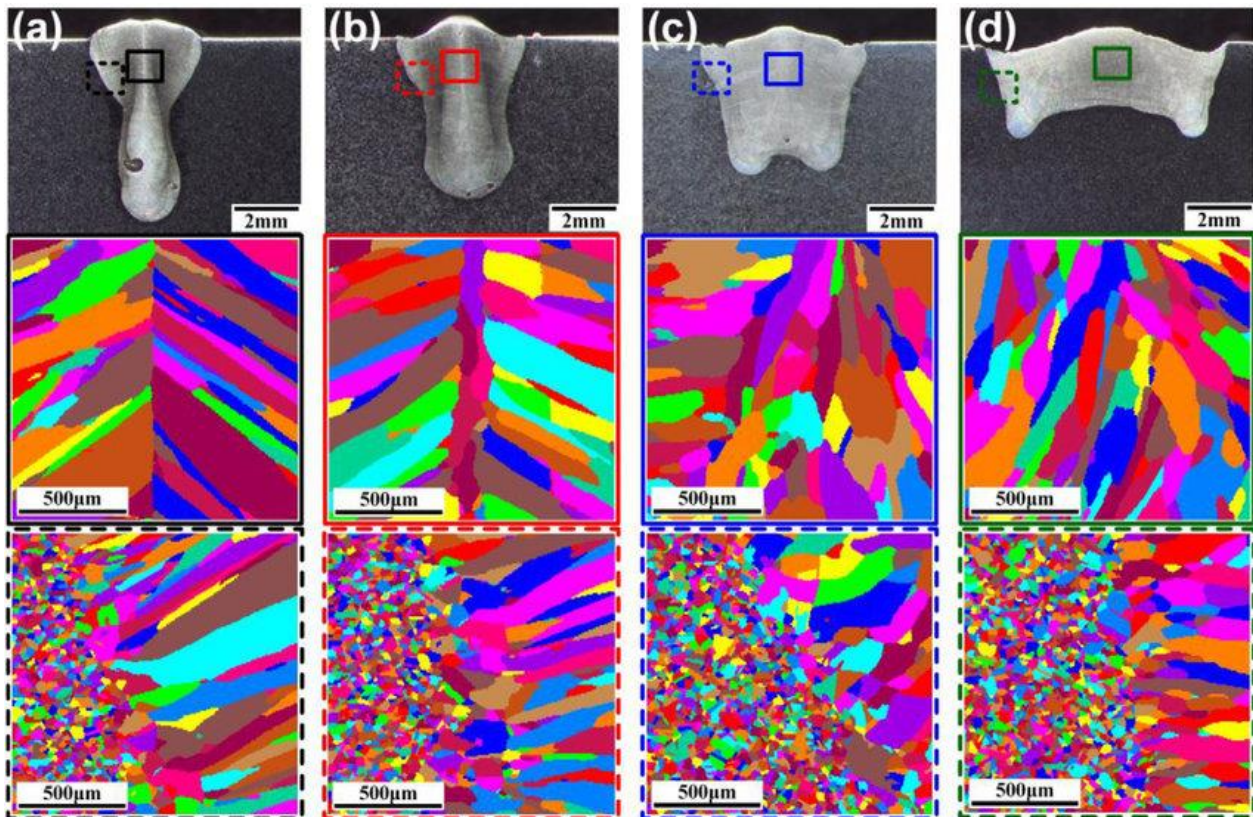


Figure 2. 4 Influence of temperature on grains [149].

The main factors that affect the weldability of carbon are:

- Hardenability: this is the main factor. It determines the behavior of steels during rapid cooling. The more steel tends to adopt a martensitic structure, the more its fragility increases and this increases the risk of cracks.

- Carbon Equivalent (CE): Carbon Equivalent is a measure that fairly well determines the hardenability of steel, as the higher the carbon content, the more likely the steel is to undergo hardening. The weldability of steel is therefore dependent on its equivalent carbon (**Table 2.2**).

Table 2. 2 Influence of equivalent carbon on the weldability of steel.

Carbon equivalent (CE)	Weldability	Preheat
Up to 0.35	Excellent	Not Necessary
0.36-0.40	Very good	Recommended
0.41-0.45	Good	Necessary
0.46-0.50	Fair	Necessary
Over 0.50	Poor	Necessary

The following metals enter into the calculation of the equivalent carbon: carbon of course (C), manganese (Mn), silicon (Si), chromium (Cr), molybdenum (Mo), vanadium (V), nickel (Ni) and copper (Cu).

The formula to use is:

$$\text{Carbon equivalent} = C + \frac{Mn + Si + Cr}{6} + \frac{Mo + V}{5} + \frac{Ni + Cu}{13}$$

In this formula, the symbol of the element indicates its mass percentage in the alloy

(For example, if we have 0.5% carbon and 0.03% manganese, then C = 0.5 and Mn = 0.03).

Another Japanese essence formula would apply to a wide range of lower carbon high yield strength steel grades (case of steels for tubes) [61]:

$$\text{Carbon equivalent} = C + \frac{Mn + Cu + Cr}{20} + \frac{Ni}{60} + \frac{Mo}{15} + \frac{V}{10} + 5B$$

The higher the carbon content, the more difficult the steels are to weld.

2.3.4 High elastic limit steels

Low carbon steels classified as high strength low alloy (HSLA) use a small number of alloying elements to achieve yield strengths greater than 275 MPa when rolled or normalized. Compared to lamellar graphite carbon steels, these steels have greater mechanical qualities and occasionally better corrosion resistance. Additionally, the weldability of HSLA steels is on par

with or better than mild steels, and the high elastic limit of these steels may be reached at low carbon content.

2.3.5 Submerged welding in powder form

Main characters

- Electrode: fusible metal wire unwound continuously.
- Protection: simultaneous supply of composite powder called flux.
- Current: direct and alternating.

2.3.6 Process description

Submerged arc welding (SAW) is the automation of covered electrode welding. It combines a fusible electrode wire, unwound from a reel, with protection obtained by vapors from a composite powder comparable to the coating and brought directly into the arc zone, but independently of the electrode.

This arrangement makes it possible to carry out multi-hour uninterrupted welds. This process is also called submerged arc welding (submerged arc welding process or SAW).

Submerged welding is carried out almost exclusively automatically with installations whose principle is shown in **Figure 2. 5** and which essentially comprise:

- A welding head comprising the torch itself, the wire drive, the reel receiving the wire reel, the powder hopper and its conduit to the torch;
- A source of direct or, in some cases, alternating current;
- An automation box and accessories.

As in any automation, the submerged welding head is fixed on a mechanism according to the two essential variants: fixed head, moving part or vice versa. As shown in **Figure 2. 5**, the current is brought to the fusible electrode by the contact tip, or wire guide, on the walls of which it rubs permanently.

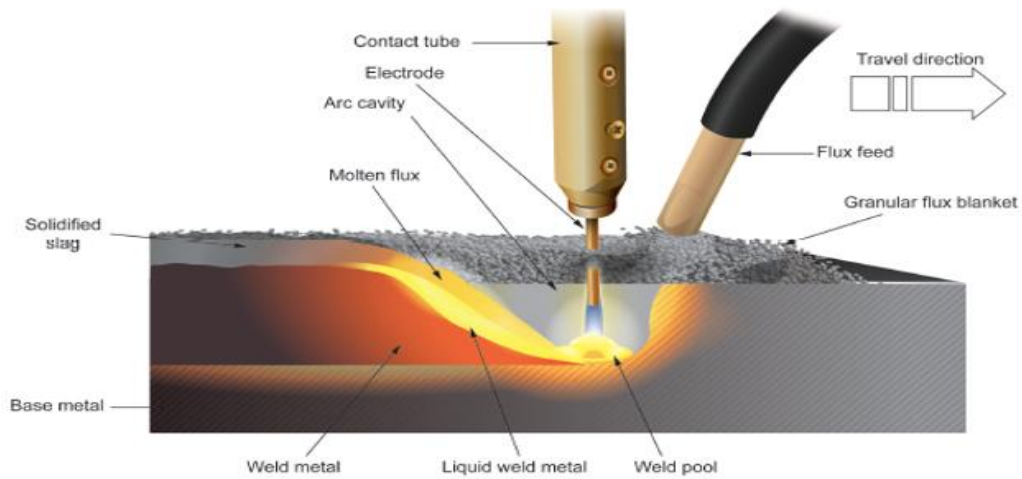


Figure 2. 5 Principle of submerged powder welding.

2.3.7 Application domain

Submerged welding is placed, compared to coated electrode welding, with practically the same advantages in terms of its metallurgical adaptability, but it solves the problem of productivity by:

- Its continuous operation thanks to the wire electrode;
- Its higher deposit rate;

This confines it to the field of medium and heavy boilermaking and, in general, to applications in which:

- The thicknesses are high (> 30 to 50 mm) and, consequently, the chamfers are significant;
- The welds are long (several meters) and uniform (no angle).

This process is practically not used manually because of the flux and wire leads which form, at the level of the torch, heavy and difficult to maneuver equipment. It lends itself, on the other hand and naturally, because that is why it was developed, to the mechanization of welding for which the flat position, necessary for the retention of the flux, is easy to observe.

2.3.8 Welding defects

A possible definition of what is meant by defect could be "Geometrical accident other than those inherent in the weld beads themselves".

We therefore encounter all the unusual notches presented by the weld bead and its immediate vicinity. We can cite, by referring for example to the following classification (see **Figure 2. 6**):

- ✚ • The cracks ;
- ✚ • Cavities;
- ✚ • Solid inclusions;
- ✚ • Lack of fusion and penetration;
- ✚ • Shape defects.

Cracks: Cracks are ruptures which are generally caused during cooling, by stresses exerted on the structures during solidification or cooling, possibly weakened, in particular by the presence of hydrogen.

Description	Cross-section of weld	Radiogram
Worm hole		
Linear Slag Inclusion -		
Gas Pore		
Porosity (Linear)		
Lack of side-wall fusion - (lack of root fusion)		
Lack of inter-run fusion		
Longitudinal Crack		
Traverse Crack		
Radiating Cracks		

Figure 2. 6 Welding defects [150].

The orientation of the location of the cracks depends on their origin. However, they enter systematically into the family of plane defects, that is to say defects in which one of the dimensions is very small compared to the other two and the circumference of which therefore constitutes a particularly marked notch.

Cavities: belong to the family of volume defects and can result from different mechanisms. We will distinguish:

- Shrink marks: following shrinkage of the metal during its cooling, the empty space formed appears visually on the surface of the bead, as well as inside the bead.
- Blowholes: formed by gas trapped during solidification, this takes the form of bubbles.

Solid inclusions: made up of slag particles or oxides.

The lack of fusion or sticking results from a lack of bond between the molten metal and the base metal while the lack of penetration represents the lack of fusion of the edges to be welded during the first pass. These defects are also plane defects.

Defects in shape: are particularly numerous and we will mention, without insisting on them:

- Excessive thicknesses and collapses;
- Misalignments;
- Channels.

2.4 Fracture mechanics

2.4.1 General

The separation into two disjoint parts of a body occurs following the propagation of a crack, which has seen the development of microcavities, microcracks and then initiation, under the action of mechanical, thermal, chemical stresses. When a material is stressed until failure, the tests show that the breaking stress σ_{-R} is a quantity presenting strong fluctuations which can even

exceed the limit for certain materials and that the mode of failure depends on the nature of the material.

Rupture can occur suddenly with almost no prior deformation for materials qualified as brittle, while it only occurs after a stage of large permanent deformation for materials qualified as ductile. We now know that brittle materials break abruptly above a certain tension, while ductile materials flow plastically under shear before breaking [151-153].

The failure mode also depends on the state of stresses, a material that has a lot of plasticity will generally develop ductile failures, but may be subject to brittle failure. A material without plasticity (ceramics, metals at very low temperatures, certain resins) will always present brittle fractures. So if plasticity is absent or remains very confined, the theories which make it possible to deal with the problem consider the material as elastic everywhere: this is linear fracture mechanics.

2.4.2 Introduction to linear fracture mechanics

Fracture mechanics is essentially concerned with the study of macroscopic cracks:

It applies when there are discontinuities in the material which modify the state of stress, deformation and displacement, so that the homogenization of the medium no longer makes sense to describe the physical phenomenon associated with the presence of a macroscopic crack.

The concepts of linear fracture mechanics and the stress intensity factor are given by Griffith and Irwin. The two main events that contributed to the development of fracture mechanics are Griffith's demonstration in 1920 that the fracture of an elastic-brittle medium can be described by a global variable later referred to as the rate of energy release and Irwin's introduction of the concept of stress intensity factor in 1956 from his study of the singularities of the stress field. The years 1960-1980 are those of the rise and then the maturity of fracture mechanics, with in particular numerical developments and the treatment of nonlinear problems.

2.4.3 Notions of fracture mechanics

2.4.3.1 Flat elasticity reminders

a. Hooke's Law

The behavior equations (or Hooke's law) can be expressed either by using the couple of elastic constants (E, ν) (E = Young's modulus, ν = Poisson's ratio) or (μ, λ) , (μ = shear modulus and λ = Lamé coefficient). These constants are linked together by the formulas [154]:

$$\left\{ \begin{array}{l} \mu = \frac{E}{2(1+\nu)} \\ \lambda = \frac{E\nu}{(1+\nu)(1-2\nu)} \end{array} \right. \text{ et: } \left\{ \begin{array}{l} \nu = \frac{\lambda}{2(\lambda + \mu)} \\ E = \mu \frac{3\lambda + 2\mu}{\lambda + \mu} \end{array} \right. \Rightarrow \frac{\nu}{E} = \frac{\lambda}{2\mu(3\lambda + 2\mu)} \quad (2.1)$$

The two expressions of HOOK's law using these two pairs of constants are:

$$\bar{\varepsilon} = \frac{1+\bar{\nu}}{E} \bar{\sigma} - \frac{\nu}{E} (\text{trace} \bar{\sigma}) \bar{I} \quad \text{Ou} \quad \bar{\sigma} = 2\mu \bar{\varepsilon} + \frac{\lambda}{3\lambda + 2\mu} (\text{trace} \bar{\sigma}) \bar{I} \quad (2.2)$$

✚ **Plane stress state : ($\sigma_{xz} = \sigma_{yz} = \sigma_z = 0$)**

$$\begin{aligned} \varepsilon_x &= \frac{1+\nu}{E} \sigma_x - \frac{\nu}{E} (\sigma_x + \sigma_y) & \varepsilon_x &= \frac{1}{2\mu} \left[\sigma_x - \frac{\lambda}{3\lambda + 2\mu} (\sigma_x + \sigma_y) \right] \\ \varepsilon_y &= \frac{1+\nu}{E} \sigma_y - \frac{\nu}{E} (\sigma_x + \sigma_y) & \varepsilon_y &= \frac{1}{2\mu} \left[\sigma_y - \frac{\lambda}{3\lambda + 2\mu} (\sigma_x + \sigma_y) \right] \\ \varepsilon_{xy} &= \frac{1+\nu}{E} \sigma_{xy} & \varepsilon_{xy} &= \frac{1}{2\mu} \sigma_{xy} \end{aligned}$$

✚ **State of plane deformation: ($\varepsilon_{xz} = \varepsilon_{yz} = \varepsilon_z = 0$)**

$$\begin{aligned} \varepsilon_x &= \frac{1+\nu}{E} [\sigma_x - \nu(\sigma_x + \sigma_y)] & \varepsilon_x &= \frac{1}{2\mu} \left[\sigma_x - \frac{\lambda}{2(\lambda + \mu)} (\sigma_x + \sigma_y) \right] \\ \varepsilon_y &= \frac{1+\nu}{E} [\sigma_y - \nu(\sigma_x + \sigma_y)] & \varepsilon_y &= \frac{1}{2\mu} \left[\sigma_y - \frac{\lambda}{2(\lambda + \mu)} (\sigma_x + \sigma_y) \right] \\ \varepsilon_{xy} &= \frac{1+\nu}{E} \sigma_{xy} & \varepsilon_{xy} &= \frac{1}{2\mu} \sigma_{xy} \end{aligned}$$

Note: We pass from relations (2.1) to (2.2) by replacing λ by $\lambda^* = \frac{2\lambda\mu}{\lambda+2\mu}$ and μ unchanged,

$$\text{In effect: } \frac{\lambda^*}{2(\lambda^*+\mu)} = \frac{\lambda}{3\lambda+2\mu} \quad (2.3)$$

We can therefore write HOOK's law for the two states in the form:

$$\begin{cases} \varepsilon_x = \frac{1}{2\mu} \left[\sigma_x - \frac{\lambda^*}{2(\lambda^* + \mu)} (\sigma_x + \sigma_y) \right] \\ \varepsilon_y = \frac{1}{2\mu} \left[\sigma_y - \frac{\lambda^*}{2(\lambda^* + \mu)} (\sigma_x + \sigma_y) \right] \\ \varepsilon_{xy} = \frac{1}{2\mu} \sigma_{xy} \end{cases} \quad (2.4)$$

With:

$$\begin{aligned} \lambda^* &= \lambda && \text{Plane deformation} \\ \lambda^* &= \frac{2\lambda\mu}{\lambda+2\mu} && \text{Plane stress} \end{aligned}$$

The transition from (2.1) to (2.2) can also be done, with the variables E and v, by replacing:

$$v \text{ by } \hat{v} = \frac{\lambda^*}{2(\lambda^*+\mu)} = \frac{\lambda}{3\lambda+2\mu} \quad \text{whether : } \hat{v} = \frac{v}{1+v}$$

$$\hat{E} \text{ by } E^* = \mu \frac{3\lambda^*+2\mu}{\lambda^*+\mu} \quad \text{whether : } E^* = \frac{E(1+2\mu)}{(1+\mu)^2} \text{ et } \frac{1+v^*}{E^*} = \frac{1+v}{E}$$

4.3.5.1 Notions of fracture mechanics in linear elasticity

We will mainly deal with brittle fracture in the macroscopic sense of a material, ie a fracture occurring without significant macroscopic plastification, which does not exclude microscopic plastification at the crack tip. The brittle fracture model assumes that the material is homogeneous and isotropic.

2.4.3.2 Available energy rate G

The quantitative link between fracture and defect size was proposed by Griffith in 1920. Griffith's model, based on an energy criterion, correctly predicted the relationship between the resistance of the elastic-brittle body and the size of the defect. Irwin then developed this energy approach by introducing the concept of energy release rate G [155]. It is shown that the thermodynamic equilibrium of an elastic structure, containing a surface crack A, and loaded by

forces, with respect to the extension of this crack, is achieved if what is called the rate of available energy G is equal to a critical value G_C . G is defined by the formula:

$$G = \frac{dp}{dA} \quad (2.5)$$

With P total potential energy of the cracked structure, i.e. sum of the potential energy of the forces and the stored elastic energy, G_C being the energy which is necessary to expend so that the crack increases its area of one unit [156]. G , which can be expressed in J, it is also called the crack extension force. If G becomes greater than G_C , crack propagation occurs, with the extra energy turning into kinetic energy. It is demonstrated that:

$$G = \frac{1}{2} F^2 \frac{\partial C}{\partial A} \quad (2.6)$$

With F : Applied force,

C : complacency of the cracked structure, i.e. proportionality ratio between the displacement caused by the force F and this force F itself.

The toughness of the material is one of the core tenets of fracture mechanics. G_C is independent of the geometry and dimension of the cracked body. The fracture toughness measured on a laboratory specimen can be applied to another structure.

2.4.3.3 Stress intensity factor K

To study the state of the stresses in a zone close to the end of the crack, it is considered that it has a zero radius of curvature at its end and thanks to the theory of elasticity, it is shown that the stresses tend towards infinity when approaching this end as $r^{-1/2}$, r being the distance to the end of the crack. This behavior is asymptotic, in the sense that if r becomes large compared to the dimension of cracks, higher power terms of r begin to intervene to describe the stress field.

The zone where the term in $r^{-1/2}$ dominates is called the zone of elastic singularity. The constraints there are of the form.

$$\sigma_{ij} = \frac{k}{\sqrt{2\pi r}} f_{ij}(\theta) + \theta(r) \quad (2.7)$$

With $f_{ij}(\theta)$: function of the polar angle with respect to the end of the crack, always the same whatever the crack, the part and the loading, $\theta(r)$ is written to recall that there are other terms tending to 0.

With K : Stress intensity factor.

The K factor brings together on its own the effects of the crack's size, the forces used, and the geometry of the damaged area. Because this one and only characteristic determines the circumstances at the crack's terminus, fracture mechanics is successful. This therefore allows easy comparisons between specimen and structure: it suffices that K is the same for the stress state at the end to be identical.

At the moment of rupture, in particular, K reaches a critical value K_c which is therefore always the same and, therefore, characteristic of the material.

The displacement of the crack lips, itself a function of K, can be broken down into three components: parallel to the plane of the crack and to the bottom, perpendicular to the bottom of the crack and parallel to the front of the crack. To each of these components corresponds an elementary failure mode, mode I for component U1, mode II for component U2 and mode III for Component U3, see **Figure 2.7**. The most dangerous fractures generally occur in mode I, so most fracture mechanics studies have focused on this mode. We then assign the factor K to the index I.

The factors K_I , K_{II} , K_{III} are a function of the length of the crack, the geometry of the part and the loading. For example, in a very large plate containing a crack of length $2a$ and subjected to a homogeneous stress σ :

$$K_I = \sigma\sqrt{\pi a} \quad (2.8)$$

It is always possible to calculate these K factors by the finite element method.

The standards give the K factors for the main recommended specimens.

There is a relationship between the available energy rate G and the stress intensity factor K_I , provided that the crack does not deviate:

$$E'G = K_I^2 \quad (2.9)$$

With $E' = E$ (Young's modulus) in plane stress, $E' = \frac{E}{(1-\nu^2)}$ (ν being the Poisson's ratio), in a state of plane strain.

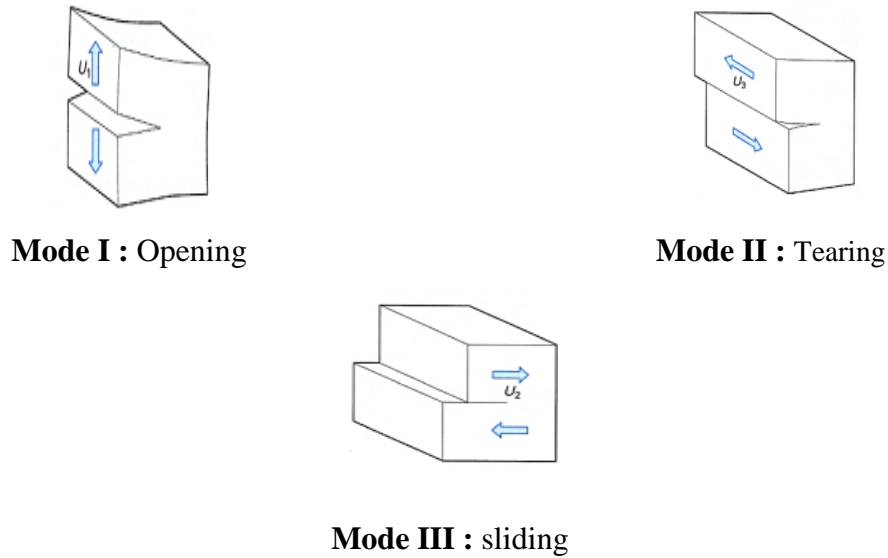


Figure 2. 7 The three failure modes.

In a cracked elastic zone, the region close to the crack tip can be broken down into three zones

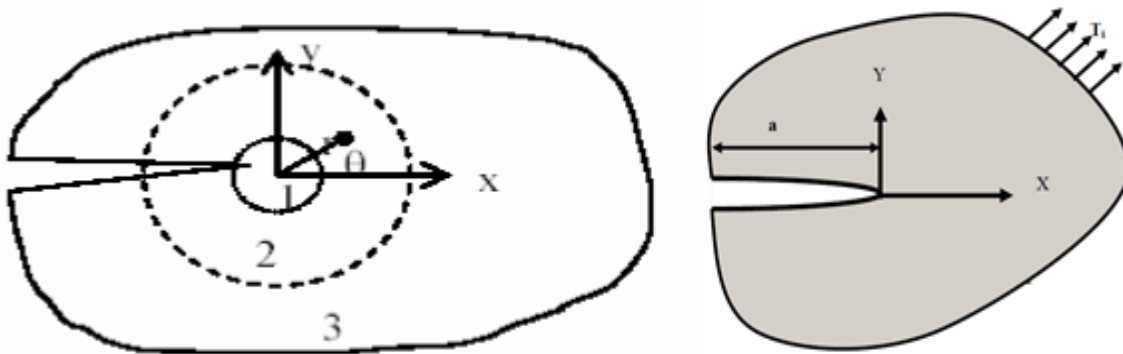


Figure 2. 8 Mechanical field zones.

- a. **The development zone:** in the direct vicinity of the crack tip, the study of this zone (considered as punctual, from a mechanical point of view) is very complex insofar as the stresses tend towards infinity (d from a theoretical point of view) with respect to the crack tip;
- b. **The singular zone:** in this zone, the stress field presents a singularity in $r^{-1/2}$
- c. **The singular zone:** in this zone, the stress field presents a singularity in $r^{-1/2}$

4.3.5.2 Stress concentration near a defect

If we consider an elliptical form defect of length $2a$ and radius at the bottom of the notch ρ , see **Figure 2.9**, the local stress at the end a is:

$$\sigma_y = \sigma \left(1 + 2 \frac{a}{b} \right) = \sigma \left(1 + 2 \sqrt{\frac{a}{\rho}} \right) \quad (2.10)$$

In the case of a very sharp notch, $\rho \ll a$ and we then have:

$$\sigma_y \approx 2\sigma \sqrt{\frac{a}{\rho}} \quad (2.11)$$

The factor $2 \sqrt{\frac{a}{\rho}}$ named stress concentration factor.

Where: σ_y , σ are respectively the stress in the y direction, the uniform tensile stress applied in the plane of the plate.

a and b are the semi-axes of the elliptical hole and ρ is the radius of curvature at the top of the hole.

In the case of a plate of infinite width and comprising a circular hole, the relation (2.11) is written:

$$\sigma_y = 3\sigma \quad (k_T = 3) \quad (2.12)$$

When the ratio b/a tends towards zero, the hole takes the form of a crack, σ_y tends towards infinity. (See **Figure 2.9**)

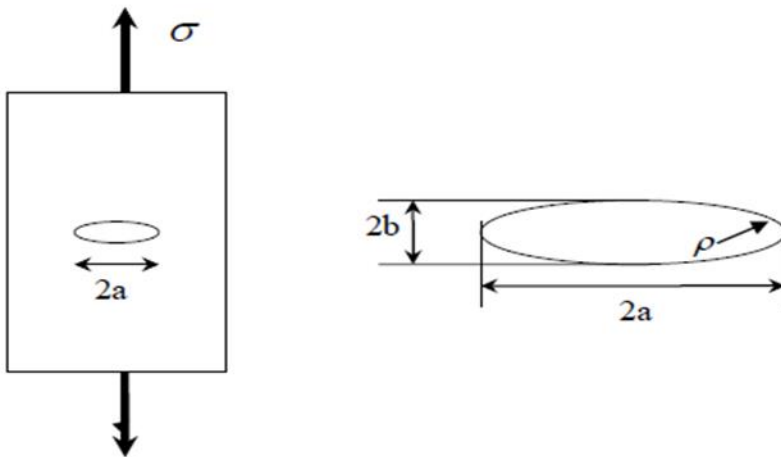


Figure 2.9 Elliptical defect in an infinite plate.

2.4.4 Application of the finite element method to fracture mechanics

The determination of the stresses and displacements necessary for the calculation of the coefficient of intensity of stress K , for the linear elastic case, and the integral J for the elasto-plastic case, constitutes one of the most important parts of the mechanics of the fracture. . For cracks of usual geometry where the analytical or approximate solution is known, one can propose to the designer lists of formulas, curves, and charts necessary for calculation.

For cracks with more complex geometry, one must use numerical calculation techniques such as the finite element method, it is a standard method for the numerical analysis of fracture mechanics problems.

Several techniques have been proposed for the evaluation of K and J from finite element analysis. However, the adequate representation of the singularity at the crack tip is still a common problem of these methods.

The use of the finite element method in the study of cracking takes into account two distinct considerations [157]:

✚ Modeling the singularity at the crack tip

The first studies using the finite element method in fracture mechanics, used elements that require extremely fine meshes in the vicinity of the singular point, to represent the singularities of the stress and deformation fields in a suitable way. However, it is advantageous to create unique crack elements to directly simulate the singularities in the area of the fracture tip for an effective investigation of cracking problems.

✚ Interpreting the results of finite element analysis

After the finite element analysis, a means must be found for the evaluation of the stress intensity factors from the results of the stress and displacement fields.

Several methods have been implemented for this type of calculation. The most obvious approach is to relate the analytical solution of the stress fields and displacements in the vicinity of the singular point to the results obtained, where extrapolation procedures are used to find the stress intensity factors. There are also other methods, which link the stress intensity factor to the rate of energy release associated with an infinitely small advancement of the crack. Another approach is to calculate the stress intensity factors from the value of an integral independent of the integration contour, such as Rice's J -integral.

2.4.5 Finite element method

2.4.5.1 Basic principle

The finite element method makes it possible to find an approximate solution of a problem governed by a system of partial differential equations with boundary conditions in a volume domain Ω . The steps of the finite element method are as follows:

- ✚ The choice of a functional of the displacement field $\Pi(u)$ which is the total deformation energy of the structure under the external stresses.
- ✚ Division of the volume Ω into N subdomains of volume Ω_e which connect to each other at the nodes. These subdomains are called finite elements.
- ✚ In each element, one chooses a field of displacement $u(x)$ which checks a priori the conditions of compatibility in the volume and the border. This field is said to be kinematically admissible.
- ✚ By the continuity of $u(x)$ through the interfaces, we realize the assembly of all the adjacent elements to obtain a global structure. We then obtain an approximation of $u(x)$.

This approximation tends towards the exact solutions $u(x)$ when N tends towards infinity and this convergence is ensured under certain conditions of regularity of the shape of the elements of the field of displacement.

- ✚ By introducing the boundary conditions, the solution of the problem is the one which minimizes the functional $\Pi(u)$. This leads to the equation:

$$[K][q] = [g] \tag{2.13}$$

Which represents the equilibrium equation discretized at the nodes.

Where:

$[K]$: is the global stiffness matrix.

$[g]$: is the global force vector.

$[q]$: is the vector of nodal displacements of the system.

This system is deduced from the principle of the minimum of the total deformation energy.

2.4.5.2 Crack definition

The surface that divides a solid into two halves locally is referred to as a crack. Consequently, the field of displacements through this surface is discontinuous. Fracture mechanics is the study of how this surface (the crack's propagation) changes over time in response to applied loads and the properties of the underlying material. The presence of a crack in a structure presents a local flexibility which affects the dynamic response, moreover, a fatigue crack is a crack which opens and closes in time according to the load conditions and the amplitude of the vibration.

2.4.6 Cracks in cylindrical pipes under pressure

Cracking is a sign of an illness, not a sickness itself. In fact, the materials are extremely susceptible to cracking because to their poor deformation capacity and little resistance to traction, compression, or pressure (see **Figure 2.10**).

However, there are some drawbacks to using new ductile materials (steel and other metal alloys) for tensile loads; ruptures have occasionally occurred for load levels well below the elastic limit. Initially, practitioners attempted to mitigate these rupture risks by oversizing the structures, but the need to lighten the structures and cut costs has sparked research on fracture mechanics.

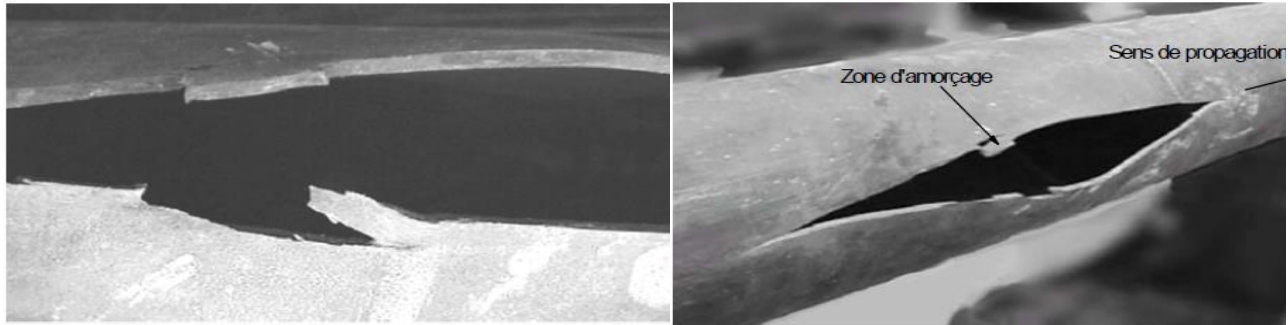


Figure 2. 10 Ductile failure of a pipe of average diameter under the effect of internal pressure.

2.5 Neural networks

2.5.1 Definition

Computer science is the science of automatic information processing, often confused with the evolution of processing machines (computers) and the configuration of software to solve different issues in all domains.

Software evolution can be done in several methods. The considerable utilized is the algorithmic (procedural) technique which needs writing down the procedure to be pursued to solve a problem. Additional current is the declarative (knowledge-based) technique which entrusts problem-solving to a set of regulations passed by a human professional in a special domain. Another technique is inspired by the processing of information carried out by the brain (known as connectionist).

2.5.2 The principal idea

At the base of the peak of artificial neural network (ANN), is that intelligent behavior is supported by a set of mental mechanisms based on neurophysiological processes. These ANNs are designed as very simplified mathematical samples motivated by the functioning of the central nervous approach, based on the idea of the biological neuron. They use simple elements (formal

neurons) strongly connected together by the connection weights procedure, input data to produce the expected outputs (Figure 2.11).

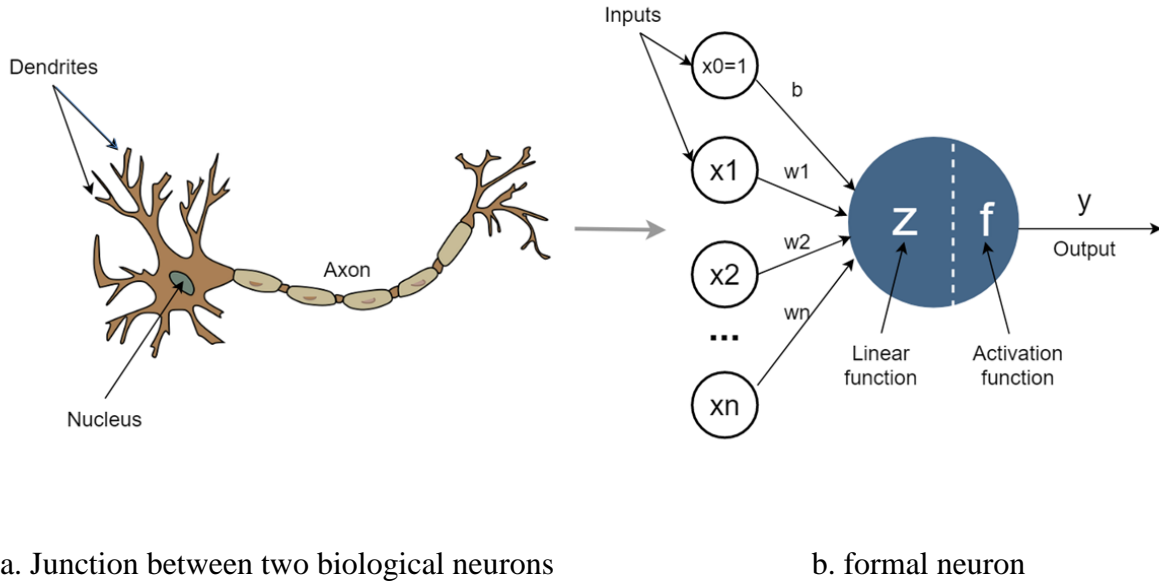


Figure 2. 11 Biological neuron modeling.

A neural network is a computational design formed of highly interconnected single processing components, which processes knowledge through their dynamic state modification in reaction to outer input (Hecht-Nielsen 1990). Generally, a formal neuron can be shown by the following expression:

$$O = f(\sum W_i I_i) \tag{2.14}$$

With, I_i , O : neuron input and output respectively, W_i : weight corresponding to each input, θ_{pk}^o θ : represents the threshold, and $f(x)$ threshold function checking $\forall x, f(x) = 1$ if $x > \theta$ and $f(x) = 0$ otherwise. The activation (transfer) function limits the output of the neuron with the minimum and maximum limits allowed, i.e. it offers an infinity of possible values between $[0, +1]$ or $[-1, +1]$.

It can take different forms: binary, linear with threshold, sigmoid. The choice of one of these functions turns out to be an important building block of ANNs. Often non-linear and more advanced functions will be required.

For information, here are some commonly used functions (Figure 2. 12):

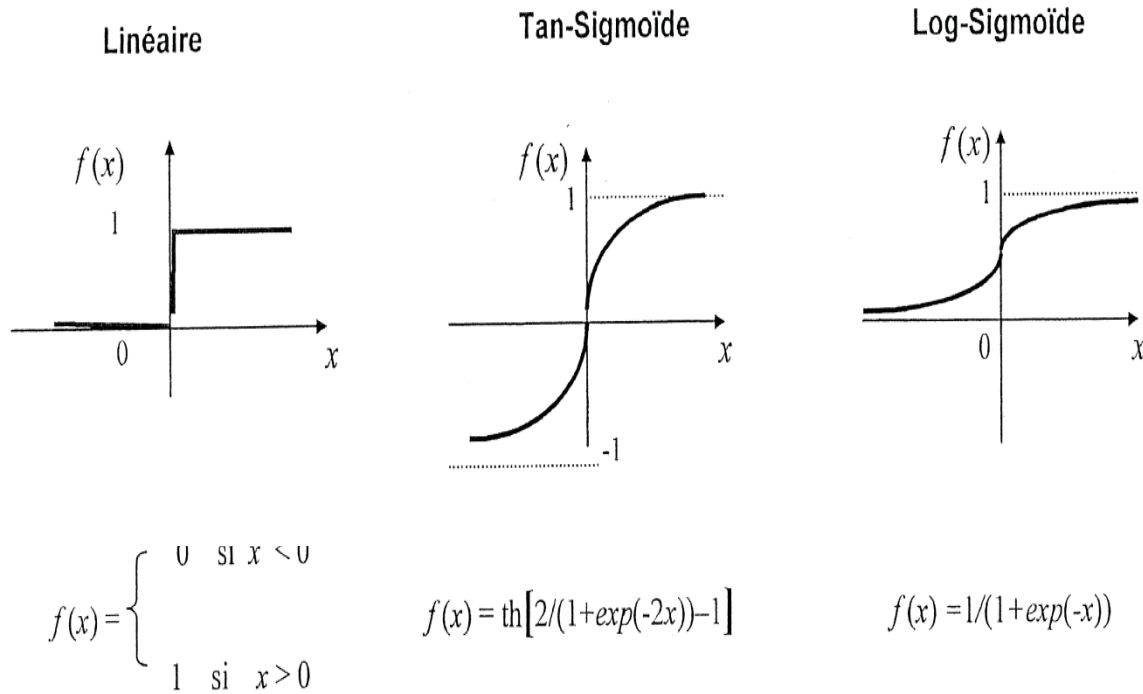


Figure 2. 12 Types of activation (transfer) functions.

2.5.3 Benefits of ANNs

ANNs does need a program, do not manage instructions and do not manipulate numbers. The defeat of part of these circuits does not stop the network from functioning. These principal properties are:

- Parallelism: it is the performance of several studies (numerical data and not symbolic) at the same time, which demonstrates the best speed of calculation of the ANN.
- Learning capability: it permits networks to accept into account constraints and data reaching from external. It is represented in certain networks by their capacity for self-organization which ensures their stability.
- Generalization: it permits the network to discover a generalized solution suitable to all samples of the situation, even if they include errors or are insufficient or not offered during training.
- Distributed memory: memory is distributed across considerable entities and the network.

2.5.4 Design and types of ANN

The design of the network is defined by the set of interconnected neurons. This design can range from complete connectivity or fully connected networks (full connection network) to regional connectivity or layered networks (one-way network), see **Figure 2.13**.

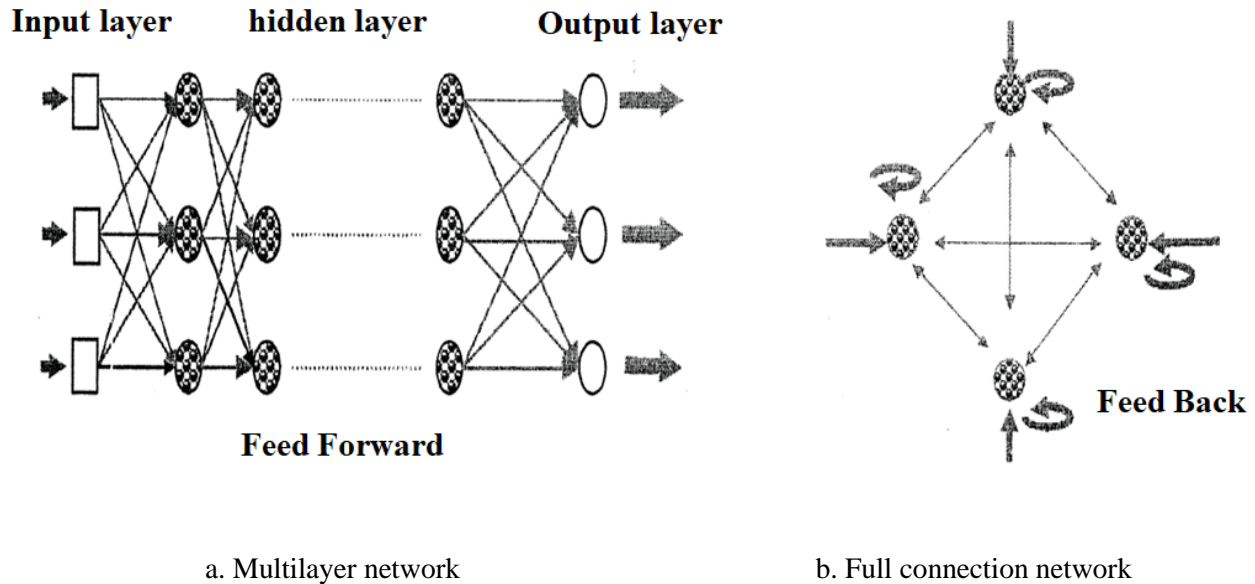


Figure 2. 13 Architecture of ANNs.

ANNs can be organized into two classes according to their development over time: static neural networks and dynamic neural networks. In the case of static neural networks, the recent output of one neuron does not influence the coming outputs of other neurons. At this point, time is not an important parameter. On the other pointer, dynamic neural networks also named recurrent networks have a time-dependent evolution and they are organized so that each neuron receives. Element or all of the network state indicates its inputs.

2.5.5 ANN mechanism

The associations between the components are adapted according to the procedure of adjustment of the weights, parallel to the regression equations (Geoffrey 1992). Several techniques have been extended to adapt the connection weights by learning regulations or algorithms from actual data. The most-known learning regulations are the Hebb rule, the Windrow-Holff (Delta) rule and the generalized Delta rule also named Backpropagation. There are specifically two classes of learning: supervised and unsupervised. This distinction is established in the form of the learning models, input/output pairs associated with multilayer static networks in the point of supervised learning, whereas just input values are available for unsupervised learning. in the point of dynamic (or recurrent) networks.

At the end of the training, the weight is specified, and then starts the phase of using the network.

Generally, learning brings place over a relatively long time (learning stage), during which the vectors of the input neurons can be offered to the network a considerable number of times (cycles or iterations). Selecting the learning parameters is the most necessary phase for ANN processing. These parameters are the learning speed, the learning error, and the number of iterations.

There are two other phases named test and validation which drive it possible to test the performance of the trained network.

2.5.6 Modeling by artificial neural networks (ANN)

2.5.6.1 Introduction

The artificial neural network (ANN) strategy is well suitable to deal with difficult systems. This approach reaches from work maintained out in the domain of artificial intelligence and is inspired by the functioning of the human brain, based mainly on the concept of biological neuron (McCulloch and Pitts 1943, Fortin et al. 1997, Najjar et al. 1997, Mas et al. 2004, Senthil Kumar et al. 2004). Each author has defined neural networks in his own way. The most classic (Haykin 1994) considers ANN as a massively distributed parallel process, which has a natural propensity to store empirical knowledge and make it available for use. It resembles the brain in two respects:

- Knowledge is acquired by the network through a learning process.
- Connections between neurons (synaptic weights) are used to store knowledge.

There is a wide variety of probable arrangements of artificial neurons (Lippmann 1987), but the considerable widely used type for prediction is the error backpropagation multilayer perceptron (Rumelhart et al. 1986, Najjar and Zhang 2000, Basheer et al. Hajmeer 2000, Senthil Kumar et al. 2004). This network includes an input layer, one or more hidden layers (multi layers perceptron), and an output layer. Each layer includes computational units (neurons) associated with other neurons by weights.

2.5.6.2 Backpropagation Multilayer Neural Networks

This model is an elongation of the perceptron model; it is probably the simplest and reasonably known of neural networks. It is a multilayer network (Multi-Layer Perceptron MLP) also named Multilayer Perceptron. It is capable to solve any difficult rational operation. This network employs the supervised learning model where the network is provided with a set of models (see **Figure 2.14**), each model consists of an input vector (numerical or actual values) and its chosen output vector. The weights are initially random, and it is through a “trial error correction” mechanism that this class of networks develops towards a stable form. This is reached by the Gradient Backpropagation rule (minimization of an error-dependent function). This technique is

the most manipulated for training static multilayer networks. It was improved by the Parallel Distributed Processing (PDP) research group.

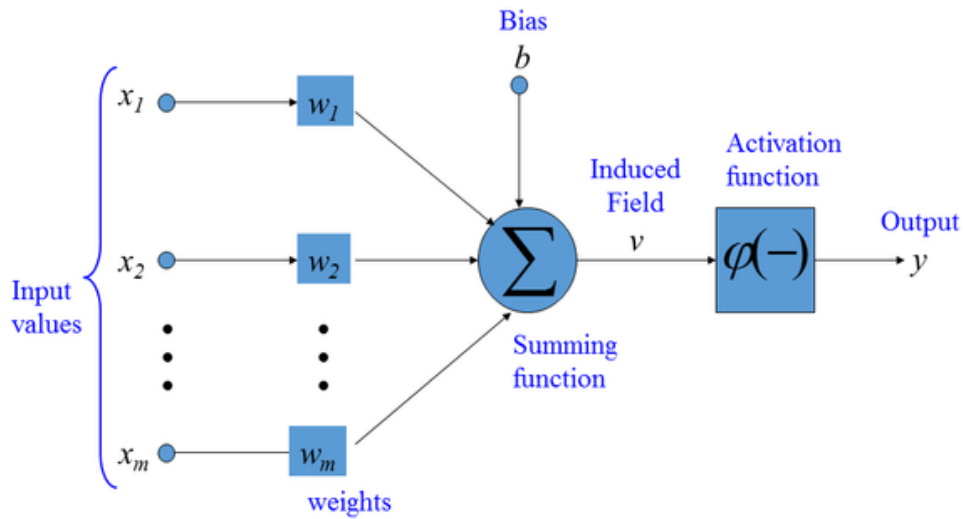


Figure 2. 14 Structure of an artificial neuron.

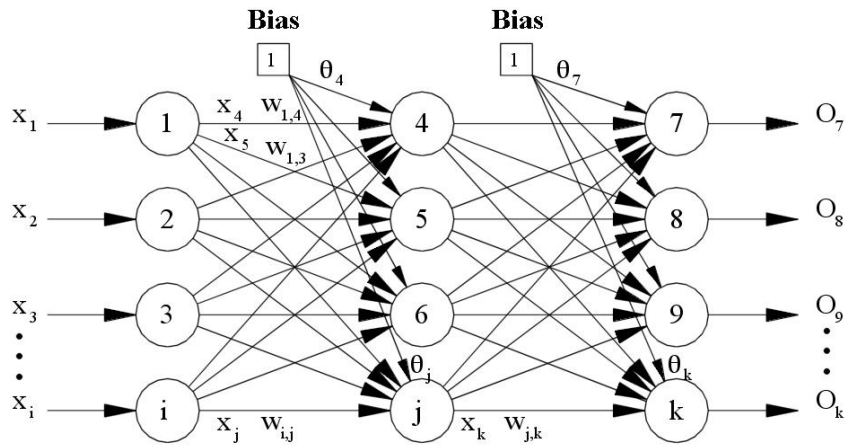


Figure 2. 15 Topology of a backpropagation multilayer neural network

In Figure 2.15:

w_{ji}^h Synaptic weight connecting the node j in h^{th} hidden layer at node i of the previous hidden layer or the input layer.

w_{kj}^o Synaptic weight connecting the node k in o^{th} hidden layer at node j of the previous hidden layer or the input layer.

θ_{pj}^h Value of the threshold of p^{th} vector of the learning base, j^{th} node of the h^{th} hidden layer.

θ_{pk}^o Value of the threshold of p^{th} vector of the learning base, k^{th} node of the output hidden layer.

The process of backpropagation of neural networks can be divided into two phases: input introduction and error backpropagation. During this technique, the synaptic weights are invariant. At the end of the first iteration, the output vector is compared to the expected vector, and an error value is estimated for each output node. This error signal is propagated in the opposite orientation from the output layer to the nodes of the adjacent hidden layer; individually the neuron obtains a share of this error according to its contribution to the output vector, i.e. according to its weight synaptic. This process is repeated each iteration, layer by layer, where the synaptic weights are going to be updated until the network converges towards a stable form.

2.5.6.3 Learning phase

Learning is supervised, i.e. an input configuration is associated with an output structure. The backpropagation algorithm is employed for network training. This algorithm is an iterative gradient designed to minimize the mean square error (MSE) between the obtained output and the desired output. This minimization is achieved by an adequate configuration of the weights. The error (e) is the difference between the desired value (t) for the output neuron and its value estimated by propagation (o).

2.5.6.4 Entering data

When the p^{th} example of the learning base is provided to the input layer, the value of the node j of the hidden layer is:

$$net_{pj}^h = \sum_{i=1}^N w_{ji}^h x_i - \theta_{pj}^h \quad (2.15)$$

The output of this node is:

$$\hat{o}_{pj}^h = f_j^h(net_{pj}^h) \quad (2.16)$$

Similarly, the output of node k of the output layer is:

$$net_{pk}^o = \sum_{j=1}^M w_{kj}^o \hat{o}_{pj}^h - \theta_{pk}^o \quad (2.17)$$

$$o_{pk} = f_k^o(net_{pk}^o) = f_k^o\left(\sum_{j=1}^M w_{kj}^o \hat{o}_{pj}^h - \theta_{pk}^o\right) \quad (2.18)$$

Where f_j^h and f_k^o represent the transfer functions of the j^{th} node of the hidden layer and the node k of the output layer. These functions must be continuous and differentiable.

2.5.6.5 Error calculation

The error made between the output vector of the neural network and the desired vector is calculated as follows:

$$\delta_{pk} = t_{pk} - o_{pk} \quad (2.19)$$

$$E_p = \frac{1}{2} \sum_{k=1}^M \delta_{pk}^2 = \frac{1}{2} \sum_{k=1}^M (t_{pk} - o_{pk})^2 \quad (2.20)$$

The backpropagation algorithm applies a correction $\Delta W(p)$ to the synaptic weights, which is proportional to the gradient $\partial E_p / \partial W(P)$, according to the following equation:

$$W(p+1) = W(p) + \Delta W(p) = W(P) - \eta \frac{\partial E_p}{\partial W(P)} \quad (2.21)$$

Where $0 < \eta < 1$ is a learning parameter. Since the gradient $\partial E_p / \partial W(P)$ is different between the nodes of the output layer and the hidden layer, the synaptic weights correction formula will be different.

2.5.7 Modification of synaptic weights linking the output layer

The total error E_p is related to the synaptic weights, related to the hidden layer by the formula:

$$E_p = \frac{1}{2} \sum_{k=1}^M \delta_{pk}^2 = \frac{1}{2} \sum_{k=1}^M (t_{pk} - o_{pk})^2 = \frac{1}{2} \sum_{k=1}^M \left(t_{pk} - f_k^o\left(\sum_{j=1}^M w_{kj}^o \hat{o}_{pj}^h - \theta_{pk}^o\right) \right)^2 \quad (2.22)$$

$$w_{ji}^h(p+1) = w_{ji}^h(p) + \Delta w_{ji}^h = w_{ji}^h(p) + \eta \delta_{pj}^k x_i \quad (2.23)$$

The gradient of E_p with respect to synaptic weights related to the hidden layer is:

$$\begin{aligned} \frac{\partial E_p}{\partial w_{ji}^h} &= \frac{1}{2} \sum_k \frac{\partial}{\partial w_{ji}^h} (t_{pk} - o_{pk})^2 \\ &= - \sum_k (t_{pk} - o_{pk}) \frac{\partial f_k^o}{\partial net_{pk}^o} \frac{\partial net_{pk}^o}{\partial \hat{o}_{pj}^h} \frac{\partial \hat{o}_{pj}^h}{\partial net_{pj}^h} \frac{\partial net_{pj}^h}{\partial w_{ji}^h} = - \sum_k (t_{pk} - o_{pk}) w_{kj}^o x_i \frac{\partial f_k^o}{\partial net_{pk}^o} \frac{\partial f_j^h}{\partial net_{pj}^h} = - \frac{\partial f_j^h}{\partial net_{pj}^h} \sum \delta_{pk}^o w_{kj}^o \end{aligned} \quad (2.24)$$

We pose the local gradient of the node j of the hidden layer.

$$\delta_{pj}^h = \frac{\partial f_j^h}{\partial net_{pj}^h} \sum \delta_{pk}^o w_{kj}^o = \delta_{pj}^h = \frac{\partial f_j^h}{\partial net_{pj}^h} \sum \delta_{pk}^o w_{kj}^o \quad (2.25)$$

So

When the transfer function is a sigmoid function of derivative $f' = f(1-f)$ the local gradient of a node of the hidden layer and that of the output layer are written respectively as follows:

$$\delta_{pj}^h = \frac{\partial f_j^h}{\partial net_{pj}^h} \sum \delta_{pk}^o w_{kj}^o = f_k^o (1 - f_k^o) \sum \delta_{pk}^o w_{kj}^o \quad (2.26)$$

$$\delta_{pk}^o = (t_{pk} - o_{pk}) \frac{\partial f_k^o}{\partial net_{pk}^o} = (t_{pk} - o_{pk}) f_k^o (1 - f_k^o) \quad (2.27)$$

It should be noted that the error terms for the hidden units must be calculated before updating the synaptic weights of the output units.

This learning or training phase requires a complete understanding of the problem. It is essential here to identify the input and output parameters. Once the decision about the network structure is made, the learning involves acquiring knowledge, determining the number of hidden layers and the number of neurons in each layer. The optimal number of these is determined by trial in order to achieve the best performance for the network, see **Figure 2.16**.

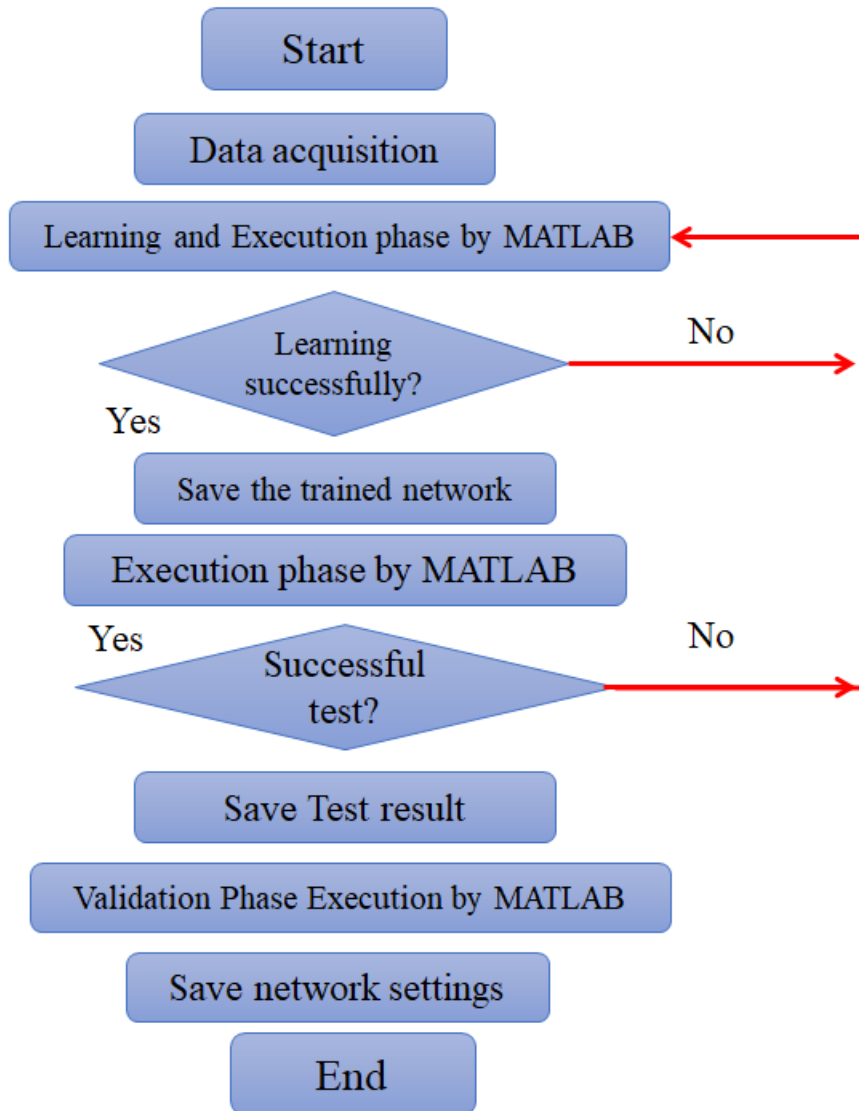


Figure 2. 16 Flowchart of Backpropagation (Hecht-Nielsen 1989) [158].

2.5.8 Recognition (test) and validation phase

Before deploying a neural network with confidence, it is essential to establish the validity of the results it produces. This validation process is often conducted in conjunction with the test phase. Both testing and validation phases involve evaluating the network's performance on data that was not used during the learning phase.

In the validation phase, the desired solutions and those generated by the neural network are compared, either qualitatively or quantitatively using statistical tests. This comparison helps assess the network's accuracy and reliability in handling new and unseen data, ensuring that it can generalize well beyond the training data.

By rigorously testing and validating the neural network, researchers and practitioners can ensure that it performs effectively and consistently in real-world scenarios, making it a reliable tool for various applications

2.5.8.1 Backpropagation multilayer neural network performance

The performance of a neural network model can be evaluated using different expressions, including:

- The coefficient of determination R^2 (Eq. 1.16) Sum of Squared Error (SSE):

$$SSE = \sum_{i=1}^N (t_i - o_i)^2 \quad (2.28)$$

- Mean Square Error (SSE):

$$MSE = \frac{1}{N} \sum_{i=1}^N (t_i - o_i)^2 \quad (2.29)$$

t_i : Desired output of model i .

o_i : Actual output of model i .

N : The total number of data.

The coefficient of determination R^2 represents the proportion of variation of the output value which is "explained" by the model, its ideal value is 1.

The number of nodes in the hidden layer is not determined a priori. The performance of the network is determined using the factor (MSE) for an increasing number of neurons of the hidden layer. The number retained corresponds to that which minimizes the quadratic error.

2.5.8.2 Methodology and implementation

In this study, a backpropagation multilayer neural network was used because of its widespread use and proven track record of performance in model optimization, prediction, and classification. Any element of the input data set must have a desired outcome in order to use supervised learning. The input layer, one or more hidden layers, and the output layer are the three different types of layers that make up the backpropagation multilayer model. In predicting the crack length and crack depth for steel pipelines or Gurson model parameters...etc, all the input data is represented by the constituents of the API X70 steel (cement, aggregates, water, etc.), the numerical parameters and mechanical properties etc. The input layer parameters that are sent to the hidden layer are represented by this model. Finally, the hidden layer provides input to the output layer. The output of this layer in our first example provides the mechanical characteristics of API X70 steel, such as the ultimate stress, yield stress, and absorbed energy, among others.

Finding the parameters to be employed in the forecasting models is the first stage. There are three sections to the data. 15% are utilized for testing, 15% are used for validation, and 70% are used for learning. Training, testing, and validation are the three stages of an ANN model implementation (**Figure 2.17**). The goal of the learning or training phase is to select the optimal approach to calculate the network connection parameters. In the test phase, the network created during the training phase is validated on data not utilized during the latter phase. Additionally, the network's capacity to generalize the training examples is assessed (by comparing the actual output of the network with desired output). The final portion of the data is subjected to the validation process.

2.5.8.3 Programming language used

Different neural network simulation programs are available and marketed (Neuron Solutions, Brain Maker, Matlab ToolBoxes, Statistica Neural Network, etc.).

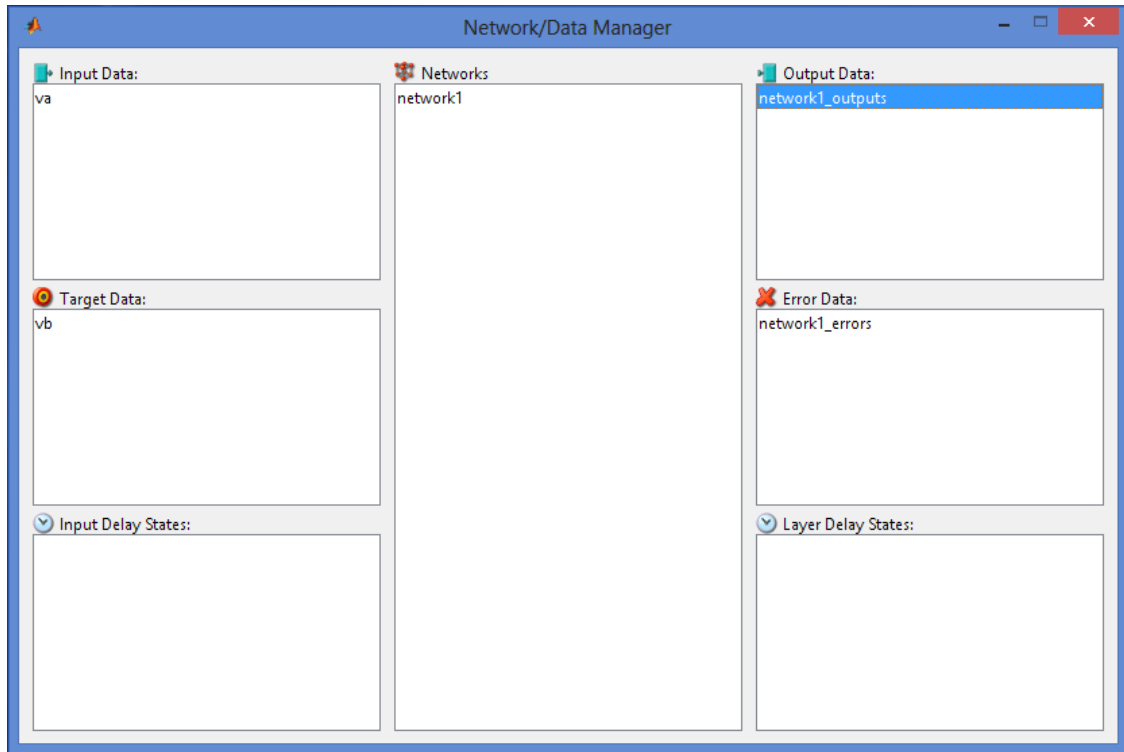


Figure 2. 17 Main panel of the NETWORK DATA MANAGER application.

The choice of simulator is made on the basis of the advantages and disadvantages of each of them. The cost, the flexibility of use, the type of platform and the ergonomics of the interface are the main criteria for evaluating each simulator. We have chosen MATLAB 7.5.0 (R2007b) software among different programming languages such as Visual Basic, Visual Fortran, Visual C++, etc. This software (MATLAB 2007) was developed to be used in an efficient and flexible simulation environment for the research and application of ANN, either generally through the development of a program or the use of the NETWORK DATA MANAGER application. The latter is developed to run on Windows with an easy to use graphical user interface. It is also used to create, manipulate, and visualize neural networks on the one hand and import, export data and results via these networks on the other hand. For illustration, the main panel of NETWORK DATA MANAGER is shown in **Figure 2.17**.

We have developed our own models under Matlab for the prediction of different case in our study.

The first step is to declare the matrix of inputs and outputs in the form of an Excel file. The normalization of the data (input and output) after processing is necessary so that they take values between -1 and 1 to be in agreement with the Tan-Sigmoid transfer function used.

The learning phase is the second step, and it entails initializing the correlation coefficients of the three phases (learning, testing, and validation), as well as the number of neurons per hidden layer after testing one hidden layer, two hidden layers, and knowing that we have tested all three layers. To do this, we create a loop that increases the number of neurons for the first hidden layer by 1 to 20 and for the second layer by the same number. The creation of a new neural network (net) which contains normalized inputs and outputs, a certain number of hidden layers and neurons per layer, passes through the use of a transfer function corresponding to each layer (Tansig : hidden layer; Purelin: output layer), of a Trainlm or Trainbr learning algorithm which respectively uses the Levenberg-Marquardt backpropagation and Bayesian Regulation backpropagation techniques.

To train the network, various parameters must be declared, such as the number of cycles during learning (iterations; epochs), the frequency of verification of the learning error against the desired error (goal), the learning rate (η : mu). You must also declare the division of the data into three parts according to the three phases (70% for learning, 15% for testing and 15% for validation). The learning cycle means a complete passage through all the neurons.

After the learning phase, we move on to the simulation of the network using the decomposition of the data between test and validation. After running this program, we get two files. The first includes training history information and gives statistical measures of network performance, such as correlation coefficients and root mean square error for the three phases and for each neural network created. The second includes the values of the (synaptic) connection weights and the biases between the neurons for each neural network created (it should be noted that we start with a network that contains a single hidden layer and a single neuron, and we gradually move to a network that contains two hidden layers of 20 neurons each).

2.5.8.4 Development of ANN models

This work includes the presentation of the two groups of models which have been developed during this work for the modeling of our cases. The first model brings together the data set to predict the mechanical properties of API X70 steel using ANN, the second model relates respectively to the different optimization codes improved ANN to identification predict the crack length and crack depth.

2.6 Conclusion

Pipeline and tank damage in the oil industry is a well-known and concerning issue that can have significant implications for safety and operational efficiency. This damage is often linked to environmental settings and service conditions, where the harsh operating environments can take a toll on the integrity of these structures.

Various types of damage can occur, posing risks to the overall structural integrity. Erosion, caused by the abrasive action of fluids, can wear away the surface of pipelines and tanks over time. Corrosion, a chemical reaction between the material and its surroundings, can weaken the structure and potentially lead to leaks or ruptures. Embrittlement is a phenomenon in which the material loses its ductility and becomes more susceptible to fracture, is another critical factor in damage. The presence of cracks, notch holes, and complex geometry defects further exacerbates the potential risks and compromises the structural strength. These damages can escalate over time, posing hazards to the environment, human safety, and operational continuity.

To address these challenges, constant monitoring, regular maintenance, and the use of advanced materials and coatings are essential. Mitigation strategies, along through stringent inspection protocols, help to ensure the continued integrity and reliability of pipelines and tanks in the oil industry. Proactively addressing these issues, the industry can enhance safety, reduce environmental impact, and optimize its operational performance.

The design of a neural network is determined by the arrangement of interconnected neurons within the network. This design can vary from fully connected networks, also known as full connection networks, to layered networks, also referred to as one-way networks. In a fully connected network, every neuron in one layer is connected to every neuron in the subsequent layer. This type of connectivity allows for a high degree of information flow and interaction between neurons, but it can also lead to a large number of connections and increased computational complexity.

On the other hand, in a layered network, neurons are organized into distinct layers, and connections are primarily unidirectional, flowing from one layer to the next. The input layer receives the initial data, and subsequent hidden layers process and transform the information before passing it to the output layer. This layered architecture is more structured and efficient, particularly for complex tasks, as it allows for the gradual extraction of features and patterns from the input data.

The choice of network design depends on the specific problem being addressed and the complexity of the data. Fully connected networks are suitable for tasks where extensive interactions between data points are necessary, while layered networks are often preferred for tasks involving pattern recognition, classification, and hierarchical data processing. Designing

effective neural network architecture is a crucial step in achieving optimal performance for the desired task.

In the forthcoming chapter, our focus shifts to the experimental investigation of API 5L X70 steel, wherein we emphasize the examination of its chemical composition and mechanical properties. The second part of the chapter will introduce a study employing numerical simulation. This section is dedicated to validating our model and delving into the impact of various parameters of the selected GTN model on the mechanical behavior of the steel. The finite element software ABAQUS, along with neural networks, will be employed in this study to achieve comprehensive insights into the steel's behavior.

*Chapter 3: Prediction of GTN parameters using
chemical properties*

3.1 Introduction

The Gurson–Tvergaard–Needleman damage model (GTN) describes the three stages of ductile tearing of steel: nucleation, growth, and coalescence of micro-voids. This chapter is divided into two main parts. In the first part, the parameters of the GTN damage model, in conjunction with the hardening law, are determined based on inverse analysis and a comparison between experimental and numerical data. The identification is broadened to include a considerable number of experimental tests drawn from our previous works and other studies conducted at ALFAPIPE Ghardaia laboratory. In the second part, an Artificial Neural Network (ANN) model is developed to predict the parameters of the GTN model coupled with the hardening law, which enables the prediction of traction and impact properties of API X70 steel pipe depending on its chemical composition. The weight of the chemical elements in percentages is considered as the inputs, and the GTN parameters are considered as the outputs. To validate the obtained ANNGTN parameters, traction and impact tests are simulated.

The numerical results are compared with the experimental ones, revealing that the developed model is highly precise and has the potential to capture the interaction of GTN parameters coupled with the hardening law and chemical composition of steel pipelines

3.2 GTN Model Constitutive description

Plastic damage is the process of plastic deformation until fracture. The damage mechanism denotes the damage evolution process of the micro-hole formed by the internal inclusions or two-phase particles of the metal being nucleated, growing up, and converging under the external force. In order to describe the mechanism of meso-damage of plastic materials and its evolution process, a suitable model should be established as presented in Ref [159]. Gurson [160], based on McClintock, Rice, and Tracey [160], assumed that plastic deformation of the material is mainly caused by micro-hole damage. Gurson [161] did not use the assumption of the infinite matrix but proposed a finite matrix with a microporous cell model. Next, Tvergaard and Needleman have modified some parameters of the Gurson model, which significantly improved its prediction with more accuracy in Ref [162]. The Gurson yield surface function corrected by Tvergaard and Needleman as presented in the following formulation:

$$\Phi = \left(\frac{\sigma_{eq}}{\sigma_e} \right)^2 + 2q_1 f^* \cosh \left(\frac{3q_2 \sigma_m}{2\sigma_e} \right) - (1 + (q_1)^2 f^{*2}) = 0 \quad (3.1)$$

where σ_{eq} denotes the macroscopic Von Mises equivalent stress; σ_e is the yield stress of the base metal in the element; σ_m is the macroscopic mean stress; f is the pore volume fraction. q_1, q_2, q_3 are the correction parameters taking into account the micro-hole around the non-uniform stress field and the adjacent holes in the middle of the interaction, usually taken equal to $q_3 = q_1^2$, $q_1 = 1.5, q_2 = 1.0, q_3 = 2.25$.

$$f^* = \begin{cases} f \\ f_c + \frac{f_u^* - f_c}{f_F - f_c} (f - f_c) \\ f_u^* \end{cases} \rightarrow \begin{cases} f \leq f_c \\ f_c < f < f_F \\ f \geq f_F \end{cases} \quad (3.2)$$

In the above formula, f_0 is the equivalent pore volume fraction, which explains the gradual decrease of the bearing capacity of the material due to the pore polymerization; f_c is the pore volume fraction at the time when the hole starts to polymerize; f_F is the broken pore volume fraction when the material is destroyed; $f_u^* = \frac{1}{q_1}$ is the limit pore volume fraction when the stress-bearing capacity is zero. The evolution of void volume fraction, f^* , can be considered as a combination of existing void growth, f_{growth}^* , and nucleation of new voids, $f_{nucleation}^*$:

$$f^* = f_{growth}^* + f_{nucleation}^* \quad (3.3)$$

Void growth can be written as a function of the rate of plastic volume change, $\dot{\epsilon}_{kk}^{pl}$:

$$f_{growth}^* = (1 - f) \dot{\epsilon}_{kk}^{pl} \quad (3.4)$$

Void nucleation is defined in a strain-controlled nucleation function that considers a normal distribution for the nucleation strain. Consequently, the void nucleation rate can be written as:

$$f_{nucleation}^* = \frac{f_n}{S_n \sqrt{2\pi}} \exp \left[-\frac{1}{2} \left(\frac{\bar{\varepsilon}^{pl} - \varepsilon_n}{S_n} \right)^2 \right] \dot{\varepsilon}^{pl} \quad (3.5)$$

Where f_n defines the void volume fraction of nucleated voids, ε_n and S_n indicate the mean value and standard deviation of the nucleation strain, respectively, $\bar{\varepsilon}^{pl}$ indicates the equivalent plastic strain and $\dot{\varepsilon}^{pl}$ defines the equivalent plastic strain rate. Finally, the initial void volume fraction f_0 denotes the presence of initial voids and is a measure for the relative density of the material. In this investigation, the GTN damage parameters are considered typical constant material as obtained in Ref [163].

3.3 GTN model and hardening parameters identification

The objective of the first part of this study is to simultaneously identify the Gurson model parameters and the hardening law for API X70 steel. Thus, a numerical inverse analysis procedure based on the finite element method is used for the modelling see **Figure 3. 1**. The numerical model outputs are coupled with an optimization tool in MATLAB.

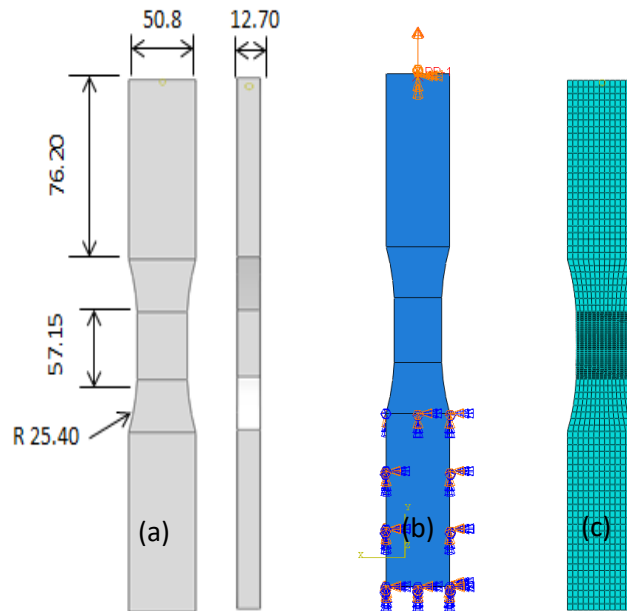


Figure 3. 1 Specimen geometry and finite element model of a notched tensile test.

A tensile test on notched specimens is used in this study using API X70 steel. The initial shrinkage of these specimens usually occurs at the notch. In **Figure 3. 1-a**, the experimental specimen with the dimensions is shown, and in **Figure 3. 1-b** and **c** the simulated model (FE) is illustrated. This model was constructed in the software Abaqus / Explicit with conditions similar to the experiment. After obtaining the results, the experimental values are matched with the numerical values for a considerable number of tests. An optimum mesh consisting of elements C3D8R are used (element with eight nodes of isoparametric type). Mesh refinement is applied at the critical region as shown in **Figure 3. 1 (c)**, where the size of element is very important for damage analysis (GTN) [164]. In this application, we used 8226 elements in the FE mesh with the assumption of quasi-static state. The steel, API X70, is believed to have isotropic elastoplastic behaviour. The elastic model part is the Hooke model with Young's modulus of $E = 210$ GPa with Poisson's ratio of $\nu = 0.3$. The density of the material is 7850 kg / m^3 . In the plastic stage, the failure criterion of von Mises is used. It is added to the porous plastic part of the GTN parameters in the Abaqus / Dynamic Explicit software [165]. Several hardening laws exist in the literature to describe the hardening behaviours of metal. In this study, the law adopted in this reverse identification procedure is the Ramberg-Osgood law according to the following equation:

$$\varepsilon = \frac{\sigma}{E} + \left(\frac{\sigma}{H}\right)^{1/n} \quad (3.6)$$

Where σ is the value of the stress, E is the modulus of elasticity of the material, H is the material constant and n is the strain hardening exponent of the material, which can be calculated from the known properties of the material.

3.4 Identification strategy

Identification strategy based on the reverse procedure makes it possible to determine the work hardening law and Gurson parameters of the studied API X70 steel. Based on the numerical model described above and in order to minimize the difference between the experimental data and the numerical values, a program under MATLAB is used for the optimization of the results. The optimal GTN parameters are obtained by minimizing the cost function (Q) (see Eq. 3.7). To decrease the number of numerical simulations, we propose a factorial design in the process of identification of GTN parameters and we study the numerical output sensitivity by comparison with the experimental design. The optimal GTN parameter value is taken at the minimum of the cost function value having less than 5 percent (5 %) or close to this value as shown in the **Figure 3. 2**. If all values are greater than 5 percent, we go to a new series of parameters proposed in a

factorial way. We already suggest less than 5 percent for the acceptable value of cost function to ensure the good performance of our simulation, this tool was widely used [166, 167] in the characterization under static, dynamic, uniaxial and biaxial stress in metal alloys. The scheme and steps of the reverse procedure are shown in **Figure 3. 3**.

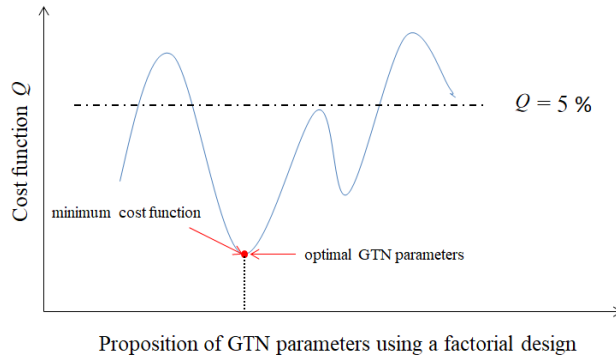


Figure 3. 2 The optimal GTN parameters.

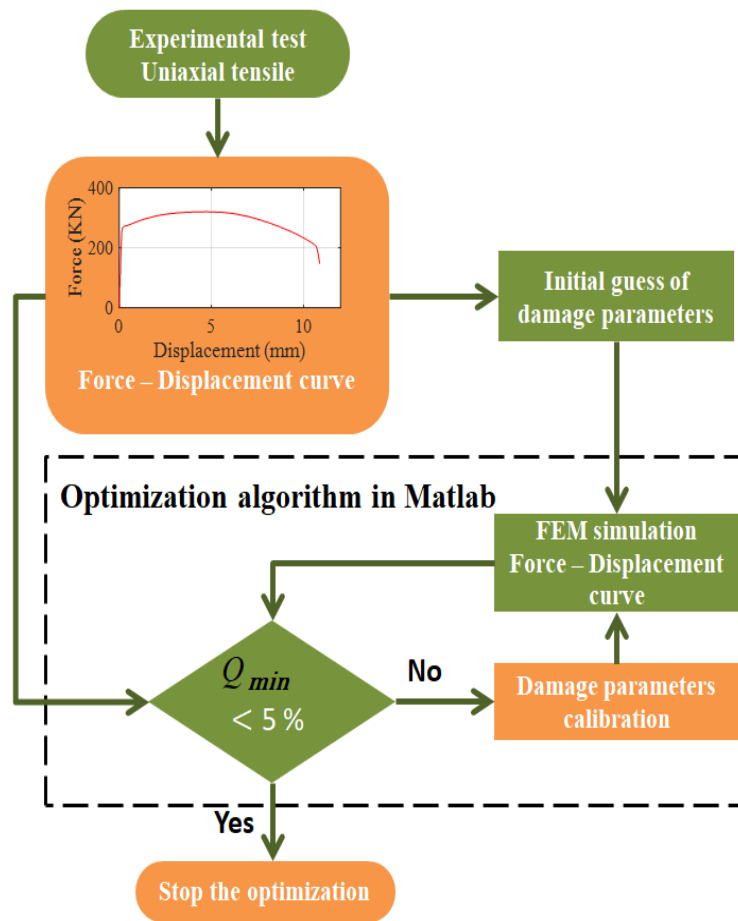


Figure 3. 3 Principle of the inverse analysis method used for the identification of parameters.

The minimized function is represented by:

$$Q = \frac{\sum_{i=1}^N (\bar{F}_{i-\text{exp}} - \bar{F}_{i-\text{num}})^2}{\sum_{i=1}^N (\bar{F}_{i-\text{exp}})^2} \quad (3.7)$$

Where $\bar{F}_{i-\text{exp}}$ (or $\bar{F}_{i-\text{num}}$) = (F_i) and $i=1, 2, \dots, N$, N is the total number of measured points in the numerical simulations and experimental.

3.5 Procedure for identifying model parameters

There are different methods for determining the damage parameters, one of which is the method of comparison between the experimental results and simulations, see for example some studies in which the damage parameters have been determined [168, 169]. In our study, we took two main parameters in the model (GTN), which greatly affect the behaviour of a ductile fracture, namely: critical void volume f_c and nucleation void size f_n with the application of the reverse method to determine their values. In the first step, by using a tensile test, the parameters of the Ramberg-Osgood hardening behaviour of direct scheduling are determined using ABAQUS software.

3.6 Results and Discussions

Figure 3. 4 Shows the displacement versus load for tested notched specimen and that obtained from simulation. The comparison is made for the GTN model coupled to the Ramberg-Osgood hardening law as presented in **Figure 3.4** and **Table 3.1**.

We note that the identified GTN parameters are similar to those of the reference [23] and give a good approximation for the experimental fracture point.

The plastic parameters ($H = 840$ MPa and $n = 0.04$) of hardening and the GTN parameters ($f_c = 0.022$ and $f_n = 0.0024$) are also used to describe the fracture point “P” (**Figure 3. 4**). A good agreement between the numerical and experimental curves can be seen.

The results of the reverse identification used are summarized in **Table 3. 1**

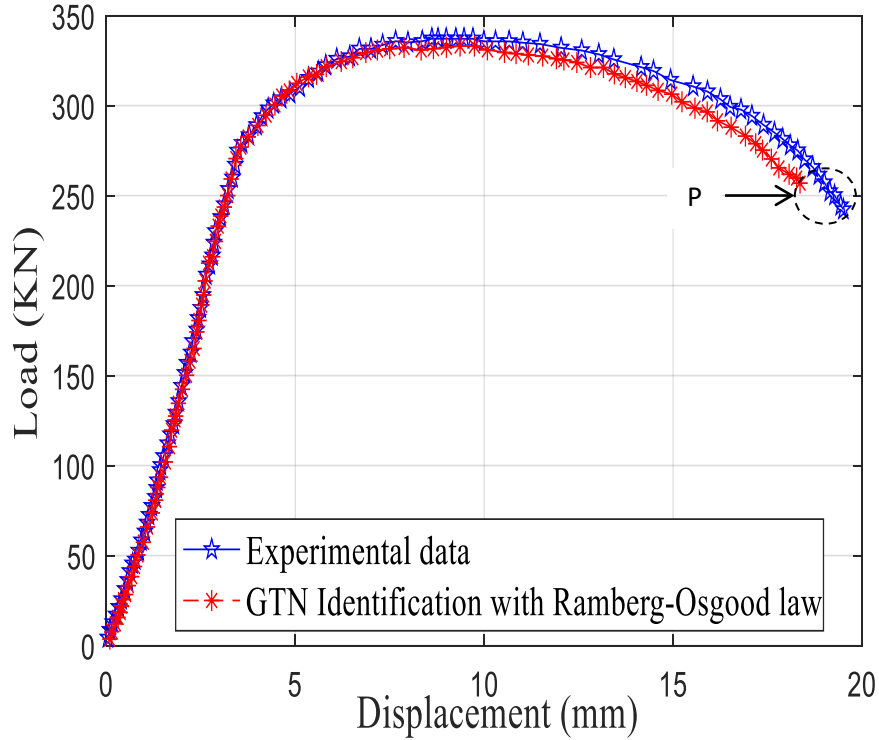


Figure 3. 4 The load vs. displacement numerical and experimental curve in the case of the coupled identification of GTN model and Osgood hardening law.

Table 3. 1 Identified GTN and Osgood parameters.

	The initial values	Range of values	Identified parameters	Ref. [170]
n	0.02	0.02 to 0.06	0.040	-
H	650	650 to 980	840	-
f_n	0.0002	0.0002 to 0.008	0.0024	0.005
f_c	0.018	0.018 to 0.03	0.022	0.02
Fixed f_F	0.18	-	0.18	0.18
Cost function	10%	-	5.26 %	-

The study is expanded to include a considerable number of experimental tests made at ALFAPIPE Ghardaia laboratory to determine GTN parameters and the constants of Ramberg-Osgood. The results obtained are presented in **Table 3. 2**.

Table 3. 2 Identified GTN and Osgood parameters for several tests.

	Parameters	Number of experimental test data (N)	Identified parameters			STDEVA
			Min	Max	Mean	
The strain hardening exponent	n	71	0.026	0.059	0.043	0.007
the constants H for the Ramberg-Osgood	H	71	694.989	973.583	828.050	63.807
nucleation micro-void volume fraction	f_n	71	0.0002	0.0074	0.0038	0,00233
critical volume fraction	f_c	71	0.019	0.023	0.021	0.001
void volume fraction (Fixed)	f_F	71	0.18	0.18	0.18	0

Notation: N is number of cases (tests). STDEVA: Standard Deviation.

3.7 Experimental methodology for the ANNGTN model

In the standard case, the development of a good and reliable ANN application depends on a good selection of training data. In many research works, the design architecture of the experimental methodology has been used, for example see Ledoux et al. [171] for the purpose of optimizing the process of parameter formation based on this technique. ANN model has been developed to predict the parameters of the Gurson-Tvergaard-Needleman Model (GTN) coupled with the hardening law that goes through the prediction of tensile and Charpy impact properties of a steel of API X70 pipeline depending on its chemical composition. The percentage by weight of chemical elements was considered as the inputs and the tensile and impact properties of Charpy were considered as the outputs in the first step and the GTN parameters and the hardening law parameters in the second step as shown in the **Figure 3. 5**.

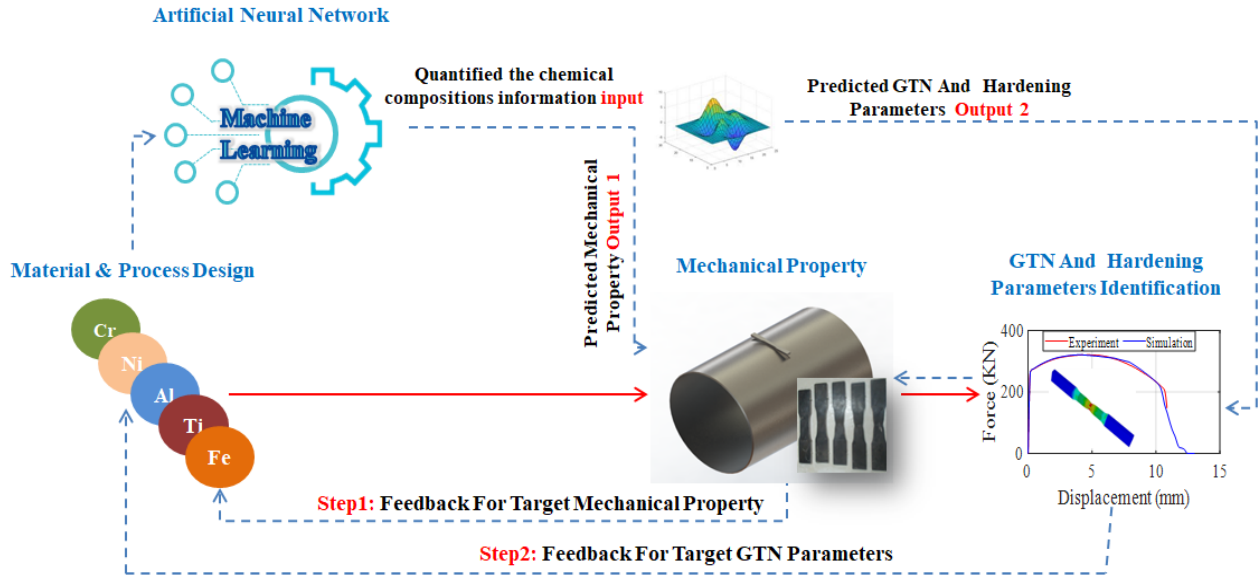


Figure 3. 5 ANN development steps to predict GTN parameters and Osgood constants.

ANNs have been widely used in several research studies to study the correlation between numerical input data and target orientations [172]. ANN model was used to predict the tensile properties of ferrite-pearlite steels as a function of alloying element and microstructural factor, and was developed to prediction of mechanical properties of Sn-9Zn-Cu solder alloys. We try to use ANN to study the relationship between GTN parameters and chemical composition.

Thus, in our study, 80% of the data provided in **Table 3.3** is used for training and 20% for testing and validation of neural networks for the prediction of mechanical properties and damage parameters. In MATLAB [173], the desired inputs and outputs or targets are imported into the workspace and the network "nntool" is created using inputs and targets. The ANN model has a multi-layered structure, which is connected by nodes with three main layers, namely the input layer (14), the hidden layer (s) (8 neurons) and the output layer (step 1 = 8 neurons and step 2 = 4 neurons) as shown in **Figure 3. 6**. The mass percentage values of API X70 elements are inputs: C, Si, Mn, Cr, Ni, Mo, Al, Co, Cu, Nb, S, P, Ti and V. The output layer (step1) represents the Charpy tensile test and impact resistance values: YS, UTS, UTS weld, EL, YT Ratio, CVN (BM-FZ-HAZ). And in step2, the parameters are: n , H , f_n , f_c .

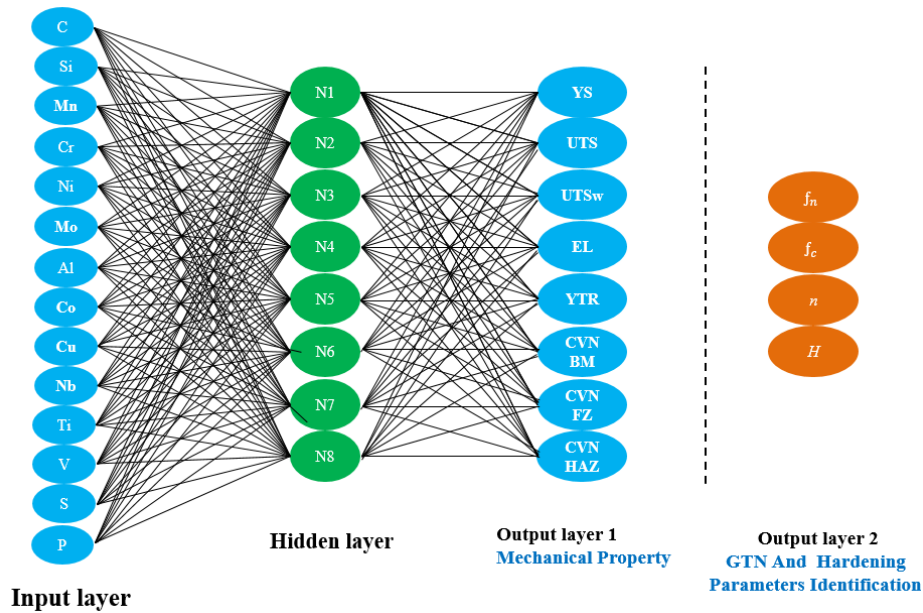


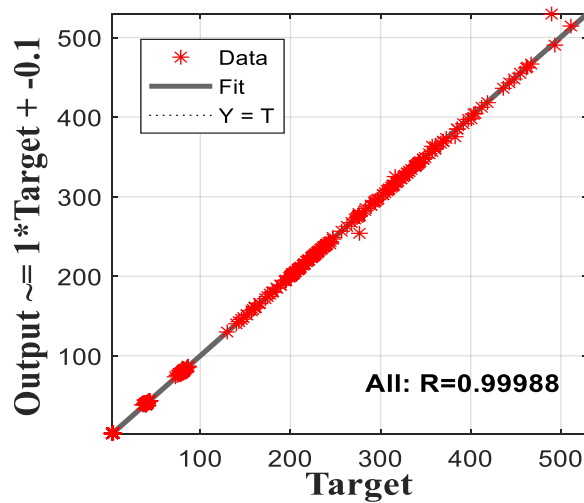
Figure 3. 6 Architecture of Neural Network.

Table 3. 3 Parameters of input data and targets data (1 and 2).

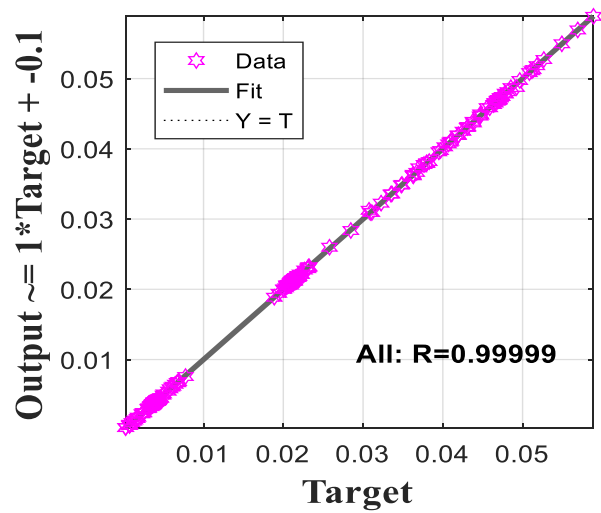
Variable	Symbol	N	Min	Max	Mean	STDEVA
Input						
Carbon (wt.%)	C	71	0.025	0.174	0.075	0.025
Silicon (wt.%)	Si	71	0.156	0.450	0.273	0.062
Manganese (wt.%)	Mn	71	0.788	1.920	1.575	0.215
Chromium (wt.%)	Cr	71	0.010	0.250	0.061	0.046
Nickel (wt.%)	Ni	71	0.011	0.400	0.069	0.070
Molybdenum (wt.%)	Mo	71	0.007	0.290	0.071	0.085
Aluminium (wt.%)	Al	71	0.003	0.050	0.034	0.009
Cobalt (wt.%)	Co	71	0.002	0.022	0.005	0.003
Copper (wt.%)	Cu	71	0.006	0.310	0.056	0.063
Niobium (wt.%)	Nb	71	0.010	0.081	0.051	0.015
Titanium (wt.%)	Ti	71	0.001	0.033	0.014	0.008
Vanadium (wt.%)	V	71	0.001	0.087	0.040	0.031
Sulfur (wt.%)	S	71	0.001	0.015	0.008	0.003
Phosphorus (wt.%)	P	71	0.008	0.040	0.020	0.006

			Output 1			
Yield strength (MPa)	YS	71	486.70	555.21	524.64	12.03
Ultimate tensile strength (MPa)	UTS	71	592.07	696.96	632.19	24.74
Ultimate tensile strength weld (MPa)	UTSweld	71	641.42	761.97	690.14	20.77
Elongation (%)	EL	71	35.86	44.17	40.36	1.46
<hr/>						
Yield to tensile ratio (%)	YTRatio	71	72.40	86.42	80.78	2.55
Charpy strength BM (J/cm ²)	KV (BM)	71	262.80	372.81	315.79	31.09
Charpy strength FZ (J/cm ²)	KV (FZ)	71	129.85	244.34	239.59	56.14
Charpy strength HAZ (J/cm ²)	KV (HAZ)	71	140.02	322.58	207.67	24.20
			Output 2			
The strain hardening exponent	n	71	0.026	0.059	0.043	0.007
the constants H for the Ramberg-Osgood	H	71	694.989	973.583	828.050	63.807
nucleation micro-void volume fraction	f_n	71	0.0002	0.0077	0.0039	0.0017
critical volume fraction	f_c	71	0.019	0.023	0.021	0.001

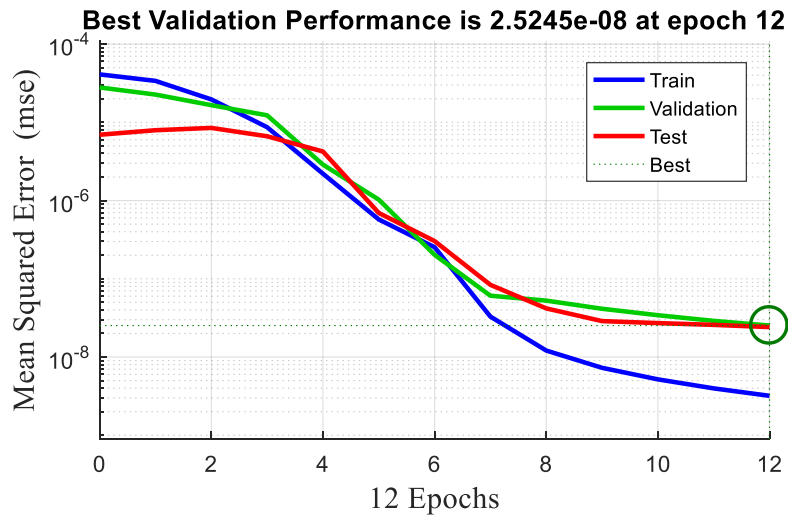
The chemical composition test input values taken by chemical analysis in laboratory are shown in the **Table 3. 3**. The obtained results with the regression analysis (**Figure 3. 7 (a)** and **(b)**) and performance analysis (**Figure 3. 7 (c)**) for the prediction of GTN parameters coupled with the work hardening law and the prediction of mechanical properties of API X70 steel as a function of chemical composition are shown.



a- Regression analysis with Mechanical Properties- Experimental data output



b- Regression analysis with GTN parameters and (n,H)-Numerical data output



c- Performance analysis with GTN parameters and (n, H)-Numerical data output

Figure 3. 7 The results obtained for the prediction of GTN parameters and Osgood constants and mechanical properties.

The test input is considered (chemical compositions) to predict different parameters. The provided results are plotted in **Figure 3. 8**.

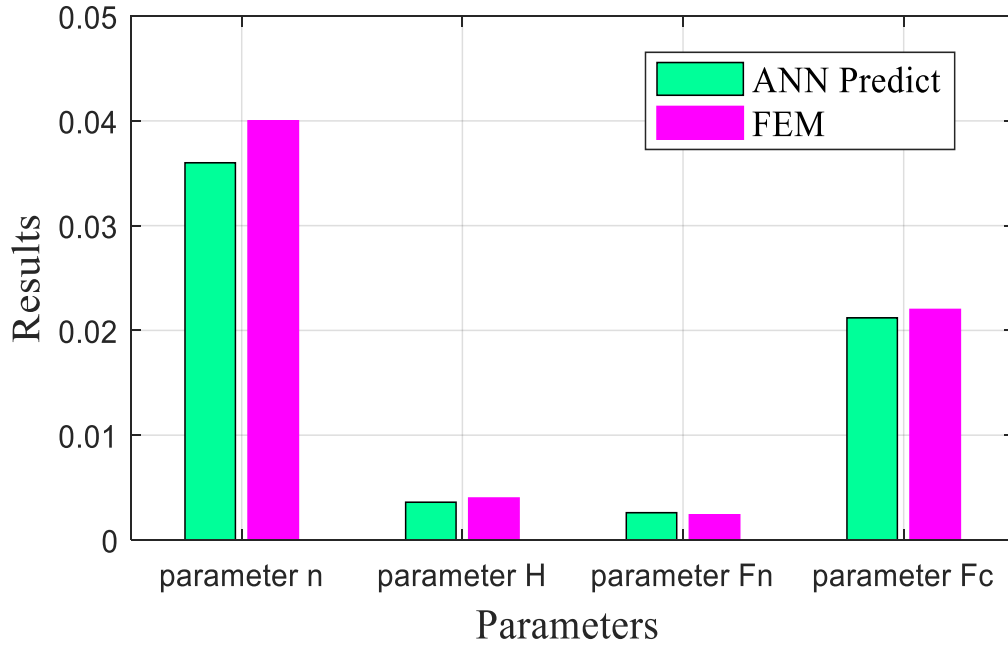


Figure 3. 8 Simulation by FEM versus predicted data (Results: values of each parameter).

3.8 Experimental and numerical analyses

3.8.1 Chemical composition of X70 steels used in this work

The material of our study is a manganese carbon steel used for the transport of hydrocarbons under a service pressure of 70 bars denomination API X70, and meets the specification imposed by the API 5L standard.

3.8.1.1 Preparation of the specimen

From the plate of the base metal we cut a specimen of dimensions $L \times L = 30\text{mm} \times 30\text{mm}$ (Figure 3. 9). The specimen is subjected to mechanical polishing with the ribbon in order to obtain a smooth surface.

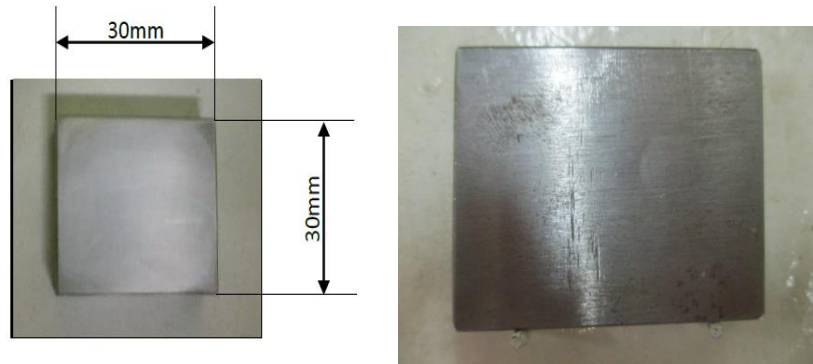


Figure 3. 9 Test specimen used for chemical composition.

3.8.1.2 Presentation of results

Using a flame spectrometer, the chemical composition of this steel was determined.

Table 3. 4 represents the chemical composition of the steel used. The composition as it emerges from the casting analyzes complies with the requirements of the standard indicated in Table 3. 5.

Table 3. 4 The chemical composition of API 5L X70 steel.

Elements	C	Si	Mn	P	S	Cr	Mo	Ni	Al	
Steel grade API X70.	0,0844	0,374	1,665	0,0131	0,0064	0,0475	0,0068	0,031	0,0393	
	Co	Cu	Nb	Ti	V	W	B	N	Fe	CE
	0,0098	0,0193	0,0515	0,007	0,0874	0,007	0,0014	0,001	97,4	0,200

Table 3. 5 Requirement of chemical composition for grade X70 analysis [27].

	C	Mn	Si	Ni	Mo	S	Cu
Min	0.050	1.000	0.150	-	-	-	-
Max	0.140	1.700	0.350	0.250	0.250	0.005	0.080
	V	Nb	Al	P			
Min	-	-	0.010	-			
Max	0.080	0.040	0.040	0.020			

3.8.1.3 Analysis and interpretation of results

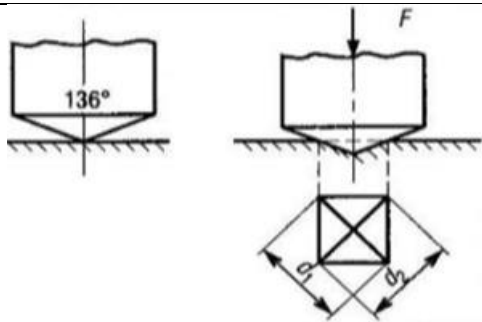
- From **Table 3. 5**, we find that API 5L X70 steel has a low carbon content.
- The low carbon content is necessary to improve the weldability and toughness of the steel.
- The carbon equivalent (CE) measured is below the maximum value (0.25%) indicated by the API standard. This is required to increase solderability.
- Elements niobium, titanium and vanadium contribute to improved yield strength, microhardness, toughness and weldability.
- The content of alloying elements does not exceed 5%, therefore API 5L X70 steel is a low alloy steel.

3.8.2 HV10 microhardness test

The hardness of a material defines the resistance of a surface of the sample to the penetration of a punch, for example a hardened steel ball (Brinell hardness) or a diamond pyramid (Vickers hardness). If it resists well, it is said to be hard, otherwise it is said to be soft. Hardness is measured on different scales depending on the type of material considered.

For our study, we use the Vickers hardness (see **Table 3. 6**).

Table 3. 6 Main hardness tests.

Test	Symbol	Principle and conduct of the test	
Vicker	HV		$H_V = 0.189 \frac{F}{d^2}$ <p>avec</p> $d = \frac{d_1 + d_2}{2}$ <p>(F en N et d_1, d_2 en mm)</p>

3.8.2.1 Preparation of specimens

Using the rest of plate 2 (plate which contains the weld bead), we cut out a test specimen of dimension 50mm × 30mm (**Figure 3. 10**). Then, we carried out a mechanical polishing with abrasive papers of silicon carbide until obtaining a smooth surface (**Figure 3. 11**). In order to reveal the different zones (base metal, ZAT, weld bead), a chemical attack with a Nital solution (4% nitric acid and 96% ethanol) was carried out.

Finally, the specimen was rinsed with water to stop the effect of etching.



Figure 3. 10 Mechanical polishing with abrasive papers.



Figure 3. 11 Specimen for the microhardness test.

3.8.2.2 *Performing microhardness tests*

The microhardness measurements were carried out on each zone using a ZWICK No. 62108 Microhardness tester (**Figure 3.12**). This machine allows us to obtain Vickers microhardness (HV10). The measurement points are distributed as shown in **Figure 3.13**.



Figure 3. 12 Microhardness tester used for microhardness measurements (Vickers type).

The measurement points are distributed as shown in **Figure 3.14**.

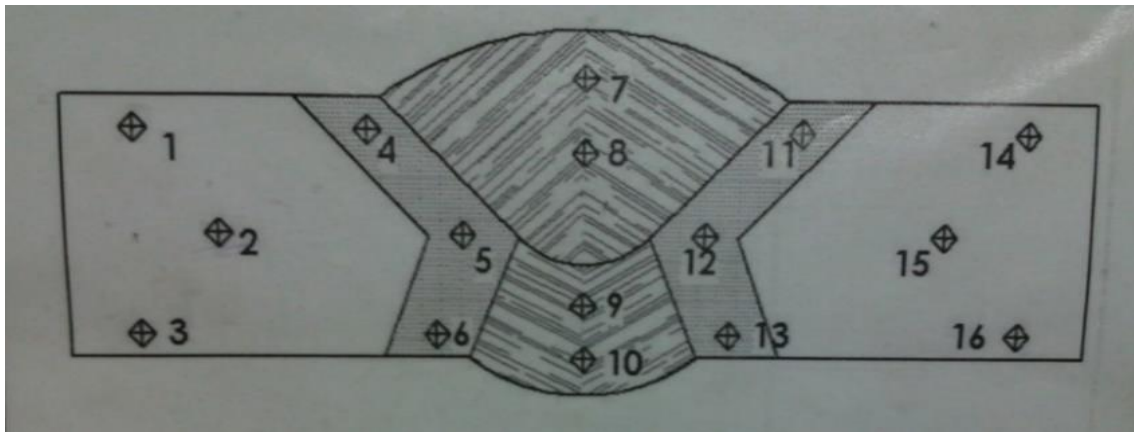


Figure 3. 13 The distribution of measuring points for microhardness

3.8.2.3 *Presentation of results*

The results obtained by making measurements on different zones (see **Figure 3.14**) are summarized in **Table 3.7**, using the following notations to differentiate between the different zones:

BM: Base Metal.

EW: External Welding.

IW: Interior Welding.

Table 3. 7 The values of microhardness (HV 10) for different measuring points.

Points/areas	BM	EW	IW
1	212		
2	210		
3	213		
4	201		
5	198		
6	203		
7		230	
8		227	
9			228
10			237
11	195		
12	201		
13	199		
14	217		
15	219		
16	215		

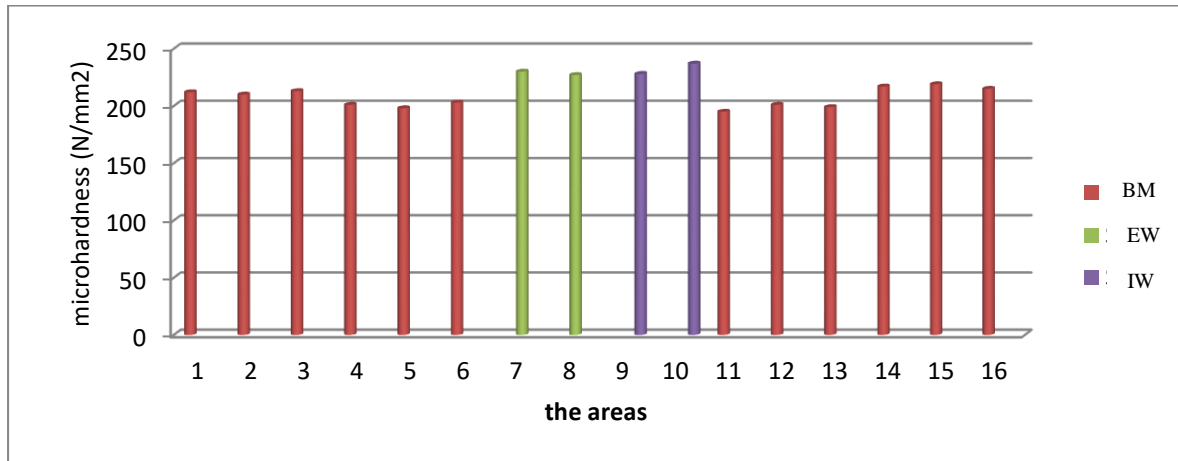


Figure 3. 14 The values of microhardness (HV 10) depending on the measuring position.

3.8.2.4 Results and discussions

The microhardness value of points 4.MB, 5.MB, 6.MB, 11.MB, 12.MB and 13.MB is significantly lower than that of points 1.MB, 2.MB, 3.MB, 14.MB, 15.MB and 16.MB. This difference in microhardness value is due to the heating of the zone during the welding passes (interior and exterior passes). We can say that this zone becomes the heat affected zone (HAZ) with respect to the zone of the base metal (**Figure 3. 15**).

- **Figure 3. 14**, exhibits fluctuating microhardness measurements. It shows many high peaks on the weld bead area whose values are 230HV, 227HV, 228HV and 237HV which are significantly higher than those of the base metal area.

- In addition, it can also be noted that even in the area of the weld bead, the microhardness values obtained at points 7. EW and 10.IW are higher than those of 8. EW and 9. IW. This superiority can be attributed to the cooling mode, which is relatively fast on the external areas in contact with the air compared to the internal areas in the core of the bead.

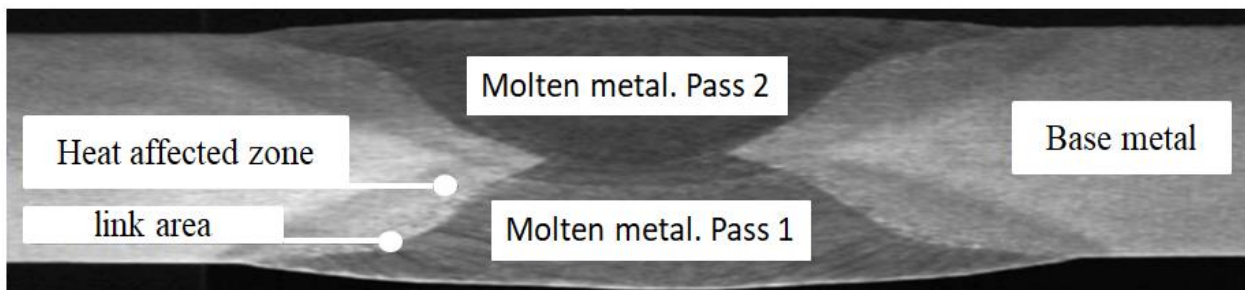


Figure 3. 15 Microscopic illustration of existing areas on a specimen containing the weld bead.

3.8.3 Experimental Tensile test on a steel pipeline specimen

The investigation of our study is concerned with manganese carbon steel pipes used for the transport of hydrocarbons under a working pressure of 70 bars with the commercial name APIX70. The material meets the specification imposed by the standard API 5L [174].

In order to determine the load-displacement curves and the mechanical properties of X70 steel, flat specimens according to French standard NF EN 10002-1 [175] were used. Uniaxial tensile tests were carried out on three specimens at room temperature using the Mohr machine

(ZAWICK) at the ALFAPIPE laboratory (**Figure 3. 16 (a)**). The initial material is presented in the form of coils

Of the same casting. The specimens were characterized by the geometrical dimensions shown in **Figure 3. 16 (b)**. Tensile tests were carried out by increasing the tensile load applied at the specimen's extremities. All tests were performed under displacement control.

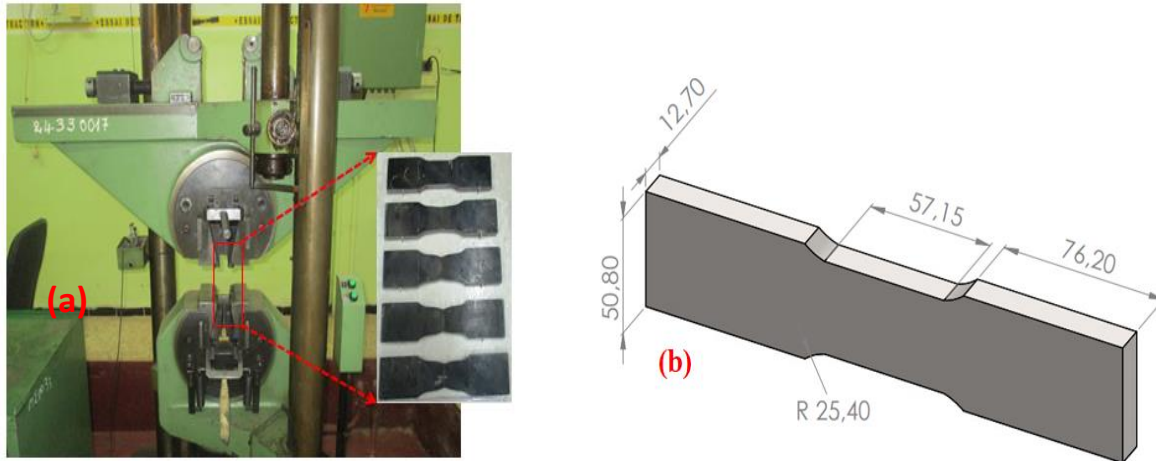


Figure 3. 16 Set up of uniaxial tensile tests with tensile extensometer (a); geometrical dimensions according to EN 10002-1 standard (b).

From a tube, we cut a ferrule. Then, we took two plates from this ferrule, one transverse to the ferrule, which contains only the base metal, and the other transverse to the weld bead. The two plates obtained are illustrated in **Figures 3. 17 (c)** and **17 (d)**. From the plates (c) and (d), we cut 3 test specimens having 50 mm wide each. The ultimate shape of a tensile test specimen is obtained by the milling process (**Figure 3. 17 (a)** and **17(b)**). The rest of the two plates were used for the other tests (impact test), see **Figure 3. 17 (e)**. The obtained results for both cases are shown in the **Tables 3.8** and **3.9**.

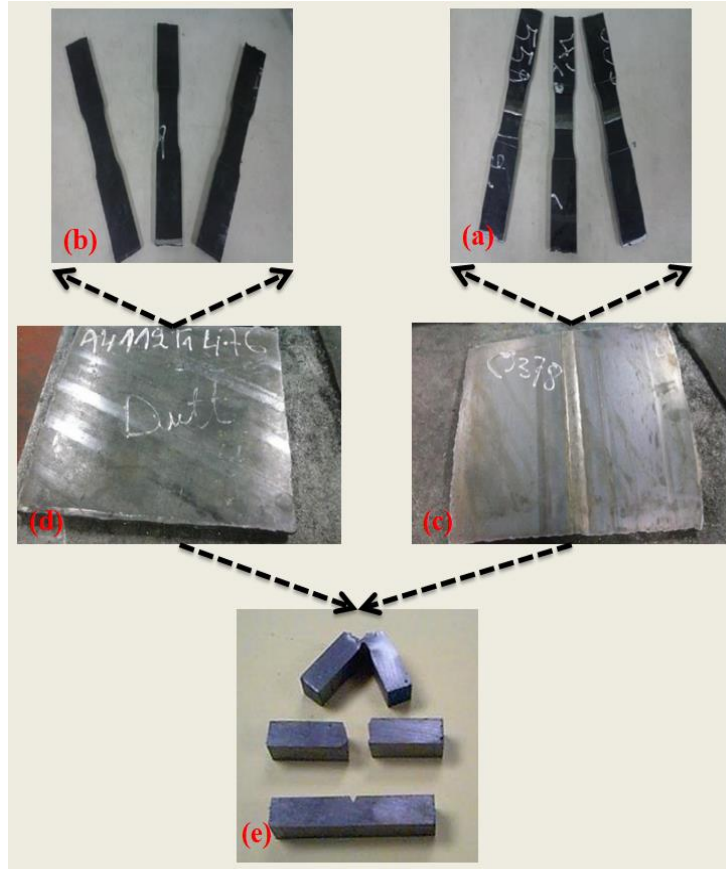


Figure 3. 17 Sample for tensile test (a, b), Butt joint of API X 70 steel using arc welding (c), Steel plate (d), sample for impact test (e).

Table 3. 8 Results of tensile tests for the base metal.

Test number	Width	Thickness	YS (MPa)	UTS (MPa)	EL (%)
1	38.1	13.04	556	670	38
2	38.3	13.05	560	671	37.7
3	38.2	13.04	561	666	37

Table 3. 9 Results of tensile tests for the weld metal.

Test number	Width	Thickness	YS (MPa)	UTS (MPa)	EL (%)
1	38.4	12.89	645	713	27.32
2	38.2	12.96	620	714	29.0
3	38.4	12.95	638	716	29.6

3.8.4 Charpy Test

The mechanical characterizations deduced from the tensile test may be insufficient because failure may happen below the yield strength under special conditions rendering the material to a brittle state. The impact test is an essential complement to the tensile test. These tests were carried out on a Charpy V sheep (see **Figure 3. 18**), at a temperature of -10 °C. The resilience test was carried out on standard CVN 10×10 test specimens, following the geometry proposed according to API 5L. The dimensions of the test specimen are given in **Figure 3. 19**. Nine specimens were prepared: three specimens machined from Base Metal (BM), three others were taken at the level of the Welded Metal (WM), and the remaining three for the Heat-Affected Zone (HAZ), i.e. transition zone.



Figure 3. 18 Resilience machine and cooler

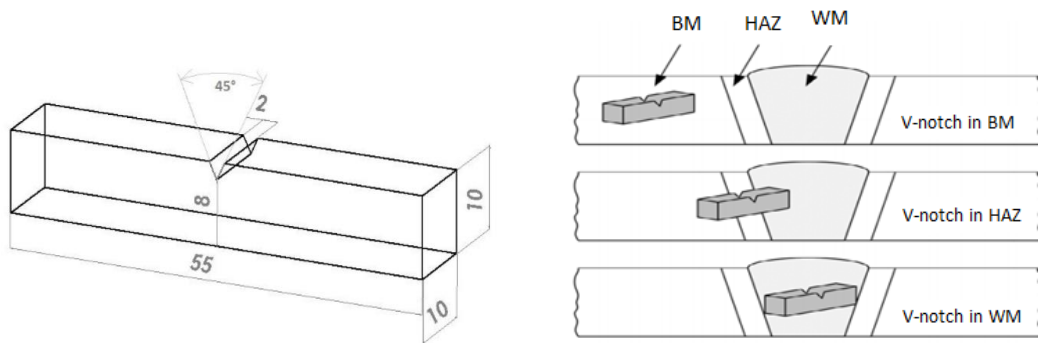


Figure 3. 19 Standardized test piece of the impact test

The variation in fracture energy, i.e. absorbed energy by the specimen, in the three zones is very large and the experimental results of the impact tests at different positions (BM-HAZ-WM) for API X 70 steel are presented in **Table 3. 10**. It is possible to notice that the energies of the test

specimens with welding are low compared to the material test specimens, which represents the effect of the welding.

Table 3. 10 Macro-characteristics of Charpy specimens cut from X70 pipe steel tested for different impact position.

Base metal			Welding			Zone transition		
Energy (J)	J/cm ²	Average (J/cm ²)	Energy (J)	J/cm ²	Average (J/cm ²)	Energy (J)	J/cm ²	Average (J/cm ²)
231.8	289.8		205.8	257.2		205.6	257.0	
237.8	297.3	286.1	152.6	190.8	210	176.6	220.7	234.7
216.8	271.0		161.8	202.2		181.0	226.3	

3.9 Finite Element Modelling

According to the results obtained by ANN, the parameters of Ramberg-Osgood and other parameters of the model of damage GTN are related to the reinforcement of the material of the matrix, taking as $q_1 = 1, 5$; $q_2 = 1.0$ and $q_3 = 2.25$. The mean equivalent plastic strain and the standard deviation of the nucleation strain are $\varepsilon_n = 0.3$ and $s_n = 0.1$, respectively. The load-displacement curve evaluated by FEM is compared with that obtained by experimental tests. Finally, the comparison between the experimental values and those obtained by simulation based on ANN-GTN parameters is presented in **Table 3.11**.

Table 3. 11 ANN-GTN model parameters.

ANN-input															
	C	Si	Mn	Cr	Ni	Mo	Al	Co	Cu	Nb	Ti	V	S	P	
MB	0.125	0.270	1.680	0.051	0.040	0.021	0.038	0.004	0.045	0.033	0.003	0.084	0.005	0.012	
WM	0.06	0.41	1.24	0.032	0.56	0.008	0.003	0.046	0.027	0.003	0.032	0.013	0.010	0.007	
ANN-Output															
	n				H				f_n				f_c		
	0.043				837.69				0.0024				0.0214		
	0.05				869.4				0.0002				0.022		

Finite element analysis of tensile test base metal and weld metal is performed using ABAQUS software. The tensile test and Charpy impact are modelled as deformable bodies. A 3D solid finite element model was implemented to reproduce the laboratory scale Charpy V-Notch experiment (CVN). The ABAQUS/Explicit solver permitted the application of the GTN damage model for the simulation of dynamic propagation of fractures. For this purpose, the model called "porous metal plasticity" was used. The geometry was created based on the standard dimensions

of the specimen, as stated previously. In each model, the mesh was created using 8-node linear brick elements with reduced integration. The mesh size is of significant importance when the GTN damage model is implemented. In this study, an element size of 0.2 mm was used. The condition of zero penetration between the hammer and the test specimen has been implemented. In addition, friction has been taken into account using a penalty function with a coefficient of friction equal to 0.1. Due to the impact load in the CVN, the acceleration and, as consequence, force measurements can show pronounced oscillations. Therefore, the velocity data was extracted and derived to obtain acceleration and force data. This method reduced the presence of oscillations and made it possible to construct the force-displacement curves for each respective simulation. The Charpy Impactor is modelled as discrete rigid body in the simulation.

The proposed model is constrained on one side as follows: $U1 = U2 = U3 = UR1 = UR2 = UR3 = 0$, and on the second side it is allowed to move in the direction of (Y), see **Figures 3.20 (a) and (b)**. In **Figure 3.10 (c)**, macrograph of the weld zone is shown, from which we take a reference length of the properties of the weld zone in the finite element model. In this study and in the simulations of ABAQUS program, we consider the HAZ region as part of the weld region. From the experimental data, the weight of the impactor is 19.8 kg and its speed is 5.5 m/s in the Y direction only with the two ends of the part being fixed (**Figures 3.21 (a) and (b)**)

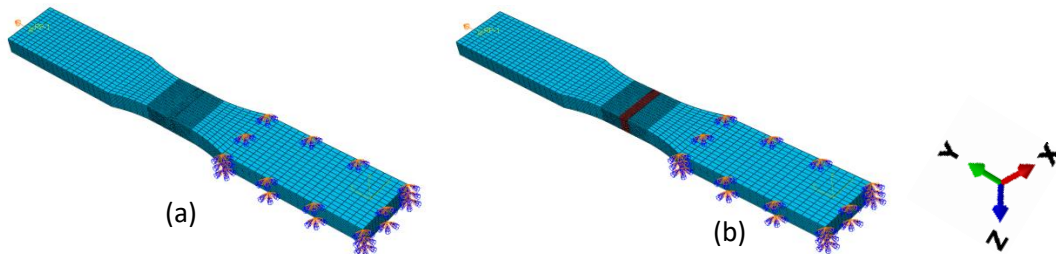


Figure 3. 20 Tensile test modelling with boundary conditions: (a) Base metal and (b) Welded metal.

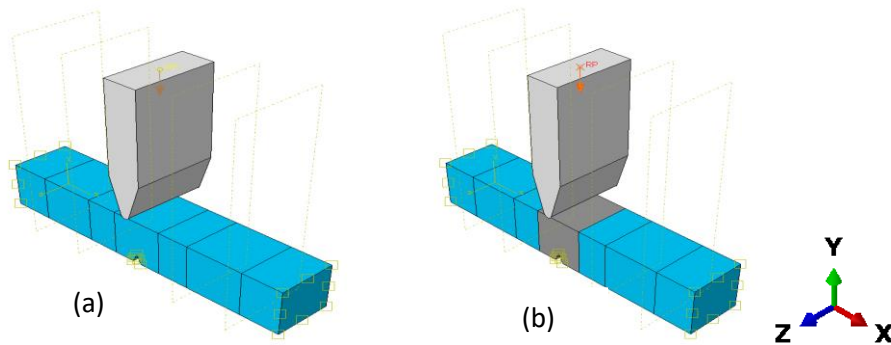


Figure 3. 21 Impact test modelling with boundary conditions: (a) Base metal and (b) Welded metal.

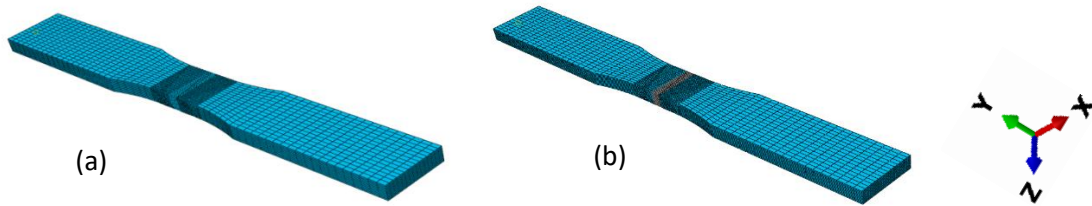


Figure 3. 22 FE model of tensile test specimens: (a) Base metal and (b) Welded metal.

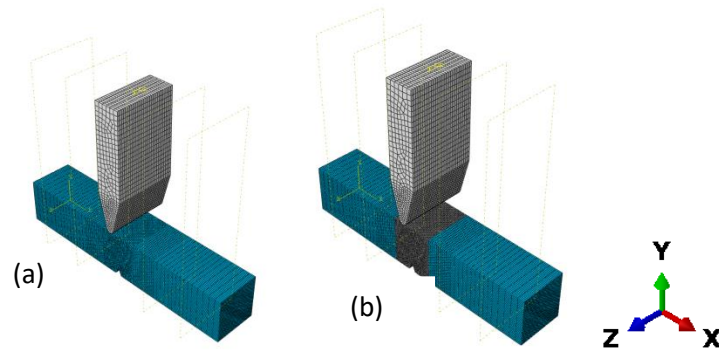


Figure 3. 23 FE model of impact test specimens: (a) Base metal and (b) Welded metal.

The mesh patterns of the base metal and welded metal traction and Charpy samples are shown in **Figures 3.22 (a) and (b)** and **Figure 3.23 (a) and (b)**, respectively. The mesh element type for both tests is a hexagonal element shape, i.e. a C3D8R element type.

3.10 Results and discussion

The results of the experimental uniaxial tensile test and FE analysis are shown in **Figure 3.24**. At the centre of the tensile test specimen, the necking behaviour with successive shrinkage and fracture of the metal in the experiment is illustrated in **Figures 3.24 (a) and (c)** and in the FE analysis is shown in **Figures 3.24 (b) and (d)**, respectively.

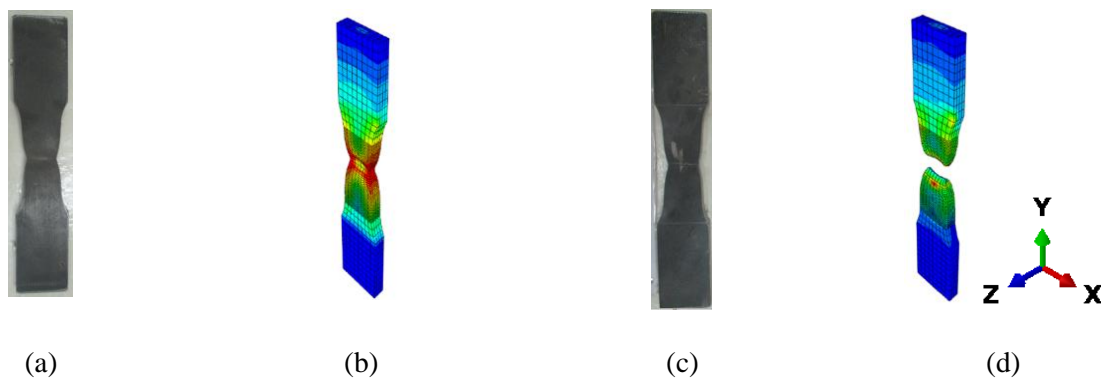


Figure 3. 24 The tensile test from experiment and FE analysis (a and b – necking, and c and d – fracture).

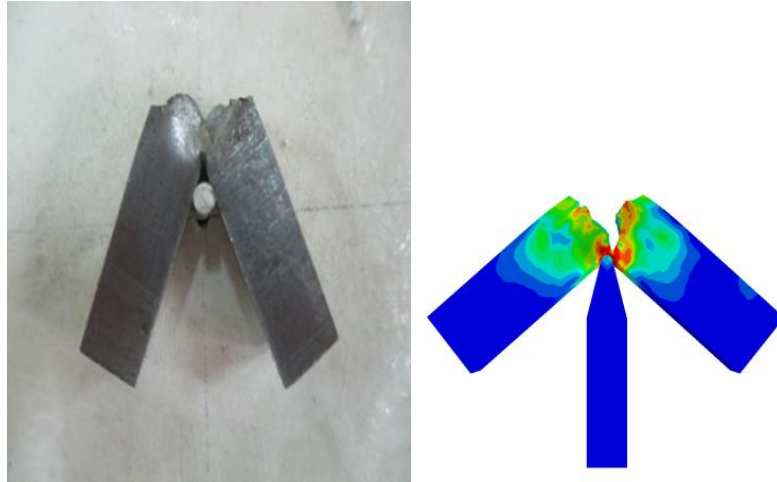


Figure 3. 25 Impact test in experiment and FE analysis.

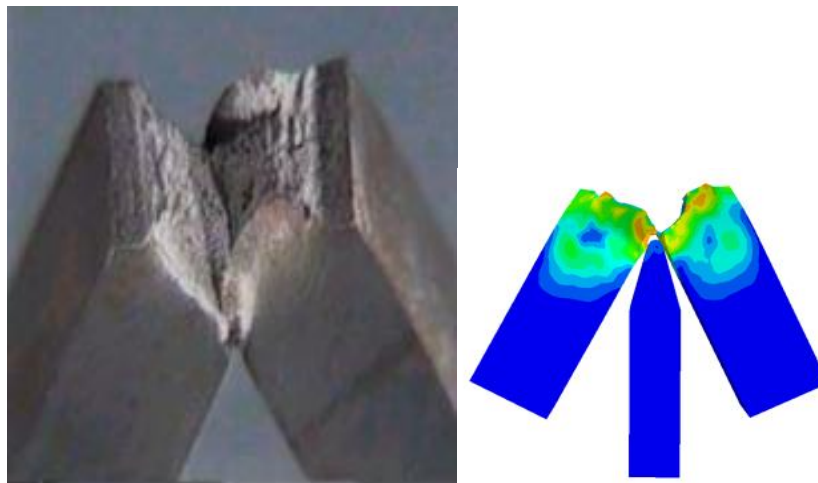


Figure 3. 26 Comparison of weld metal impact test between experimental and FE analysis.

The experimental fracture area indicates a ductile failure mode and that the fracture is identical to the FE analysis as shown in **Figure 3.25**. In addition, the narrowing and fracture location of the weld metal sample from an experimental analysis and FE is shown in **Figure 3.26**. Experimental analysis and FE show good agreement for weld metal describing failure behaviour. The engineering stress versus engineering strain curves from the experimental and FE analyses are shown in **Figure 3.27**.

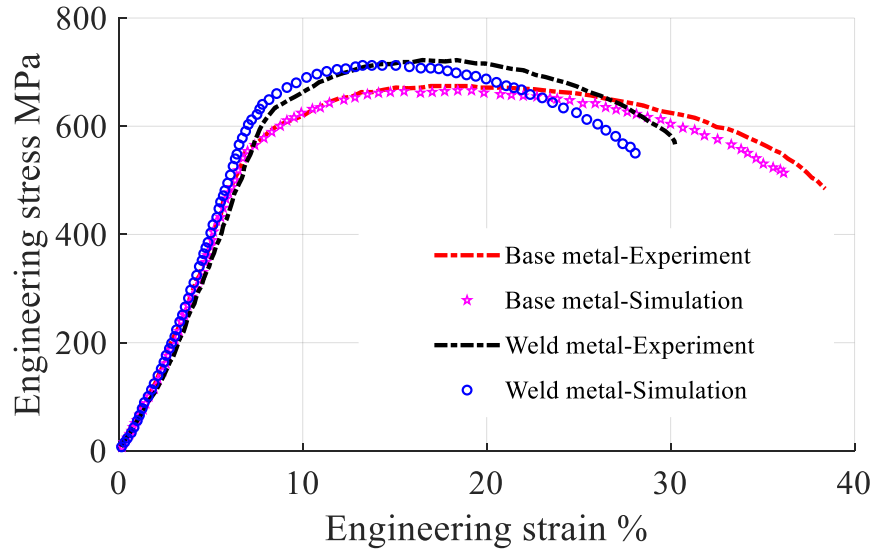


Figure 3. 27 Engineering stress versus engineering strain plot for base metal and weld metal.

The fractured specimens base metal and weld metal also exhibit a ductile type fracture. **Figure 3.28** shows the graphical representation of the energy displacement graph obtained by the base metal and weld bead impact test simulation.

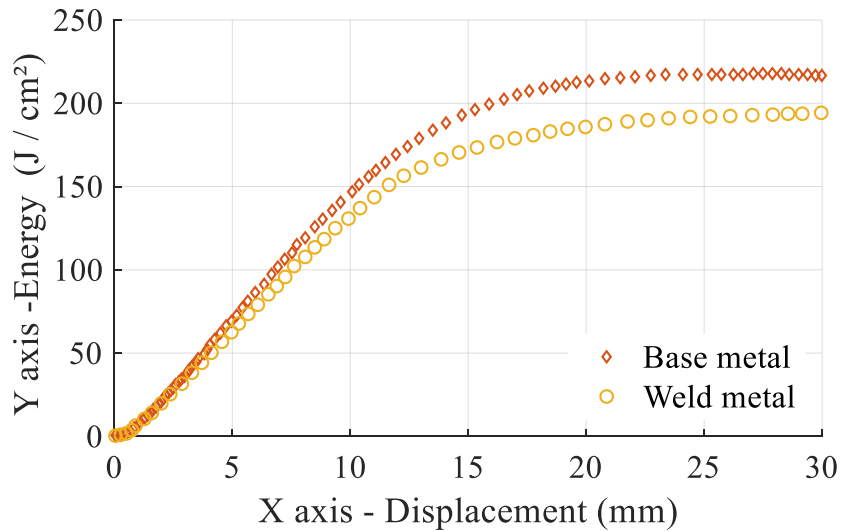


Figure 3. 28 Energy–Displacement graph (simulation-impact energy).

The graphical representation in **Figure 3.28** shows on the X axis in terms of displacement (mm) and on the Y axis in terms of impact energy absorbed by the base metal and weld seam (J/cm²). The experimental load displacement curve and the corresponding numerical prediction

for the tests are shown in **Figure 3.29**. By comparing FE and experimental results, one may notice that a good correlation with the experimental data is obtained.

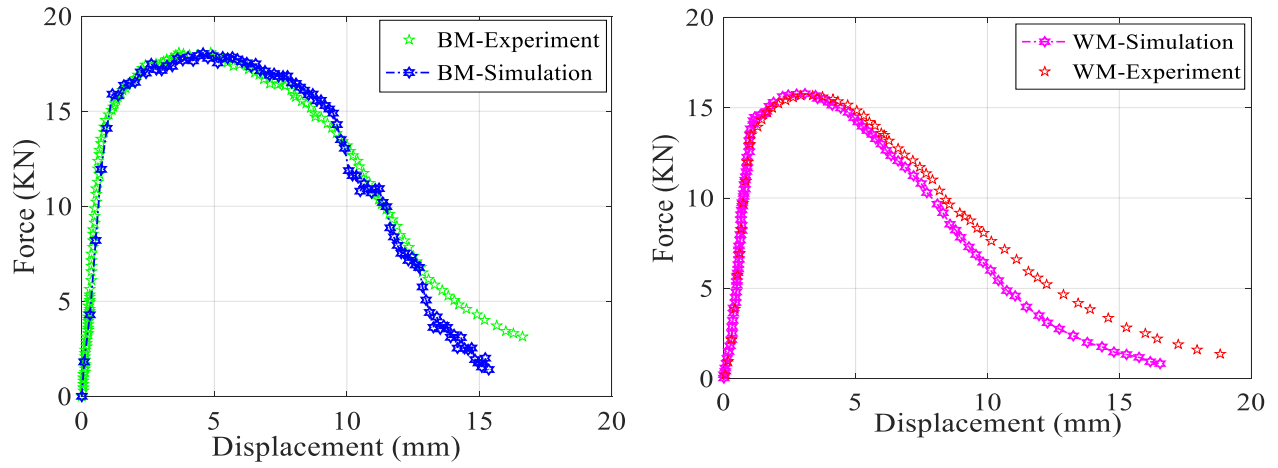


Figure 3. 29 Experimental and numerical force-displacement curves for the CVN experiment.

From **Table 3.12**, we can see a comparison between the experimental results and the ANN prediction of the mechanical properties of API X70 steel. In addition, the simulation results obtained from ABAQUS based on the values of the original parameters of prediction ANNGTN torque with the law of hardening are also given in **Table 3.12**.

Table 3. 12 Comparison of mechanical properties for the three different sources.

Results		Experimental	Prediction ANN	Error (%)	simulation based on ANNGTN parameters	Error (%)
Yield strength (MPa)	YS	559	526	5.90	545	2.50
Ultimate tensile strength (MPa)	UTS	669	628	6.13	663	0.90
Ultimate tensile strength (MPa)	UTSw	714	643	9.94	650	8.96
Elongation (%)	EL	37.5	39.51	5.09	33	12
Yield to tensile ratio (%)	YTR	84	88	4.76	80	4.76
Charpy strength BM (J/cm2)	KV (BM)	286.1	317	9.75	302	5.56
Charpy strength FZ (J/cm2)	KV (FZ)	210	180	14.29	191	9.01

○ *Effect of specimen at different temperatures*

Several impact tests were performed at different temperatures and the specimens were cooled using a special type of cooler designed to provide cooling temperatures down to -60°C .

These tests are carried out on a Charpy machine. We have carried out tests [-20°C ; $+20^{\circ}\text{C}$] at the ALFAPIPE mechanical test laboratory, in accordance with API 5L X70.

The dimensions of the test piece are given in **Figure 3.19**, the resilience test was carried out on standard CVN $10 * 10$ test specimens, the geometry of which according to API 5L.

From **Table 3.13**, it is shown that as the temperatures of the specimen have high values, the corresponding impact energy required for failure increases rapidly due to the steel being moved to the ductile zone. At high temperatures, while at low temperatures, steel behaves like a brittle material, which requires quite a bit of energy to fracture.

Table 3. 13 Macro-characteristics of Charpy specimens cut from X70 pipe steel tested for impact testing.

	$t, ^{\circ}\text{C}$	Energy (J/cm^2)			Energy (J/cm^2)
		Test 1	Test 2	Test 3	Average (1,2,3)
Base metal (BM)	20	262.8	254.1	266.5	261.13
	0	248	242	238	242.67
	-10	216	210	210	212
	-20	206	205	203	204.67

The assigned physical material properties are shown in **Table 3.14**. Current stress and Charpy impact models are subjected to plastic strain, therefore plasticity material properties at different temperatures (-20 , -10.0 and 20°C) for base metal are assigned using tensile test result data as shown in **Figure 3.30**.

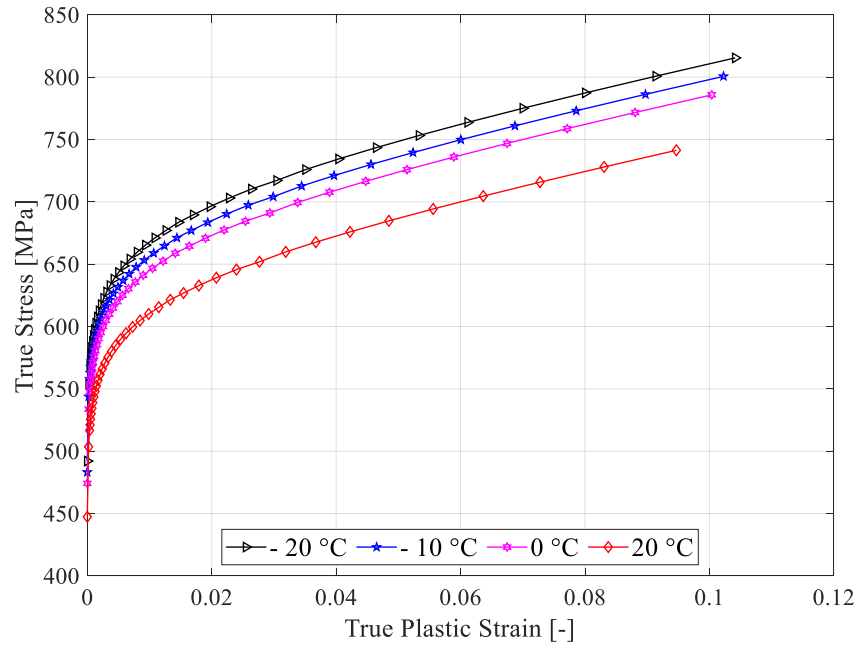


Figure 3. 30 True stress versus True strain at different temperatures.

The thermophysical properties of API 5L X70 steel using for this simulation is shown in **Table 3.14**.

Table 3. 14 Thermophysical properties of API grade X70 steel [176].

Material	Conductivity(W / m ° C)	Specific heat (J / Kg ° C)	Thermal expansion (u m /m ° C)
API X70	52	420	8.5

The finite element analysis of the impact test specimen was performed using a mesh size of 0.2 mm around the notch area. The simulation parameters at different temperatures of (-20, -10.0 and 20 ° C) are shown in **Table 3.15**.

The GTN damage model parameters are:

Table 3. 15 GTN parameters used in the simulations.

Temperature	Parameters	$q1$	$q2$	ε_n	fn	fc	Parameters	$q1$	$q2$	ε_n	fn	fc
Step1:20 °C; Step2:0 °C; Step3: -10 °C; Step4: -20 °C.	1	1.5	1	0.3	0.012	0.0002	39	1.43	0.95	0.5	0.02	0.0042
	2	1.47	1	0.3	0.012	0.0002	40	1.5	0.95	0.5	0.02	0.0042
	3	1.43	1	0.3	0.012	0.0002	41	1.47	0.95	0.5	0.02	0.0042
	4	1.4	1	0.3	0.012	0.0002	42	1.4	0.95	0.5	0.02	0.0042
	5	1.5	0.975	0.3	0.012	0.0002	43	1.43	1	0.5	0.02	0.0042
	6	1.5	0.95	0.3	0.012	0.0002	44	1.43	0.975	0.5	0.02	0.0042
	7	1.5	0.925	0.3	0.012	0.0002	45	1.43	0.925	0.5	0.02	0.0042
	8	1.5	1	0.4	0.012	0.0002	46	1.43	0.95	0.3	0.02	0.0042
	9	1.5	1	0.5	0.012	0.0002	47	1.43	0.95	0.4	0.02	0.0042
	10	1.5	1	0.7	0.012	0.0002	48	1.43	0.95	0.7	0.02	0.0042
	11	1.5	1	0.3	0.016	0.0002	49	1.43	0.95	0.5	0.012	0.0042
	12	1.5	1	0.3	0.02	0.0002	50	1.43	0.95	0.5	0.016	0.0042
	13	1.5	1	0.3	0.024	0.0002	51	1.43	0.95	0.5	0.024	0.0042
	14	1.5	1	0.3	0.028	0.0002	52	1.43	0.95	0.5	0.028	0.0042
	15	1.5	1	0.3	0.012	0.0022	53	1.43	0.95	0.5	0.02	0.0002
	16	1.5	1	0.3	0.012	0.0042	54	1.43	0.95	0.5	0.02	0.0022
	17	1.5	1	0.3	0.012	0.005	55	1.43	0.95	0.5	0.02	0.005
	18	1.5	1	0.3	0.012	0.0062	56	1.43	0.95	0.5	0.02	0.0062
	19	1.5	1	0.3	0.012	0.008	57	1.43	0.95	0.5	0.02	0.008
	20	1.47	0.975	0.4	0.016	0.0022	58	1.4	0.925	0.7	0.024	0.005
	21	1.5	0.975	0.4	0.016	0.0022	59	1.5	0.925	0.7	0.024	0.005
	22	1.43	0.975	0.4	0.016	0.0022	60	1.47	0.925	0.7	0.024	0.005
	23	1.4	0.975	0.4	0.016	0.0022	61	1.43	0.925	0.7	0.024	0.005
	24	1.47	1	0.4	0.016	0.0022	62	1.4	1	0.7	0.024	0.005
	25	1.47	0.95	0.4	0.016	0.0022	63	1.4	0.975	0.7	0.024	0.005
	26	1.47	0.925	0.4	0.016	0.0022	64	1.4	0.95	0.7	0.024	0.005
	27	1.47	0.975	0.3	0.016	0.0022	65	1.4	0.925	0.3	0.024	0.005
	28	1.47	0.975	0.5	0.016	0.0022	66	1.4	0.925	0.4	0.024	0.005
	29	1.47	0.975	0.7	0.016	0.0022	67	1.4	0.925	0.5	0.024	0.005
	30	1.47	0.975	0.4	0.012	0.0022	68	1.4	0.925	0.7	0.012	0.005
	31	1.47	0.975	0.4	0.02	0.0022	69	1.4	0.925	0.7	0.016	0.005
	32	1.47	0.975	0.4	0.024	0.0022	70	1.4	0.925	0.7	0.02	0.005
	33	1.47	0.975	0.4	0.028	0.0022	71	1.4	0.925	0.7	0.028	0.005
	34	1.47	0.975	0.4	0.016	0.0002	72	1.4	0.925	0.7	0.024	0.0002
	35	1.47	0.975	0.4	0.016	0.0042	73	1.4	0.925	0.7	0.024	0.0022
	36	1.47	0.975	0.4	0.016	0.005	74	1.4	0.925	0.7	0.024	0.0042
	37	1.47	0.975	0.4	0.016	0.0062	75	1.4	0.925	0.7	0.024	0.0062
	38	1.47	0.975	0.4	0.016	0.008	76	1.4	0.925	0.7	0.024	0.008

✓ Results

Simulated Load-displacement/time curve

Typical load Vs displacement/time curve obtained from the FEM simulation is shown in **Figure 3.31**. Similar to the analysis of the experimental results, the load-displacement curve is divided into three parts: I-before the general yield point, II-between the general yield point and the peak point, and III-after the maximum point till the final fracture. All three points are marked in **Figure 3.31**.

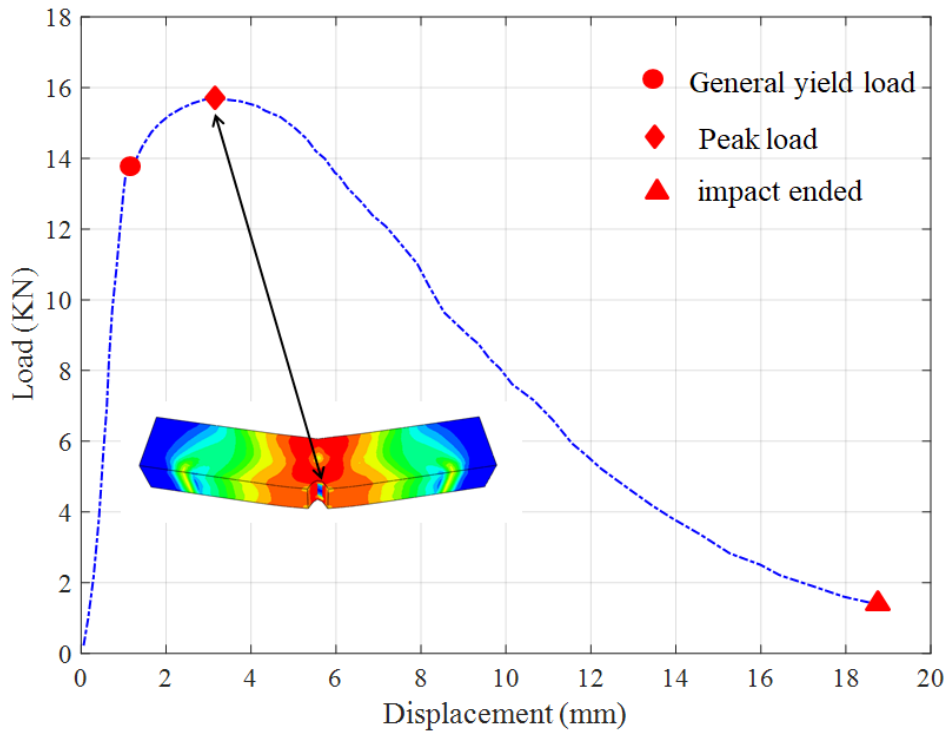


Figure 3. 31 The simulated load-displacement curve for Impact testing-X70.

It can be seen in **Figure 3.31** that the load increases linearly with the displacement in Part I. between the general yield point and the peak point the material starts to be deformed plastically. In Part III, the crack propagates and the load decreases to end of impact and the final separation is observed. All results at different temperatures and GTN parameters values of FEM simulated load values are summarized in **Table 3.16**.

Table 3. 16 Summary of experiment and FEM simulation results for the impact specimen.

Material Specimen	Temperature	Experiment				FEM simulation			
		general yield		peak load		general yield		peak load	
		Min	Max	Min	Max	Min	Max	Min	Max
Group1	20 °C	17.78	18.65	19.05	19.98	14.07	15.15	15.01	24.22
Group2	0 °C	16.66	17.36	17.85	18.6	14.72	15.67	15.53	25.33
Group3	-10 °C	14.7	15.12	15.75	16.2	15.64	16.11	15.96	26.92
Group4	-20 °C	14.21	14.42	15.225	15.45	15.85	16.37	16.23	27.28

Figure 3.32 shows examples of the effect of the value of GTN parameters on the resulting fracture surface for Charpy specimen, and Figure 3.33 shows the simulated impact test and the experimentally tested one.

Two faces fracture area can be observed in both pictures.

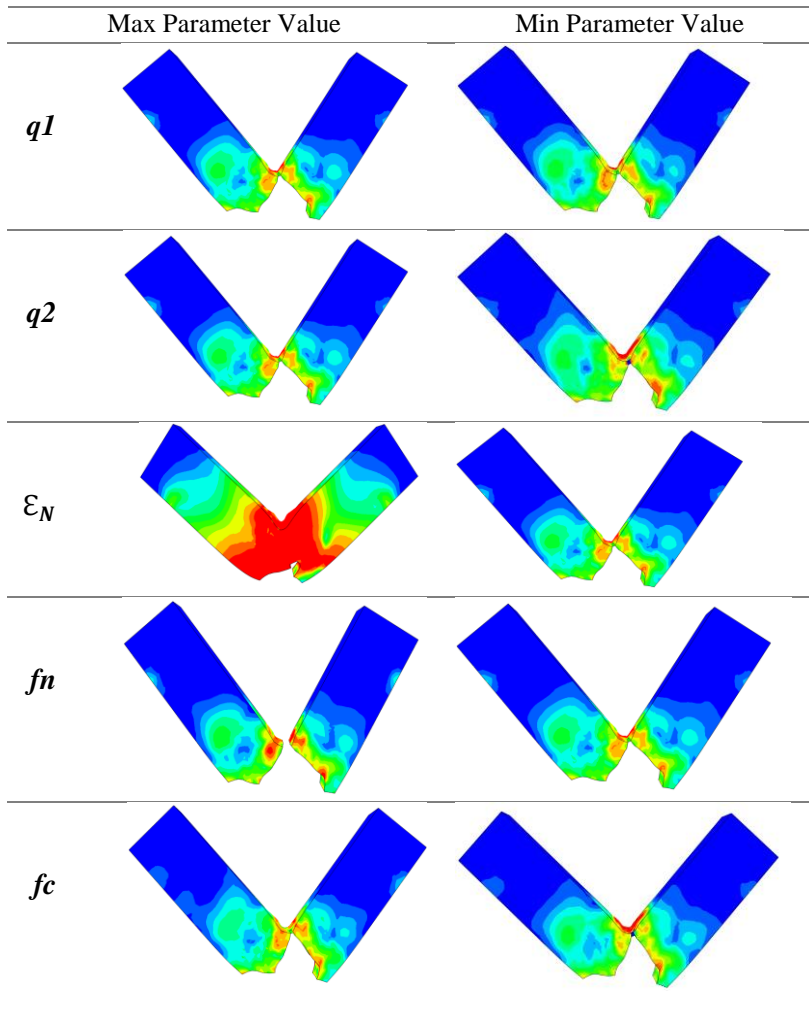


Figure 3. 32 Examples of the effect of GTN parameters on the resulting fracture surface.

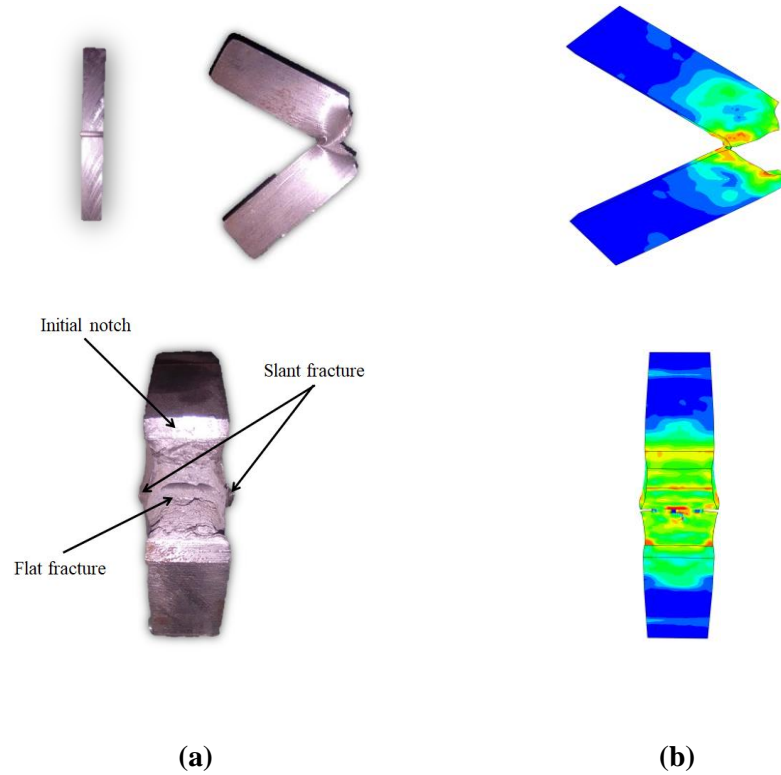


Figure 3. 33 The fractured impact specimen: tested specimen (a); Simulated specimen (b).

3.11 Predicting and analyzing of initiation and maximum impact loading

3.11.1 Artificial neural network (ANN)

The fractures simulation by GTN model in Abaqus software provides detailed information and data of the load fracture initiation and propagation in a ductile impact testing specimen. In this case, the development of ANN application depends on a good selection of training data. In this work, ANN model has been developed to predict the initial and maximum values of loading in impact test at different temperatures. The percentages by weight of GTN parameters were considered as the inputs and the initial and maximum loads were considered as the outputs as shown in **Figure 3.34**.

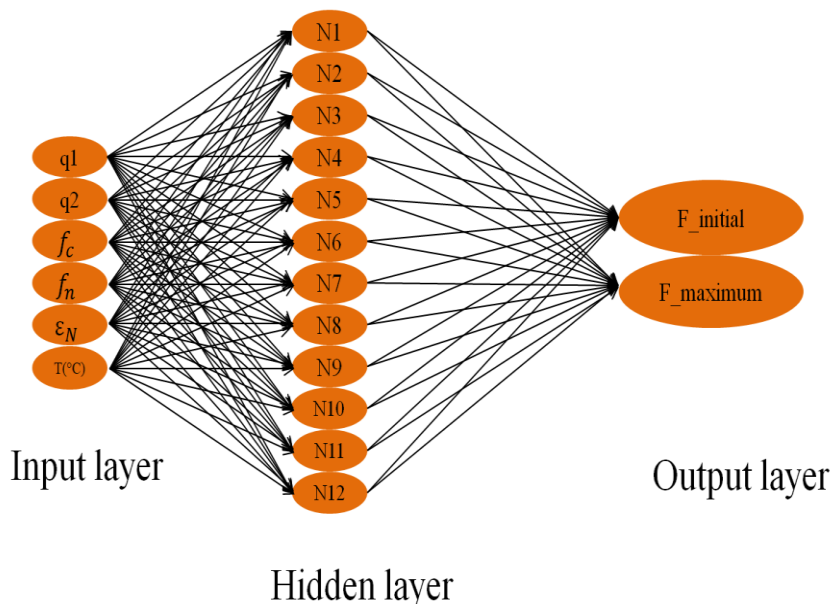


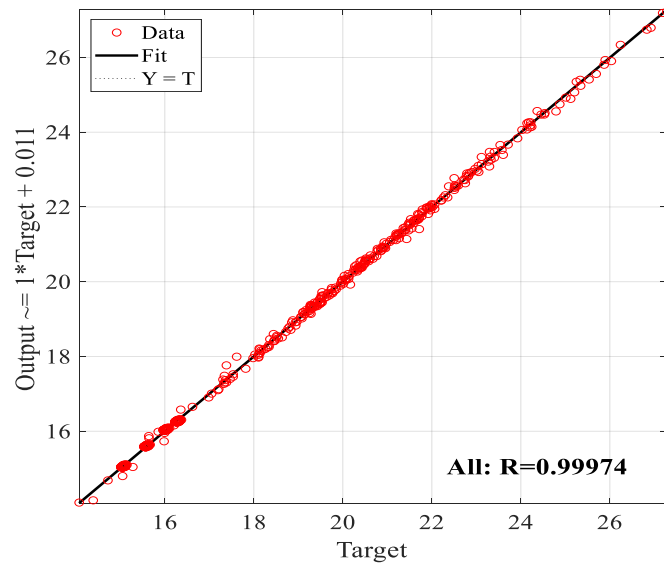
Figure 3. 34 Architecture of Neural Network.

ANNs have been widely used in several research studies to investigate the correlation between numerical input data elements and target orientation in Refs [177, 178]. We try to use ANN to study the relationship and the sensitivity between the GTN parameters and the initial and maximum loads for the specimen fracture.

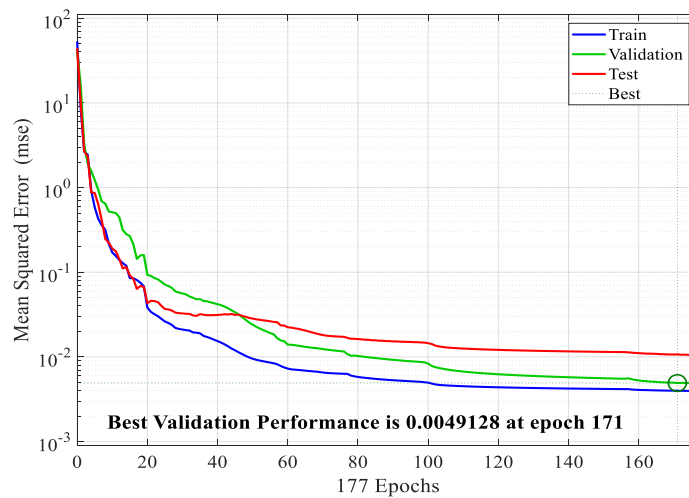
Thus, in our study, the 80% of the data provided in **Table 4.16** is used for training and 20% for testing and validation of neural networks for the prediction of initial and maximum load at different temperatures. In MATLAB, the desired inputs and outputs or targets are imported into the workspace and the network "nntool" is created using inputs and targets. The ANN model has a multi-layered structure, which is connected by nodes with three main layers, namely the input layer (6), the hidden layer (s) (12 neurons) and the output layer (2 neurons) as shown in **Figure 3.34**. The mass percentage values of API X70 steel elements are inputs: q_1 , q_2 , ϵ_N , f_n , f_c , and $T(^{\circ}C)$. The output layer represents the initial and maximum load values: $F_{initial}$ and $F_{maximum}$.

3.11.2 Results and discussion

The obtained results with the regression analysis (see **Figure 3.35 (a)**) and performance analysis (see **Figure 3.35 (b)**) for the prediction of the initial and maximum load values in impact testing at different temperatures of API X70 steel as a function of GTN model parameters are provided using ANN.



a- Regression analysis



b- Performance analysis

Figure 3. 35 The results obtained for the prediction of initial and maximum loads.

The test input is considered (GTN model parameters) to predict different values of load (initial and maximum) and at different temperatures. The provided results are plotted in **Figures. 3. 36** and **3.37**.

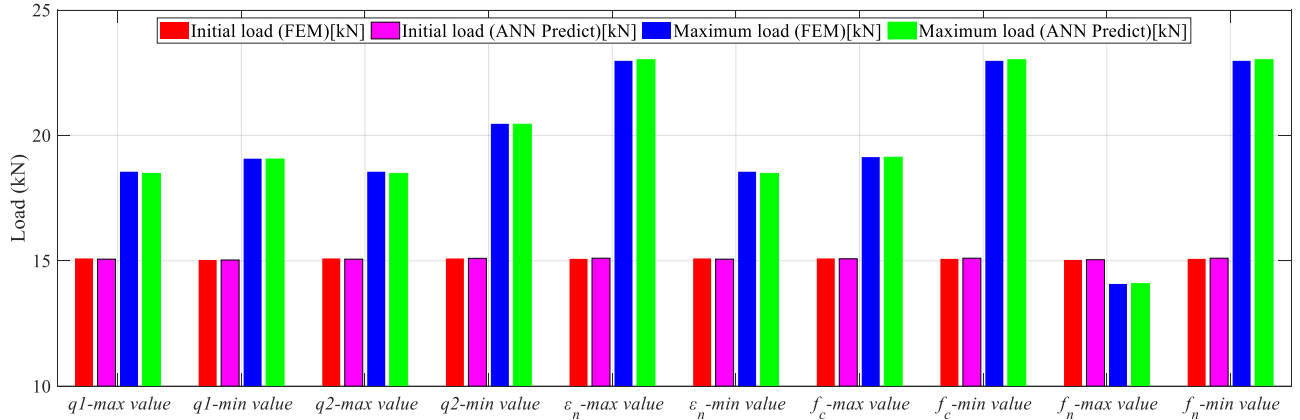


Figure 3. 36 The initial and maximum loads with number of parameters GTN model (min and max values).

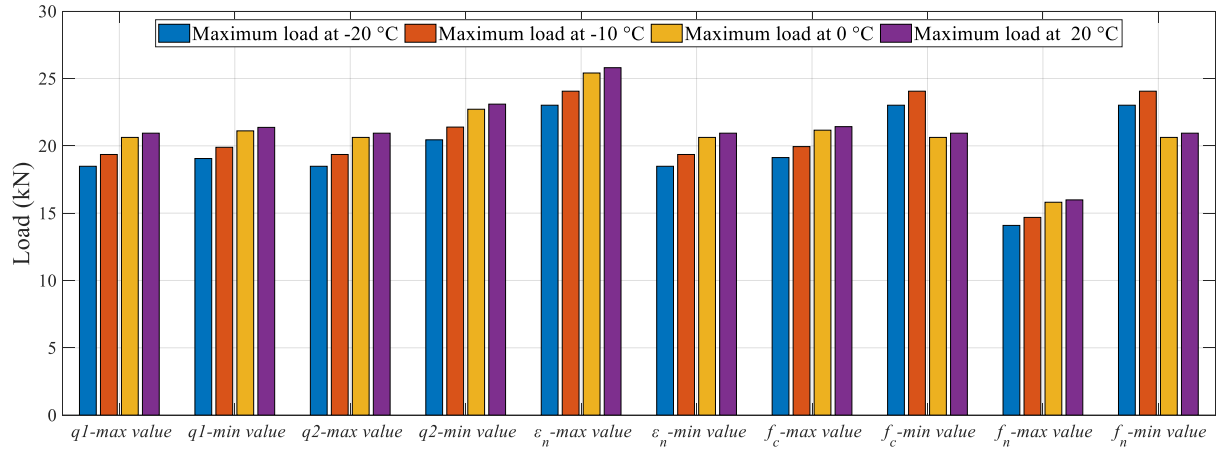


Figure 3. 37 The maximum loads at different temperatures and max GTN parameters values of impact testing.

3.12 Conclusion

An artificial neural network model was developed in this work to predict the parameters of the GTN damage model and the constants of the Ramberg-Osgood hardening law of API X70 steel pipelines. Based on the data obtained, the following conclusions can be drawn:

- Despite the high number of parameters and simulations, the approach applied in this study allows to determine the parameters with minimal errors and good accuracy using a reverse identification procedure.
- The minimum difference between the numerical results in the case of coupled identification allows the identification to be broadened to include a considerable number of experimental tests from the previous results obtained at the ALFAPIPE Ghardaia laboratory.
- Subsequently, the identified GTN parameters are used to develop an ANN model to predict two principal parameters of the GTN damage model, namely f_n and f_c , coupled with hardening law.
- The developed model offers the basic metal chemical composition API X70 as an input because it directly influences the mechanical properties of this steel.
- The results obtained by the ANNGTN were used in the numerical model of the tensile test and of the Charpy test. After that the numerical load-displacement curve was compared with the experimental results and provided good results.
- It can be said that the ANN has been used successfully to facilitate the prediction of GTN parameters and mechanical properties of steel, thanks to the good compatibility of the experimental and numerical analyses.
- The developed model has a great capacity to make the prediction of the results before making mechanical tests and determines the variation in mechanical properties by the simulation according to the chemical compositions of steel.

An Artificial Neural Network model was developed in this work to predict the initial and maximum loads and to analyze the GTN damage parameters at different temperatures for dynamic fracture propagation in X70 steel pipeline. Based on the data obtained, the following conclusions can be drawn:

- The calibration of certain parameters requires data and experimental tests and therefore the result of this calibration depends on the latter, which varies according to the condition of the tests. So in this work we try to predict and analyze the influences of number GTN parameters on the initial and maximum load and in a temperature range in the Charpy

- From the results, we can say that each GTN model parameter influences the final results by different percentages and this allows taking the sensitivity of the parameters into consideration in the calibration part.
- Use of the damage model exists in many studies and researches, but the values of the GTN parameters in the calibration of the models are not fixed and equal to them. Therefore, our study goes through the study of the sensitivity of the initial and maximum loads in the test of the impact according to the changes of the values of the parameters of the model GTN and in a limited temperature interval.
- The developed model has a great capacity to make the prediction of the results before making calibration and determines the variation between different parameters by the simulation according to the mechanical properties of X70 Steel.

The forthcoming chapter presents crack identification through static analysis using ANNs enhanced with various optimization algorithms.

*Chapter 4: Identification of a Single Crack length
in API X 70 steel Using Stress, Strain and
Displacement*

4.1 Introduction

Intelligent systems have recently gained recognition for their ability to solve extremely complicated and multidimensional problems. Artificial Neural Networks (ANN) has achieved considerable success in overcoming such challenges, but they do have some limitations. In this chapter, we delve into the application of the WOA-ANN hybrid model for predicting crack length based on various input values, such as strains, stresses, and displacements, to assess the accuracy of this presented technique.

The proposed technique is compared with other approaches, including GA-ANN, AOA-ANN, and WOABAT-ANN. By coupling metaheuristic optimization algorithms with ANN, the aim is to enhance its efficiency. The connectivity between neurons carries some weight, and neurons are also associated with biases. These connection weights and biases are adjusted to minimize the error function based on the input values and corresponding target output values provided, a process commonly known as Back Propagation (BP).

The investigated approach is relevant to real engineering applications and involves controlling the state of structures. Standard ASTM test specimens are selected to study the evolution of fracture mechanics parameters. Subsequently, an analytical model is developed by simulating the tests using the Finite Element Method (FEM) and validated with experimental results. FEM is utilized to analyze the tensile failure process of one-sided notch samples with the mesoscopic GTN damage model and to extract the data required for WOA-ANN. Once the database is collected, our model is ready to predict different scenarios.

The obtained results using WOA-ANN demonstrate higher efficiency compared to other techniques.

4.2 Experimental crack identification of API X70 steel pipeline using Improved Artificial Neural Networks based on Whale Optimization Algorithm

4.2.1 Numerical models

The FE analysis of the tensile test of base metal is improved using ABAQUS software. A 3D solid FE model was implemented in order to reproduce the fracture tensile experiment on a laboratory scale. ABAQUS explicit solver allowed the application of the GTN damage model for the simulation of dynamic crack propagation. For this purpose, a model called “porous metal plasticity” is used.

The geometry was created based on the standard dimensions of the specimen (ASTM). In each model, the mesh was created using an eight nodes linear brick (C3D8R).

The accuracy of the numerical calculation is strongly linked to the quality of the mesh around the crack structure. The mesh size has more significant importance when the GTN damage model is used. In this study, approximate element size is 0.2. Using the data from the results of the previous uniaxial tensile tests, we have implemented the materials plasticity properties. The boundary conditions in the numerical model are fixed in the bottom end including all degree of freedom (DOF). Next, another side at the top of the model is allowed to move only in the direction of the load in the y-axis, as shown in **Figure 4. 1**.

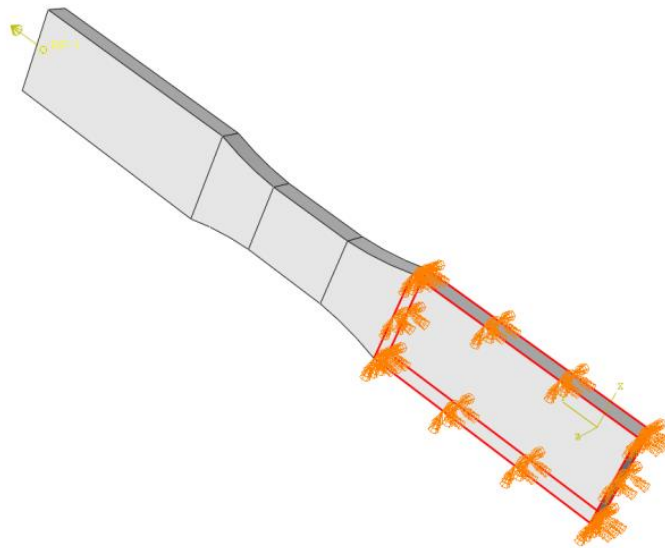


Figure 4. 1 Boundary conditions for the modeled tensile test specimens of base metal.

In this section, the numerical simulation is performed to be used for the simulation of different crack lengths in the critical zone, the refinement mesh is considered where the high-stress concentration is expected, in particular at the interface as indicated in **Figure 4. 2-a**. The dimensions of the specimen are presented in **Figure 4. 2-b**.

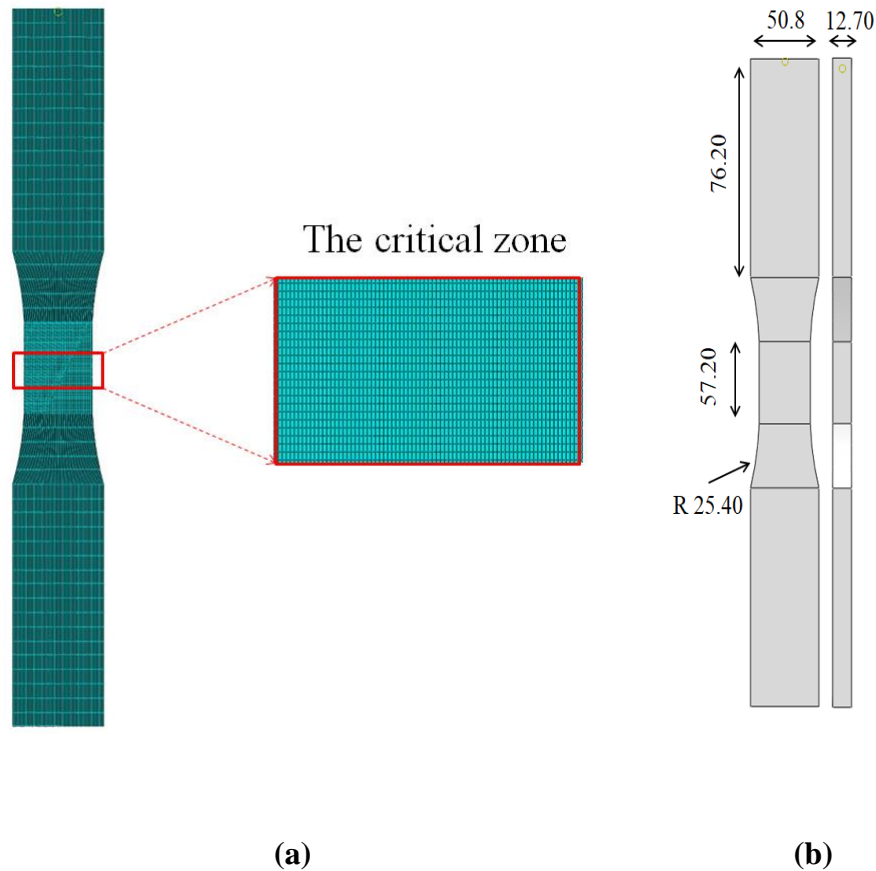


Figure 4. 2 a- Mesh refinement in the critical zone b-The geometry.

4.2.2 Load-displacement simulation curve

Based on the experimental results, the obtained load-displacement curve from the FEM simulation in ABAQUS is plotted in **Figure 4. 3**. Three regions are considered in this curve: **I**- before the yield point, **II**-between the yield point and the ultimate point, and **III**-after the maximum point till the final fracture. All points P1, P2, P3, and P4, are represented in **Figure 4. 3**.

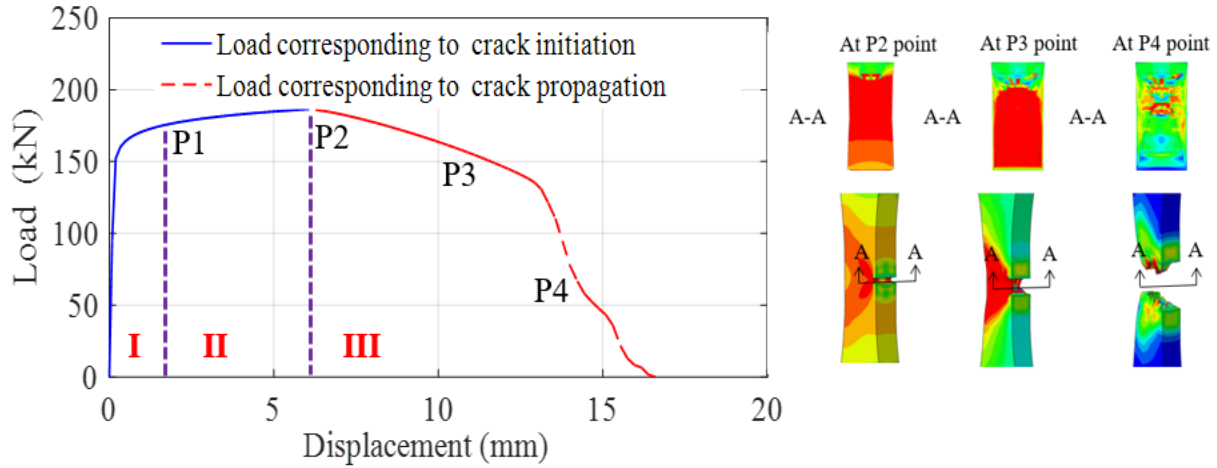


Figure 4. 3 Load-displacement simulation curve of single edge crack of API X70.

In **Figure 4. 3**, Firstly, a region **I** that the load increases linearly with the displacement to the yield point P1, the material API X70 steel deformed plastically. Secondly, in region **II**, between P1 and P2, the load with the displacement continuously increases. Thirdly, in region **III**, the necking is observed and represented by the specimen area reduced to the final separation is observed at P4. Crack behavior is presented based on experimental analysis using a camera at different times see **Figure 4. 4-a**. A good agreement of the specimen geometries predicted in the simulation based on stress contours is presented in **Figure 4. 4-b**.

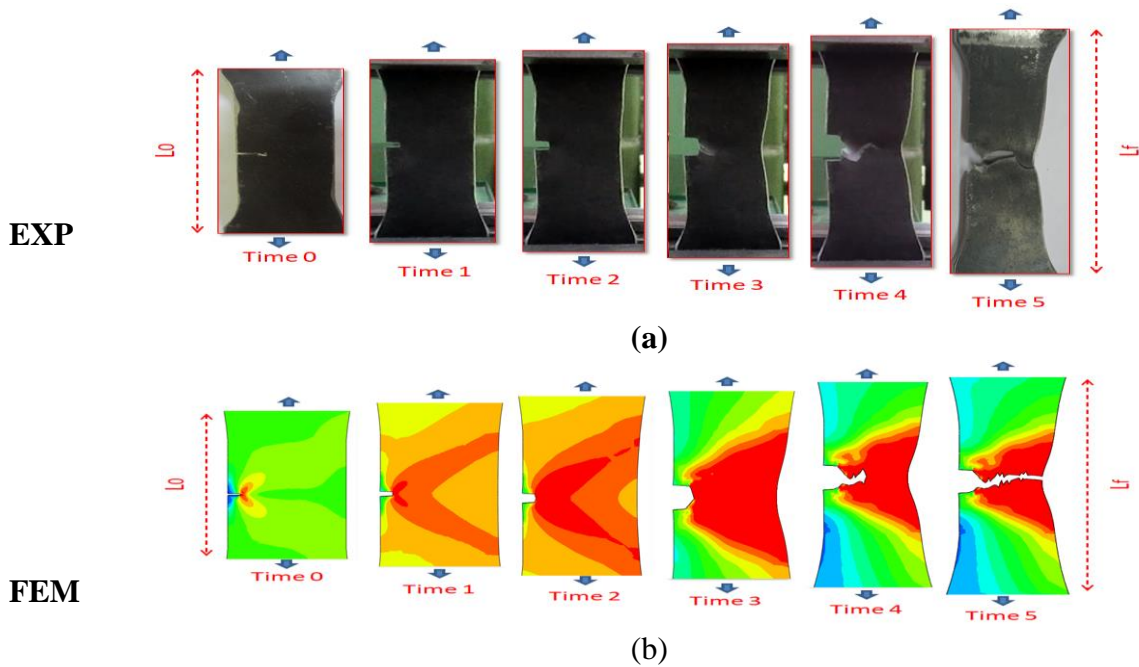


Figure 4. 4 Fracture process of API X70 steel during the test: Experiment (a) and FEM simulation (b).

4.3 Experimental tensile test of pipeline steel

4.3.1 The tensile test of a specimen without crack

The material of our study is a manganese carbon steel used for the transport of hydrocarbons under a working pressure of 70 bars with the name API X70. In order to determine the load-deformation curves and the mechanical properties of API X70 steel, flat specimens according to standard NF EN 10002-1 [70] were used under simple traction at room temperature in the tensile testing machine (ZwickRoell) at ALFAPIPE (Algerian manufacturing pipes laboratory) see **Figure 4. 5**. The initial material is presented in coils of the same casting. The thickness of the test specimens and the geometrical dimension of all the specimens are shown in **Figure 4. 5**.



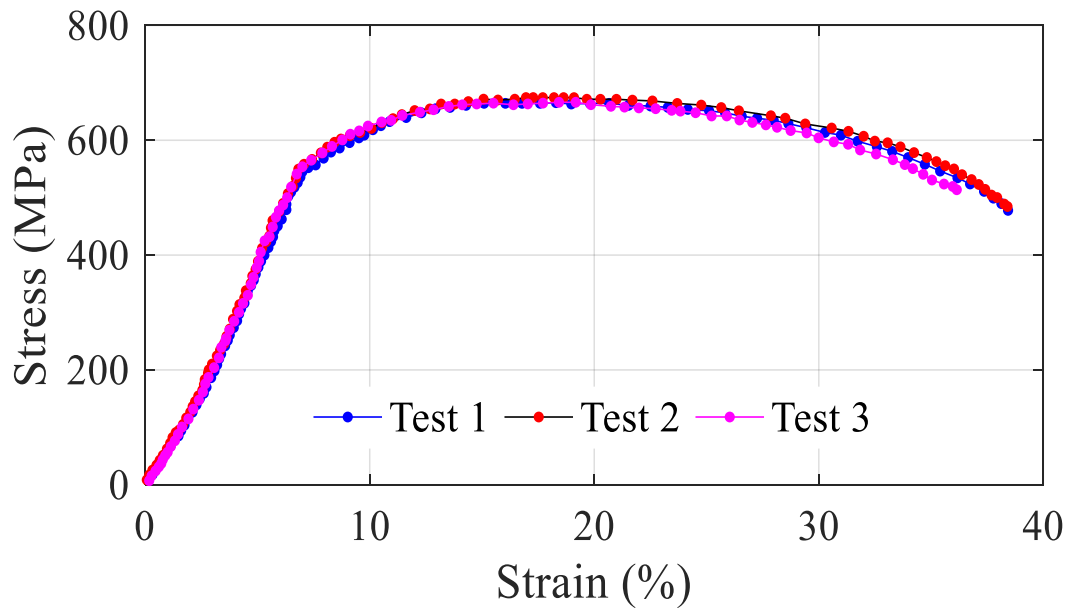
Figure 4. 5 Test specimen with a tensile extensometer in the tensile testing machine.

The experimental results for the tensile tests 1, 2, and 3 give the evolution of the stress according to the strain of the material as shown in **Figure 4. 6**. The general appearance of these curves shows ductile behaviour. **Table 4. 1** shows the mechanical properties of API X70 pipeline steel, which can be used for numerical simulation, with E Young's modulus, ν the Poisson's ratio, YS the yield strength according to the standard, UTS is the ultimate tensile strength, $EL\%$ is the elongation at break, and k and n are the parameters of Hollomon.

Table 4. 1 Mechanical properties of API X70 steel.

E (MPa)	ν	Yield strength YS (MPa)	Ultimate tensile strength UTS (MPa)	Elongation EL %	k	n
$2.10 \cdot 10^5$	0.3	558	672	38	850	0.095

The tensile tests were carried out using a Zwick/Roell materials testing machine type tensile machine, which is directly connected with a computerized system for the acquisition of experimental data.

**Figure 4. 6** Stress-strain diagrams of API X70 pipeline steel.

Comparison between experimental and numerical results using the GTN model are shown in **Table 4. 2**.

Table 4. 2 Comparison between the experimental and numerical results of the tensile test.

	YS (MPa)	UTS (MPa)	$(\Delta L)_u$ (mm)	ϵ_u (-)
Experimental (average between tests 1,2, and 3)	558	671	7.62	0.15
Simulation (GTN model)	547	659	6.75	0.135

4.3.2 The tensile test of a specimen with cracks

In this section, different crack lengths are considered; $L = 4, 7, \text{ and } 10 \text{ mm}$. Two specimens are tested for each crack length for highly accurate results. To realize the test specimens, we have extracted a sufficient plate that we have cut from the pipe. Next, a plate is taken from this sample, one transverse to the shell, which contains only the base metal, see **Figure 4. 7-b**. The obtained plate is illustrated in **Figure 4. 7-c**.

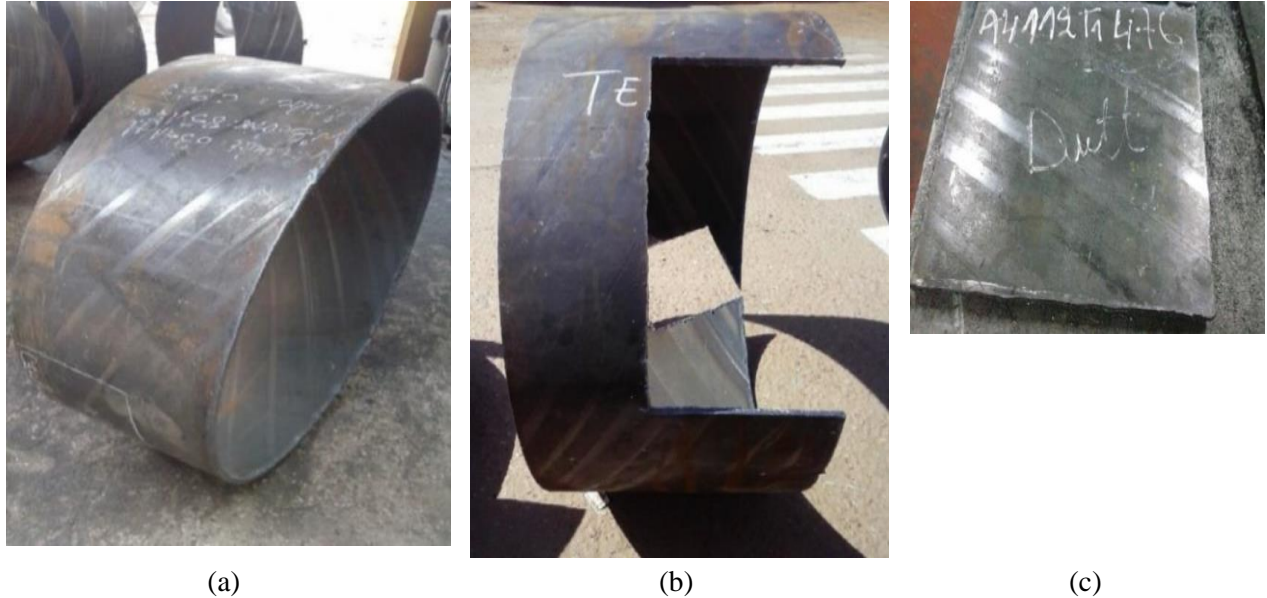


Figure 4. 7 A part of pipe (a), Removal of the transverse base metal (b), and Plate "1" completely from base metal (c).

To produce the specimens, a mechanical saw was used in order to cut the plate into two parts sufficient for the production of two specimens per plate. After cutting the plate, the specimens are manufactured by the milling process to obtain the specimens standard dimensions, see **Figure 4. 8**.



Figure 4. 8 Specimens used for tensile testing.

Next, different crack lengths with 4, 7, and 10 mm, are illustrated in **Figure 4. 9**.

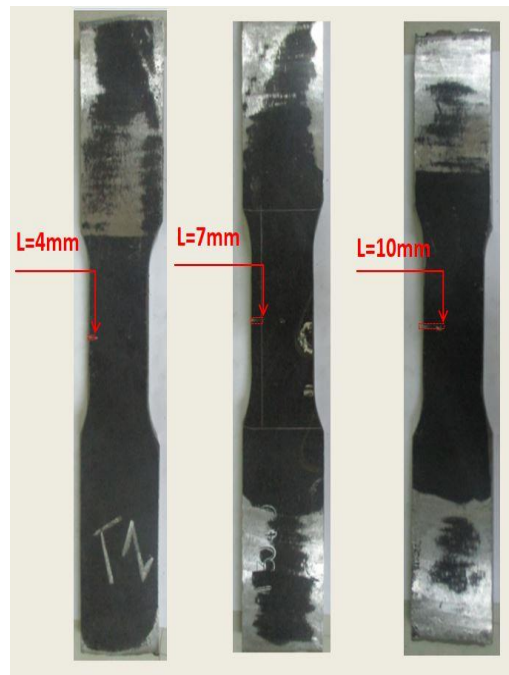


Figure 4. 9 Test specimens carried out for tensile tests according to different crack lengths.

The mechanical properties of a test specimen with three different crack lengths ($l=4$ mm, 7 mm, and 10 mm) from the experimental analysis and FEM results are presented in **Table 4. 3**.

Table 4. 3 Comparison between experimental and FEA stress results for different crack length.

	Yield Stress YS (Mpa)			Maximum Stress MS (Mpa)		
	Experimental Average (test 1-2)	FEM	% Error	Experimental Average (test 1-2)	FEM	% Error
$L=4\text{mm}$	540	548	1.46	614	612	0.33
$L=7\text{mm}$	505.5	514	1.55	574.5	563	2.00
$L=10\text{mm}$	446	464	3.28	507	497	1.63

The obtained results in **Table 4. 3** are more effective, the error percentage between the experimental and FEM is less than 3.5% for test specimens with notches. Therefore, to better

predict the crack length using WOA-ANN, more data are collected from FEM for different crack lengths after validation.

4.4 Improved Artificial Neural Network for crack prediction using WOA

Once an ANN is adequately trained, it can be used as a black-box model to link complex input and output datasets. Weights and biases connect the neurons together. The input layer, hidden layer, and output layer are the three layers of an ANN network. The hidden and output layers contain all neurons, while the input layer is devoid of them. **Figure 4. 10** illustrates a typical ANN model.

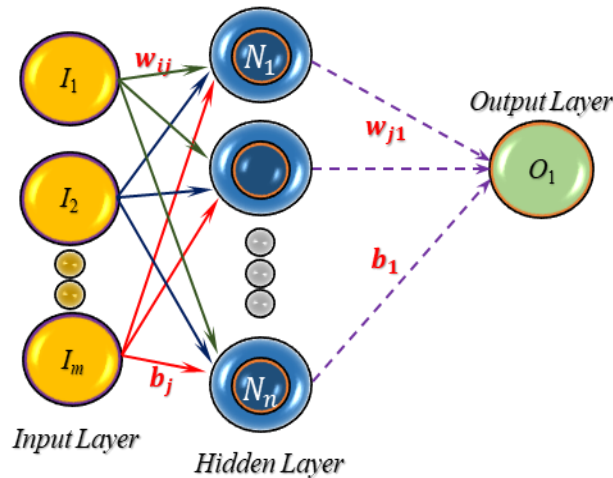


Figure 4. 10 A typical ANN architecture.

w_{ij} is the weights of neuron connection between i^{th} input node and j^{th} neuron in the hidden layers. b_j represents the bias associated with j^{th} neuron in the hidden layer. w_j is the weights of neuron connection between j^{th} neuron in a hidden and single neuron in the output layers. b_1 represents bias associated with the single neuron in output layer neuron. Indices $i = 1, 2, \dots, m$ and $j = 1, 2, \dots, n$ is input features and hidden layer neurons respectively. The total number of parameters used in the network is $n*(m + 2) + 1$. Following the creation of the ANN model's structure, training with known input and output sets is carried out to determine the optimum weights and biases of the neurons. Various strategies are typically used to determine the optimum weights and biases for the ANN. In this study, MATLAB was used to perform optimum network training using WOA. Whales are creatures of fancy. They are considered as the world's largest mammals. Up to 30 m long and 180 tons' weight, an adult whale can grow. The remarkable thing about whales is that they are viewed with emotion as highly intelligent creatures. The location of prey

can be recognized and encircled by humpback whales. The optimal design location in the search space is not known in advance. WOA assumes that the target prey is close to the optimum and is the current best candidate solution. Other search agents will then try to update their positions to the best search agent when it is identified. The following equations represent this behaviour:

$$\vec{D} = \left| \vec{C} \cdot \vec{X}^*(t) - \vec{X}(t) \right| \quad (4.1)$$

$$\vec{X}(t+1) = \vec{X}^*(t) - \vec{A} \cdot \vec{D} \quad (4.2)$$

where, the latest iteration is defined by t , coefficient vectors are \vec{A} and \vec{C} , \vec{X} position vector, and \vec{X}^* is a position vector of the best solution obtained so far.

\vec{A} and \vec{C} can be calculated using the following formulations:

$$\vec{A} = 2\vec{a} \cdot \vec{r} - \vec{a} \quad (4.3)$$

$$\vec{C} = 2 \cdot \vec{r} \quad (4.4)$$

Then, a spiral equation is created to approximate the helix-shaped movement of humpback whales between the location of Whale and prey as presented in the following formulation:

$$\vec{X}(t+1) = \vec{D}' \cdot e^{bl} \cdot \cos(2\pi l) + \vec{X}^*(t) \quad (4.5)$$

where $\vec{D}' = \left| \vec{X}^*(t) - \vec{X}(t) \right|$

(X, Y) : Whale located.

(X^*, Y^*) : Prey located.

Humpback whales swim within a decreasing circle around the prey and along a spiral-shaped direction at the same time. Furthermore, to model this concurrent behaviour, we expect that there is 50 % chance of choosing between either the shrinking encircling process or the spiral model to adjust the location of whales through optimization. The mathematical model is given as follows:

$$\vec{X}(t+1) = \begin{cases} \vec{X}^*(t) - \vec{A} \cdot \vec{D} & \text{if } p \geq 0.5 \\ \vec{D}' \cdot e^{bl} \cdot \cos(2\pi l) + \vec{X}^*(t) & \text{if } p < 0.5 \end{cases} \quad (4.6)$$

where p is a random number in $[0,1]$. For more details, the author may refer to Ref. [179].

The mathematical model is expressed as:

$$\vec{D} = \left| \vec{C} \cdot \overrightarrow{X_{rand}} - \vec{X} \right| \quad (4.7)$$

$$\vec{X}(t+1) = \overrightarrow{X_{rand}}(t) - \vec{A} \cdot \vec{D} \quad (4.8)$$

Where $\overrightarrow{X_{rand}}$ is a random position vector (a random whale) chosen from the current population.

More details about this algorithm can be found in Ref [179].

The objective function used to minimize root-mean-square error (RMSE) of the network, which is described in the following formulation:

$$\text{RMSE} = \sqrt{\frac{\sum_{l=1}^n (O_l - I_l)^2}{nd}} \quad (4.9)$$

where O_l denotes the output corresponding to l^{th} data point in the training set by the network, I_l denotes the actual output as consider in the target set. nd is the number of data points used in the training dataset. The RMSE has been used as the objective function as mentioned of the ANN whose parameters (weights and biases) have to be optimised to improve the training. WOA is compared with GA-ANN, AOA-ANN, and WOA-BAT-ANN using different inputs. The number of collected data is 61 using different crack lengths from 4 mm to 34 mm.

4.5 Results and discussion

To study the effectiveness of WOA-ANN, different optimization techniques GA-ANN, AOA-ANN, and WOA-BAT-ANN are used with different inputs such as stress, strain, and displacement. The number of hidden layers (Hidden neurons) is considered to select the adequate number using three scenarios with crack length 10 mm, 15 mm, 32 mm. The parameters used for all optimization techniques are 100 populations, and 100 Iterations. The characteristic of the computer used for the calculation are Intel(R) Core(TM) i7-6700HQ CPU @ 2.60GHz 2.59 GHz and the RAM memory is 16 GB. The results are shown in **Figure 4. 11**.

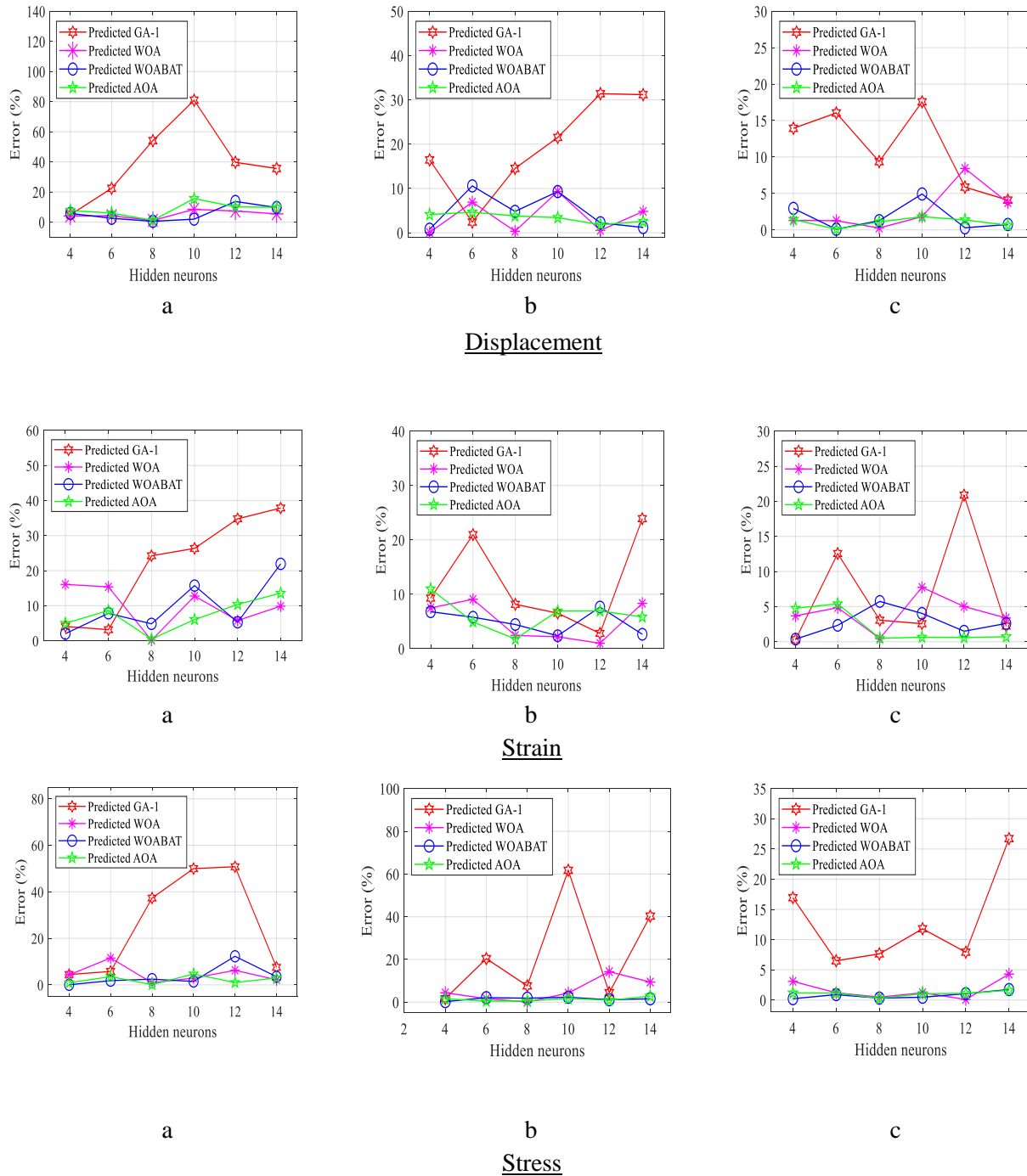
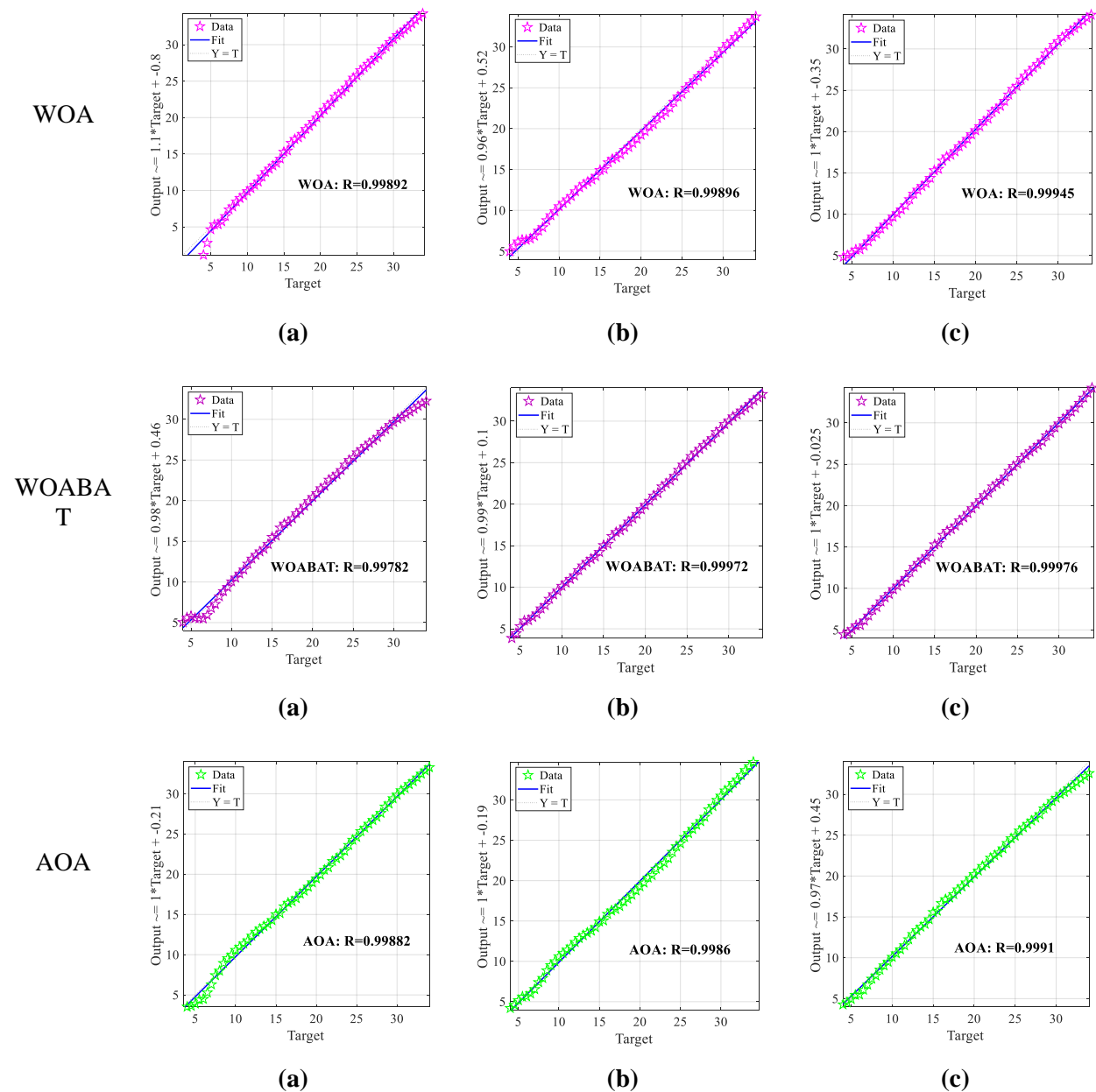


Figure 4. 11 Different hidden neurons with different scenarios.

Notation :Crack length : a=10 mm, b=15 mm, and c=32 mm.

The results show that the most optimum network obtained considering WOA, WOA-BAT, AOA, and GA has eight hidden neurons using different inputs based on the fitting examination. Next, five scenarios with actual crack lengths 10 mm, 15 mm, 24 mm, 28 mm, and 32 mm are considered using eight hidden neurons to predict the exact crack lengths. Based on the previous results, GA fails to predict the exact crack length. However, the population size is increased from 100 to 2000. **Figure 4. 12** shows the training performance of the best network using different inputs (displacement, strain and stress), including different optimization techniques.



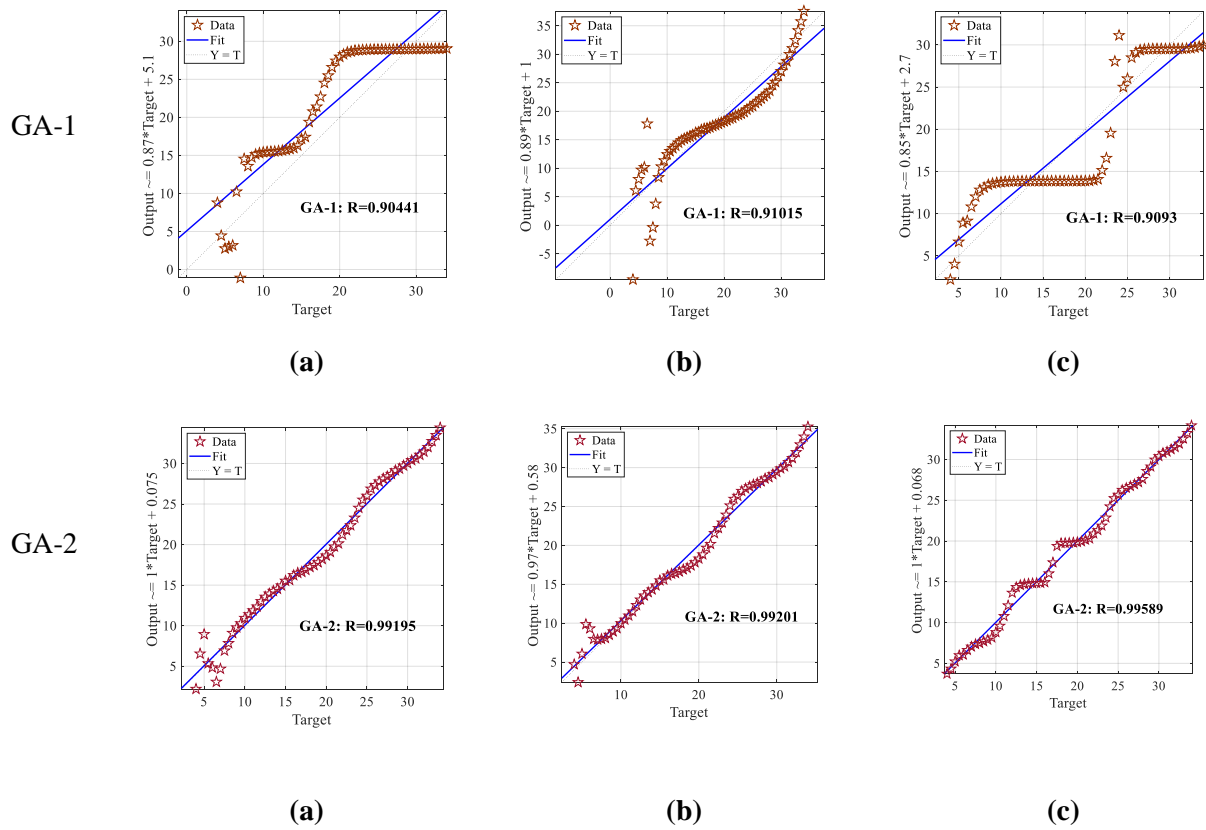
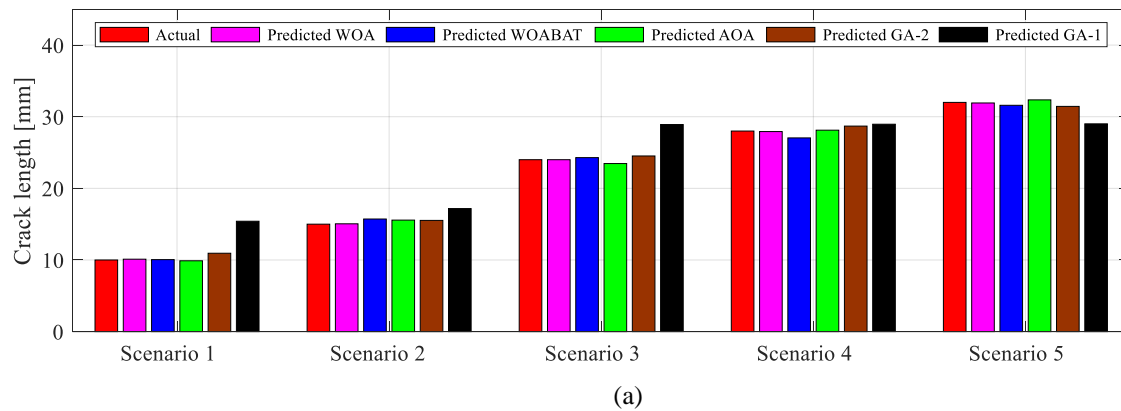
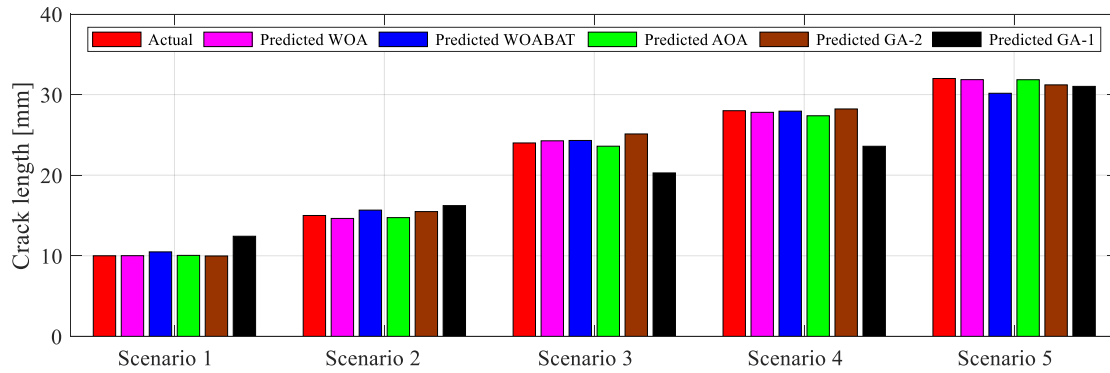


Figure 4. 12 Regression analysis: a) Displacement, b) Strain, c) Stress.

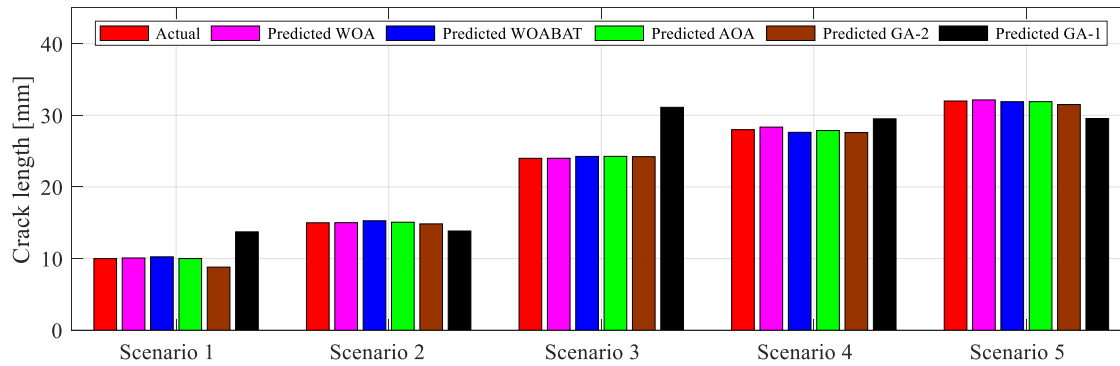
Notation: GA-1: 100 populations-100 iterations, and GA-2: 2000 populations-100 iterations.

After the training performance, the model is ready to predict the five considered scenarios. The obtained results are presented in **Figure 4. 13**.





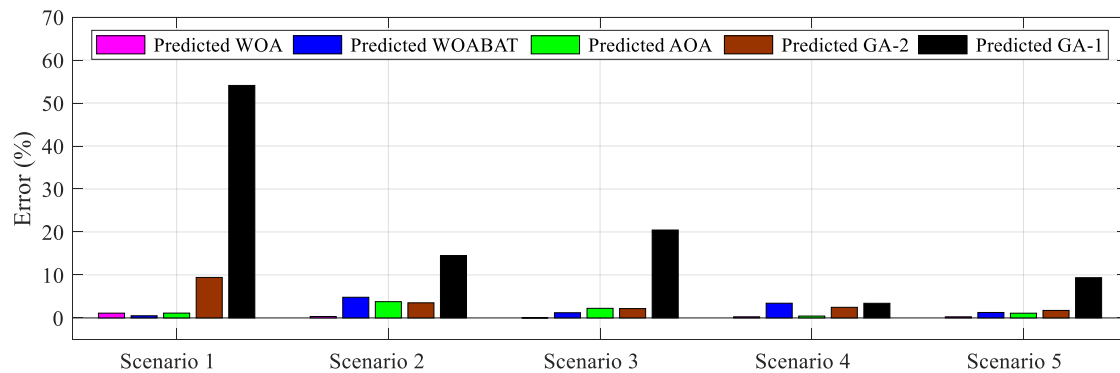
(b)



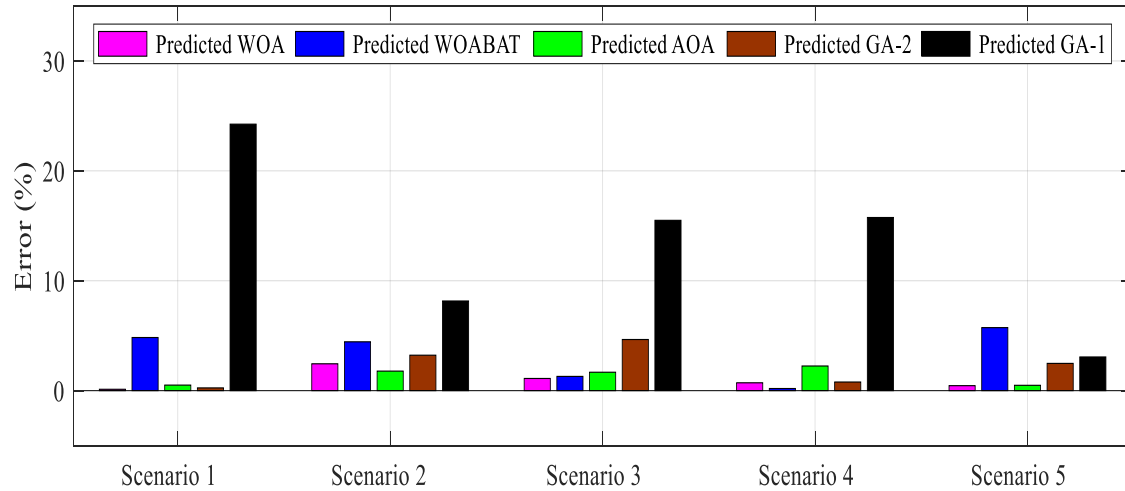
(c)

Figure 4. 13 Predicted crack length using 61 collected databases; a-Displacement, b-Strain, c-Stress.

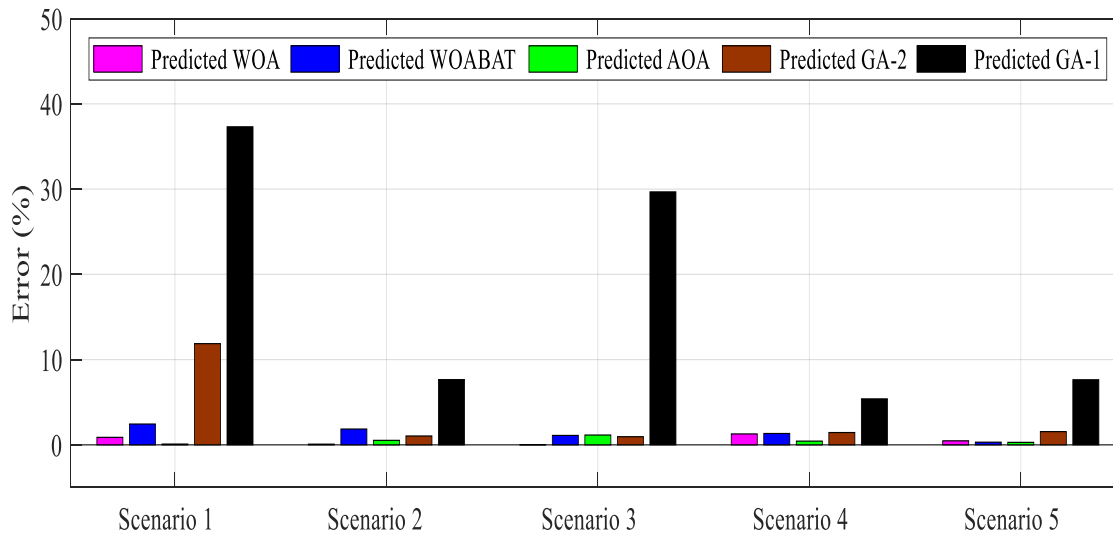
Based on the presented results, the most effective predicted results can be found by WOA compared with the actual crack length using different inputs. For better evaluation, the errors between exact and predicted crack length for all scenarios using various optimizations techniques are presented in Figure 4. 14.



(a)



(b)



(c)

Figure 4. 14 Error percentage using 61 collected databases; a-Displacement, b-Strain, c-Stress.

Table 4. 4. Summarized the results of three inputs (strain-stress-displacement) compared with actual crack length, including errors between actual and predicted. Thus, the CPU times are computed for each scenario and shown in Table 4. 5.

Table 4. 4 Error percentage of predicted WOA, WOA-BAT, AOA, GA-1, and GA-2 for each crack length scenario.

Crack length	Optimisation	Data inputs					
		Displacement	Error (%)	Strain	Error (%)	Stress	Error (%)
L=10 mm	WOA	10.111	1.110	10.012	0.120	10.088	0.880
	WOABAT	10.050	0.500	10.483	4.830	10.244	2.440
	AOA	9.888	1.120	10.050	0.500	10.009	0.090
	GA-2	10.942	9.421	9.976	0.245	8.813	11.870
	GA-1	15.409	54.089	12.425	24.246	13.731	37.307
L=15 mm	WOA	15.050	0.333	14.634	2.440	15.012	0.080
	WOABAT	15.721	4.807	15.666	4.440	15.278	1.853
	AOA	15.567	3.780	14.734	1.773	15.079	0.527
	GA-2	15.527	3.512	15.483	3.221	14.844	1.039
	GA-1	17.177	14.514	16.223	8.153	13.853	7.649
L=24 mm	WOA	24.001	0.004	24.265	1.104	24.006	0.025
	WOABAT	24.289	1.204	24.310	1.292	24.265	1.104
	AOA	23.464	2.233	23.599	1.671	24.276	1.150
	GA-2	24.521	2.172	25.116	4.650	24.229	0.955
	GA-1	28.908	20.452	20.281	15.494	31.121	29.671
L=28 mm	WOA	27.928	0.257	27.801	0.711	28.358	1.279
	WOABAT	27.042	3.421	27.947	0.189	27.627	1.332
	AOA	28.121	0.432	27.373	2.239	27.878	0.436
	GA-2	28.692	2.470	28.218	0.780	27.596	1.444
	GA-1	28.954	3.405	23.590	15.751	29.509	5.391
L=32 mm	WOA	31.918	0.256	31.856	0.450	32.151	0.472
	WOABAT	31.595	1.266	30.166	5.731	31.900	0.313
	AOA	32.351	1.097	31.846	0.481	31.907	0.291
	GA-2	31.442	1.744	31.208	2.476	31.504	1.551
	GA-1	29.005	9.359	31.021	3.060	29.557	7.633

The obtained results describe the effectiveness of used optimization techniques. First, a critical observation was made from the results using GA-1 using different inputs. Furthermore, after increasing the population size and iterations, the results are improved (GA-2).

Table 4. 5 CPU time of WOA, WOA-BAT, AOA, and GA for each crack length scenario.

Crack length	Optimisation	CPU Time based on different database inputs (Sec)		
		Displacement	Strain	Stress
L=10 mm				
	WOA	80.9837	94.9460	87.8769
	WOABAT	2288.975006	2499.596441	2726.764726
	AOA	80.6388	85.0736	78.0631
	GA-2	3038.0734	3167.739	3082.5555
	GA-1	156.58166	155.37554	163.83296
L=15 mm				
	WOA	85.8602	83.7848	84.2638
	WOABAT	2713.802802	2433.929142	2797.347175
	AOA	85.8118	76.3816	75.0310
	GA-2	3189.2067	3050.9033	3084.3608
	GA-1	163.45587	171.36059	160.12588
L=24 mm				
	WOA	82.1883	85.4778	80.7935
	WOABAT	2196.416295	2411.864277	2879.339001
	AOA	75.4474	78.5609	81.2045
	GA-2	2956.2631	2949.6275	3185.1473
	GA-1	148.49252	154.43498	160.82294
L=28 mm				
	WOA	87.0286	75.0774	87.2644
	WOABAT	2044.215224	2814.371634	3327.286624
	AOA	75.9095	78.2227	80.6060
	GA-2	2872.9348	3202.2556	3290.9627
	GA-1	152.56876	176.48117	162.28916
L=32 mm				
	WOA	82.1251	75.9302	83.6858
	WOABAT	1995.307727	2314.740854	3254.794972
	AOA	76.9729	78.1226	83.6941
	GA-2	2856.5266	3105.268	3345.6769
	GA-1	157.83188	170.99801	163.864

The best computational time can be found in WOA and AOA between 75-95 seconds compared with significant differences in WOABAT, and GA-

4.6 Conclusion

A comprehensive analysis was done for the development of hybrid ANN with optimization techniques to predict crack length using different parameters (Hidden layer neurons, bias, and weight). Recent optimization techniques are used to improve ANN for better prediction compared with other techniques to describe the effectiveness of the presented method. Different inputs such as strains, stresses, and displacements are compared using WOA-ANN, GA-ANN, AOA-ANN, and WOA-BAT-ANN. Numerical and experimental tests are investigated for validation in both cases uncracked and cracked specimens. After validating the model, different crack lengths are supposed to build a database. The following observations have been reached based on this study:

- 1- Artificial neural network with eight neurons in the hidden layer is the most optimum network in all optimization techniques.
- 2- GA-ANN has a critical result with less population and generation (100-100).
- 3- The best CPU time found by WOA and AOA compared with GA and WOA-BAT.

Based on the results obtained on this work, we can cite these points:

- ✓ The simulation by the GTN model parameters gives good results allowing making necessary modifications with good calibration with the experimental models.
- ✓ According to the results of the experimental tensile tests, the existence of the notches of the pipelines under pressure directly influence the yield stress and the ultimate stress but this influence increases rapidly with the increase in the notch depth compared to the thickness of the pipe.
- ✓ The presence of notches is a point of localization of stress and knowing the influence the presence and the depth of the notches plays a very important role, and its passing by creation of the ANN model based of the experimental and numerical data makes it possible to predict the elastic and maximum stress as a function of the depth in our study.
- ✓ The output of our ANN model gives very good results in the prediction of notches depth in part of the faulty pipelines and allows help to make the right decision in the notch situation and helps our in optimizing the right geometry of composite patch in certain necessary cases.

The last chapter investigates impact protection in API X70 pipeline steel, studying ductile and brittle fracture modes through experimental tests and numerical simulations. Machine Learning models predict peak load and crack initiation energy for dynamic brittle fracture with varying crack lengths.

*Chapter 5: Prediction of the peak load and crack
initial energy of dynamic brittle fracture using
improved ANN*

5.1 Introduction

In this final chapter, a robust technique is presented to predict the peak load and crack initiation energy of dynamic brittle fracture in X70 steel pipes using an improved artificial neural network (IANN). The primary objective is to investigate the behavior of API X70 steel based on two experimental tests: the Drop Weight Tear Test (DWTT) and the Charpy V-notch impact (CVN) for steel pipe specimens.

The mechanical properties influencing the brittle fracture behavior of API X70 steel pipes are predicted using numerical approaches with different crack lengths. To simulate the impact of API X70 steel pipes at lower temperatures through a numerical approach, a cohesive approach using the extended Finite Element Method (XFEM) is employed.

The data obtained from these simulations are then used as input for the proposed IANN, which utilizes Balancing Composite Motion Optimization (BCMO), Particle Swarm Optimization (PSO), and Jaya optimization algorithms to predict the peak load values and crack initiation energy of dynamic brittle fractures in API X70 steel with varying crack lengths.

The results demonstrate the effectiveness of ANN-PSO and ANN-BCMO, as evidenced by the convergence of the results and the accuracy of the prediction of peak load and crack initiation energy. These findings highlight the potential of using artificial neural networks in conjunction with optimization algorithms to predict critical fracture properties in API X70 steel pipes, thereby contributing to a deeper understanding of their behavior and performance.

5.2 Cohesive segment approach based on extended finite elements

Belytschko and Black [180] introduced the XFEM technique. Regional enrichment processes can be effectively integrated into a FE approximation using an extension of the traditional FEM based on the principle of unity separation. Static and moving damage can both be simulated using XFEM's damage and crack modeling. To work on the structural mesh, crack propagation simulation using XFEM does not require basic descriptions of cracks and fracture routes. The crack's direction is determined by the resolution. The fissures are allowed to reproduce via elements, allowing the rupture of the huge material to be modeled. Enrichment operations are defined as near-tip asymptotic procedures that capture the singularity at the notch's tip and a discontinuous procedure that designates the displacement jump over the crack's surfaces. The division of unit enrichment approximation for a part displacement vector u is:

$$u = \sum_{I=1}^N N_I(x)[u_I + H(x)a_I + \sum_{\alpha=1}^4 F_{\alpha}(x)b_I^{\alpha}] \quad (5.1)$$

Where;

$N_I(x)$: These are the standard nodal shape functions.

u_i : The usual nodal displacement vector associated with the finite element solution's continuous component.

a_i : The nodal enriched degree of freedom vector's product.

$H(x)$: The discontinuous jump function that goes with it.

b_i^a : The nodal enriched degree of freedom vector's product.

$F_\alpha(x)$: The asymptotic crack-tip functions of elastic materials.

$H(x)$ Can be used as:

$$H(x) = \begin{cases} 1 & \text{if } (x - x^*) \cdot n \geq 0 \\ -1 & \text{otherwise} \end{cases} \quad (5.2)$$

Where;

x : The point of Gauss.

x^* : The crack's point that is closest to x .

n : The unit's normal outward from the crack is x^* .

$F_\alpha(x)$ Are portrayed by

$$F_\alpha(x) = [\sqrt{r} \sin \frac{\theta}{2}, \sqrt{r} \cos \frac{\theta}{2}, \sqrt{r} \sin \theta \sin \frac{\theta}{2}, \sqrt{r} \sin \theta \cos \frac{\theta}{2}] \quad (5.3)$$

(r, θ) At the crack tip, a polar coordinate system is used. $\theta = 0$ The crack at the tip is tangent.

XFEM methods are based on the cohesive tensile-separation behavior [181, 182], which may be modified to simulate crack initiation and propagation in brittle or ductile fracture API X70 steel. Crack initiation and solution-dependent propagation passage in dimensional materials can be simulated using the XFEM-based cohesive segment approach.

On the level of the enriched elements, the damage and initiation of fractures, guide the start of the deterioration of the cohesive response. When stresses or strains meet the damage initiation conditions defined in the model, the degradation mechanism begins. The largest primary stress criteria was used to model damage onset in this study, and it may be represented as:

$$f = \left\{ \frac{\langle \sigma_{\max} \rangle}{T_{\max}} \right\} \quad (5.4)$$

Where;

T_{\max} : The maximum principal stress that can be applied.

$\langle \sigma_{\max} \rangle$: The standard interpretation of the Macaulay bracket.

When the highest main stress ratio (as described in the presentation slide) comes into contact with a value of one, the fracture is deemed to be initiated. Then, after reaching equilibrium, a new crack is presented or

the size of an existing crack is increased when the failure criterion reaches 1.0 within a given tolerance f_{tol} :

$$1.0 \leq f \leq 1.0 + f_{tol} \quad (5.5)$$

If $f \geq 1.0 + f_{tol}$ The time increment is adjusted until the crack initiation requirement is satisfied. The value of f_{tol} was discovered to be 0.05 in this study.

Once the corresponding initiation requirement is met, the crack growth law reflects the rate at which the cohesive stiffness diminishes. The average general damage at the intersection of the surfaces of the cracks and the edges of the cracked elements of the model is designated by the scalar damage parameter D . It has a value of 0 at the start. D gets monotonous from 0 to 1 during multiple loadings once the damage is initiated if the damage evolution is implemented. The damage simulates the portions of normal tension and shear according to:

$$t_n = \begin{cases} (1-D)T_n \dots \text{if} \dots T_n \geq 0 \\ T_n \dots \dots \dots \text{otherwise} \end{cases} \quad (5.6)$$

$$t_s = (1-D)T_s \quad (5.7)$$

$$t_t = (1-D)T_t \quad (5.8)$$

Where T_n, T_t, T_s The elastic traction separation behavior for the current partitions without crack indicates the normal and shear stress elements and the effective separation is defined as:

$$\delta_{\max} = \sqrt{\langle \delta_n \rangle^2 + \delta_s^2 + \delta_t^2} \quad (5.9)$$

An exponential model has been suggested to explain the growth of the damage variable D . The following relationship, in particular, is maintained by such a model.

$$D = \int_0^{\delta_{\max}} \frac{T_{\max}}{\Gamma} d\delta \quad (5.10)$$

T_{\max} Denotes the cohesive stress, and δ denotes the efficacious displacement. Furthermore, Γ denotes the cohesive energy, whereas δ_{\max} denotes the effective displacement at ultimate failure. When the damage (crack initiation) criterion (MPs criterion) was chosen, the newly introduced crack was defined to remain vertical to the MPs direction when the fracture condition was satisfied.

5.3 Experimental

5.3.1 Material characteristics of API X70 steel

In Algeria's high-pressure gas transportation pipelines and networks, API X70 steel and API X65 steel are the most frequently used for pipeline transportation. Spiral welding was used to construct the pipes that are being considered.

The true stress-strain curves for the tested steel are represented in **Figure 5. 1**. The average mechanical properties of API X70 steel were obtained from test data and are presented in **Table 5. 1** along with goal values laid out by API 5L. As can be observed from the results, that the material met the API requirements for API X70 pipeline steel (yield strength > 482.65 MPa, tensile strength > 565.056 MPa) [99]

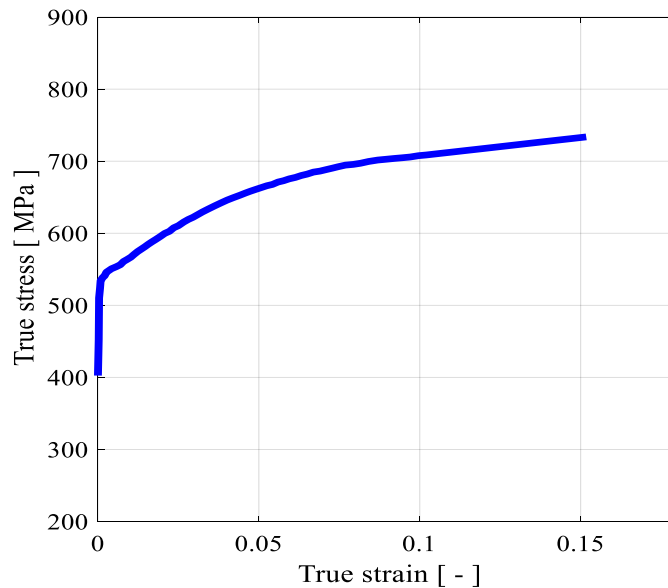


Figure 5. 1 The yield stress and plastic strain of API X70 steel.

Table 5. 1 Mechanical properties of API X70 steel [27].

Parameters	E (MPa)	ν	Yield Strength YS[Mpa]	Ultimate tensile strength UTS [Mpa]	Elongation EL [%]	Hollomon parameters	
						k	n
Values	$2.10 \cdot 10^5$	0.3	558	672	38	850	0.095

5.3.2 DWTT specimens and experimental set up

Figure 5. 2 represents the dimensions and geometry of the DWTT specimen. A test plate was first selected and cut from the principal pipe part to prepare test samples. Second, in accordance with the test standard API [64], test samples were taken from this test plate and flattened to remove their initial curvature. It should be mentioned that none of the test specimens had any seam welds and were made entirely of base metal.

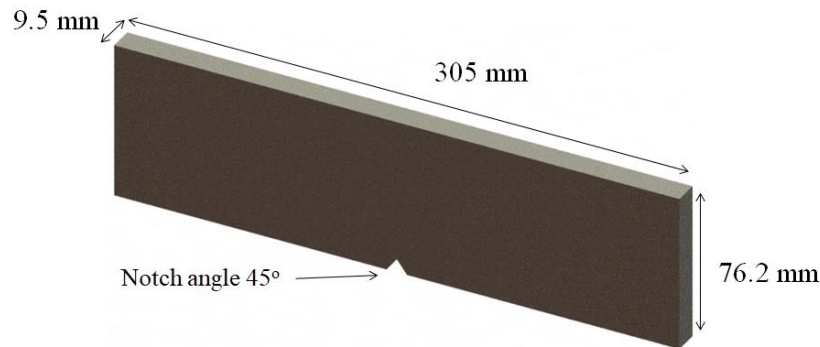


Figure 5. 2 Specimen and dimensions used for DWTT.

For the DWTT experiment, the impactor was designed with a cross section of 9.5 mm x 76.2 mm and a length of 152.5 mm (see **Figure 5. 2**), an initial velocity of 5.4 m/s, and a mass of 1209 kg. The hammer X70 material properties limits were applied to the specimen in **Figure 5. 3**. A Zwick Roell machine was used to carry out the DWT tests (See **Figure 5.3**)



Figure 5. 3 Specimen used for DWTT and the impact machine for steel X70

Table 5. 2 Experimental conditions for DWTT.

Grade	Weight [Kg]	Height [mm]	Velocity [m/s]	DWTT energy [J]
X70	1209	1497	5.4	17952

Noting that before performing the impact test, the specimen must be cooled using a cooler (**Figure 5. 5.a**)

5.3.3 CVN specimens and experimental set up

The CVN specimens were prepared in accordance with ASTM E23 standard with dimensions of 10*10*55 mm (see **Figure 5. 4-a**)[\[183\]](#). A hammer, two anvils, and the CVN specimen, and a starting velocity of 5.5 m/s and a mass of 19.8 kg for the CVN experiments. In **Figure 5. 4-b**, three Base Metal (BM), three Welded Metal (WM), and three Heat-Affected Zone (HAZ) or transition zone specimens totaling nine and other specimens for testing at different temperatures in base metal (BM) were produced. The experimental results of the API X 70 steel impact tests conducted at various locations (BM-HAZ-WM see **Figure 5. 5.c**) indicate that the fracture energy, or absorbed energy by the specimen, varies significantly between the three zones.

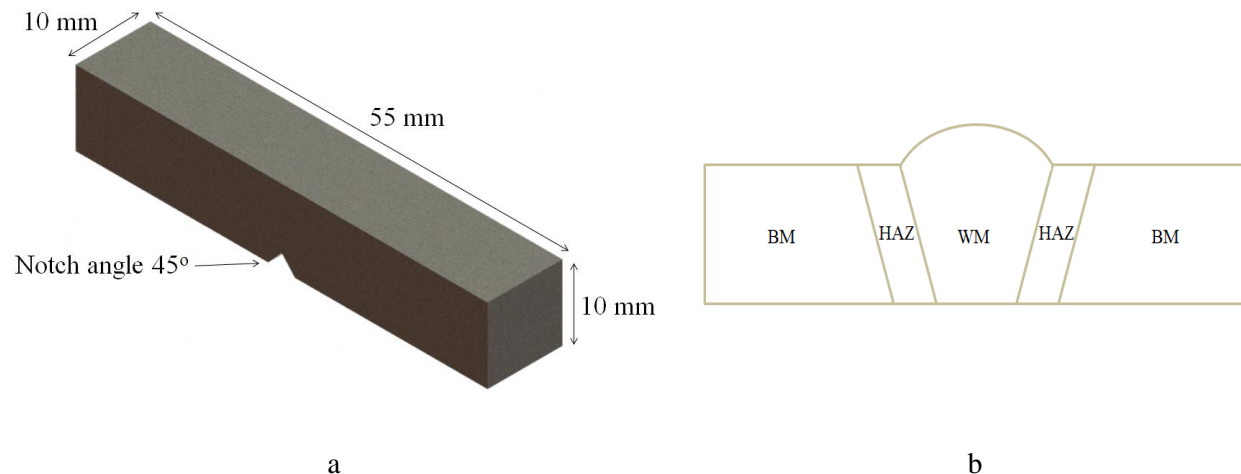


Figure 5. 4 Specimen and dimensions used for CVN and various locations.

A Zwick Roell machine was used to carry out the CVN using Charpy Impact Testing Machine (See **Figure 5. 5-b**).

Noting that before performing the impact test, the specimens must be cooled using a cooler (**Figure 5. 5-a**)

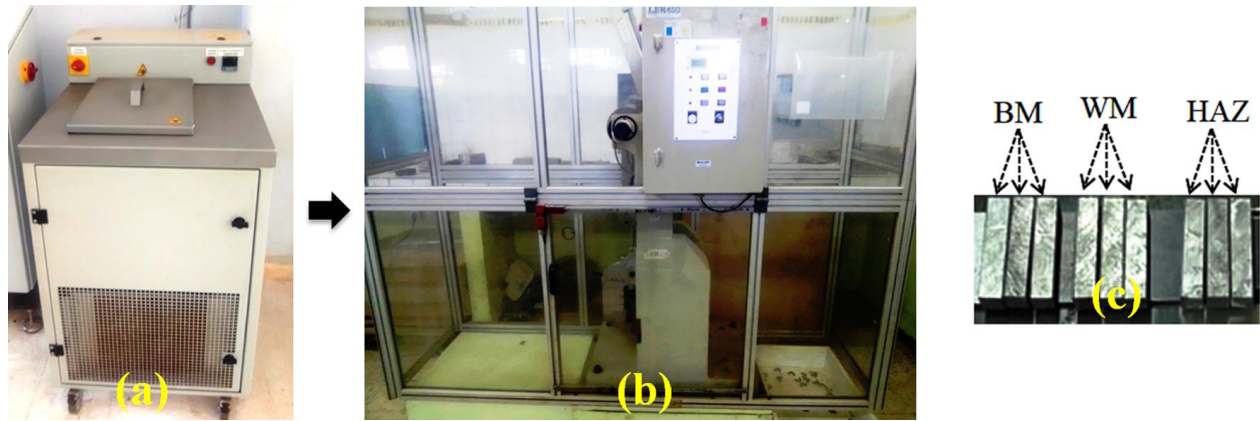


Figure 5. 5 Specimen used for CVN and the impact machine for steel X70.

5.3.4 Experimental results

5.3.4.1 DWTT impact

The obtained results on the base metal with a notch are formed for two tests and illustrated in Figure 5. 6 in the temperature range of 20 °C and -10 °C.

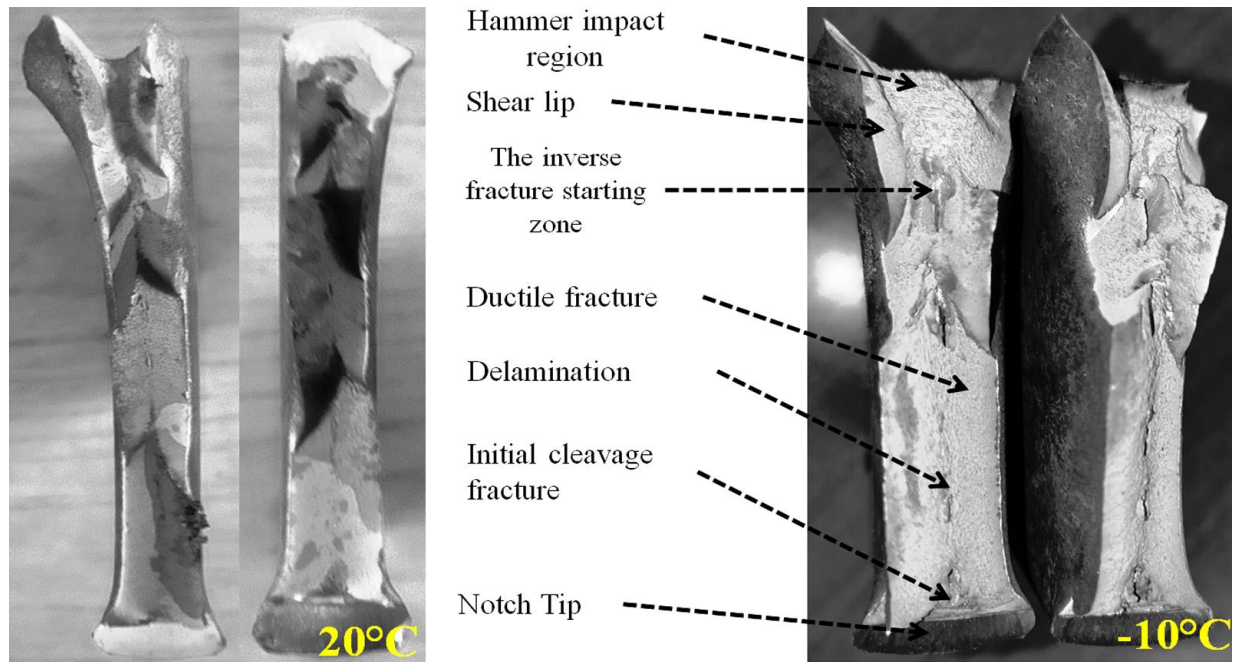


Figure 5. 6 The obtained results on the base metal with DWTT.

The initial fracture mode looked at the notch tip is ductile on all specimens of API X70 tested in the temperature range of 20 °C and -10 °C, as illustrated in **Figure 5. 6** for an API X70 pipeline steel specimen. At -10 °C, a very few of separations started to show on the ductile fractured area. These fracture appearances are indicative of the inverse fracture, indicated by a line on the photos in **Figure 5. 6**. At -10 °C, the impact side away from the initial bending neutral axis had a minor density and this is where the inverse fracture started. For each energy term and various energy components, the following figure is presented (see **Figure 5. 7**).

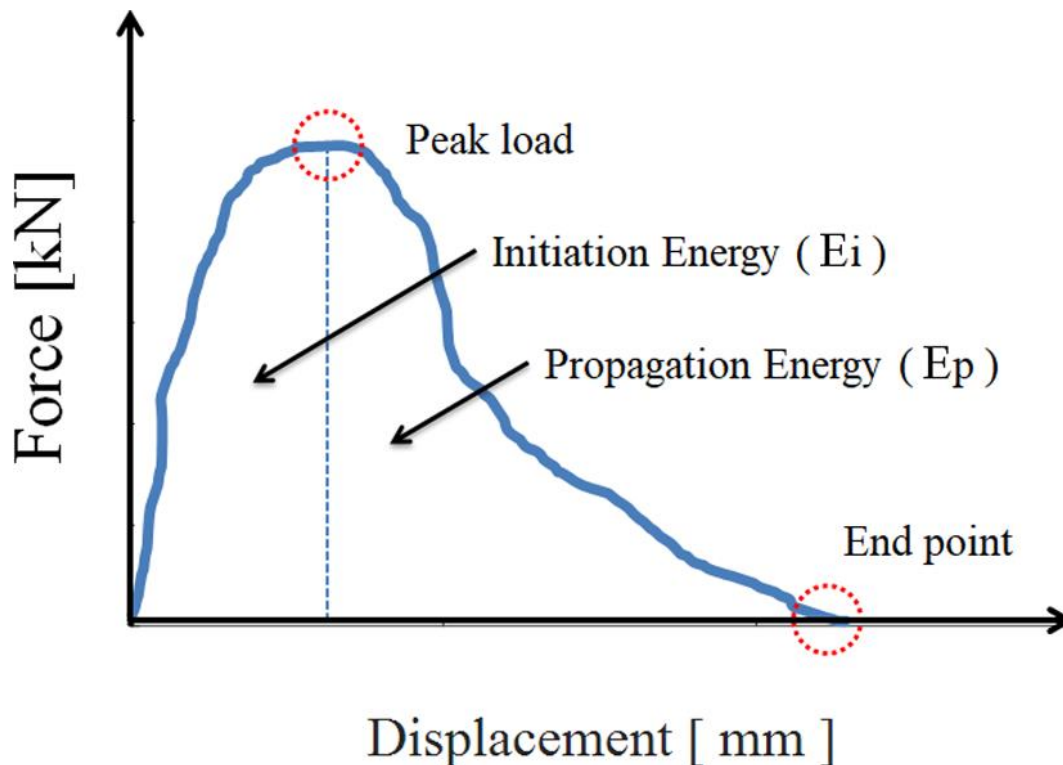


Figure 5. 7 Contribution of different energy components, such as (E_i) initiation energy and (E_p) propagation energy.

5.3.4.2 CVN impact

The results obtained from the energy absorbed and the resilience for each type of specimen are presented respectively in **Table 5. 3, 4** and **5**. Noting that the resilience is obtained by dividing the energy absorbed by the section (S) of the specimen where ($S=0.8 \text{ cm}^2$).

A digital display is integrated into the resilience machine to display directly the energy absorbed and the angle of ascent. We made three types of specimens (see **Figure 5.5-c**):

- Notch created in the center of the base metal (specimen completely in base metal).

- Notch initiated in the center of the weld metal.
- Notch initiated at the HAZ.

Table 5. 3 Absorbed energy values for the different zones.

Absorbed energy (J)				
Test	1	2	3	Average
Base metal	210.2	203.3	213.2	208.9
HAZ	184.4	177.1	172.6	178.0
Weld metal	139.9	144.3	149.8	144.6

Table 5. 4 Resilience values for different zones

Resilience (J/cm ²)				
Test	1	3	3	Average
Base metal	262.8	254.1	266.5	261.1
ZAT	230.5	221.4	215.7	222.5
Weld metal	174.9	180.4	187.3	180.8

Table 5. 5 Absorbed energy values for the different temperatures.

		Absorbed energy (J/cm ²)			
		T (°C)	Test 1	Test 2	Test 3
Base metal (BM)	20	262.8	254.1	266.5	261.13
	0	248	242	238	242.67
	-10	216	210	210	212
	-20	206	205	203	204.67

Tables 5.3, 4 and 5 present the obtained results. Since their energies are lower than those of the material test specimens, it is reasonable to see that the test specimens with welding explain the impact of the welding. It is interesting to note that API 5L X70 steel is a ductile steel, which also justifies its choice for the manufacture of pipelines. In addition, it can also be seen that the ductility decreases approaching the weld bead because the HAZ is more ductile than the weld bead and less ductile than the base metal.

5.4 Simulation of CVN impact and determination of peak load and absorbed energy in different crack lengths

In this part, improved numerical CVN impact tests using XFEM are studied to obtain the approximation parameters at low temperature, and used in different cases of crack lengths simulation, to build a database after validation of the experimental model, which will be used for training different optimization techniques, in order to get the best prediction of peak force and absorbed energy as a function of different crack lengths.

5.4.1 Model dimensions and meshes

ABAQUS software was used to model the Charpy V-notch impact and its steps. The prototype is made up of three parts: a hammer, two anvils, and a CVN specimen that may be meshed on its own. **Figure 5.8** depict the model's FE mesh as well as a rendered view.

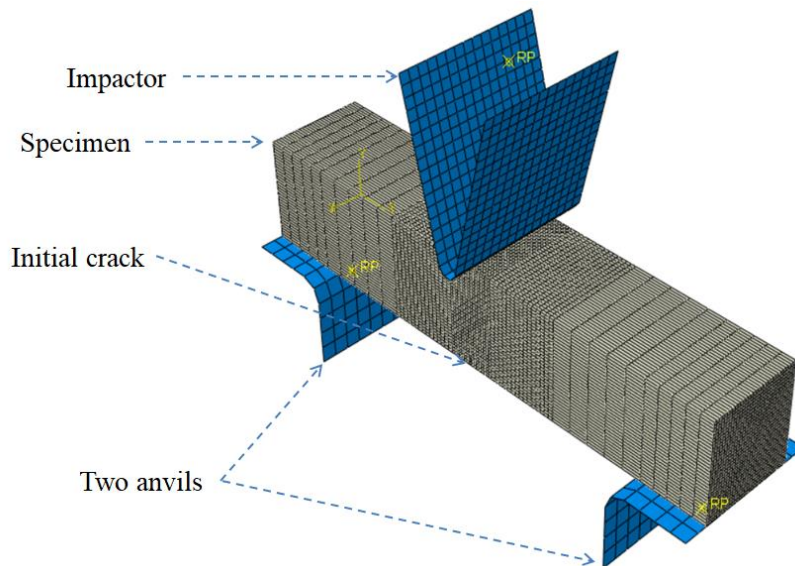


Figure 5.8 CVN specimen with an initial crack and 3D meshing with applied velocity.

The simulation setting was modeled using an 8-node linear brick with decreased integration and hourglass control (C3D8R). The anvils and hammer are represented by a fixed piece of rigid form. Between two stiff anvils and the impactor, the sample is placed at the probable locations of propagation of the fracture and a mesh size of 0.3 was used in the critical part which gradually improved in the center of the specimen.

Moreover, the mesh size was reduced to 0.3 mm in this part to perfectly capture the gradient of multiaxial stresses at the crack tip. Coulomb's law of friction with a coefficient of friction of 0.1 was used to explain the contact between the impactor and the sample, as well as between the sample and the anvils. The impactor and support surfaces were represented as slave surfaces, while the sample surface was represented as a master surface. The impactor was shown to be able to travel vertically while the supports remained constrained. The impactor had a mass of 19.8 kg and an initial speed of 5.5 m/s. Explicit codes are utilized to capture the complex reaction of the system as a function of time. The XFEM service is currently not supported by the ABAQUS Dynamic/Explicit solver. The Dynamic/Implicit solution was used to address this problem in this study.

5.4.2 Material parameters

To model the Charpy V-notch impact and its steps, an extrapolated flow curve at -196 C that was employed in finite element modeling (see **Figure 5. 9**).

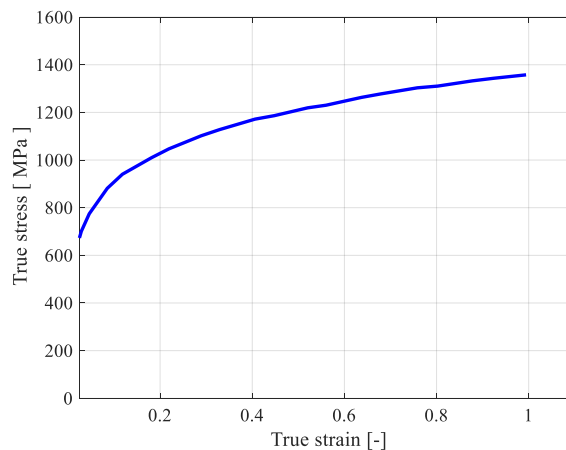


Figure 5. 9 The true stress–strain curve at -196 C for API X70 [30]

The cohesive energy is the sole characteristic that is affected by strain rate (fracture energy). The cohesive energy was calibrated using data from the impact test. As a result, the behavior of isotropically hardened elastoplastic materials has been described. The enrichment area was chosen within the damage propagation region of interest, which was the mesh refinement part.

Crack modeling replicates the cracking of the enriched zone in the solution field and its eventual defeat.

The first reaction is linear, while a fracture initiation criterion and a damage propagation law make up the defeat mechanism. On the cohesive stress of $T_{\max} = 1.4\sigma_y$, the damage initiation was modeled and established. According to Schider [8], the cohesive stress was determined by examining the crack process at the microscopic scale using the so-called unit cell technique. The stress triaxiality at the fracture tip changes as the impact load increases. In the unit cell technique, the highest value of the triaxiality of the stress at the crack tip was utilized to estimate the cohesive stress. The ultimate load capacity can be calculated using the unit cell technique during the crack initiation process under the stress of triaxiality. The cohesion energy was calculated using the following formula:

$$\Gamma = G_{IC} = \frac{K_{IC}^2}{E / (1 - \nu^2)} \quad (5.11)$$

Where G_{IC} : Fracture energy.

K_{IC} : Fracture toughness.

E : Young's modulus.

ν : Poisson's ratio.

The following equation can be derived using Barsom and Rolfe's [10] connection between CVN energy (KCV) and fracture toughness for the descending shelf of the DBTT curve:

$$K_{IC} = 6.76(KCV)^{3/4} \quad (5.12)$$

The fracture toughness values $25 \text{ MPa}\sqrt{\text{m}}$ were chosen in this study by entering them into XFEM in the fracture energies for Mode I and Mode II, respectively in the mixed-mode [184].

5.4.3 Results and discussion

The example of distribution in the model during crack propagation (initial crack length equal to 2 mm) using the XFEM method is shown in **Figure 5. 10**.

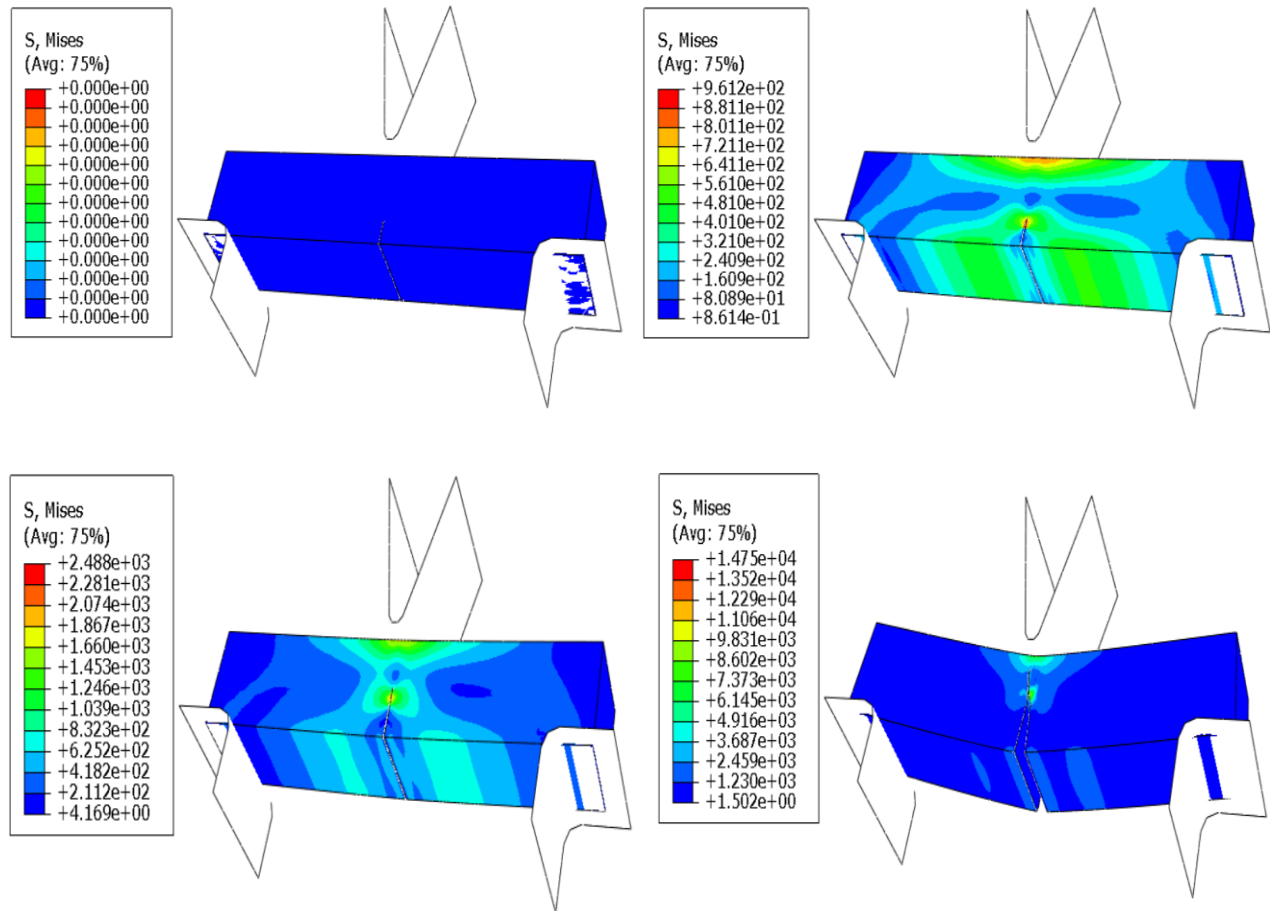


Figure 5. 10 Von Mises distribution in model during crack initiation and propagation.

The parameters of the XFEM method for API X70 were chosen based on a comparison of the numerical and experimental results (see **Figure 5. 11.a**), taking into account the impact of the type and number of mesh elements used in this investigation. It's important to note that the figure depicts the maximum contact point (peak load 'Point (P)') as the crack starting onset as shown in **Figure 5. 11.b**. The first crack length (a_0) was considered to be equal to the depth of the initial artificial notch $a=2\text{mm}$.

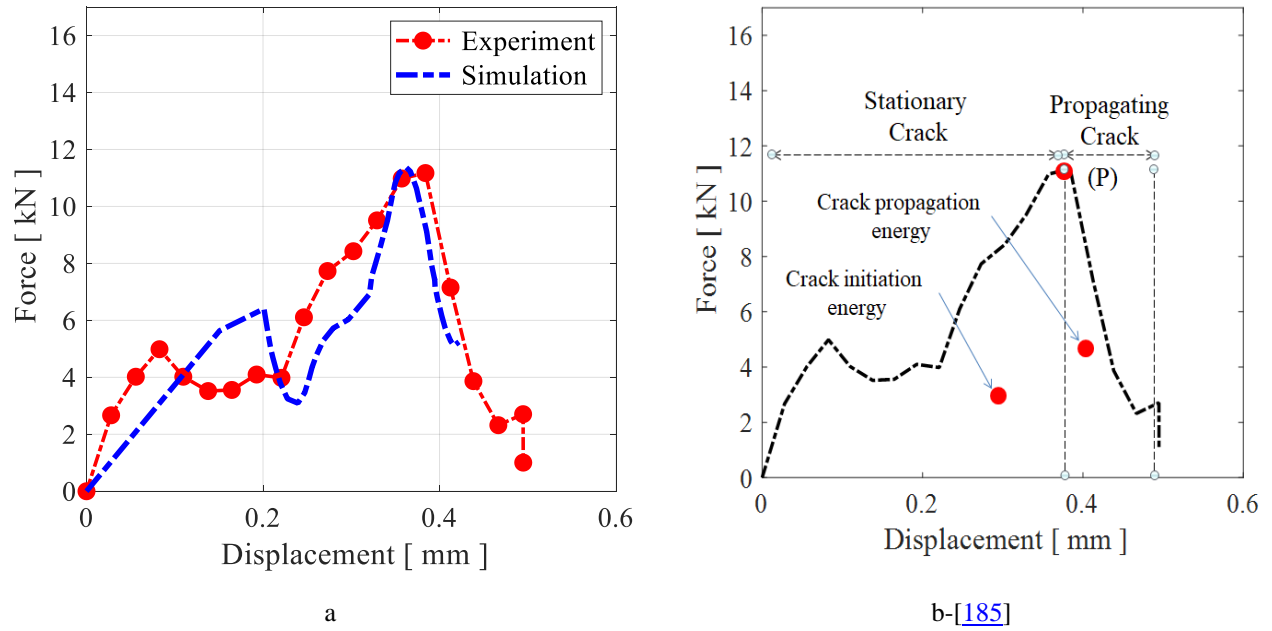


Figure 5. 11 a- shows the CVN test simulation result compared to experimental observation; b- shows the maximal contact point (peak load) as the crack starting onset.

Increasing the crack length in the structures will cause their resistance to decrease and they will not be able to resist more loading, in our case, the increase in crack length in the samples will decrease the thickness of the samples and higher stress intensity will be generated at the crack tip, resulting will be getting a decrease in the peak load and energy absorbed, the obtained results are used to simulate more states of the initial crack length of API X70 pipeline steel samples at low temperature through a numerical approach based cohesive segment in extended Finite Element Method (XFEM).

5.5 Optimization technique

5.5.1 Initialization part (Balancing composite motion optimization (BCMO))

According to the following equation, the population distribution is uniformly initialized in the solution space during the first generation.

$$X_i = X_i^l + rand(1, d) * (X_i^U - X_i^L) \tag{5.13}$$

where *rand* is a *d*-dimensional vector that satisfies a uniform distribution in the interval [0, 1], X_i^L and X_i^U are the lower and upper limits of the *i*th individual, respectively.

5.5.2 Identifying the optimal individual and the current global point

According to the equation below, the i^{th} individual's absolute movement in each generation can be a two-component composite consisting of a relative motion to the j^{th} individual's superior ranking and a transportation motion of the j^{th} individual to the global optimization point o :

$$v_i = v_{i/j} + v_j \quad (5.14)$$

where v_i and v_j represent, respectively, the i^{th} and j^{th} individual's movement vectors with respect to o . The relative movement vector is shown as $v_{i/j}$.

Next, a point about instant global optimization o_{in} The actual global optimization point o is replaced with o_{in} . Simply define, $X_{o_{in}}^t = X_1^{t-1}$ assigns o_{in} . Additionally, updated o_{in} should be defined using the prior best of X_1^{t-1} and trial individual u_1^t using the objective function.

$$X_{o_{in}}^t = \begin{cases} u_1^t & \text{If } f(u_1^t) < f(X_1^{t-1}) \\ X_1^{t-1} & \text{otherwise} \end{cases} \quad (5.15)$$

where u_1^t is determined using the following population data for the current generation:

$$u_1^t = u_c + v_{k_1/k_2}^t + v_{k_2/1}^t \quad u_c = \frac{LB+UB}{2} \quad (5.16)$$

where the center of upper and lower design space is indicated by the symbol u_c

- Composite motion of individuals in solution space.

The movement of the global search v_j in BCMO is determined by:

$$v_j = \alpha_j (X_{o_{in}} - X_j) \quad (5.17)$$

where α_j denotes for the first order derivative, which may be calculated using the formula shown below:

$$\alpha_j = L_{GS} * dv_j; L_{GS} = \begin{cases} e^{-\frac{1j}{dNP}r_j^2} & \text{If } TV_j > 0.5 \\ e^{-\frac{1}{d}(1-\frac{j}{NP})r_j^2} & \text{otherwise} \end{cases} \quad (5.18)$$

where TV_j is the trial number, L_{GS} is the global size scaling of the movement, and dv_j is a direction vector.

Three optimization algorithms are used to improve ANN parameters, the actual peak load and energy absorbed with various crack lengths will be predicted in this section. The Artificial Neural Network (ANN) is a computer technique focused on biological nervous systems, and the first one implements an upgraded Artificial Neural Network using BCMO. Analysis, administrative procedures, detection, and picture identifying are only a few of the areas and industrial applications where ANN can be applied. ANN exercise parameters (bias and weight) may be improved by lowering the discrepancy between actual and desired products, and these parameters could then be used to create the network using BCMO. As a resolution, the BCMO algorithm examines all values of the training parameters (weight and bias). We used BCMO with Particle Swarm Optimization (PSO) and Jaya algorithms. In this investigation, the parameters utilized in this work were held constant in different optimization codes to estimate peak load and absorbed energy at peak force.

An input zone, a hidden zone, and an output zone are the three main components of an ANN network. Where w_{ij} is the weight of an input neuron's association with another neuron in the hidden folds, b_j is the bias. More explanation and detail in this paper Refs [140, 186-188].

5.5.4 Results and discussion

Where the crack length is input in training, the peak force and absorbed energy in the steel as considered as outputs (the target set), see **Table 5.6**.

Table 5. 6 Inputs and outputs parameters used in this study.

Parameter	Minimum	Maximum	Number of collected data
Output			
Peak load (N)	5737.248	12199.330	31.000
Absorbed energy (mJ)	1392.290	3370.590	31.000
Input			
Crack lengths (mm)	0.156	9.531	31.000

PSO, BCMO and Jaya algorithms are employed using crack lengths as inputs to change the weights and biases of ANN to investigate the utility of different optimization strategies. The number of hidden layer sizes (hidden neurons) is calculated using two of our outputs peak load and absorbed energy to determine the appropriate number (see **Figure 5. 12**). All of the proposed optimization approaches employ the same parameters: 200 populations and 200 iterations. The PC used for the analysis has an Intel(R) Core (TM) i7-6700HQ CPU running at 2.60GHz and a RAM memory of 16 GB. The consequences are illustrated in **Figures 5. 13 and 14**.

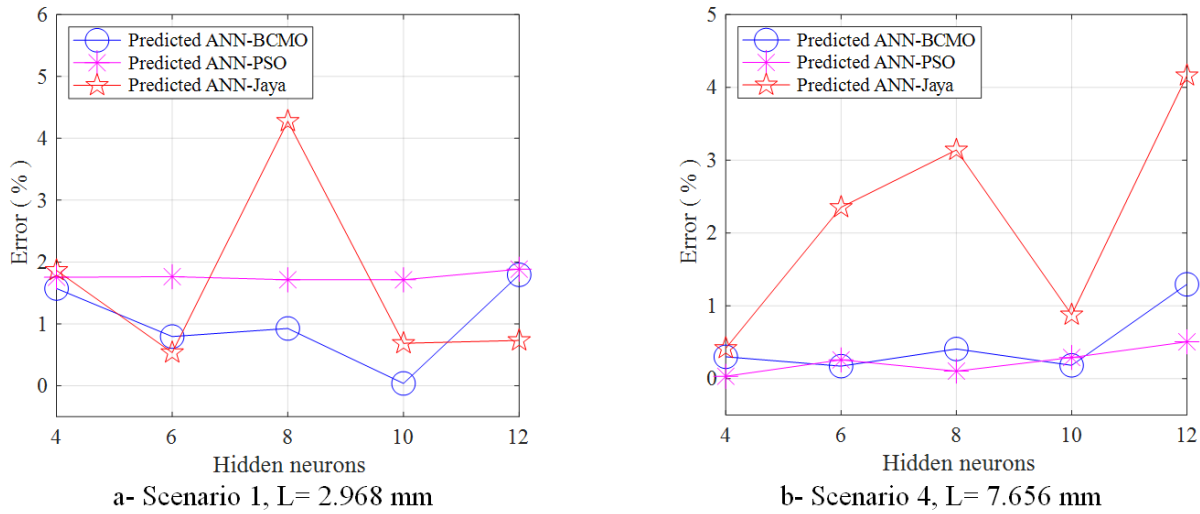


Figure 5. 13 Different neurons with different scenarios load.

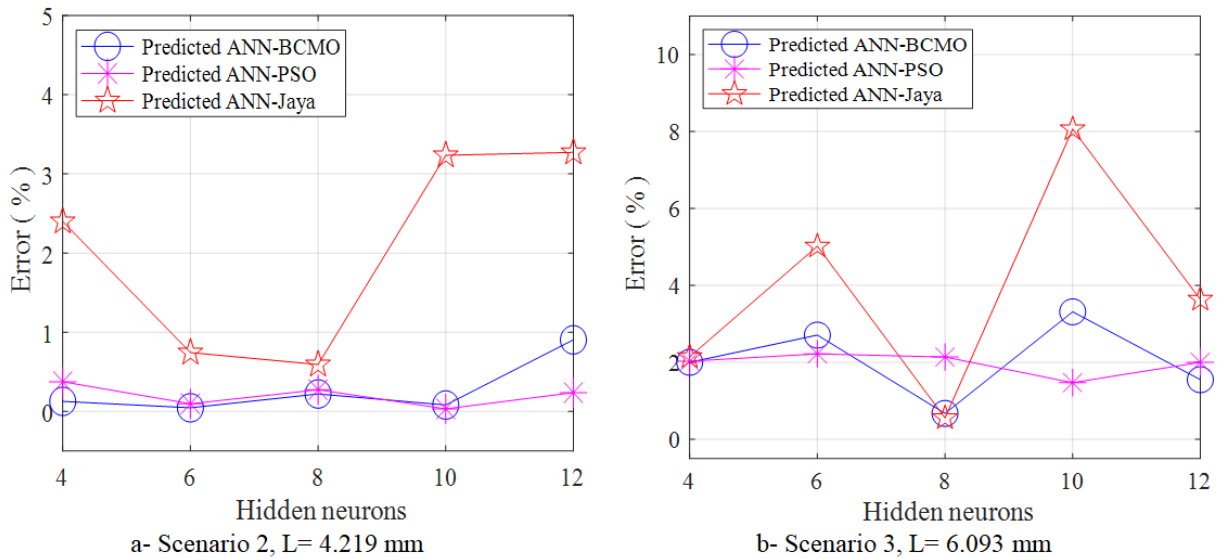


Figure 5. 14 Different hidden neurons with different scenarios energy.

The research indicates that the most effective network, which took into account ANN-BCMO, ANN-PSO, and ANN-Jaya, has ten hidden neurons employing various outputs depending on the fitting analysis. In order to determine the precise peak load and energy absorbed, four scenarios with crack lengths of 2.968 mm, 4.531 mm, 6.093 mm, 28 mm, and 7.656 mm are taken into consideration.

The regression analysis of different optimization codes in this study is shown in **Figures 5. 15 and 16.**

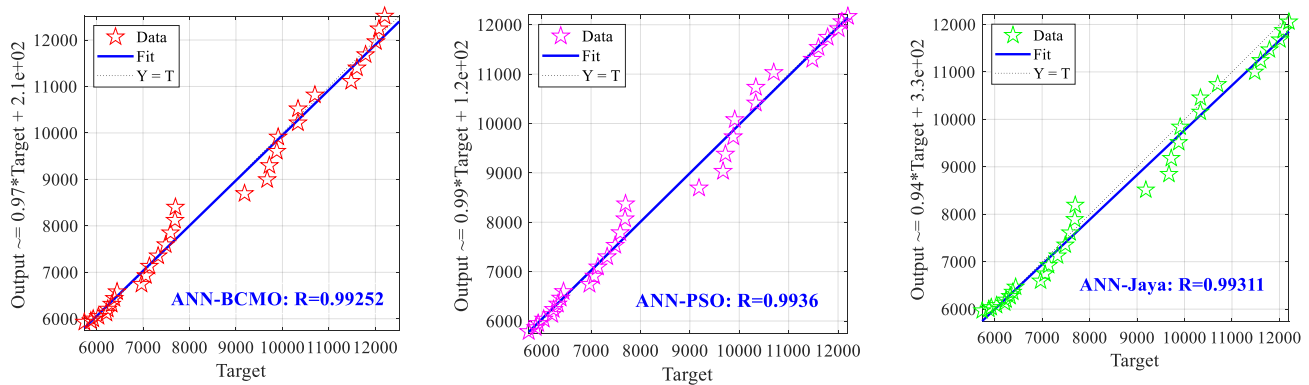


Figure 5. 15 Regression analysis for peak load data (Hidden neuron=10).

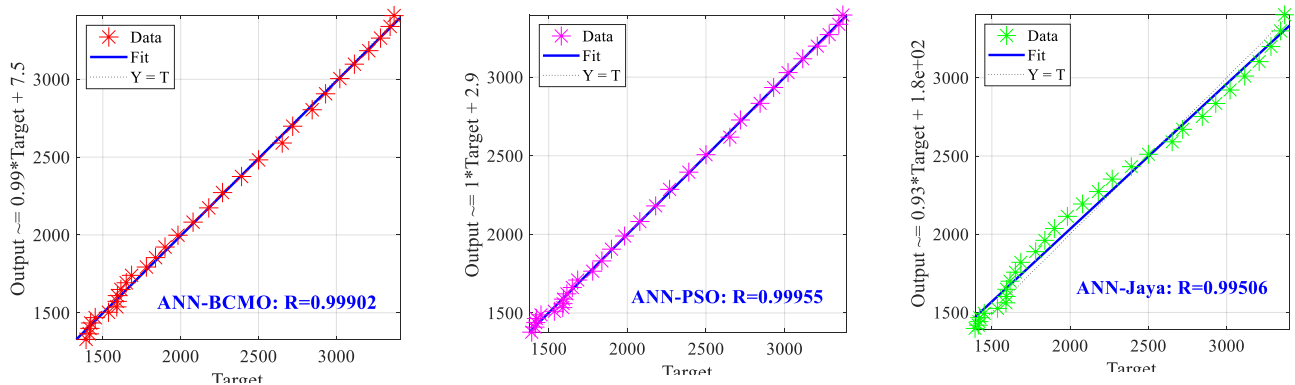


Figure 5. 16 Regression analysis for absorbed energy data (Hidden neuron=10)

After the training performance, the comparisons between the peak load and absorbed energy actual and predicted by PSO, BCMO and Jaya algorithm for all cases and all scenarios are represented in **Figures 5. 17, 18 and Table 5.7.**

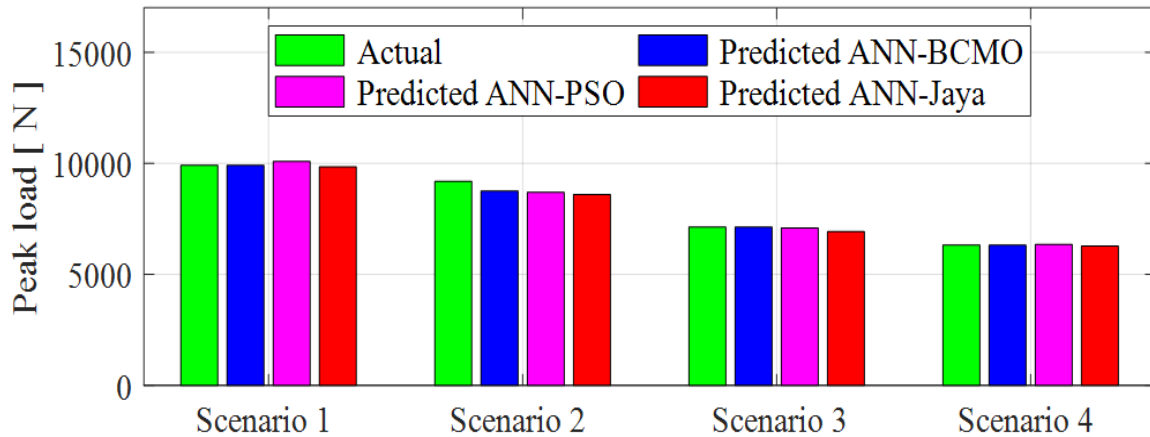


Figure 5. 17 Predicted peak load using 31 collected databases (Scenario 1'L= 2.968mm'; Scenario 2'L= 4.531mm'; Scenario 3'L= 6.093 mm'; Scenario 4'L= 7.656 mm').

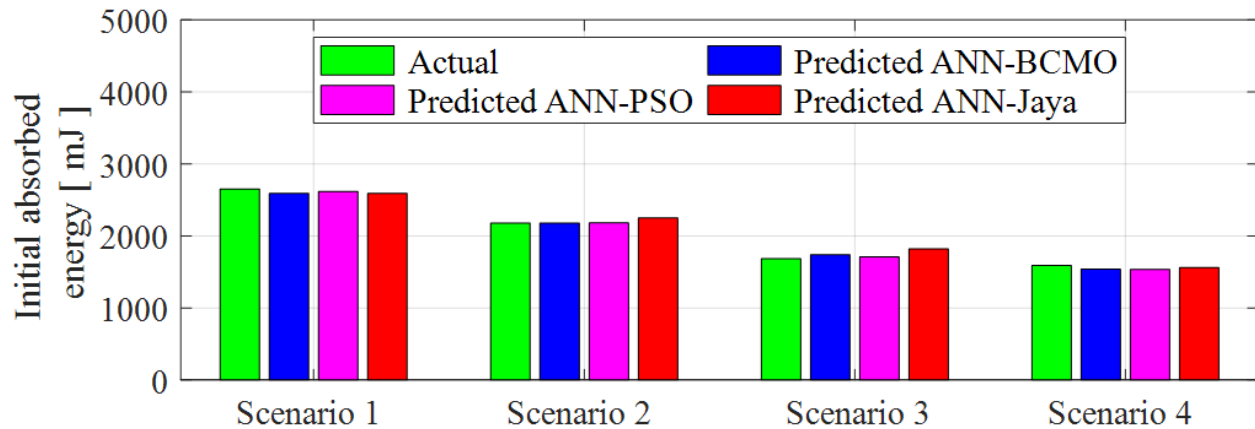


Figure 5. 18 Predicted absorbed energy using 31 collected databases (Scenario 1'L= 2.968mm'; Scenario 2'L= 4.531mm'; Scenario 3'L= 6.093 mm'; Scenario 4'L= 7.656 mm').

Based on the results, PSO can provide the effectiveness results compared to the actual peak load and absorbed energy while utilizing various crack length inputs. The errors between exact and estimated peak load and absorbed energy for four scenarios utilizing various optimization approaches are illustrated in **Figures 5. 19** and **20** for a more reasonable evaluation. With varying situations load, different hidden layer sizes (hidden neurons) are used.

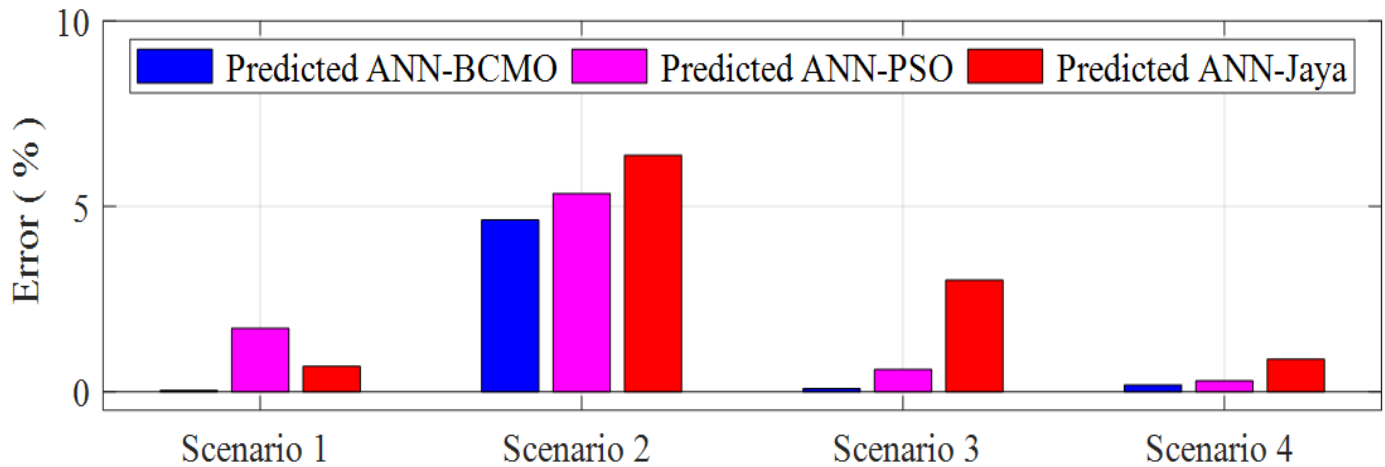


Figure 5. 19 Error percentage of peak load using 31 collected databases (Scenario 1'L= 2.968mm'; Scenario 2'L= 4.531mm'; Scenario 3'L= 6.093 mm'; Scenario 4'L= 7.656 mm').

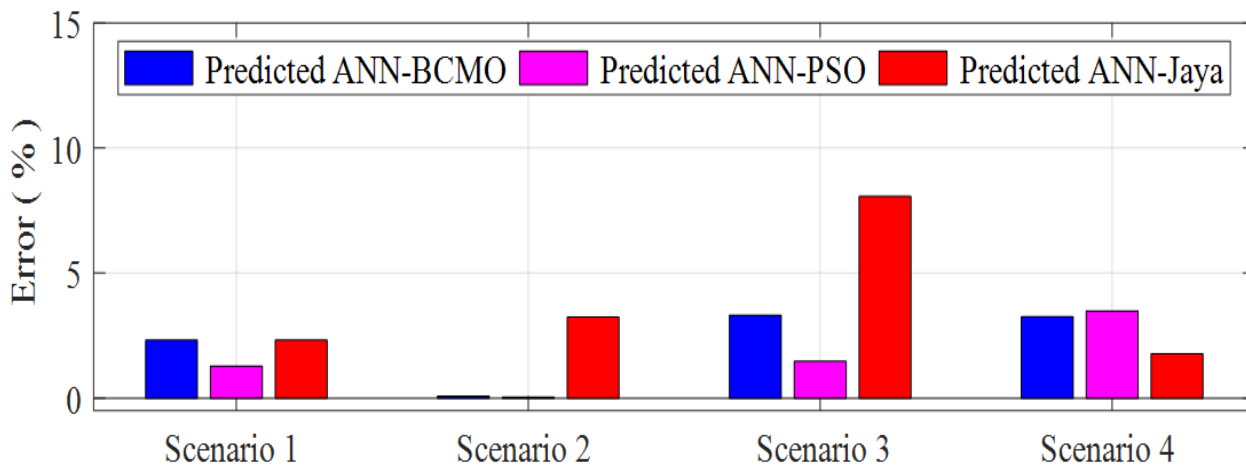


Figure 5. 20 Error percentage of absorbed energy using 31 collected databases (Scenario 1'L= 2.968mm'; Scenario 2'L= 4.531mm'; Scenario 3'L= 6.093 mm'; Scenario 4'L= 7.656 mm').

Tables 5.7 and 5.8. Summarized the results of crack lengths inputs compared with actual peak load and absorbed energy, including the difference in error values between the actual and estimated results. The CPU time for each proposed scenario are computed and presented in Table 5.8.

Table 5. 7 Error percentages of predicted PSO, BCMO and Jaya algorithm for each peak load scenario.

Scenarios	Hidden neurons	H=4	Error (%)	H=6	Error (%)	H=8	Error (%)	H=10	Error (%)	H=12	Error (%)
L=2.9688 mm P=9908.338 N	BCMO	10064.000	1.571	9987.000	0.794	10000.000	0.925	9911.900	0.036	10086.000	1.793
	PSO	10082.000	1.753	10083.000	1.763	10078.000	1.712	10078.000	1.712	10095.000	1.884
	JAYA	10093.000	1.864	9961.300	0.535	10332.000	4.276	9840.500	0.685	9835.900	0.731
L=4.5313 mm P=7697.8 N	BCMO	8391.600	9.013	8443.700	9.690	8449.500	9.765	8402.700	9.157	8447.200	9.735
	PSO	8391.300	9.009	8382.300	8.892	8400.200	9.125	8371.500	8.752	8390.000	8.992
	JAYA	8606.900	11.810	8479.100	10.150	8569.700	11.327	8194.200	6.449	8380.800	8.873
L=6.0938 mm P=7137.262 N	BCMO	7085.700	0.722	7164.300	0.379	7154.000	0.235	7131.300	0.084	7066.200	0.996
	PSO	7083.200	0.757	7076.700	0.849	7076.900	0.846	7094.200	0.603	7059.500	1.090
	JAYA	7278.500	1.979	7248.600	1.560	7105.100	0.451	6922.400	3.010	7290.400	2.146
L=7.6563 mm P=6325.385 N	BCMO	6344.300	0.299	6314.600	0.171	6299.700	0.406	6313.900	0.182	6243.500	1.295
	PSO	6323.400	0.031	6341.600	0.256	6318.900	0.103	6343.700	0.290	6357.300	0.505
	JAYA	6299.100	0.416	6474.200	2.353	6126.800	3.139	6270.000	0.876	6588.600	4.161

Table 5. 8 Error percentages of predicted PSO, BCMO and Jaya algorithm for each absorbed energy scenario.

Scenarios	Hidden neurons	H=4	Error (%)	H=6	Error (%)	H=8	Error (%)	H=10	Error (%)	H=12	Error (%)
L=2.9688 mm E=2652.09 mJ	BCMO	2608.500	1.644	2606.600	1.715	2605.300	1.764	2590.600	2.319	2621.200	1.165
	PSO	2616.600	1.338	2610.000	1.587	2613.000	1.474	2618.200	1.278	2611.600	1.527
	JAYA	2585.200	2.522	2715.800	2.402	2519.900	4.984	2590.600	2.319	2663.300	0.423
L=4.5313 mm E=2079.43 mJ	BCMO	2089.200	0.470	2102.700	1.119	2062.900	0.795	2082.300	0.138	2093.000	0.653
	PSO	2074.700	0.227	2087.500	0.388	2078.300	0.054	2081.600	0.104	2078.800	0.030
	JAYA	2059.200	0.973	2185.500	5.101	1995.500	4.036	2193.300	5.476	2054.300	1.209
L=6.0938 mm E=1684.66 mJ	BCMO	1718.400	2.003	1730.300	2.709	1696.000	0.673	1740.500	3.315	1710.800	1.552
	PSO	1718.900	2.032	1722.100	2.222	1720.700	2.139	1709.500	1.474	1718.400	2.003
	JAYA	1720.800	2.145	1769.200	5.018	1675.300	0.556	1820.500	8.063	1623.400	3.636
L=7.6563 mm E=1589.57 mJ	BCMO	1519.100	4.433	1517.700	4.521	1517.000	4.565	1537.900	3.251	1492.700	6.094
	PSO	1531.700	3.641	1518.700	4.458	1527.800	3.886	1534.200	3.483	1531.200	3.672
	JAYA	1521.100	4.307	1523.000	4.188	1501.800	5.522	1561.400	1.772	1402.100	11.794

*Notation: L= Crack length (mm); P= Peak load (N); E= Absorbed energy (mJ).

The results show how smoothly the optimization strategies, particularly when absorbed energy data is applied, performed. First, a critical finding was drawn from the ANN-Jaya results employing a variety of output scenarios.

Table 5. 8 CPU time of ANN-PSO. ANN-BCMO. and ANN-Jaya algorithm.

		Best CPU time				
Peak load output	BCMO	271.990064	273.217883	317.297330	291.338334	298.854786
	PSO	296.361061	301.474612	414.808215	292.326594	342.148799
	JAYA	405.826414	346.794978	305.384011	276.172631	288.996327
Energy absorbed	BCMO	291.692811	291.125877	304.623502	308.377327	437.229567
	PSO	333.740750	292.598183	309.506450	302.132373	471.979203
	JAYA	454.014712	357.087412	286.427631	288.263229	415.414165

The computational time can be taken in different optimisation techniques between 270-475 seconds.

5.6 Conclusion

The impact test was used in this experiment to examine the dynamic fracture properties of API X70 pipeline steel. To investigate the resistance of materials subjected to impact loading conditions, the CVN tests were conducted at various temperatures. The validity of numerical and experimental tests is examined in CVN impact specimens. Different crack lengths are expected to generate a database after the model has been validated, it is reasonable to suppose that the test specimens with welding explain the impact of the welding because their energies are lower than those of the material test specimens. It's interesting to note that API 5L X70 steel is ductile steel, which also supports the decision to use it for pipeline construction. Because the HAZ is more ductile than the weld bead and less ductile than the base metal, it can also be seen that the ductility diminishes as it approaches the weld joint. This article presents an experimental part of fracture mechanics for API X70 steel, as well as a study of convergence between different optimization algorithm codes (BCMO, PSO and Jaya) to predict the maximum load and initial energy absorbed in a base metal sample at a lower temperature represented by the brittle state.

To design a hybrid ANN using optimization techniques to predict peak load and absorbed energy using various parameters, a thorough analysis was conducted (Hidden layer neurons, bias, and weight). The results of this investigation have led to the following conclusions:

- Using diverse hidden layer neurons, a detailed inquiry was conducted for the construction of hybrid ANNs with optimization approaches to estimate peak load and absorbed energy.
- Current optimization techniques are used with the same crack lengths in the inputs are compared using PSO, BCMO and Jaya algorithm.

- An artificial neural network with ten neurons in the hidden layer neurons is the most optimal network in global optimization approaches in this collected database.
- Jaya algorithm has critical results with different types of outputs (peak load and absorbed energy) with less population and generation (200-200).
- The best results found by PSO and BCMO compared to Jaya algorithm and particularly in the case of data represented by absorbed energy.

General conclusion

The goal of the current work, as stated at the outset, was to create a numerical model that relates to the three-dimensional analysis of stress concentration in a perforated plate under tension and the impact of different types of defects on the mechanical behavior of a plate under strain. In the first section, we described an experimental characterization of the API 5L X70 steel that the ALFAPIPE GHARDAIA company uses to make pipelines. We also looked at the effects of a circular hole and a crack in straight specimens that were subjected to tensile loading on the development of the mechanical properties of steel.

In order to deal with the issue of a plate having a lateral form defect and corroborate Griffith's hypothesis, we also used the ABAQUS calculation software, in its version 6.16, which represents one of the numerical tools based on the finite element approach. We were able to draw the following conclusions thanks to the results:

- The weld bead used to weld pipelines has resistance to higher fracture and microhardness than base metal and lower resilience than HAZ and base metal.
- The API 5L X70 steel used for the manufacture of pipelines has properties particular meeting the conditions of choice for such a use because of its high elastic limit, good ductility, and widely acceptable microhardness.
- Massive holes increase the degree of stress factors.

This action demonstrates unequivocally that the existence of holes in a plate is a location of stress concentration that can cause the onset and spread of fractures.

- This concentration rises sharply and gets weaker and weaker as the hole gets bigger. As a result, rounded holes are less hazardous than sharp ones. The radius of the semicircular defect has a significant impact on both the stress intensity factor K_I and the energy restitution rate G_I .

The K_I and G_I factors, on the other hand, barely change with the angle of opening for the notch type defect, and we may even argue that they are nearly constant. The 88 values of the K_I and G_I factors for a lateral fracture depend on the size of the crack and might be high compared to other types of faults.

- When compared to other types of faults, lateral semi-circular faults produce the least amount of stresses.
- Cracks are the flaws that most affect the stress field, which is highly dependent on the size of the crack.

We have included a definition, a broad overview, and the key phases of design and production for pipeline technology, additionally to welding flaws and steel characteristics.

The chemical and mechanical characterisation of API 5L X70 steel was covered in the chapter that followed. Welding's influence on the latter's mechanical behavior will also be covered.

Based on the analysis of the mechanical properties and the modal analysis of the structure represented in the specific case of the pipes, we produced a bibliographical analysis and synthesis of the methods of crack identification. These comprised... (eg: WOA, AOA, PSO, Jaya...etc). Therefore, a variety of factors are utilized to identify cracks; however, for the remainder of our

work, we will pay particular attention to the mechanical parameters (stress, deformation, and displacement) based on the enhancement of the ANN utilizing various optimization techniques.

In order to forecast the parameters of the GTN damage model and the constants of the Ramberg-Osgood hardening law for API X70 steel pipelines, an artificial neural network model was created. The following conclusions can be made from the obtained data:

- Despite the large number of parameters and simulations, the strategy used in this work enabled their determination using a reverse identification technique with a low error rate and good accuracy.
- The identification can be expanded to cover a significant number of experimental tests from the prior results acquired at the ALFAPIPE Ghardaia laboratory because there is a minimum difference between the numerical results in the case of coupled identification.
- Then, using the detected GTN parameters, an ANN model is created to forecast the two key parameters of the GTN damage model, and paired with the hardening law.
- Because it directly affects the mechanical properties of this steel, the developed model incorporates API X70's basic metal chemical composition as an input.
- The tensile test and the Charpy test numerical models both used the ANNGTN's results as input. The comparison of the computational load-displacement curve with the experimental findings that followed produced positive results.
- Due to the strong compatibility of the experimental and numerical studies, it can be claimed that the ANN has been employed successfully to facilitate the prediction of GTN parameters and mechanical properties of steel.
- The proposed model has a remarkable ability to forecast outcomes prior to performing mechanical testing, and it can also be used to simulate variations in mechanical properties based on the chemical composition of steel.

In order to estimate the starting and maximum loads as well as to examine the GTN damage parameters at various temperatures for dynamic fracture propagation in X70 steel pipeline, an Artificial Neural Network model was created in this study. The following conclusions can be made from the data obtained:

- Data and experimental tests are needed for the calibration of some parameters, and as a result, the calibration's outcome depends on the latter, which fluctuates depending on the test conditions. In order to improve findings and reduce the number of simulations, we use modulation of neural

networks in this study to try to anticipate and assess the effects of a number of GTN parameters on the initial and maximum load as well as in a temperature range in the Charpy impact test.

- Based on the findings, we can conclude that each GTN model parameter affects the results in a different percentage, which enables the calibration phase to take the parameter sensitivity into account.

- The damage model is used in several studies and investigations, but the GTN parameter values used to calibrate the models are not constant and identical. As a result, our study investigates the sensitivity of the initial and maximum loads in the impact test to changes in the parameter values of the GTN model and throughout a finite temperature range.

- The created model has a strong ability to forecast results prior to calibration and identifies variance between various parameters by simulating them in accordance with the mechanical properties of X70 Steel.

To build a hybrid ANN using optimization techniques to forecast fracture length using various parameters, a thorough analysis was conducted (Hidden layer neurons, bias, and weight). To describe the efficacy of the proposed method, recent optimization techniques are employed to enhance ANN for better prediction when compared to other methodologies. The WOA-ANN, GA-ANN, AOA-ANN, and WOA-BAT-ANN algorithms are used to compare various inputs, including strains, stresses, and displacements. The validity of numerical and experimental tests is examined for both uncracked and cracked specimens. Different crack lengths are expected to generate a database after the model has been validated. The results of this investigation have led to the following conclusions:

1- Among all optimization strategies, an artificial neural network with eight neurons in the hidden layer is the most ideal network.

2- GA-ANN has a significant outcome with fewer generation and population (100-100).

3- The most efficient CPU time as determined by WOA and AOA when compared to GA and WOA-BAT

We can cite the following points based on the work's findings:

- The GTN model parameters' simulation produces good results that enable making the necessary adjustments with accurate calibration against the experimental models.
- The findings of experimental tensile testing show that the presence of notches in pipelines under pressure directly influences the elastic limit and the ultimate stress, but that this influence grows quickly as the notch depth is increased relative to the pipe thickness.

- The presence of notches is a place where stress localization occurs, and understanding the impact of their presence and depth is crucial. By using experimental and numerical data to build an ANN model, we were able to predict the elastic and maximum stress as a function of the depth in our study.
- The output of our ANN model provides very good results in the prediction of notch depth in some defective pipelines, enables assistance in making the appropriate choice in the notch situation, and aids in optimizing the appropriate geometry of composite patch in some necessary instances.

In this experiment, the dynamic fracture characteristics of API X70 pipeline steel were investigated using the impact test. The CVN tests were carried out at various temperatures in order to examine the resistance of materials subjected to impact loading conditions. In CVN impact specimens, the reliability of numerical and experimental tests is investigated. After the model has been validated, it is anticipated that different fracture lengths will provide a database. It is logical to assume that test specimens with welding explain the influence of the welding because their energies are lower than those of the material test specimens.

The fact that API 5L X70 steel is ductile steel is significant and supports the choice of the substance for pipeline building. Because the HAZ is more ductile than the weld bead and less ductile than the base metal, it is also evident that ductility diminishes as it approaches the weld joint. This article presents an experimental component of fracture mechanics for API X70 steel as well as a study of convergence between various optimization algorithm codes in order to forecast the maximum load and initial energy absorbed in a base metal sample at a lower temperature indicative of the brittle state (BCMO, PSO, and Jaya).

A thorough investigation was done in order to create a hybrid ANN that uses optimization approaches to forecast peak load and absorbed energy using different parameters (Hidden layer neurons, bias, and weight). The investigation's findings have produced the following conclusions

- A thorough investigation was undertaken for the building of hybrid ANNs with optimization methods to estimate peak load and absorbed energy using a variety of hidden layer neurons. PSO, BCMO, and the Jaya algorithm are used to compare current optimization strategies with inputs that have the same crack lengths.
- In this gathered database, the most advantageous artificial neural network is one with 10 hidden layer neurons, according to global optimization methods.
- The Jaya algorithm produces important outcomes with various outputs (peak load and absorbed energy) and low population and generation (200-200).
- PSO and BCMO discovered the best outcomes when compared to the Jaya algorithm, especially when it came to data represented by absorbed energy.

References

1. Gillich, G.-R., et al., *A robust damage detection method based on multi-modal analysis in variable temperature conditions*. Mechanical Systems and Signal Processing, 2019. **115**: p. 361-379 DOI: <https://doi.org/10.1016/j.ymssp.2018.05.037>.
2. Khatir, S., et al. *Crack Identification Using eXtended IsoGeometric Analysis and Particle Swarm Optimization*. in *Proceedings of the 7th International Conference on Fracture Fatigue and Wear*. 2019. Singapore: Springer Singapore.
3. Rezaiee-Pajand, M., A. Karimipour, and J.M.N. Abad, *Crack Spacing Prediction of Fibre-Reinforced Concrete Beams with Lap-Spliced Bars by Machine Learning Models*. Iranian Journal of Science and Technology, Transactions of Civil Engineering, 2021. **45**(2): p. 833-850 DOI: 10.1007/s40996-020-00441-6.
4. Ding, Z., J. Li, and H. Hao, *Structural damage identification using improved Jaya algorithm based on sparse regularization and Bayesian inference*. Mechanical Systems and Signal Processing, 2019. **132**: p. 211-231 DOI: <https://doi.org/10.1016/j.ymssp.2019.06.029>.
5. Gomes, G.F., et al., *Optimized damage identification in CFRP plates by reduced mode shapes and GA-ANN methods*. Engineering Structures, 2019. **181**: p. 111-123 DOI: <https://doi.org/10.1016/j.engstruct.2018.11.081>.
6. Benaissa, B., et al., *YUKI Algorithm and POD-RBF for Elastostatic and dynamic crack identification*. Journal of Computational Science, 2021. **55**: p. 101451 DOI: <https://doi.org/10.1016/j.jocs.2021.101451>.
7. Tran-Ngoc, H., et al., *Efficient Artificial neural networks based on a hybrid metaheuristic optimization algorithm for damage detection in laminated composite structures*. Composite Structures, 2021. **262**: p. 113339 DOI: <https://doi.org/10.1016/j.compstruct.2020.113339>.
8. Banharsakun, A., *Hybrid ABC-ANN for pavement surface distress detection and classification*. International Journal of Machine Learning and Cybernetics, 2017. **8**(2): p. 699-710 DOI: 10.1007/s13042-015-0471-1.
9. Gomes, G.F., et al., *A Review of Vibration Based Inverse Methods for Damage Detection and Identification in Mechanical Structures Using Optimization Algorithms and ANN*. Archives of Computational Methods in Engineering, 2019. **26**(4): p. 883-897 DOI: 10.1007/s11831-018-9273-4.
10. Zenzen, R., et al., *A modified transmissibility indicator and Artificial Neural Network for damage identification and quantification in laminated composite structures*. Composite Structures, 2020. **248**: p. 112497 DOI: <https://doi.org/10.1016/j.compstruct.2020.112497>.
11. Tran-Ngoc, H., et al., *An efficient artificial neural network for damage detection in bridges and beam-like structures by improving training parameters using cuckoo search algorithm*. Engineering Structures, 2019. **199**: p. 109637 DOI: <https://doi.org/10.1016/j.engstruct.2019.109637>.
12. Moës, N., J. Dolbow, and T. Belytschko, *A finite element method for crack growth without remeshing*. International Journal for Numerical Methods in Engineering, 1999. **46**(1): p. 131-150 DOI: [https://doi.org/10.1002/\(SICI\)1097-0207\(19990910\)46:1<131::AID-NME726>3.0.CO;2-J](https://doi.org/10.1002/(SICI)1097-0207(19990910)46:1<131::AID-NME726>3.0.CO;2-J).
13. Belytschko, T. and T. Black, *Elastic crack growth in finite elements with minimal remeshing*. International Journal for Numerical Methods in Engineering, 1999. **45**(5): p. 601-620 DOI: [https://doi.org/10.1002/\(SICI\)1097-0207\(19990620\)45:5<601::AID-NME598>3.0.CO;2-S](https://doi.org/10.1002/(SICI)1097-0207(19990620)45:5<601::AID-NME598>3.0.CO;2-S).

14. Sukumar, N., et al., *Modeling holes and inclusions by level sets in the extended finite-element method*. Computer Methods in Applied Mechanics and Engineering, 2001. **190**(46): p. 6183-6200 DOI: [https://doi.org/10.1016/S0045-7825\(01\)00215-8](https://doi.org/10.1016/S0045-7825(01)00215-8).
15. Holland, J.H., *Adaptation in natural and artificial systems: an introductory analysis with applications to biology, control, and artificial intelligence*. 1992: MIT press.
16. Waisman, H. and T. Belytschko, *Parametric enrichment adaptivity by the extended finite element method*. International Journal for Numerical Methods in Engineering, 2008. **73**(12): p. 1671-1692 DOI: <https://doi.org/10.1002/nme.2137>.
17. Bhardwaj, G., et al., *Numerical simulations of cracked plate using XIGA under different loads and boundary conditions*. Mechanics of Advanced Materials and Structures, 2016. **23**(6): p. 704-714 DOI: 10.1080/15376494.2015.1029159.
18. Nguyen-Thanh, N., et al., *An extended isogeometric thin shell analysis based on Kirchhoff–Love theory*. Computer Methods in Applied Mechanics and Engineering, 2015. **284**: p. 265-291 DOI: <https://doi.org/10.1016/j.cma.2014.08.025>.
19. Habib, S.H., et al., *Numerical Simulation of cracked orthotropic materials using extended isogeometric analysis*. Journal of Physics: Conference Series, 2017. **842**: p. 012061 DOI: 10.1088/1742-6596/842/1/012061.
20. Caddemi, S. and A. Morassi, *Crack detection in elastic beams by static measurements*. International Journal of Solids and Structures, 2007. **44**(16): p. 5301-5315 DOI: <https://doi.org/10.1016/j.ijsolstr.2006.12.033>.
21. Chatzi, E.N., et al., *Experimental application and enhancement of the XFEM–GA algorithm for the detection of flaws in structures*. Computers & Structures, 2011. **89**(7): p. 556-570 DOI: <https://doi.org/10.1016/j.compstruc.2010.12.014>.
22. Waisman, H., E. Chatzi, and A.W. Smyth, *Detection and quantification of flaws in structures by the extended finite element method and genetic algorithms*. International Journal for Numerical Methods in Engineering, 2010. **82**(3): p. 303-328 DOI: <https://doi.org/10.1002/nme.2766>.
23. Sun, H., H. Waisman, and R. Betti, *Nondestructive identification of multiple flaws using XFEM and a topologically adapting artificial bee colony algorithm*. International Journal for Numerical Methods in Engineering, 2013. **95**(10): p. 871-900 DOI: <https://doi.org/10.1002/nme.4529>.
24. Qin, S., et al., *Model Updating in Complex Bridge Structures using Kriging Model Ensemble with Genetic Algorithm*. KSCE Journal of Civil Engineering, 2018. **22**(9): p. 3567-3578 DOI: 10.1007/s12205-017-1107-7.
25. Rytter, A., *Vibrational based inspection of civil engineering structures*. 1993.
26. Shi, Z.Y., S.S. Law, and L.M. Zhang, *Structural Damage Detection from Modal Strain Energy Change*. Journal of Engineering Mechanics, 2000. **126**(12): p. 1216-1223 DOI: 10.1061/(ASCE)0733-9399(2000)126:12(1216).
27. Tiachacht, S., et al., *Damage assessment in structures using combination of a modified Cornwell indicator and genetic algorithm*. Engineering Structures, 2018. **177**: p. 421-430 DOI: <https://doi.org/10.1016/j.engstruct.2018.09.070>.
28. Yan, W.-J., T.-L. Huang, and W.-X. Ren, *Damage Detection Method Based on Element Modal Strain Energy Sensitivity*. Advances in Structural Engineering, 2010. **13**(6): p. 1075-1088 DOI: 10.1260/1369-4332.13.6.1075.
29. Yan, W.-J. and W.-X. Ren, *Closed-form modal flexibility sensitivity and its application to structural damage detection without modal truncation error*. Journal of Vibration and Control, 2013. **20**(12): p. 1816-1830 DOI: 10.1177/1077546313476724.
30. Pandey, A.K. and M. Biswas, *Damage Detection in Structures Using Changes in Flexibility*. Journal of Sound and Vibration, 1994. **169**(1): p. 3-17 DOI: <https://doi.org/10.1006/jsvi.1994.1002>.

31. Hwang, H.Y. and C. Kim, *Damage detection in structures using a few frequency response measurements*. Journal of Sound and Vibration, 2004. **270**(1): p. 1-14 DOI: [https://doi.org/10.1016/S0022-460X\(03\)00190-1](https://doi.org/10.1016/S0022-460X(03)00190-1).
32. Sinou, J.-J., *A review of damage detection and health monitoring of mechanical systems from changes in the measurement of linear and non-linear vibrations*. Mechanical vibrations: measurement, effects and control, 2009: p. 643-702.
33. Kim, J.T. and N. Stubbs, *CRACK DETECTION IN BEAM-TYPE STRUCTURES USING FREQUENCY DATA*. Journal of Sound and Vibration, 2003. **259**(1): p. 145-160 DOI: <https://doi.org/10.1006/jsvi.2002.5132>.
34. Xiang, J., M. Liang, and Y. He, *Experimental investigation of frequency-based multi-damage detection for beams using support vector regression*. Engineering Fracture Mechanics, 2014. **131**: p. 257-268 DOI: <https://doi.org/10.1016/j.engfracmech.2014.08.001>.
35. Stutz, L.T., et al., *Structural damage identification built on a response surface model and the flexibility matrix*. Journal of Sound and Vibration, 2018. **434**: p. 284-297 DOI: <https://doi.org/10.1016/j.jsv.2018.02.063>.
36. Khatir, S., et al., *Delamination detection in laminated composite using Virtual crack closure technique (VCCT) and modal flexibility based on dynamic analysis*. Journal of Physics: Conference Series, 2017. **842**: p. 012084 DOI: 10.1088/1742-6596/842/1/012084.
37. Dincal, S. and N. Stubbs, *Damage evaluation of Timoshenko beams using invariant stress resultants*. Engineering Structures, 2013. **56**: p. 2052-2064 DOI: <https://doi.org/10.1016/j.engstruct.2013.08.022>.
38. Jassim, Z.A., et al., *A review on the vibration analysis for a damage occurrence of a cantilever beam*. Engineering Failure Analysis, 2013. **31**: p. 442-461 DOI: <https://doi.org/10.1016/j.engfailanal.2013.02.016>.
39. Dahak, M., N. Touat, and N. Benseddiq, *On the classification of normalized natural frequencies for damage detection in cantilever beam*. Journal of Sound and Vibration, 2017. **402**: p. 70-84 DOI: <https://doi.org/10.1016/j.jsv.2017.05.007>.
40. Zenzen, R., et al. *Structural Health Monitoring of Beam-Like and Truss Structures Using Frequency Response and Particle Swarm Optimization*. in *Proceedings of the 1st International Conference on Numerical Modelling in Engineering*. 2019. Singapore: Springer Singapore.
41. Klippel, H., et al., *Johnson Cook Flow Stress Parameter for Free Cutting Steel 50SiB8*. arXiv preprint arXiv:2007.14087, 2020.
42. Madhusudhan, D., et al. *Modeling and simulation of Charpy impact test of maraging steel 300 using Abaqus*. in *IOP Conf. Ser. Mater. Sci. Eng.* 2018.
43. Nazari, A., *Simulation Charpy impact energy of functionally graded steels by modified stress-strain curve through mechanism-based strain gradient plasticity theory*. Computational materials science, 2012. **51**(1): p. 225-232.
44. Senthil, K., et al., *Experimental and numerical studies on mild steel plates against 7.62 API projectiles*. Procedia Engineering, 2017. **173**: p. 369-374.
45. Zhang, X.L., et al. *Study on the dynamic behaviors of X70 pipeline steel by numerical simulation*. in *Advanced Materials Research*. 2010. Trans Tech Publ.
46. Tvergaard, V. and A. Needleman, *Analysis of the cup-cone fracture in a round tensile bar*. Acta metallurgica, 1984. **32**(1): p. 157-169.
47. Gurson, A.L., *Continuum theory of ductile rupture by void nucleation and growth: Part I—Yield criteria and flow rules for porous ductile media*. 1977.
48. Tvergaard, V., *Influence of voids on shear band instabilities under plane strain conditions*. International Journal of fracture, 1981. **17**(4): p. 389-407.

49. Tvergaard, V., *On localization in ductile materials containing spherical voids*. International Journal of fracture, 1982. **18**(4): p. 237-252.
50. Hancock, J. and A. Mackenzie, *On the mechanisms of ductile failure in high-strength steels subjected to multi-axial stress-states*. Journal of the Mechanics and Physics of Solids, 1976. **24**(2-3): p. 147-160.
51. Seo, E.J., et al., *Microstructure-mechanical properties relationships for quenching and partitioning (Q&P) processed steel*. Acta Materialia, 2016. **113**: p. 124-139 DOI: <https://doi.org/10.1016/j.actamat.2016.04.048>.
52. Sharma, L. and R. Chhibber, *Microstructure evolution and electrochemical corrosion behaviour of API X70 linepipe steel in different environments*. International Journal of Pressure Vessels and Piping, 2019. **171**: p. 51-59 DOI: <https://doi.org/10.1016/j.ijpvp.2019.01.013>.
53. Lu, J., et al., *Strengthening Mechanisms and Their Relative Contributions to the Yield Strength of Microalloyed Steels*. Metallurgical and Materials Transactions A, 2012. **43**(9): p. 3043-3061 DOI: 10.1007/s11661-012-1135-3.
54. Saoudi, A., et al., *Assessment and statistical correlation of mechanical properties of double sided single pass submerged arc welded line pipe steel*. Engineering Science and Technology, an International Journal, 2020. **23**(2): p. 452-461 DOI: <https://doi.org/10.1016/j.jestch.2019.06.006>.
55. Bandyopadhyay, P.S., et al., *Structure and Properties of a Low-Carbon, Microalloyed, Ultra-High-Strength Steel*. Metallurgical and Materials Transactions A, 2011. **42**(4): p. 1051-1061 DOI: 10.1007/s11661-010-0523-9.
56. Bose-Filho, W.W., A.L.M. Carvalho, and M. Strangwood, *Effects of alloying elements on the microstructure and inclusion formation in HSLA multipass welds*. Materials Characterization, 2007. **58**(1): p. 29-39 DOI: <https://doi.org/10.1016/j.matchar.2006.03.004>.
57. Zou, Y., et al., *Austenite stability and its effect on the toughness of a high strength ultra-low carbon medium manganese steel plate*. Materials Science and Engineering: A, 2016. **675**: p. 153-163 DOI: <https://doi.org/10.1016/j.msea.2016.07.104>.
58. Show, B.K., et al., *Effect of vanadium and titanium modification on the microstructure and mechanical properties of a microalloyed HSLA steel*. Materials Science and Engineering: A, 2010. **527**(6): p. 1595-1604 DOI: <https://doi.org/10.1016/j.msea.2009.10.049>.
59. Gong, P., E.J. Palmiere, and W.M. Rainforth, *Dissolution and precipitation behaviour in steels microalloyed with niobium during thermomechanical processing*. Acta Materialia, 2015. **97**: p. 392-403 DOI: <https://doi.org/10.1016/j.actamat.2015.06.057>.
60. Mohebbi, M.S., et al., *The impact of Nb on dynamic microstructure evolution of an Nb-Ti microalloyed steel*. Materials Science and Engineering: A, 2018. **723**: p. 194-203 DOI: <https://doi.org/10.1016/j.msea.2018.03.054>.
61. Wang, C., et al., *Transmission electron microscopy of martensite/austenite islands in pipeline steel X70*. Materials Science and Engineering: A, 2006. **438-440**: p. 267-271 DOI: <https://doi.org/10.1016/j.msea.2006.02.118>.
62. Mitchell, E.B., et al., *Microstructure and Thickness Effects on Impact Behavior and Separation Formation in X70 Pipeline Steel*. JOM, 2021. **73**(6): p. 1966-1977 DOI: 10.1007/s11837-021-04562-9.
63. Simha, C.H.M., S. Xu, and W.R. Tyson, *Computational modeling of the drop-weight tear test: A comparison of two failure modeling approaches*. Engineering Fracture Mechanics, 2015. **148**: p. 304-323 DOI: <https://doi.org/10.1016/j.engfracmech.2015.06.085>.
64. Skalny, P., *Evaluation and Identifying the Ductile Fracture Area of X70 Steel from DWTT Broken Specimens*. Procedia Structural Integrity, 2016. **2**: p. 3727-3734 DOI: <https://doi.org/10.1016/j.prostr.2016.06.463>.

65. Mortazavi, E., R.A. Najafabadi, and A. Meysami, *Effect of heat input on microstructure and mechanical properties of dissimilar joints of AISI 316L steel and API X70 high-strength low-alloy steel*. Journal of Iron and Steel Research International, 2017. **24**(12): p. 1248-1253 DOI: 10.1016/S1006-706X(18)30024-4.
66. Cao, Y., et al., *Determination of Johnson–Cook parameters and evaluation of Charpy impact test performance for X80 pipeline steel*. International Journal of Mechanical Sciences, 2020. **179**: p. 105627 DOI: <https://doi.org/10.1016/j.ijmecsci.2020.105627>.
67. Madhusudhan, D., et al., *Modeling and simulation of Charpy impact test of maraging steel 300 using Abaqus*. IOP Conference Series: Materials Science and Engineering, 2018. **330**: p. 012013 DOI: 10.1088/1757-899x/330/1/012013.
68. Jang, Y.-Y., et al., *Evaluations of Ductile and Cleavage Fracture Using Coupled GTN and Beremin Model in API X70 Pipelines Steel*. 2019.
69. Yoon, S.H., et al., *Development of GTN Model Parameters for Simulating Ductile Fracture Behavior of X 70 Carbon Steel SENT Specimens*. 2019.
70. Ouladbrahim, A., et al., *Prediction of Gurson Damage Model Parameters Coupled with Hardening Law Identification of Steel X70 Pipeline Using Neural Network*. Metals and Materials International, 2021 DOI: 10.1007/s12540-021-01024-4.
71. Xie, F., et al., *Stress corrosion cracking behavior induced by Sulfate-reducing bacteria and cathodic protection on X80 pipeline steel*. Construction and Building Materials, 2021. **308**: p. 125093 DOI: <https://doi.org/10.1016/j.conbuildmat.2021.125093>.
72. Cabrini, M., et al., *Environmentally assisted cracking and hydrogen diffusion in traditional and high-strength pipeline steels*. Corrosion Reviews, 2015. **33**(6): p. 529-545 DOI: doi:10.1515/corrrev-2015-0051.
73. Bott, I.d.S., et al., *High-strength steel development for pipelines: A brazilian perspective*. Metallurgical and Materials Transactions A, 2005. **36**(2): p. 443-454 DOI: 10.1007/s11661-005-0315-9.
74. Sha, Q. and D. Li. *Microstructure and Properties of Low Manganese API X70 Pipeline Steel for Sour Service Application*. in *Proceedings of the 8th Pacific Rim International Congress on Advanced Materials and Processing*. 2016. Cham: Springer International Publishing.
75. Shi, X., et al., *Novel Cu-bearing high-strength pipeline steels with excellent resistance to hydrogen-induced cracking*. Materials & Design, 2016. **92**: p. 300-305 DOI: <https://doi.org/10.1016/j.matdes.2015.12.029>.
76. Mohtadi-Bonab, M.A., J.A. Szpunar, and S.S. Razavi-Tousi, *Hydrogen induced cracking susceptibility in different layers of a hot rolled X70 pipeline steel*. International Journal of Hydrogen Energy, 2013. **38**(31): p. 13831-13841 DOI: <https://doi.org/10.1016/j.ijhydene.2013.08.046>.
77. Contreras, A., et al., *Slow strain rate corrosion and fracture characteristics of X-52 and X-70 pipeline steels*. Materials Science and Engineering: A, 2005. **407**(1): p. 45-52 DOI: <https://doi.org/10.1016/j.msea.2005.07.028>.
78. Han, S.Y., et al., *Effects of microstructure and yield ratio on strain hardening and Bauschinger effect in two API X80 linepipe steels*. Materials Science and Engineering: A, 2012. **551**: p. 192-199 DOI: <https://doi.org/10.1016/j.msea.2012.05.007>.
79. Zhong, Y., et al., *In situ TEM study of the effect of M/A films at grain boundaries on crack propagation in an ultra-fine acicular ferrite pipeline steel*. Acta Materialia, 2006. **54**(2): p. 435-443 DOI: <https://doi.org/10.1016/j.actamat.2005.09.015>.
80. Sun, W., et al., *Influence of Nb, V and Ti on peak strain of deformed austenite in Mo-based micro-alloyed steels*. Journal of Materials Processing Technology, 2002. **125-126**: p. 72-76 DOI: [https://doi.org/10.1016/S0924-0136\(02\)00287-X](https://doi.org/10.1016/S0924-0136(02)00287-X).

81. Capozucca, R. and E. Magagnini, *Experimental vibration response of homogeneous beam models damaged by notches and strengthened by CFRP lamina*. Composite Structures, 2018. **206**: p. 563-577 DOI: <https://doi.org/10.1016/j.compstruct.2018.08.082>.
82. Capozucca, R. and E. Magagnini, *RC beam models damaged and strengthened with GFRP strips under bending loading and free vibration*. Composite Structures, 2020. **253**: p. 112730 DOI: <https://doi.org/10.1016/j.compstruct.2020.112730>.
83. Nilsson, K.-F., N. Jakšić, and V. Vokál, *An elasto-plastic fracture mechanics based model for assessment of hydride embrittlement in zircaloy cladding tubes*. Journal of Nuclear Materials, 2010. **396**(1): p. 71-85 DOI: <https://doi.org/10.1016/j.jnucmat.2009.10.056>.
84. Broek, D., *Elementary engineering fracture mechanics*. 2012: Springer Science & Business Media.
85. Cruse, T.A., *Boundary element analysis in computational fracture mechanics*. Vol. 1. 2012: Springer Science & Business Media.
86. François, D., A. Pineau, and A. Zaoui, *Mechanical behaviour of materials: volume ii: fracture mechanics and damage*. Vol. 191. 2012: Springer Science & Business Media.
87. Hertzberg, R.W., R.P. Vinci, and J.L. Hertzberg, *Deformation and fracture mechanics of engineering materials*. 2020: John Wiley & Sons.
88. Antolovich, S.D., A. Saxena, and W.W. Gerberich, *Fracture mechanics – An interpretive technical history*. Mechanics Research Communications, 2018. **91**: p. 46-86 DOI: <https://doi.org/10.1016/j.mechrescom.2018.03.003>.
89. Noell, P.J., J.D. Carroll, and B.L. Boyce, *The mechanisms of ductile rupture*. Acta Materialia, 2018. **161**: p. 83-98 DOI: <https://doi.org/10.1016/j.actamat.2018.09.006>.
90. Fang, J., J.-w. Zhang, and X. Huang, *Industrial application of Instrumented DWTT in evaluating material resistance to ductile fracture for modern pipeline steels*. EPJ Web of Conferences, 2015. **94**.
91. Rudland, D.L., et al., *Characterizing dynamic fracture toughness of linepipe steels using the pressed-notch drop-weight-tear test specimen*. Engineering Fracture Mechanics, 2004. **71**(16): p. 2533-2549 DOI: <https://doi.org/10.1016/j.engfracmech.2003.12.007>.
92. Nakai, H., K. Shibamura, and S. Aihara, *Numerical model for unstable ductile crack propagation and arrest in pipelines using finite difference method*. Engineering Fracture Mechanics, 2016. **162**: p. 179-192 DOI: <https://doi.org/10.1016/j.engfracmech.2016.03.048>.
93. Jackiewicz, J., *Use of a modified Gurson model approach for the simulation of ductile fracture by growth and coalescence of microvoids under low, medium and high stress triaxiality loadings*. Engineering Fracture Mechanics, 2011. **78**(3): p. 487-502 DOI: <https://doi.org/10.1016/j.engfracmech.2010.03.027>.
94. Lian, Y.D., et al., *Application of GTN Model in Tensile Fracture of Pipeline Steel*. Key Engineering Materials, 2018. **777**: p. 451-456 DOI: 10.4028/www.scientific.net/KEM.777.451.
95. Gholipour, H., F.R. Biglari, and K. Nikbin, *Experimental and numerical investigation of ductile fracture using GTN damage model on in-situ tensile tests*. International Journal of Mechanical Sciences, 2019. **164**: p. 105170 DOI: <https://doi.org/10.1016/j.ijmecsci.2019.105170>.
96. Khalaj, G., M. Khoeini, and M. Khakian-Qomi, *ANN-based prediction of ferrite fraction in continuous cooling of microalloyed steels*. Neural Computing and Applications, 2013. **23**(3): p. 769-777 DOI: 10.1007/s00521-012-0992-4.
97. Özel, T. and Y. Karpuz, *Predictive modeling of surface roughness and tool wear in hard turning using regression and neural networks*. International Journal of Machine Tools and Manufacture, 2005. **45**(4): p. 467-479 DOI: <https://doi.org/10.1016/j.ijmachtools.2004.09.007>.
98. Brahme, A., M. Winning, and D. Raabe, *Prediction of cold rolling texture of steels using an Artificial Neural Network*. Computational Materials Science, 2009. **46**(4): p. 800-804 DOI: <https://doi.org/10.1016/j.commatsci.2009.04.014>.

99. Ouladbrahim, A., et al., *Sensitivity analysis of the GTN damage parameters at different temperature for dynamic fracture propagation in X70 pipeline steel using neural network*. Frattura ed Integrità Strutturale, 2021. **15**(58): p. 442-452 DOI: 10.3221/IGF-ESIS.58.32.
100. Zenzen, R., et al., *A modified transmissibility indicator and Artificial Neural Network for damage identification and quantification in laminated composite structures*. Composite Structures, 2020. **248**: p. 112497.
101. Khatir, S., et al., *An improved Artificial Neural Network using Arithmetic Optimization Algorithm for damage assessment in FGM composite plates*. Composite Structures, 2021. **273**: p. 114287.
102. Seguini, M., et al., *Crack prediction in pipeline using ANN-PSO based on numerical and experimental modal analysis*. Smart Struct. Syst, 2021. **27**: p. 507.
103. Khatir, S., et al., *An efficient hybrid TLBO-PSO-ANN for fast damage identification in steel beam structures using IGA*. Smart Structures and Systems, 2020. **25**(5): p. 605-617.
104. Mohtadi-Bonab, M.A. and H. Ghesmati-Kucheki, *Important Factors on the Failure of Pipeline Steels with Focus on Hydrogen Induced Cracks and Improvement of Their Resistance: Review Paper*. Metals and Materials International, 2019. **25**(5): p. 1109-1134 DOI: 10.1007/s12540-019-00266-7.
105. Jack, T.A., et al., *Investigation of the hydrogen induced cracking behaviour of API 5L X65 pipeline steel*. International Journal of Hydrogen Energy, 2020. **45**(35): p. 17671-17684 DOI: <https://doi.org/10.1016/j.ijhydene.2020.04.211>.
106. Shibanuma, K., et al., *Crack tip opening angle during unstable ductile crack propagation of a high-pressure gas pipeline*. Engineering Fracture Mechanics, 2018. **204**: p. 434-453 DOI: <https://doi.org/10.1016/j.engfracmech.2018.10.020>.
107. Okodi, A., et al., *Crack propagation and burst pressure of longitudinally cracked pipelines using extended finite element method*. International Journal of Pressure Vessels and Piping, 2020. **184**: p. 104115 DOI: <https://doi.org/10.1016/j.ijpvp.2020.104115>.
108. Mohtadi-Bonab, M.A., et al., *Microstructural aspects of intergranular and transgranular crack propagation in an API X65 steel pipeline related to fatigue failure*. Engineering Failure Analysis, 2018. **94**: p. 214-225 DOI: <https://doi.org/10.1016/j.engfailanal.2018.08.014>.
109. Ren, L., et al., *Pipeline corrosion and leakage monitoring based on the distributed optical fiber sensing technology*. Measurement, 2018. **122**: p. 57-65 DOI: <https://doi.org/10.1016/j.measurement.2018.03.018>.
110. Amaya-Gómez, R., et al., *Modeling of pipeline corrosion degradation mechanism with a Lévy Process based on ILI (In-Line) inspections*. International Journal of Pressure Vessels and Piping, 2019. **172**: p. 261-271 DOI: <https://doi.org/10.1016/j.ijpvp.2019.03.001>.
111. Xu, Y., et al., *Understanding the influences of pre-corrosion on the erosion-corrosion performance of pipeline steel*. Wear, 2020. **442-443**: p. 203151 DOI: <https://doi.org/10.1016/j.wear.2019.203151>.
112. Pippin, R. and A. Hohenwarter, *Fatigue crack closure: a review of the physical phenomena*. Fatigue & Fracture of Engineering Materials & Structures, 2017. **40**(4): p. 471-495 DOI: <https://doi.org/10.1111/ffe.12578>.
113. Bounouara, A., H. Hamadache, and A. Amirat, *Investigation on the effect of ball burnishing on fracture toughness in spiral API X70 pipeline steel*. The International Journal of Advanced Manufacturing Technology, 2018. **94**(9): p. 4543-4551 DOI: 10.1007/s00170-017-1181-5.
114. Seupel, A., G. Hütter, and M. Kuna, *On the identification and uniqueness of constitutive parameters for a non-local GTN-model*. Engineering Fracture Mechanics, 2020. **229**: p. 106817 DOI: <https://doi.org/10.1016/j.engfracmech.2019.106817>.

115. Chen, D., et al., *Efficient parameters identification of a modified GTN model of ductile fracture using machine learning*. Engineering Fracture Mechanics, 2021. **245**: p. 107535 DOI: <https://doi.org/10.1016/j.engfracmech.2021.107535>.
116. Li, G. and S. Cui, *Meso-mechanics and damage evolution of AA5182-O aluminum alloy sheet Based on the GTN model*. Engineering Fracture Mechanics, 2020. **235**: p. 107162 DOI: <https://doi.org/10.1016/j.engfracmech.2020.107162>.
117. Hashim, F.A., et al., *Archimedes optimization algorithm: a new metaheuristic algorithm for solving optimization problems*. Applied Intelligence, 2021. **51**(3): p. 1531-1551 DOI: 10.1007/s10489-020-01893-z.
118. Yin, Z., X. Bi, and C. Xu, *Ammonia-Oxidizing Archaea (AOA) Play with Ammonia-Oxidizing Bacteria (AOB) in Nitrogen Removal from Wastewater*. Archaea, 2018. **2018**: p. 8429145 DOI: 10.1155/2018/8429145.
119. Le-Thanh, L., et al., *Optimal design of an Origami-inspired kinetic façade by balancing composite motion optimization for improving daylight performance and energy efficiency*. Energy, 2021. **219**: p. 119557 DOI: <https://doi.org/10.1016/j.energy.2020.119557>.
120. Ouladbrahim, A., et al., *Experimental crack identification of API X70 steel pipeline using improved Artificial Neural Networks based on Whale Optimization Algorithm*. Mechanics of Materials, 2022. **166**: p. 104200 DOI: <https://doi.org/10.1016/j.mechmat.2021.104200>.
121. Abdel-Basset, M., L. Abdel-Fatah, and A.K. Sangaiah, *Chapter 10 - Metaheuristic Algorithms: A Comprehensive Review*, in *Computational Intelligence for Multimedia Big Data on the Cloud with Engineering Applications*, A.K. Sangaiah, M. Sheng, and Z. Zhang, Editors. 2018, Academic Press. p. 185-231.
122. Song, B., Z. Wang, and L. Zou, *An improved PSO algorithm for smooth path planning of mobile robots using continuous high-degree Bezier curve*. Applied Soft Computing, 2021. **100**: p. 106960 DOI: <https://doi.org/10.1016/j.asoc.2020.106960>.
123. Gholami, J., et al., *Powerful enhanced Jaya algorithm for efficiently optimizing numerical and engineering problems*. Soft Computing, 2022. **26**(11): p. 5315-5333 DOI: 10.1007/s00500-022-06909-z.
124. Zhang, Y., A. Chi, and S. Mirjalili, *Enhanced Jaya algorithm: A simple but efficient optimization method for constrained engineering design problems*. Knowledge-Based Systems, 2021. **233**: p. 107555 DOI: <https://doi.org/10.1016/j.knosys.2021.107555>.
125. Khatir, S. and M. Abdel Wahab, *A computational approach for crack identification in plate structures using XFEM, XIGA, PSO and Jaya algorithm*. Theoretical and Applied Fracture Mechanics, 2019. **103**: p. 102240 DOI: <https://doi.org/10.1016/j.tafmec.2019.102240>.
126. Khatir, S., et al., *Improved ANN technique combined with Jaya algorithm for crack identification in plates using XIGA and experimental analysis*. Theoretical and Applied Fracture Mechanics, 2020. **107**: p. 102554 DOI: <https://doi.org/10.1016/j.tafmec.2020.102554>.
127. Filin, V.Y. and A.V. Ilyin, *On the fracture mechanics based development of cleavage fracture resistance criteria for the materials of large-size welded structures*. Procedia Structural Integrity, 2019. **14**: p. 758-773 DOI: <https://doi.org/10.1016/j.prostr.2019.07.054>.
128. Hong, S., et al., *Effects of Specimen Thickness and Notch Shape on Fracture Modes in the Drop Weight Tear Test of API X70 and X80 Linepipe Steels*. Metallurgical and Materials Transactions A, 2011. **42**(9): p. 2619-2632 DOI: 10.1007/s11661-011-0697-9.
129. Kim, J.-S., et al., *Finite element simulation of drop-weight tear test of API X80 at ductile-brittle transition temperatures*. International Journal of Mechanical Sciences, 2021. **191**: p. 106103 DOI: <https://doi.org/10.1016/j.ijmecsci.2020.106103>.
130. Santos Pereira, L.d., R.F. Moço, and G.H. Bolognesi Donato, *Ductile fracture of advanced pipeline steels: study of stress states and energies in dynamic impact specimens - CVN and DWTT*.

- Procedia Structural Integrity, 2018. **13**: p. 1985-1992 DOI: <https://doi.org/10.1016/j.prostr.2018.12.219>.
131. Rao, R.V. and V. Patel, *An improved teaching-learning-based optimization algorithm for solving unconstrained optimization problems*. Scientia Iranica, 2013. **20**(3): p. 710-720 DOI: <https://doi.org/10.1016/j.scient.2012.12.005>.
132. Osaba, E., et al., *A Tutorial On the design, experimentation and application of metaheuristic algorithms to real-World optimization problems*. Swarm and Evolutionary Computation, 2021. **64**: p. 100888 DOI: <https://doi.org/10.1016/j.swevo.2021.100888>.
133. Abdollahzadeh, B., F.S. Gharehchopogh, and S. Mirjalili, *African vultures optimization algorithm: A new nature-inspired metaheuristic algorithm for global optimization problems*. Computers & Industrial Engineering, 2021. **158**: p. 107408 DOI: <https://doi.org/10.1016/j.cie.2021.107408>.
134. Zhang, J., et al., *Multi-objective optimization of concrete mixture proportions using machine learning and metaheuristic algorithms*. Construction and Building Materials, 2020. **253**: p. 119208 DOI: <https://doi.org/10.1016/j.conbuildmat.2020.119208>.
135. !!! INVALID CITATION !!! [4-7].
136. Huynh, H.D., et al., *A polygonal XFEM with new numerical integration for linear elastic fracture mechanics*. Engineering Fracture Mechanics, 2019. **213**: p. 241-263 DOI: <https://doi.org/10.1016/j.engfracmech.2019.04.002>.
137. van Dongen, B., A. van Oostrum, and D. Zarouchas, *A blended continuum damage and fracture mechanics method for progressive damage analysis of composite structures using XFEM*. Composite Structures, 2018. **184**: p. 512-522 DOI: <https://doi.org/10.1016/j.compstruct.2017.10.007>.
138. Li, H., J. Li, and H. Yuan, *A review of the extended finite element method on macrocrack and microcrack growth simulations*. Theoretical and Applied Fracture Mechanics, 2018. **97**: p. 236-249 DOI: <https://doi.org/10.1016/j.tafmec.2018.08.008>.
139. Shlyannikov, V.N. and I.S. Ishtyryakov, *Crack growth rate and lifetime prediction for aviation gas turbine engine compressor disk based on nonlinear fracture mechanics parameters*. Theoretical and Applied Fracture Mechanics, 2019. **103**: p. 102313 DOI: <https://doi.org/10.1016/j.tafmec.2019.102313>.
140. Khatir, S., et al., *An improved Artificial Neural Network using Arithmetic Optimization Algorithm for damage assessment in FGM composite plates*. Composite Structures, 2021. **273**: p. 114287 DOI: <https://doi.org/10.1016/j.compstruct.2021.114287>.
141. Dadrasi, A., et al., *Experimental study and optimization of fracture properties of epoxy-based nano-composites: Effect of using nano-silica by GEP, RSM, DTM and PSO*. Engineering Fracture Mechanics, 2020. **232**: p. 107047 DOI: <https://doi.org/10.1016/j.engfracmech.2020.107047>.
142. Le-Duc, T., Q.-H. Nguyen, and H. Nguyen-Xuan, *Balancing composite motion optimization*. Information Sciences, 2020. **520**: p. 250-270 DOI: <https://doi.org/10.1016/j.ins.2020.02.013>.
143. Poli, R., J. Kennedy, and T. Blackwell, *Particle swarm optimization*. Swarm Intelligence, 2007. **1**(1): p. 33-57 DOI: 10.1007/s11721-007-0002-0.
144. Warid, W., et al., *Optimal Power Flow Using the Jaya Algorithm*. Energies, 2016. **9**(9) DOI: 10.3390/en9090678.
145. Aggoune, F., *évaluation de l'endommagement des tubes dans leurs conditions d'exploitation*. Magister en Génie Mécanique, Dept Génie Mécanique, Constantine Univ., MENTOURI, 2010.
146. Singh, R., et al. *Zigbee and Long-Range Architecture Based Monitoring System for Oil Pipeline Monitoring with the Internet of Things*. Sustainability, 2021. **13**, DOI: 10.3390/su131810226.
147. *Précis de métallurgie extractive des minerais d'or conventionnels et réfractaires*. 2020, Editions L'Harmattan: Paris.

148. Layus, P., et al., *Study of the sensitivity of high-strength cold-resistant shipbuilding steels to thermal cycle of arc welding*. International Journal of Mechanical and Materials Engineering, 2018. **13**(1): p. 3 DOI: 10.1186/s40712-018-0090-1.
149. Jiang, Z., et al., *Grain refinement and laser energy distribution during laser oscillating welding of Invar alloy*. Materials & Design, 2020. **186**: p. 108195 DOI: <https://doi.org/10.1016/j.matdes.2019.108195>.
150. Mohrbacher, H., *Reverse metallurgical engineering towards sustainable manufacturing of vehicles using Nb and Mo alloyed high performance steels*. Advances in Manufacturing, 2013. **1**(1): p. 28-41 DOI: 10.1007/s40436-013-0002-9.
151. Curnier, A., *Méthodes numériques en mécanique des solides*. 1993: PPUR presses polytechniques.
152. Charmet, J.-C., *Mécanique du solide et des matériaux Elasticité-Plasticité-Rupture*. ESPCI-Laboratoire d'Hydrodynamique et Mécanique Physique, 2005: p. 113-144.
153. Egorushkin, V.E. and V.E. Panin, *Physical foundations of nonlinear fracture mechanics*. Mechanics of Solids, 2013. **48**(5): p. 525-536 DOI: 10.3103/S0025654413050087.
154. Erdogan, F., *Stress Intensity Factors*. Journal of Applied Mechanics, 1983. **50**(4b): p. 992-1002 DOI: 10.1115/1.3167212.
155. Paris, P.C., *A brief history of the crack tip stress intensity factor and its application*. Meccanica, 2014. **49**(4): p. 759-764 DOI: 10.1007/s11012-014-9896-y.
156. Gdoutos, E.E., *Fracture mechanics criteria and applications*. Vol. 10. 2012: Springer Science & Business Media.
157. Fang, G., et al., *A method to couple state-based peridynamics and finite element method for crack propagation problem*. Mechanics Research Communications, 2019. **95**: p. 89-95 DOI: <https://doi.org/10.1016/j.mechrescom.2019.01.005>.
158. Hecht-Nielsen, R. *Neurocomputer Applications*. in *Neural Computers*. 1989. Berlin, Heidelberg: Springer Berlin Heidelberg.
159. Xue, L., *Ductile fracture modeling: theory, experimental investigation and numerical verification*. 2007, Massachusetts institute of technology.
160. Aldakheel, F., P. Wriggers, and C. Miehe, *A modified Gurson-type plasticity model at finite strains: formulation, numerical analysis and phase-field coupling*. Computational Mechanics, 2018. **62**(4): p. 815-833 DOI: 10.1007/s00466-017-1530-0.
161. Jiang, W., Y. Li, and J. Su, *Modified GTN model for a broad range of stress states and application to ductile fracture*. European Journal of Mechanics - A/Solids, 2016. **57**: p. 132-148 DOI: <https://doi.org/10.1016/j.euromechsol.2015.12.009>.
162. Li, J., et al., *Numerical simulation of incremental sheet forming based on GTN damage model*. The International Journal of Advanced Manufacturing Technology, 2015. **81**(9): p. 2053-2065 DOI: 10.1007/s00170-015-7333-6.
163. Jang, Y.-Y., et al., *Evaluations of Ductile and Cleavage Fracture Using Coupled GTN and Beremin Model in API X70 Pipelines Steel*, in *ASME 2019 38th International Conference on Ocean, Offshore and Arctic Engineering*. 2019.
164. Miloud, M.H., I. Zidane, and M. Mendas, *Coupled identification of the hardening behavior laws and Gurson–Tvergaard–Needleman damage parameters–Validation on tear test of 12NiCr6 CT specimen*. Frattura ed Integrità Strutturale, 2019. **13**(49): p. 630-642.
165. Abaqus, C., *Analysis user's manual, Version 6.12*. 2012, ABAQUS.
166. Gavrus, A., *Identification automatique des paramètres rhéologiques par analyse inverse*. 1996.
167. Diot, S., et al., *Minimization of friction influence on the evaluation of rheological parameters from compression test: Application to a forging steel behavior identification*. Journal of engineering materials and technology, 2009. **131**(1).

168. Kuna, M. and M. Springmann, *Determination of ductile damage parameters by local deformation fields*, in *Fracture of Nano and Engineering Materials and Structures*. 2006, Springer. p. 535-536.
169. Djouabi, M., A. Ati, and P.-Y. Manach, *Identification strategy influence of elastoplastic behavior law parameters on Gurson–Tvergaard–Needleman damage parameters: Application to DP980 steel*. *International Journal of Damage Mechanics*, 2019. **28**(3): p. 427-454.
170. Paermentier, B. and R. Hojjati Talemi, *Numerical modelling of dynamic ductile fracture propagation in different lab-scale experiments using GTN damage model*. *Frattura ed Integrità Strutturale*, 2020. **52**: p. 105-112.
171. Ledoux, Y., et al., *Optimisation of a stamping process by a design of experiment linked to a modal analysis of geometric defects*. *Archives of civil and mechanical engineering*, 2006. **6**(1): p. 5-17.
172. Abbassi, F., et al., *Parameter identification of a mechanical ductile damage using Artificial Neural Networks in sheet metal forming*. *Materials & Design*, 2013. **45**: p. 605-615.
173. Higham, D.J. and N.J. Higham, *MATLAB guide*. 2016: SIAM.
174. Bakhshi, N. and F. Taheri-Behrooz, *Length effect on the stress concentration factor of a perforated orthotropic composite plate under in-plane loading*. 2019 DOI: <http://dx.doi.org/10.12989/cme.2019.1.1.071>.
175. Bouledroua, O., et al., *Qualification d'un Acier API 5L X70: Etude Expérimentale et Validation Numérique*. Nature & Technology, Hassiba Ben Bouali University of Chlef, Algeria et Université Paul Verlaine de Metz, France, 2015.
176. Raafat, E., et al., *Fatigue and thermal stress analysis of submerged steel pipes using ANSYS software*. *Ocean Engineering*, 2019. **193**: p. 106574 DOI: <https://doi.org/10.1016/j.oceaneng.2019.106574>.
177. Gholami, H., S. Shahrooi, and M. Shishesaz, *Predicting the Burst Pressure of High-Strength Carbon Steel Pipe with Gouge Flaws Using Artificial Neural Network*. *Journal of Pipeline Systems Engineering and Practice*, 2020. **11**(4): p. 04020034 DOI: 10.1061/(ASCE)PS.1949-1204.0000478.
178. Abarghouee, H., et al., *Modelling of hot flow behavior of API-X70 microalloyed steel by genetic algorithm and comparison with experiments*. *International Journal of Pressure Vessels and Piping*, 2021. **189**: p. 104261 DOI: <https://doi.org/10.1016/j.ijpvp.2020.104261>.
179. Mirjalili, S. and A. Lewis, *The Whale Optimization Algorithm*. *Advances in Engineering Software*, 2016. **95**: p. 51-67 DOI: <https://doi.org/10.1016/j.advengsoft.2016.01.008>.
180. Talemi, R.H., *Numerical simulation of dynamic brittle fracture of pipeline steel subjected to DWTT using XFEM-based cohesive segment technique*. *Frattura ed Integrità Strutturale*, 2016. **10**(36): p. Pages 151-159 DOI: 10.3221/IGF-ESIS.36.15.
181. Bellali, M.A., et al., *XFEM and CZM modeling to predict the repair damage by composite patch of aircraft structures: Debonding parameters*. *Composite Structures*, 2021. **266**: p. 113805 DOI: <https://doi.org/10.1016/j.compstruct.2021.113805>.
182. Omar, Z., et al., *Predicting the Flexural Behaviour of CFRP-Strengthened Concrete Beam using Combined XFEM and Cohesive Zone Model*. *Journal of Applied Science and Engineering*, 2022. **25**(6): p. 925-938 DOI: 10.6180/jase.202212_25(6).0003.
183. Dagostini, V.d.S., et al., *Microstructural analysis and mechanical behavior of the HAZ in an API 5L X70 steel welded by GMAW process*. *Welding in the World*, 2021. **65**(6): p. 1051-1060 DOI: 10.1007/s40194-021-01102-6.
184. Behroozinia, P., R. Mirzaeifar, and S. Taheri, *A review of fatigue and fracture mechanics with a focus on rubber-based materials*. *Proceedings of the Institution of Mechanical Engineers, Part L: Journal of Materials: Design and Applications*, 2017. **233**(5): p. 1005-1019 DOI: 10.1177/1464420717719739.
185. Hojjati-Talemi, R., S. Cooreman, and D. Van Hoecke, *Finite element simulation of dynamic brittle fracture in pipeline steel: A XFEM-based cohesive zone approach*. *Proceedings of the Institution*

- of Mechanical Engineers, Part L: Journal of Materials: Design and Applications, 2016. **232**(5): p. 357-370 DOI: 10.1177/1464420715627379.
186. Sheela, K.G. and S.N. Deepa, *Review on Methods to Fix Number of Hidden Neurons in Neural Networks*. Mathematical Problems in Engineering, 2013. **2013**: p. 425740 DOI: 10.1155/2013/425740.
187. Guha, R., D.T. Stanton, and P.C. Jurs, *Interpreting Computational Neural Network Quantitative Structure–Activity Relationship Models: A Detailed Interpretation of the Weights and Biases*. Journal of Chemical Information and Modeling, 2005. **45**(4): p. 1109-1121 DOI: 10.1021/ci050110v.
188. Ahmadianfar, I., O. Bozorg-Haddad, and X. Chu, *Gradient-based optimizer: A new metaheuristic optimization algorithm*. Information Sciences, 2020. **540**: p. 131-159 DOI: <https://doi.org/10.1016/j.ins.2020.06.037>.